

Nanotechnology for Electrooptical and Photovoltaic Devices

Guest Editors: Teen-Hang Meen, Stephen D. Prior, Liang-Wen Ji,
and Yu-Jen Hsiao





Nanotechnology for Electrooptical and Photovoltaic Devices

International Journal of Photoenergy

Nanotechnology for Electrooptical and Photovoltaic Devices

Guest Editors: Teen-Hang Meen, Stephen D. Prior,
Liang-Wen Ji, and Yu-Jen Hsiao



Copyright © 2013 Hindawi Publishing Corporation. All rights reserved.

This is a special issue published in "International Journal of Photoenergy." All articles are open access articles distributed under the Creative Commons Attribution License, which permits unrestricted use, distribution, and reproduction in any medium, provided the original work is properly cited.

Editorial Board

M. Sabry Abdel-Mottaleb, Egypt
Nihal Ahmad, USA
Nicolas Alonso-Vante, France
Wayne A. Anderson, USA
Vincenzo Augugliaro, Italy
Detlef W. Bahnemann, Germany
Mohammad A. Behnajady, Iran
Ignazio Renato Bellobono, Italy
Raghu N. Bhattacharya, USA
Pramod H. Borse, India
Gion Calzaferri, Switzerland
Adriana G. Casas, Argentina
Wonyong Choi, Korea
Věra Cimrova, Czech Republic
Vikram Dalal, USA
Dionysios D. Dionysiou, USA
Mahmoud M. El-Nahass, Egypt
Ahmed Ennaoui, Germany
Chris Ferekides, USA
Beverley Glass, Australia
M. A. Gondal, Saudi Arabia
Shinya Higashimoto, Japan
Yadong Jiang, China

Chun-Sheng Jiang, USA
Shahed Khan, USA
Cooper Harold Langford, Canada
Yuexiang Li, China
Stefan Lis, Poland
N. Mohammad Mahmoodi, Iran
Dionissios Mantzavinos, Greece
Ugo Mazzucato, Italy
Jacek Miller, Poland
Jarugu N. Moorthy, India
Franca Morazzoni, Italy
Fabrice Morlet-Savary, France
Ebinazar B. Namdas, Australia
M. da Graça P. Neves, Portugal
Leonidas Palilis, Greece
Leonardo Palmisano, Italy
Ravindra K. Pandey, USA
David Lee Phillips, Hong Kong
Pierre Pichat, France
Gianluca Li Puma, UK
Xie Quan, China
Tijana Rajh, USA
Peter Robertson, UK

Avigdor Scherz, Israel
Lukas Schmidt-Mende, Germany
Panagiotis Smirniotis, USA
Zofia Stasicka, Poland
Juliusz Sworakowski, Poland
Nobuyuki Tamaoki, Japan
Gopal N. Tiwari, India
Nikolai V. Tkachenko, Finland
Veronica Vaida, USA
Roel van De Krol, Germany
Mark van Der Auweraer, Belgium
Ezequiel Wolcan, Argentina
Man Shing Wong, Hong Kong
David Worrall, UK
Fahrettin Yakuphanoglu, Turkey
Minjoong Yoon, Republic of Korea
Hongtao Yu, USA
Jimmy C. Yu, Hong Kong
Jun-Ho Yum, Switzerland
Klaas Zachariasse, Germany
Lizhi Zhang, China
Jincai Zhao, China

Contents

Nanotechnology for Electrooptical and Photovoltaic Devices, Teen-Hang Meen, Stephen D. Prior, Liang-Wen Ji, and Yu-Jen Hsiao
Volume 2013, Article ID 292485, 1 page

Postannealing Effect at Various Gas Ambients on Ohmic Contacts of Pt/ZnO Nanobilayers toward Ultraviolet Photodetectors, Chung-Hua Chao, Mao-Yi Chen, Chii-Ruey Lin, Yueh-Chung Yu, Yeong-Der Yao, and Da-Hua Wei
Volume 2013, Article ID 372869, 9 pages

Two-Axis Solar Heat Collection Tracker System for Solar Thermal Applications, Tsung-Chieh Cheng, Wei-Cheng Hung, and Te-Hua Fang
Volume 2013, Article ID 803457, 7 pages

High Efficiency of Dye-Sensitized Solar Cells Based on Ruthenium and Metal-Free Dyes, Che-Lung Lee, Wen-Hsi Lee, and Cheng-Hsien Yang
Volume 2013, Article ID 250397, 6 pages

Design of High Efficiency Illumination for LED Lighting, Yong-Nong Chang, Hung-Liang Cheng, and Chih-Ming Kuo
Volume 2013, Article ID 471384, 8 pages

The Investigation on Color Purity of Blue Organic Light-Emitting Diodes (BOLED) by Hole-Blocking Layer, Kan-Lin Chen, Chien-Jung Huang, Wen-Ray Chen, Chih-Chieh Kang, Wen-How Lan, and Yu-Chen Lee
Volume 2013, Article ID 878537, 6 pages

Dye-Sensitized Solar Cells with Optimal Gel Electrolyte Using the Taguchi Design Method, Jenn-Kai Tsai, Wen Dung Hsu, Tian-Chiuan Wu, Jia-Song Zhou, Ji-Lin Li, Jian-Hao Liao, and Teen-Hang Meen
Volume 2013, Article ID 617126, 5 pages

Triazoloisoquinoline-Based/Ruthenium-Hybrid Sensitizer for Efficient Dye-Sensitized Solar Cells, Che-Lung Lee, Wen-Hsi Lee, and Cheng-Hsien Yang
Volume 2013, Article ID 984516, 5 pages

To Enhance Performance of Light Soaking Process on ZnS/CuIn_{1-x}Ga_xSe₂ Solar Cell, Yu-Jen Hsiao, Chung-Hsin Lu, and Te-Hua Fang
Volume 2013, Article ID 561948, 5 pages

Fabrication and Characterization of CuInSe₂ Thin Film Applicable for a Solar Energy Light Absorption Material via a Low Temperature Solid State Reaction, Kuo-Chin Hsu, Yaw-Shyan Fu, Pei-Ying Lin, I-Tseng Tang, and Jiunn-Der Liao
Volume 2013, Article ID 156964, 7 pages

Preparation of Vertically Aligned ZnO/TiO₂ Core-Shell Composites for Dye-Sensitized Solar Cells, Lung-Chuan Chen, Shuei-Feng Tsai, Jean-Hong Chen, and Gaun-Wen Wang
Volume 2013, Article ID 417964, 9 pages

Low Cost Amorphous Silicon Intrinsic Layer for Thin-Film Tandem Solar Cells, Ching-In Wu, Shouu-Jinn Chang, Kin-Tak Lam, Shuguang Li, and Sheng-Po Chang
Volume 2013, Article ID 183626, 5 pages

Improved Efficiency of Flexible Organic Light-Emitting Diodes by Insertion of Ultrathin SiO₂ Buffer Layers, Chien-Jung Huang, Kan-Lin Chen, Po-Wen Sze, Wen-Ray Chen, Teen-Hang Meen, and Shi-Lun Wu
Volume 2013, Article ID 437304, 5 pages

Using Flexible Polyimide as a Substrate to Deposit ZnO:Ga Thin Films and Fabricate p-i-n α -Si:H Thin-Film Solar Cells, Fang-Hsing Wang, Cheng-Fu Yang, and Min-Chu Liu
Volume 2013, Article ID 263213, 7 pages

Optimal Color Stability for White Organic Light-Emitting Diode (WOLED) by Using Multiple-Ultra-Thin Layers (MUTL), Kan-Lin Chen, Chien-Jung Huang, Wen-Ray Chen, Fong-Yi Lin, Teen-Hang Meen, and Chih-Chieh Kang
Volume 2013, Article ID 173289, 6 pages

Study of Small Molecule Organic Solar Cells Performance Based on Boron Subphthalocyanine Chloride and C₆₀, Jhong-Ciao Ke, Yeong-Her Wang, Kan-Lin Chen, Pao-Hsun Huang, and Chien-Jung Huang
Volume 2013, Article ID 803126, 5 pages

Investigating the Properties of CIS Absorber Layer by Using the Spray Coating Method, Chien-Chen Diao, Cheng-Fu Yang, Chia-Ching Wu, Wen-How Lan, and Yen-Lin Chen
Volume 2013, Article ID 905271, 7 pages

Optimal Design for the Diffusion Plate with Nanoparticles in a Diffusive Solar Cell Window by Mie Scattering Simulation, Ruei-Tang Chen, Chih-Chieh Kang, Jeng-Feng Lin, Tzu-Chi Lin, and Chih-Wen Lai
Volume 2013, Article ID 481637, 5 pages

Study of the Behavior of Titanium Alloys as the Cathode for Photovoltaic Hydrogen Production, Chien-Lung Huang, Yu-Jia Gao, Tao-Liang Chuang, Vincent K. S. Hsiao, and Tair-I Wu
Volume 2013, Article ID 857491, 6 pages

The Effects of Dilute Sulfuric Acid on Sheet Resistance and Transmittance in Poly(3,4-thylenedioxythiophene): Poly(styrenesulfonate) Films, Teen-Hang Meen, Kan-Lin Chen, Yu-Hao Chen, Wen-Ray Chen, Dei-Wei Chou, Wen-How Lan, and Chien-Jung Huang
Volume 2013, Article ID 843410, 6 pages

Editorial

Nanotechnology for Electrooptical and Photovoltaic Devices

Teen-Hang Meen,¹ Stephen D. Prior,² Liang-Wen Ji,³ and Yu-Jen Hsiao⁴

¹ Department of Electronic Engineering, National Formosa University, Yunlin 632, Taiwan

² Aeronautics, Astronautics and Computational Engineering, The University of Southampton, Southampton SO17 1BJ, UK

³ Institute of Electro-Optical and Materials Science, National Formosa University, Yunlin 632, Taiwan

⁴ National Nano Device Laboratories, Tainan 741, Taiwan

Correspondence should be addressed to Teen-Hang Meen; thmeen@nfu.edu.tw

Received 1 December 2013; Accepted 1 December 2013

Copyright © 2013 Teen-Hang Meen et al. This is an open access article distributed under the Creative Commons Attribution License, which permits unrestricted use, distribution, and reproduction in any medium, provided the original work is properly cited.

Nanomaterials which provide one of the greatest potentials for improving performance and extended capabilities of products in a number of industrial sectors are a new class of materials, having dimensions in the 1~100 nm range. Nanostructures can be divided into zero-dimensional, one-dimensional, and two-dimensional based on their shapes. The recent emphasis in the nanomaterials research is put on 1D nanostructures at the expense of 0D and 2D ones, perhaps due to the intriguing possibility of using them in a majority of short-term future applications. The most successful examples are seen in the microelectronics, where “smaller” has always meant a greater performance ever since the invention of transistors, for example, higher density of integration, faster response, lower cost, and less power consumption.

In recent years, optoelectronic and solar cells devices have been a highly developing field, due to the flexibility and light weight for energy conversion, which has the potential to be deployable. Therefore, the field of electrooptical and photovoltaic devices has been the subject of reviews. Electrooptical and photovoltaic devices are environmentally sustainable, in particular considering the availability of the nanostructured raw materials. Science and technology developments in electrooptical and photovoltaic devices over the next several years and their influence on the economics of electrooptical and PV installations are likely to establish which energy technologies become dominant for decades to come. The chance to share and discuss these crucial electrooptical and PV developments in a timely and influential forum is important.

This special issue selects 19 papers about dye-sensitized solar cells, small molecule organic solar cells, ZnS/CuIn_{1-x}Ga_xSe₂ solar cell, thin-film solar cells, photovoltaic devices, and other related fields. This special issue enables interdisciplinary collaboration between science and engineering technologists in the academic and industrial fields.

Teen-Hang Meen
Stephen D. Prior
Liang-Wen Ji
Yu-Jen Hsiao

Research Article

Postannealing Effect at Various Gas Ambients on Ohmic Contacts of Pt/ZnO Nanobilayers toward Ultraviolet Photodetectors

Chung-Hua Chao,¹ Mao-Yi Chen,¹ Chii-Ruey Lin,¹ Yueh-Chung Yu,²
Yeong-Der Yao,² and Da-Hua Wei¹

¹ Institute of Manufacturing Technology and Graduate Institute of Mechanical and Electrical Engineering,
National Taipei University of Technology, Taipei 106, Taiwan

² Institute of Physics, Academia Sinica, Taipei 115, Taiwan

Correspondence should be addressed to Yueh-Chung Yu; phycyu@phys.sinica.edu.tw and Da-Hua Wei; dhwei@ntut.edu.tw

Received 20 September 2013; Accepted 18 November 2013

Academic Editor: Teen-Hang Meen

Copyright © 2013 Chung-Hua Chao et al. This is an open access article distributed under the Creative Commons Attribution License, which permits unrestricted use, distribution, and reproduction in any medium, provided the original work is properly cited.

This paper describes a fabrication and characterization of ultraviolet (UV) photodetectors based on Ohmic contacts using Pt electrode onto the epitaxial ZnO (0002) thin film. Plasma enhanced chemical vapor deposition (PECVD) system was employed to deposit ZnO (0002) thin films onto silicon substrates, and radio-frequency (RF) magnetron sputtering was used to deposit Pt top electrode onto the ZnO thin films. The as-deposited Pt/ZnO nanobilayer samples were then annealed at 450°C in two different ambients (argon and nitrogen) to obtain optimal Ohmic contacts. The crystal structure, surface morphology, optical properties, and wettability of ZnO thin films were analyzed by X-ray diffraction (XRD), field emission scanning electron microscopy (FE-SEM), atomic force microscopy (AFM), photoluminescence (PL), UV-Vis-NIR spectrophotometer, and contact angle meter, respectively. Moreover, the photoconductivity of the Pt/ZnO nanobilayers was also investigated for UV photodetector application. The above results showed that the optimum ZnO sample was synthesized with gas flow rate ratio of 1:3 diethylzinc [DEZn, Zn(C₂H₅)₂] to carbon dioxide (CO₂) and then combined with Pt electrode annealed at 450°C in argon ambient, exhibiting good crystallinity as well as UV photo responsibility.

1. Introduction

It is known that only ultraviolet A (UVA) with wavelength ranging from 320 to 400 nm of the sunlight can pass through the atmosphere and reach the earth's surface. The UVA might harm human's skin, and therefore it is an important issue to develop ultraviolet (UV) photodetector in the UVA-wavelength region. Many wide band gap materials such as GaN, AlGaIn, ZnSe, and diamond have been used for the UV photodetector applications [1–6]. Compared with the above materials, zinc oxide (ZnO) is considered as potential candidate compound for UV detector owing to its wide direct band gap of 3.37 eV at room temperature, relatively large exciton binding energy of 60 meV, nontoxicity, outstanding thermal and chemical stability, and low power threshold for optical pumping as well as rich raw

materials [7, 8]. However, due to the challenge of p-type doping in ZnO structures, fabrication of ZnO p-n junction based on UV photodetector is still under development [9]. Hence, either Ohmic contact based photoconductive type or Schottky contact based photovoltage type of ZnO metal-semiconductor-metal (MSM) is another way to develop UV photodetector [10, 11]. Comparing the differences between Ohmic and Schottky contact types, the Ohmic contact based photoconductive type device is typically more easily made and more understood. High quality ZnO films with good Ohmic contact are essential for fabricating high performance UV photodetector, which is based on a strong oxygen chemisorption and physisorption mechanism on both the grain boundaries and surface [12, 13].

Over the past few decades, various growth techniques of stoichiometric ZnO phase have been used, such as thermal

evaporation, radio-frequency (RF) magnetron sputtering, pulsed laser deposition (PLD), molecular beam epitaxy (MBE), metal organic chemical vapor deposition (MOCVD), and plasma enhanced chemical vapor deposition (PECVD) [14–18]. Among these techniques, the PECVD system is a promising one for fabricating large-area uniform ZnO thin films in order to apply for future electronic devices and sensors because it has numerous advantages, namely, low cost and high growth rates. On the other hand, the plasma bombardment can increase the density of thin films and enhance the ion decomposition reaction rate, which was used to improve the thin films crystallinity [19]. Thus, the PECVD system was used to grow ZnO thin films onto silicon substrates with various gas flow rate ratios of diethylzinc (DEZn) to carbon dioxide (CO₂) and at a fixed temperature of 400°C in this presented work. On the other hand, there are some reports on Ohmic contacts of ZnO-based devices using ZrB₂/Pt/Au, Ti/Au, Pt/Ni/Au or Ni/Pt, and so forth as the contact-electrode metals [20–23]. Due to high thermal and electrical conductivity, good temperature and chemical stability, platinum (Pt) is a better material for electrode application. Herein, Pt as electrode material of Ohmic contact was used to deposit onto ZnO films by RF magnetron sputtering.

However, there is little report on the effects of post-annealing on electrical properties of Pt/ZnO contacts through deposition of epitaxial ZnO films onto Si substrates. In addition, Pt metal forms an Ohmic contact with n-type ZnO. Thus, ZnO/Pt heterostructures could offer a range of advantages for the realization of optoelectronic devices such as UV photodetectors. The electrical properties of Pt/ZnO film contacts are a key to the use of ZnO films in such devices, and a study of such properties is vital in determining the potential of such heterostructure for device applications. The main aim of the present paper is to systematically study the effects of different gas flow rate ratios of DEZn to CO₂ on crystalline quality and uniformity of epitaxial ZnO films, modification of native defects in ZnO films, and the electrical properties of Pt/ZnO nanobilayer films contact and explore the potential application of UV photodetector. This presented study was separated into two parts. The first part was the synthesis of epitaxial ZnO films on silicon substrates by PECVD system with various CO₂ flow rates. The second part was the deposition of Pt to form Ohmic contacts onto ZnO films by RF magnetron sputtering. The standard lift-off process was used to fabricate the UV detectors with interdigitated electrodes. Furthermore, the as-prepared UV devices were postannealed via rapid thermal annealing (RTA) at various temperatures and with different ambients (argon and nitrogen) to obtain Ohmic contacts. The crystalline structure, surface morphology, optical properties, and wettability of ZnO thin films were investigated by X-ray diffraction (XRD), field emission scanning electron microscopy (FE-SEM), atomic force microscopy (AFM), room temperature photoluminescence spectra (PL), and contact angle meter, respectively. *I-V* curves were used to determine the Ohmic

contacts efficiency. Finally, the photoresponse of the devices at room temperature in air was discussed.

2. Experimental Procedures

ZnO thin films were deposited on silicon (100) substrates employing PECVD system, which used diethylzinc [DEZn, Zn (C₂H₅)₂] and carbon dioxide (CO₂) gas as precursors for supplying zinc and oxygen sources, respectively. The 15 cm diameter showerhead served as the top electrode and was connected with a 13.56 MHz radio-frequency (RF) power that could generate the plasma through a match network. The bottom electrode was grounded and served as the sample stage. The distance between top electrode and bottom electrode was fixed at 30 mm. All the 10 mm × 10 mm silicon substrates were cleaned by using acetone, alcohol, and de-ionized water, for half an hour in an ultrasonic cleaner. The system was evacuated to base pressure at 3×10^{-6} Torr by rotary pump and turbo pump, respectively. Subsequently, the argon plasma induced from RF generator in the chamber was used to clean the substrate surface oxide layer for 15 minutes. The working pressure of the chamber was kept at 6 Torr and RF power was fixed at 70 W, and the substrates were heated at 400°C during ZnO thin films growth. A series of ZnO thin films with the fixed thickness of 500 nm were synthesized on the silicon substrates with different gas flow rate ratios of DEZn to CO₂ (1:1, 1:2, and 1:3). Crystalline structure of ZnO thin films was characterized by X-ray diffraction (XRD) with Cu K_α radiation ($\lambda = 1.54 \text{ \AA}$). The surface morphology of ZnO films was observed by field emission scanning electron microscopy (FE-SEM). The surface topography and roughness of thin films were further analyzed from the atomic force microscope (AFM). Photoluminescence (PL) was carried out at room temperature to study the optical properties of the ZnO thin films through a He-Cd laser (325 nm). The optical transmittance was recorded by using a MP100-ME UV-Vis-NIR spectrophotometer and the wettability of ZnO thin films was also measured by contact angle meter, respectively.

As for UV photodetector fabrication, the interdigitated Pt (thickness ~100 nm) Ohmic contact electrode was fabricated via conventional UV lithography, wet-etching methods, and RF magnetron sputtering to form finger-pattern onto epitaxial ZnO (0002) films. The finger-pattern of the contact electrodes was 30 μm wide (14pairs) and had an interelectrode spacing of 150 μm. The photo image of interdigitated electrode is shown in Figure 1. In order to form Ohmic contacts, ZnO and Pt would be directly connected. Unfortunately, the work functions of the above materials are not close, 5.65 eV and 4.3 eV, respectively. For the sake of overcoming mismatch of work functions, the rapid thermal annealing (RTA) was used instead to form Ohmic contacts. Postannealing was performed at different temperatures between 350°C and 550°C for 10 min at argon and nitrogen ambients, respectively. The Ahilent HP 1456S measurement system combined with a 38 mW/cm² mercury arc lamp (Hamamatsu-deuterium L2D2) was used as the UV (365 nm) light source to measure current-voltage (*I-V*) characteristic and photoresponse, respectively.

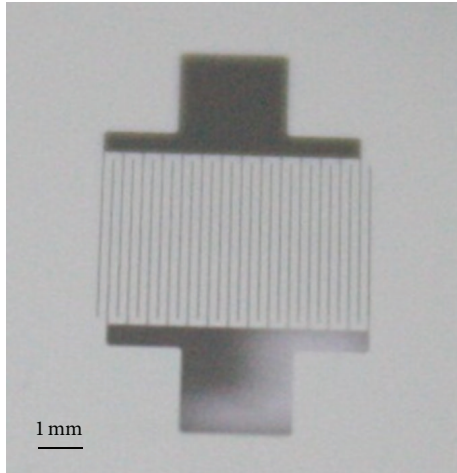


FIGURE 1: The photo image is for the interdigitated electrode.

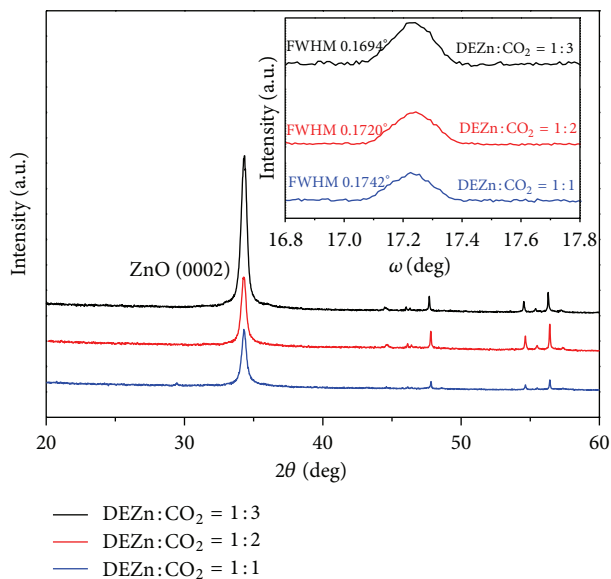


FIGURE 2: X-ray diffraction patterns for the ZnO (0002) thin films synthesized with different gas flow rate ratios of DEZn to CO_2 . Inset showed the corresponding rocking curve (ω) scan and FWHM values of ZnO (0002) peak.

3. Results and Discussion

3.1. Material Optimization. Figure 2 shows the X-ray diffraction (XRD) patterns for the ZnO thin films synthesized by PECVD system with different gas flow rate ratios of DEZn to CO_2 . The XRD patterns of all ZnO samples exhibit only a strong c -axis (0002) diffraction peak located at 34.4° , indicating that epitaxial thin films possess a hexagonal wurtzite structure. The lowest surface energy of the (0002) basal plane in ZnO leads to a preferred orientation in the [0001] direction; as a result, ZnO thin films have been grown with c -axis orientation onto epitaxial substrate under optimum growth conditions [24]. However, the crystalline quality of the ZnO thin films is related to the gas flow rate ratio of DEZn

to CO_2 . During the ZnO phase growth, CO_2 concentration played an important role due to the oxygen ions originating from CO_2 which that were relatively low in the chamber when gas flow rate value was 1:1, which indicated the zinc ions had no sufficient chance to react with oxygen ions to form a high property ZnO phase. Consequently, with the increasing gas flow rate of CO_2 , the diffraction peak of the ZnO (0002) gradually became sharp and narrow. The strongest of (0002) diffraction peaks was obtained at the gas flow rate value of 1:3 (DEZn to CO_2). The inset in Figure 2 showed the full width at half maximum (FWHM) of ZnO (0002) diffraction peak, which was determined by X-ray rocking curve (ω) scan. The FWHM of the (0002) diffraction peak of the ZnO thin film with gas flow rate ratio of 1:3 shows an extremely small value of 0.1694° , while the ZnO thin films with gas flow rate ratios of 1:2 and 1:1 exhibit relatively large values of 0.1720° and 0.1742° , respectively. The X-ray rocking curve mostly demonstrates the degree of the tilt component, and the tilt itself is related to screw-type threading dislocations. Therefore, the optimum synthesized condition of epitaxial ZnO (0002) film with the gas flow rate ratio of DEZn to CO_2 is 1:3 in this presented work. This parameter can effectively reduce screw dislocation density with the highest crystalline quality of stoichiometric ZnO thin film.

In-plane surface morphology of epitaxial ZnO (0002) films was observed by FE-SEM as shown in Figures 3(a)–3(c). PECVD system is a promising technique for synthesizing ZnO phase by using DEZn and CO_2 mixtures. Also, it is especially easy to break the oxygen–oxygen bonds from CO_2 to react with zinc atoms from DEZn, leading to the compact surface [25]. The SEM top view images clearly show that all of the ZnO thin films have smoothability of compact surfaces with curvature boundary and are densely packed with spherical grains. Additionally, the thickness of all ZnO thin films is about 500 nm with self-assembled columnar structures along the c -axis [0001] determined by cross section images in the inset of Figures 3(a)–3(c). From the AFM surface topography images as shown in Figures 3(d)–3(f), the average surface roughness values (root-mean-square (RMS)) with the gas flow rate ratios of DEZn to CO_2 (1:1, 1:2, and 1:3) showed 6.46 nm, 6.82 nm, and 8.97 nm ($1\ \mu\text{m} \times 1\ \mu\text{m}$), respectively. The above results indicated that the epitaxial ZnO (0002) thin film could provide a suitable nanometer-scale smoothness topography for the subsequent deposition of Pt top electrode onto its surface.

Figure 4 illustrates the room temperature PL spectrum. The spectra mainly consist of two emission bands: a near-band-edge (NBE) emission and a broad defect-related visible emission (500–700 nm). The result exhibits that the main emission bands intensity is closely related to the gas flow rate ratios of DEZn to CO_2 . All the epitaxial ZnO (0002) thin films show a strong NBE emission band which is attributed to the recombination of free-excitons through an exciton-exciton collision process [26]. However, with varying the gas flow rate ratios of DEZn to CO_2 (ranging from 1:3 to 1:1), the intensity of NBE emission became weaker with slight red shift, accompanied with the visible emission band became stronger. In general, the lattice distortions and localization of charges from interface defects or point defects may cause

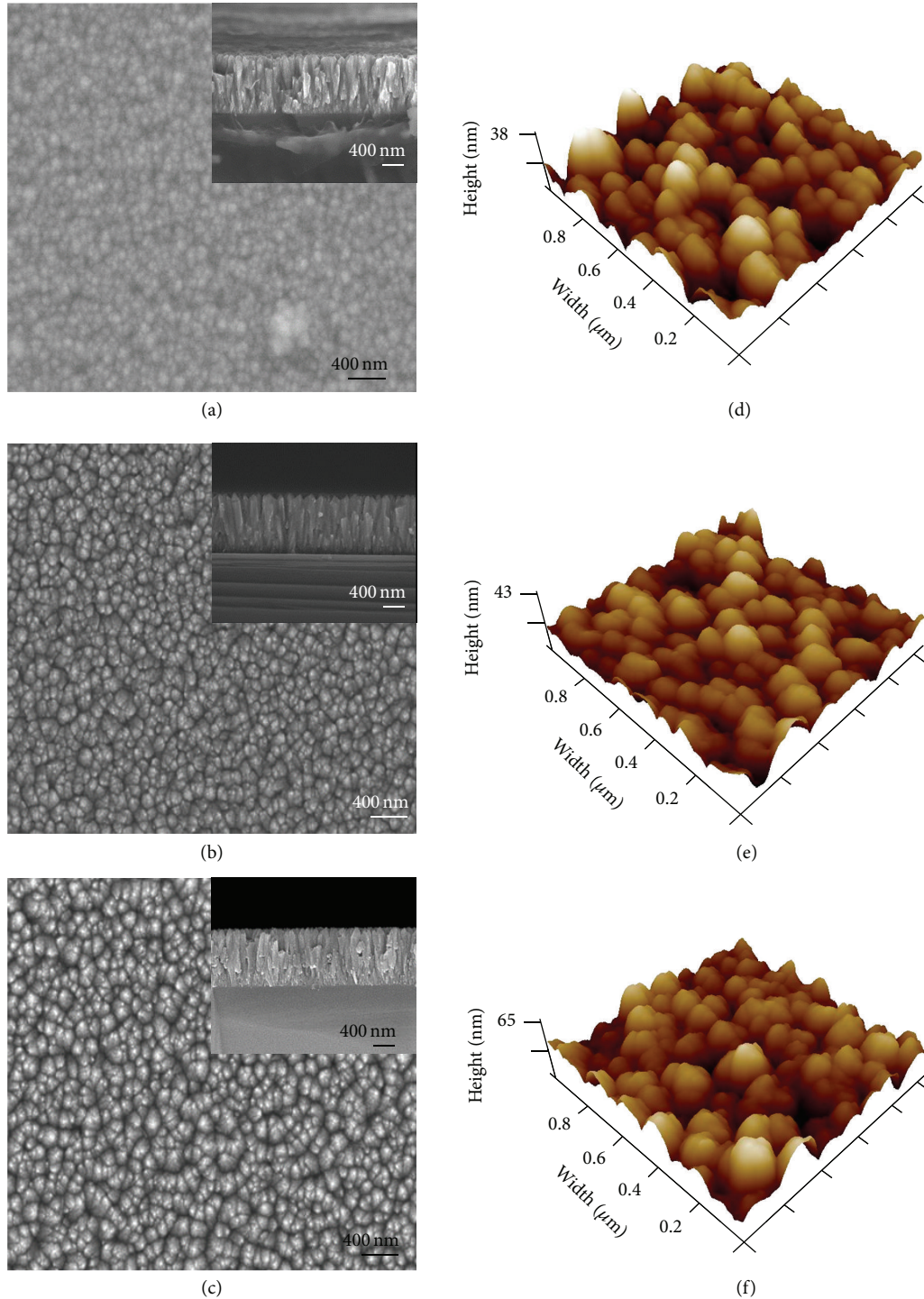


FIGURE 3: In-plane and out-of-plane field emission scanning electron microscopy images for ZnO (0002) thin films synthesized with gas flow rate ratios of DEZn to CO_2 of (a) 1:1, (b) 1:2, and (c) 1:3; the corresponding AFM images ($1 \times 1 \mu\text{m}^2$) with gas flow rate ratios of (d) 1:1, (e) 1:2, and (f) 1:3, respectively.

the red shift of emission band [27]. On the other hand, the visible emission band is generally referred to the impurities and various structural defects in the ZnO thin films such as zinc interstitial and oxygen vacancy [28]. When thin film quality of ZnO was improved via providing sufficient oxygen

ions, the density of defect was reduced and resulted in a strong intensity of NBE emission with blue shift in the UV region and the visible emission gradually disappeared. According to the above results, the epitaxial ZnO (0002) thin film grown under the optimum gas flow rate ratio of 1:3 (DEZn to CO_2)

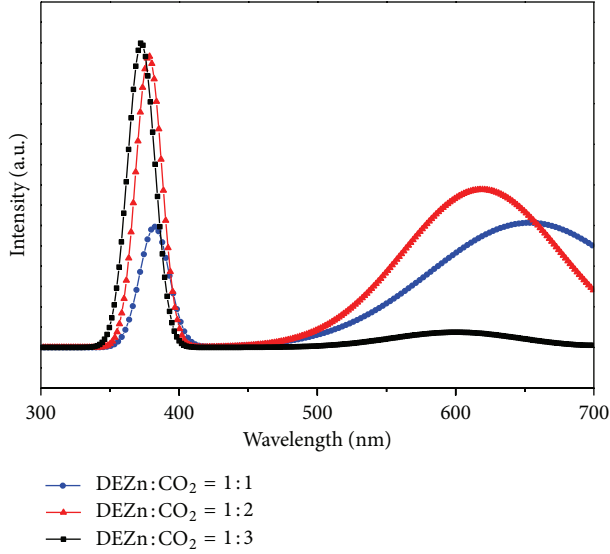
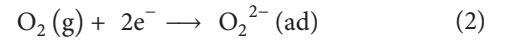
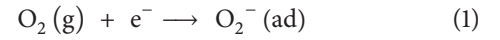


FIGURE 4: Photoluminescence spectra for the ZnO (0002) thin films synthesized with different gas flow rate ratios of DEZn to CO₂.

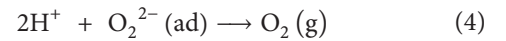
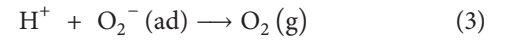
is a promising approach for application in the realization of ultraviolet (UV) photon detectors.

3.2. UV Photodetector Fabrication and Responsivity. Current-voltage (*I-V*) characteristics of the Pt/ZnO nanobilayer devices annealed at various temperatures (350°C, 450°C, and 550°C) in argon ambience for 10 min are shown in Figure 5(a). Only an obvious linear behavior could be observed for the Pt/ZnO device annealed at 450°C, which indicated that the high quality Ohmic contact has been achieved at the Pt/ZnO interface. The device was further annealed at 450°C in nitrogen ambience for 10 min, and corresponding *I-V* characteristics of device were as shown in Figure 5(b). The Ohmic effect of Pt/ZnO device annealed in nitrogen ambience shows better performance than that of annealing in argon ambience. The schematic diagram for the UV photodetector device is shown in the inset of Figure 5(a), in which interdigitated Pt electrode was deposited onto the optimal ZnO (0002) thin films. The formation of thermally stable and low resistance Ohmic contacts is critical to realizing high quality ZnO-based optoelectronic devices. The high contact resistance between semiconductor and metal gives rise to the degradation of optoelectronic device performance through thermal stress and contact failure. Thermally stable and low contact resistance can be achieved either by performing surface modification to reduce the semiconductor-metal barrier height or by increasing the effective carrier concentration of the surface, which allow an increase in carrier tunnelling probability. Hence, Ohmic contact metallization should be one of the main purposes in improving the optoelectronic device performance. However, the formation of Ohmic contact method in ZnO-based optoelectronic device has not been investigated extensively, and it is limited mostly to n-type contacts.

Figure 6 shows the dark current and photocurrent characteristics of the UV photodetector as a function of bias voltage ranged from -5V to 5V for Pt/ZnO thin films structure. It can be seen that only the Pt/ZnO device annealed in argon ambience exhibits the photoconductive behavior as shown in Figure 6(a). Furthermore, both the dark and photo currents increase linearly with increasing bias voltage, indicating that the Pt top electrode forms the Ohmic contact onto the ZnO (0002) thin film. Without UV light illumination, the observed dark current was about 4.8 mA at a 5 V bias. When the Pt/ZnO device was illuminated under a 365 nm wavelength with the energy of 38 mW/cm², the photocurrent was approximately 36 mA at a 5 V bias, indicating that the UV photodetector composed of Pt/ZnO nanobilayer films structure has high photoresponsivity. The origin of photocurrent by the adsorption and desorption of oxygen molecules has been highly considered [29, 30]. Before UV illumination, the ZnO films were exposed to air in the dark and oxygen molecules, which could be adsorbed on the ZnO surface in order to extract free electrons according to the following:



The negative oxygen ions adhered to the surface and created a depletion of electron at the grain boundaries of ZnO thin films. These negative oxygen ions cannot contribute to the conductivity to the thin film, which makes the thin film produce a low conductive surface. However, upon exposure to UV irradiation, the negative oxygen ions can form neutral by capturing a photogenerated hole, which is expressed in the following:



The wavelength of UV light ~365 nm closely matches the band gap of ZnO ~3.37 eV; high energy photons get absorbed by the ZnO layer and generate electron-hole pairs consequently. The photogenerated holes recombine with electrons of the adsorbed oxygen ions through surface recombination and simultaneously release oxygen atoms from the surface. As a result, lowering of depletion layer height at the grain boundary region takes place. These accumulated unpaired electrons in the conduction band of ZnO will contribute to increasing the photoconductivity of the ZnO-based UV devices.

The dark current and photocurrent characteristics of UV photodetector composed of Pt/ZnO nanobilayer films structure annealed in nitrogen are also shown in Figure 6(b). The *I-V* characteristics of dark and photo-currents are overlapping, which means the device has no photoresponsivity. When the Pt/ZnO films structure was annealed in nitrogen ambience, the nitrogen atoms might not only act as acceptors and form a doped layer near the surface of the ZnO thin film but also produce a thin nitride layer. The increase in the carrier concentration with the nitride layer can lower the barrier

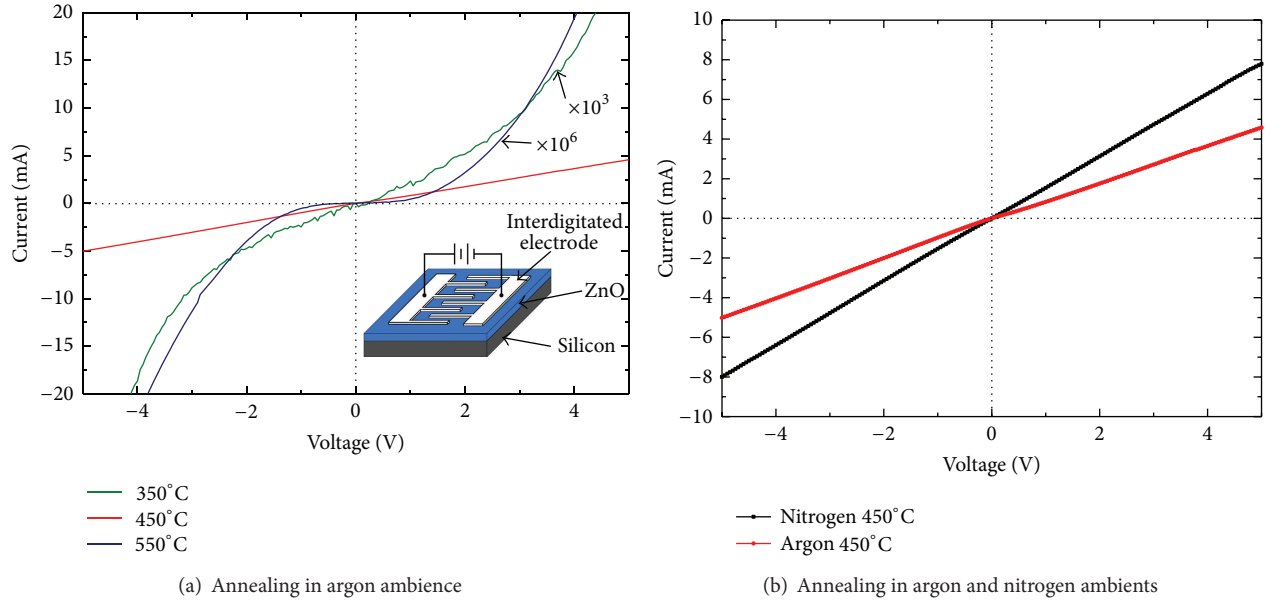


FIGURE 5: (a) Current-voltage (I - V) characteristic of the ultraviolet (UV) photodetector with Pt/ZnO nanobilayer films structure annealed in argon ambience at different temperatures (350°C, 450°C, and 550°C), and the inset showed the schematic structure of UV photodetector device. (b) The dark I - V characteristic of the Pt/ZnO nanobilayer structure annealed at 450°C in argon and nitrogen ambients, respectively.

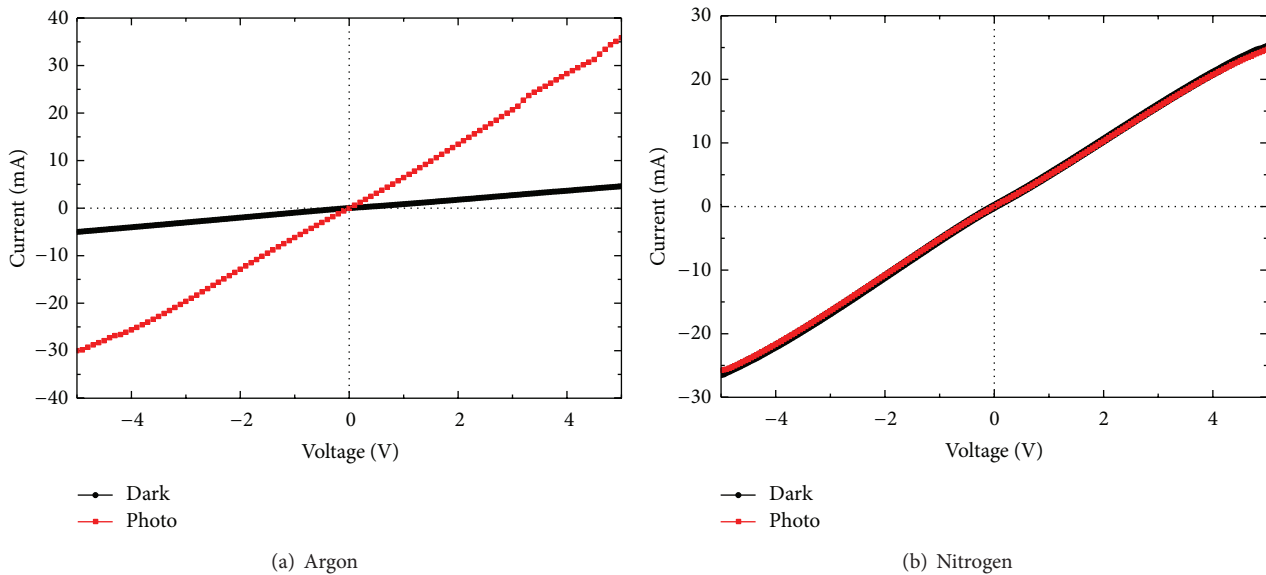


FIGURE 6: The dark current and photocurrent characteristics for the UV photodetector composed of Pt/ZnO nanobilayer films structure annealed in (a) argon and (b) nitrogen ambients, respectively.

height of the Ohmic contact, which was formed between the Pt electrode and ZnO thin film. It will lead to higher current value with lower resistance compared with the device annealed in argon ambience. At the same time, the nitride layer onto the ZnO thin film surface would directly prevent UV light irradiation for the surface of ZnO thin film. Hence, the aforementioned electric field generated from the depletion region of the ZnO thin film surface will be forbidden. The UV photodetector device composed of Pt/ZnO bilayer

films structure annealed in nitrogen ambience is not suitable for UV sensor owing to the lack of photoconductivity.

The reproducibility of the photodetector device annealed in argon ambience was tested by repeatedly switching UV light on and off for the same time intervals as shown in Figure 7. When the device was illuminated by the UV light, the current increased sharply and remained in a stable state. After the removal of light source, the device recovered to an original level. The response and recovery times of the device

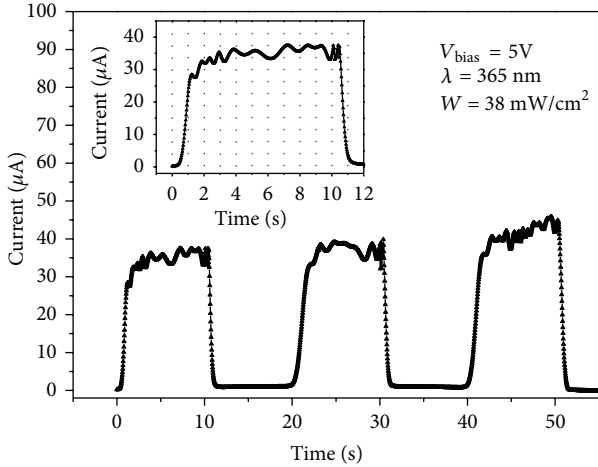


FIGURE 7: Photocurrent as a function of measured time obtained by switching on and off UV illumination on the photodetector composed of Pt/ZnO nanobilayer films structure.

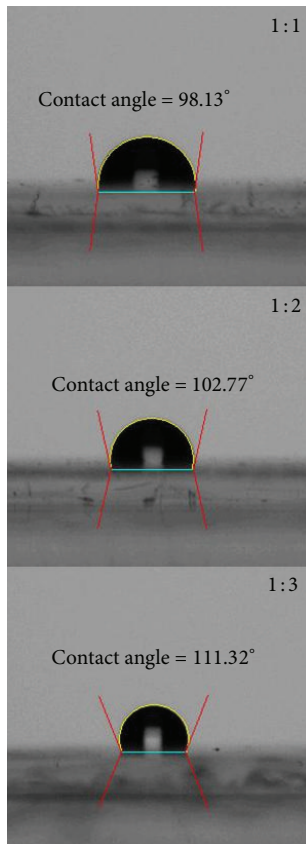


FIGURE 8: Water contact angle images accompanied with the measured values for the ZnO (0002) thin films synthesized at different gas flow rate ratios of DEZn to CO₂.

are 2 s and 1.5 s, respectively, as shown in the inset of Figure 7. The result shows great reproducibility and good stability for the UV photodetector device at least 3 times without change. The quick response and stability obtained from the device are useful for UV photodetector application.

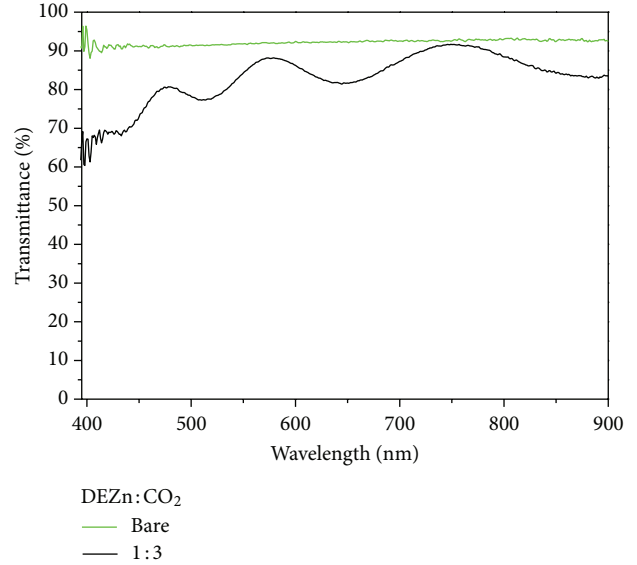


FIGURE 9: Optical transmittance spectra for the ZnO (0002) thin film synthesized at gas flow rate ratio of 1:3 compared with the bare glass substrate.

On the other hand, the wettability of epitaxial ZnO (0002) thin films was characterized by a contact angle goniometer (Pentad FTA 125). If the water contact angle with the surface is smaller than 90°, then the surface is termed as hydrophilic. On the contrary, if the water contact angle with the surface is greater than 90° then the surface is termed as hydrophobic. Figure 8 shows the water contact angle values of ZnO films with various gas flow rate ratios of 1:1, 1:2, and 1:3 are 98.13°, 102.77°, and 111.32°, respectively. In general, the high hydrophobic property was formed by modifying surfaces with low surface energy coating [31] or increasing surface roughness [32]. In our presented work, the measured results indicated that the surface of ZnO thin films was more hydrophobic with increasing surface roughness. Compared with the water contact angle values of ZnO films with various gas flow rate ratios, the largest surface roughness was obtained with the gas flow rate ratio of 1:3 (8.97 nm), leading to the largest hydrophobicity consistent with the observed results from Figure 3.

Additionally, in order to investigate the transparency of epitaxial ZnO (0002) thin film, the ZnO (0002) thin film was also synthesized onto glass substrates for future high-transmittance ZnO-based optoelectronic devices. The transmittance spectrum showed that ZnO (0002) thin film exhibits high transmittance in the 400–900 nm range and with higher than 80% visible transmittance as shown in Figure 9.

4. Conclusions

Epitaxial ZnO (0002) thin film was at first synthesized on silicon substrate with gas flow rate ratio of 1:3 (DEZn to CO₂) by PECVD system, which exhibited good crystallinity, low surface roughness, high optical properties, and good visible

transparency. The Ohmic contacts were formed between Pt top electrode and ZnO thin films together annealed at 450°C in argon and nitrogen ambients for 10 min. However, the UV photodetector composed of Pt/ZnO nanobilayers structure only annealed in argon ambience shows a lower dark current of 4.8 mA and a higher photocurrent of 36 mA at 5 V bias voltage. Therefore, a simple method is presented which used Pt contact electrode onto epitaxial ZnO (0002) thin film and is suitable for potential device application of UV photodetector, showing a good Ohmic contacts behavior as well as UV photoresponsibility.

Conflict of Interests

The authors declare that there is no conflict of interests regarding the publication of this paper.

Acknowledgments

The authors acknowledge financial support of the main research project of the National Science Council of Taiwan under Grant no. NSC 101-2221-E-027-042.

References

- [1] M.-L. Tu, Y.-K. Su, S.-J. Chang, and R. W. Chuang, "GaN UV photodetector by using transparency antimony-doped tin oxide electrode," *Journal of Crystal Growth*, vol. 298, pp. 744–747, 2007.
- [2] G. Hellings, J. John, A. Lorenz, P. Malinowski, and R. Mertens, "AlGaN schottky diodes for detector applications in the UV wavelength range," *IEEE Transactions on Electron Devices*, vol. 56, no. 11, pp. 2833–2839, 2009.
- [3] T. K. Lin, S. J. Chang, Y. K. Su et al., "ZnSe MSM photodetectors prepared on GaAs and ZnSe substrates," *Materials Science and Engineering B*, vol. 119, no. 2, pp. 202–205, 2005.
- [4] Y. Iwakaji, M. Kanasugi, O. Maida, and T. Ito, "Characterization of diamond ultraviolet detectors fabricated with high-quality single-crystalline chemical vapor deposition films," *Applied Physics Letters*, vol. 94, no. 22, Article ID 223511, 2009.
- [5] C. H. Chen, "GaN-based metal-insulator-semiconductor ultraviolet photodetectors with HfO₂ insulators," *Japanese Journal of Applied Physics*, vol. 528, part 2, Article ID 08JF08, 2013.
- [6] J. Zhang and S. Sakai, "Optical properties characterization of InGaN/GaN near UV photodetector with surface nanostructure fabricated by nano-imprinting," *Advanced Materials Research*, vol. 399-401, pp. 629–634, 2012.
- [7] T. T. Guo, G. B. Dong, F. Y. Gao, Y. Xiao, Q. Chen, and X. G. Diao, "High performance ZnO:Al films deposited on PET substrates using facing target sputtering," *Applied Surface Science*, vol. 282, p. 467, 2013.
- [8] L. Q. Zhang, B. Liu, Y. H. Lu et al., "Non-polar p-type Zn_{0.94}Mn_{0.05}Na_{0.01}O texture: growth mechanism and codoping effect," *Journal of Applied Physics*, vol. 113, Article ID 083513, 2013.
- [9] X.-L. Guo, H. Tabata, and T. Kawai, "Pulsed laser reactive deposition of p-type ZnO film enhanced by an electron cyclotron resonance source," *Journal of Crystal Growth*, vol. 223, no. 1-2, pp. 135–139, 2001.
- [10] Q. A. Xu, J. W. Zhang, K. R. Ju, X. D. Yang, and X. Hou, "ZnO thin film photoconductive ultraviolet detector with fast photoresponse," *Journal of Crystal Growth*, vol. 289, no. 1, pp. 44–47, 2006.
- [11] D. Basak, G. Amin, B. Mallik, G. K. Paul, and S. K. Sen, "Photoconductive UV detectors on sol-gel-synthesized ZnO films," *Journal of Crystal Growth*, vol. 256, no. 1-2, pp. 73–77, 2003.
- [12] A. Y. Polyakov, N. B. Smirnov, A. V. Govorkov et al., "Persistent photoconductivity in p-type ZnO(N) grown by molecular beam epitaxy," *Applied Physics Letters*, vol. 90, no. 13, Article ID 132103, 2007.
- [13] W. Yang, R. D. Vispute, S. Choopun, R. P. Sharma, T. Venkatesan, and H. Shen, "Ultraviolet photoconductive detector based on epitaxial Mg_{0.34}Zn_{0.66}O thin films," *Applied Physics Letters*, vol. 78, no. 18, pp. 2787–2789, 2001.
- [14] X.-Y. Liu, Y.-A. Li, S. Liu, H.-L. Wu, and H.-N. Cui, "ZnO/Cu/ZnO multilayer films: structure optimization and investigation on photoelectric properties," *Thin Solid Films*, vol. 520, no. 16, pp. 5372–5377, 2012.
- [15] B. Liu, T. T. Zhou, M. G. Ma et al., "Realization of non c-axis oriented ZnO thin films on quartz through Mn-Li co-doping," *Materials Letters*, vol. 108, p. 153, 2013.
- [16] H. C. Park, D. Byun, B. Angadi et al., "Photoluminescence of Ga-doped ZnO film grown on c-Al₂O₃ (0001) by plasma-assisted molecular beam epitaxy," *Journal of Applied Physics*, vol. 102, no. 7, Article ID 073114, 2007.
- [17] A. Marzouki, A. Lussou, F. Jomard et al., "SIMS and Raman characterizations of ZnO:N thin films grown by MOCVD," *Journal of Crystal Growth*, vol. 312, no. 21, pp. 3063–3068, 2010.
- [18] M. Macias-Montero, A. Borrás, Z. Saghi et al., "Vertical and tilted Ag-NPs@ZnO nanorods by plasma-enhanced chemical vapour deposition," *Nanotechnology*, vol. 23, no. 25, Article ID 255303, 2012.
- [19] M. D. Barankin, E. Gonzalez II, A. M. Ladwig, and R. F. Hicks, "Plasma-enhanced chemical vapor deposition of zinc oxide at atmospheric pressure and low temperature," *Solar Energy Materials and Solar Cells*, vol. 91, no. 10, pp. 924–930, 2007.
- [20] J. S. Wright, R. Khanna, K. Ramani et al., "ZrB₂/Pt/Au Ohmic contacts on bulk, single-crystal ZnO," *Applied Surface Science*, vol. 253, no. 5, pp. 2465–2469, 2006.
- [21] J.-M. Lee, K.-K. Kim, S.-J. Park, and W.-K. Choi, "Low-resistance and nonalloyed ohmic contacts to plasma treated ZnO," *Applied Physics Letters*, vol. 78, no. 24, pp. 3842–3844, 2001.
- [22] J.-M. Lee, K.-K. Kim, H. Tampo, A. Yamada, and S. Niki, "Ohmic contact behavior of Pt/Ni/Au to p-ZnO," in *2006 MRS Spring Meeting*, pp. 50–55, USA, April 2006.
- [23] Y. F. Lu, Z. Z. Ye, Y. J. Zeng, L. P. Zhu, J. Y. Huang, and B. H. Zhao, "Low-resistivity Ni/Pt Ohmic contacts to p-type N-doped ZnO," *Solid-State Electronics*, vol. 54, no. 7, pp. 732–735, 2010.
- [24] N. Fujimura, T. Nishihara, S. Goto, J. Xu, and T. Ito, "Control of preferred orientation for ZnO_x films: control of self-texture," *Journal of Crystal Growth*, vol. 130, no. 1-2, pp. 269–279, 1993.
- [25] Z. Z. Zhi, Y. C. Liu, B. S. Li et al., "Effects of thermal annealing on ZnO films grown by plasma enhanced chemical vapour deposition from Zn(C₂H₅)₂ and CO₂ gas mixtures," *Journal of Physics D*, vol. 36, no. 6, pp. 719–722, 2003.
- [26] S. H. Bae, S. Y. Lee, H. Y. Kim, and S. Im, "Effects of post-annealing treatment on the light emission properties of ZnO thin films on Si," *Optical Materials*, vol. 17, no. 1-2, pp. 327–330, 2001.

- [27] C. L. Yang, J. N. Wang, W. K. Ge, L. Guo, S. H. Yang, and D. Z. Shen, "Enhanced ultraviolet emission and optical properties in polyvinyl pyrrolidone surface modified ZnO quantum dots," *Journal of Applied Physics*, vol. 90, no. 9, pp. 4489–4493, 2001.
- [28] B. Lin, Z. Fu, and Y. Jia, "Green luminescent center in undoped zinc oxide films deposited on silicon substrates," *Applied Physics Letters*, vol. 79, no. 7, pp. 943–945, 2001.
- [29] C. Soci, A. Zhang, B. Xiang et al., "ZnO nanowire UV photodetectors with high internal gain," *Nano Letters*, vol. 7, no. 4, pp. 1003–1009, 2007.
- [30] H. Kind, H. Yan, B. Messer, M. Law, and P. Yang, "Nanowire ultraviolet photodetectors and optical switches," *Advanced Materials*, vol. 14, pp. 158–160, 2002.
- [31] A. Nakajima, K. Hashimoto, T. Watanabe, K. Takai, G. Yamauchi, and A. Fujishima, "Transparent superhydrophobic thin films with self-cleaning properties," *Langmuir*, vol. 16, no. 17, pp. 7044–7047, 2000.
- [32] X. Feng, L. Feng, M. Jin, J. Zhai, L. Jiang, and D. Zhu, "Reversible super-hydrophobicity to super-hydrophilicity transition of aligned ZnO nanorod films," *Journal of the American Chemical Society*, vol. 126, no. 1, pp. 62–63, 2004.

Research Article

Two-Axis Solar Heat Collection Tracker System for Solar Thermal Applications

Tsung-Chieh Cheng, Wei-Cheng Hung, and Te-Hua Fang

Department of Mechanical Engineering, National Kaohsiung University of Applied Sciences, Kaohsiung 807, Taiwan

Correspondence should be addressed to Tsung-Chieh Cheng; tcchengme@cc.kuas.edu.tw

Received 15 September 2013; Accepted 15 October 2013

Academic Editor: Teen-Hang Meen

Copyright © 2013 Tsung-Chieh Cheng et al. This is an open access article distributed under the Creative Commons Attribution License, which permits unrestricted use, distribution, and reproduction in any medium, provided the original work is properly cited.

An experimental study was performed to investigate the effect of using a continuous operation two-axes tracking on the solar heat energy collected. This heat-collection sun tracking which LDR (light dependent resistor) sensors installed on the Fresnel lens was used to control the tracking path of the sun with programming method of control with a closed loop system. The control hardware was connected to a computer through Zigbee wireless module and it also can monitor the whole tracking process information on a computer screen. An experimental study was performed to investigate the effect of using two-axes tracking on the solar heat energy collected. The results indicate that sun tracking systems are being increasingly employed to enhance the efficiency of heat collection by polar-axis tracking of the sun. Besides, the heating power was also measured by designed power measurement module at the different focal length of Fresnel lens, and the design of shadow mask of LDR sensors is an important factor for solar photothermal applications. Moreover, the results also indicated that the best time to obtain the largest solar irradiation power is during 11:00–13:00 in Taiwan.

1. Introduction

Because of the energy crisis and the environmental awareness, to develop renewable energies has become one of the important targets in the future. There are many approaches that could be developed for renewable energies. Finding energy sources to satisfy the world's growing demand is one of society's foremost challenges for the next halfcentury. Solar energy is clean, renewable, and abundant in every part of our world. There are two main energy types of solar energy collection. One is photoelectric conversion and the other is photothermal conversion. For photothermal application, solar stirling engine which is a photothermal engine that converts sunlight heat energy into mechanical motion to form the electrical power by using air or an inert gas as the working fluid operating on a highly efficient thermodynamic cycle is a kind of green power. For photothermal applications, in order to receive heat energy from the sunlight, the solar tracker, a device in an optimum position perpendicular to the solar radiation during daylight hours, is necessary to increase the collected heat energy. Therefore, in this paper, an experimental study was performed to investigate the effect of

using a continuous operation two-axes tracking on the solar heat energy collected.

Over the years, several researchers have studied the solar tracking systems with different modes and electromechanical module to improve the efficiency of solar systems. The design of tracker was based on some criteria: low cost, easy maintenance, modular, low energy consumption, and easy adjustment in case of different location [1]. From previous studies, there are two tracking types to track the sun. One is active type and the other is passive type [2]. In a passive system the tracker follows the sun from east to west without using any type of electric motor to power the movement, but the active type needs motor, control IC, track procedure, and detect components responding to the solar direction. Passive solar trackers are based on thermal expansion of a matter (usually Freon), on low boiling point compressed gas fluid, or on shape memory alloys. Clifford and Eastwood [3] presented the passive solar tracker design which incorporates two bimetallic strips made of aluminum and steel, positioned on a wooden frame symmetrically on either side of a central horizontal axis. The efficiency of this passive solar tracker with tracking method had the potential to increase solar panel

efficiency by up to 23%. Mwithiga and Kigo [4] designed and constructed a dryer which consisted of a gauge 20 mild steel flat absorber plate formed into a topless box and the results showed that the solar dryer can be used to successfully dry grains. Poulek [5] developed a single axis passive solar tracker based on a shape memory alloy (SMA). It was concluded the efficiency of the SMA actuators (-2%) is approximately two orders of magnitude higher than that of bimetallic actuators. However, the passive tracker had many drawbacks, like low tracking efficiency than active tracker, susceptible to high winds, or sluggish in getting moving in cold temperatures. Therefore, the approach of solar tracker was trend to develop at active mode solar tracker.

Active tracking systems are powered by small electric motors and require some type of control module to direct them. The controller had two modes that can identify the active tracker to location of the sun. One is electrooptical sensors such as solar cell or LDR (Light Dependent Resistance) or photodiodes based on the structure of trackers (closed loop system); another is according to the function which adopted the azimuth and solar altitude angles or polar axis (open loop system). Abouzeid [6] presents a new tracking system with a firm step movement of either 15° or 7.5° . The system is controlled automatically using a programmable logic array plus an EEPROM carrying all necessary commands required for different operation cases (Abouzeid, 2001). Oner et al. [7] design a spherical motor controlled by a microcontroller for a PV-tracking system with the ability to move on two axes. The spherical motors which have the linear and circular movement ability in three independent dimensions can be used for precisely tracking the sun as a solution. Roth et al. [8] has published a low-cost automatic closed-loop sun tracker, built and tested. A four-quadrant photodetector senses the position of the sun and two small DC motors move the instrument platform keeping the sun's image at the center of the four-quadrant photodetectors. The situation of tracking under cloudy conditions, when the sun is not visible, a computing program calculates the position of the sun and takes control of the movement, until the detector can sense the sun again. Rubio et al. [9] show a hybrid tracking system that consists of a combination of open-loop tracking strategies based on solar movement models and closed-loop strategies using a dynamic feedback controller. The results have been presented that show the benefits of the new strategy with respect to a classical open-loop strategy when errors in the estimation of the sun's position. Alata et al. [10] demonstrated the design and simulation of time controlled sun tracking system. The approach starts by generating the input/output data. Then, the subtractive clustering algorithm, along with least square estimation (LSE), generates the fuzzy rules that describe the relationship between the input/output data of solar angles that change with time. The fuzzy rules are tuned by an adaptive neurofuzzy inference system (ANFIS). This open-loop control system is designed for each of the previous types of sun tracking systems and the electrooptical trackers give very good results during good weather conditions. Some studies [11–13] also use four photoresistors with cylindrical shades, electrooptical unit, or electrooptical unit as a sun sensor. Its controller contains differential amplifiers,

comparators, and output components to provide fairly good accuracy and reliable operation. Abdallah and Nijmeh [14] investigated the two axes tracking and the results indicate that the two axes tracking surface showed a better performance with an increase in the collected energy of up to 41.34% compared with the fixed surface. Neville [15] presented a theoretical comparative study between the energy available to a two axes tracker, an east-west tracker and a fixed surface. It was found that the energy available to the ideal tracker is higher by 5–10% and 50% higher than the east-west tracker and the fixed surface, respectively. Sungur [16] designed aboth axes sun tracking system with programmable logic control and with the function of solar azimuth angle and solar altitude angle to follow the sun's position. He found that the energy more than 42.6% in the two-axes sun-tracking system was obtained when compared to the fixed system. Barakat et al. [17] made a two-axes sun tracking system between closed-loop system and with complicated typical electronic control circuits. They found that the energy available to the two-axes tracker is higher by 20%. Bakos [18] developed the two-axes tracking using a continuous operation on the solar energy collected. He set the position of the photoresistors and the results indicate that solar energy on the moving surface was significantly larger (up to 46.46%) than the fixed surface. Khalifa and Al-Mutawalli [19] investigated the effect of using a two-axis sun tracking system on the thermal performance of compound parabolic concentrators (CPC). They indicated that the tracking CPC collector showed a better performance with an increase in the collected energy of up to 75% compared with an identical fixed collector. Mousazadeh et al. [20] established equations to compare the relation between tracking collector and fixed collector about energy gains. This amount of energy can be obtained from tracking collector more 57% than fixed collector.

However, for solar stirling electrical generator, the idea of concentrating solar energy to generate electricity has ingeniously made use of the concept in concentrator optics especially for designing a specific geometry of reflectors or lenses to focus sunlight onto a small receiving heating element. Many previous researches also have discussed that many existing concentrator systems will produce nonuniform focused illumination [21, 22] and it will decrease the energy collection of the sun. In this paper, a concept came from a realization that the need to concentrate the solar energy with the available Fresnel concentrating lens on the heating element of stirling engine to have higher efficiency in power generation. Therefore, we design the active two-axis solar tracker with Fresnel lens to collect the thermal power of solar efficiently and to offer a steady heat source for photo-thermal applications.

2. Experiments

2.1. The Structure of Two-Axis Heat-Collection Solar Tracker System. The proposed two axes heat collection solar tracker system as shown in Figure 1 consists of the following three parts:

- (i) the heat-collection Fresnel lens module,

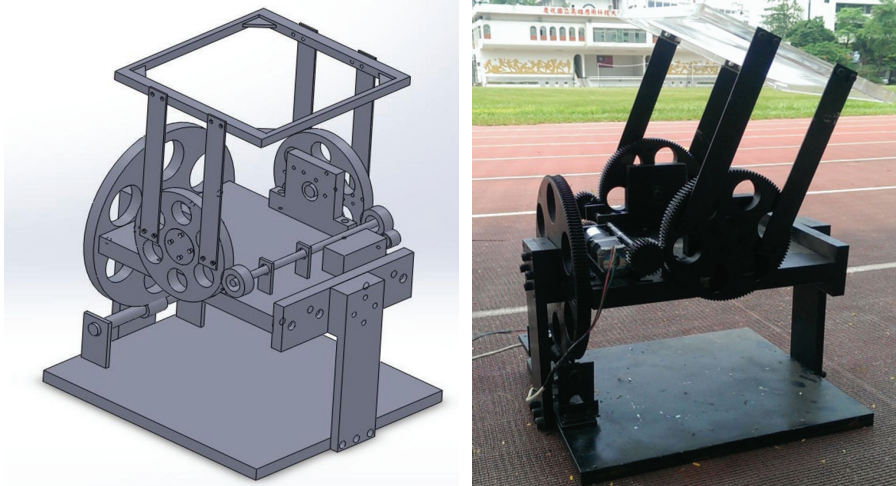


FIGURE 1: Schematic diagram of two-axis heat-collection solar tracker with constant focal distance.

- (ii) the control system, and
- (iii) the wireless data recorder system.

For the solar tracker system, increasing the solar input power and reducing the energy consumption of solar tracker are important goals in this paper. For reducing power consumption of solar tracker, we adopted the low-power motor to reduce energy loss and use the small gear to drive the large gear so the reducer will produce additional torque to move the polar axis structure of solar tracker. The heat collection Fresnel lens was used to concentrate the radiation power of sunlight and heat the heating head of Stirling engine. However, because the position of heating head of Stirling engine must be put on the focus of sunlight, it is important to note that the focus of Fresnel lens must be fixed on the heating head to collect the solar heat energy at any time. For this purpose, two-axis tracking method was used to trace the trajectory of the sun. Besides, because the change of sun tracks on north-south axis (N-S axis) is very small in a day, the Stirling engine was arranged on the N-S axis plate to reduce the power consumption of moving step motor and the Fresnel lens was installed on the east-west axis (E-W axis) to collect the power of sun. This two-axis solar tracker was controlled by the step motor, reducer, worm, worm gear and make sure that the focus of Fresnel lens is always on the heating head of Stirling engine. Besides, in our experiment, a portable wireless data acquisition system for temperature in real-time process dynamics was recorded by using the 802.15.4, ZigBee protocol, that is specially designed for the sensors network to facilitate data storage purposes. ZigBee is the only standards-based wireless technology designed to address the unique needs of low-cost and low-power wireless sensor and control networks. This wireless data logger senses and monitors the variations in the temperature of simulated Stirling head and the received temperature data can be displayed on a display and simultaneously on a computer.

2.2. Control System of Solar Tracker. The block diagram of our two-axis solar tracker as shown in Figure 2 composed of the following parts:

- (i) the electromechanical movement mechanism,
- (ii) the sensors unit, and
- (iii) the control system software.

The mechanism of electromechanical displacement consists of two 12-volt stepper motors, one for N-S axis and the other for E-W axis displacements and an electronic circuit. Light-dependent resistor sensor (LDR sensor) is a component that has a resistance that changes with the light intensity that falls upon it. In order to track the position of the sun accurately, there are four light-dependent resistor sensors (LDR sensors, NSL19-M51 RS, an electrocomponents company, Northants) to identify the intensity of the sunlight. Each two light-dependent resistor sensors were placed on the Fresnel lens along the east-west and north-south direction to control the N-S axis and E-W axis movement by two stepper motors, respectively. LDRs which produce a DC voltage level coincident with the light intensity of sun radiation detect the position of sunlight and then send the signals to the ADAM. So it is connected to one of the analog-to-digital converter (ADAM 4017/452) single pins to generate an 8-bit number (0–255) which tells the computer program some information about light intensity at that time and determine the device operating mode. The difference in illumination between each of the two sensors, the servo motion control card (SMCC) which produced pulse to driver, control the step motor, and do two-axis operation (N-S and E-W axis motion), promotes an adjustment of the tracker position towards the sun. The angular interval spanned by the tracker goes from 80° east up to 80° west and 50° south up to 50° north. This operation mode forms a closed-loop system for sun tracking as illustrated in Figure 2. A proper program to control, monitor, and collect data was developed by using the software Labview to determine the solar angles. The control panel was set up at

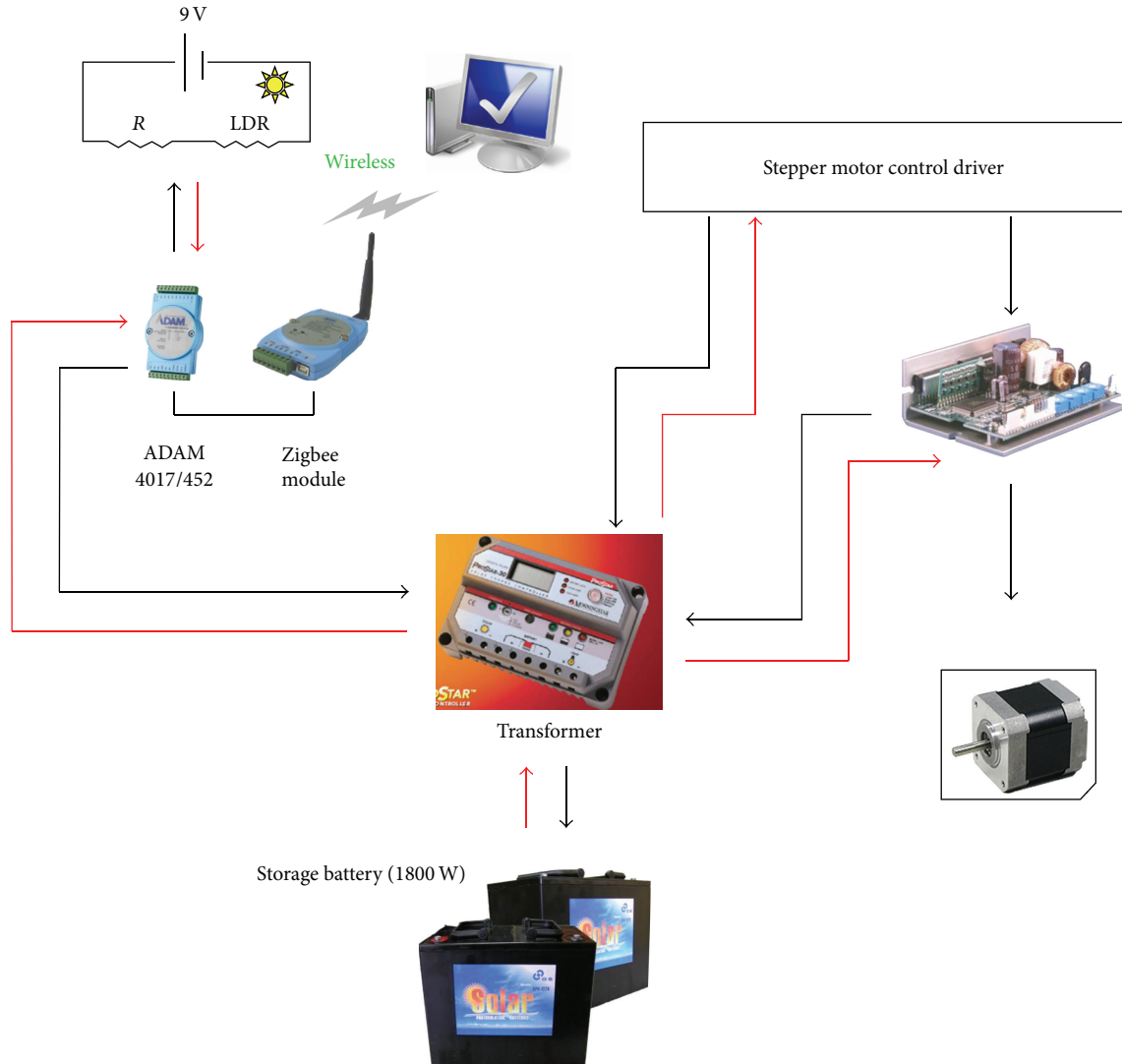


FIGURE 2: The schematic diagram of solar tracker control system.

the start time to receive and monitor the whole tracking process information about N-S axis or E-W axis directions. The relation between different sensor's voltage and SMCC control pulse can be defined from internal program to reduce the tracking times and the logic consequences of the controlling process of our heat collection solar tracking system.

3. Results and Discussion

3.1. The Effect of the Structure of LDR Sensors. The design of the shadow mask of LDR sensors is an important factor because the better design will increase the accuracy of tracking sunlight and shorten the tracking time. In our experiment, the five different shadow types of LDR sensors: (a) 1/4 bowl type, (b) 1/2 bowl type, (c) bowl type, (d) board type, and (e) square type were designed to determine the best module for sun tracking as shown in Figure 3(a). The test between tracking pulses and angle was limited by the same rotating angles from $0^\circ \sim 60^\circ$ of solar tracker. In this experiment, we adjusted and fixed the fluorescent angle to

measure the track of solar tracker as shown in Figure 3(b). If the tracking angles are the same, shorter tracking times means that the tracking speed is higher and the design of this shadow mask has better sensitivity. As the results from Figure 3(b), the board type is the best shadow mask design as the angle is less than 20 degrees, but 1/4 bowl is the best shadow mask design to track the sunlight as the angle is greater than 20 degrees. According to these results, we found that the tracking time of sunlight is strongly dependent on the geometry of shadow mask. Therefore, in this paper, we use board type to be the shadow mask of LDRs because the angle of each tracking step is smaller than 20 degree.

3.2. The Measurement Method and Results of Heat Power of Sun. It is hard to measure the sun heat power because the power gain from the sun by Fresnel lens will cause very high temperature at focus. For this reason, in this paper, we designed the power gain measurement system by the temperature raising rate as illustrated in Figure 4. In our experiment, we put the copper block at the focus of Fresnel

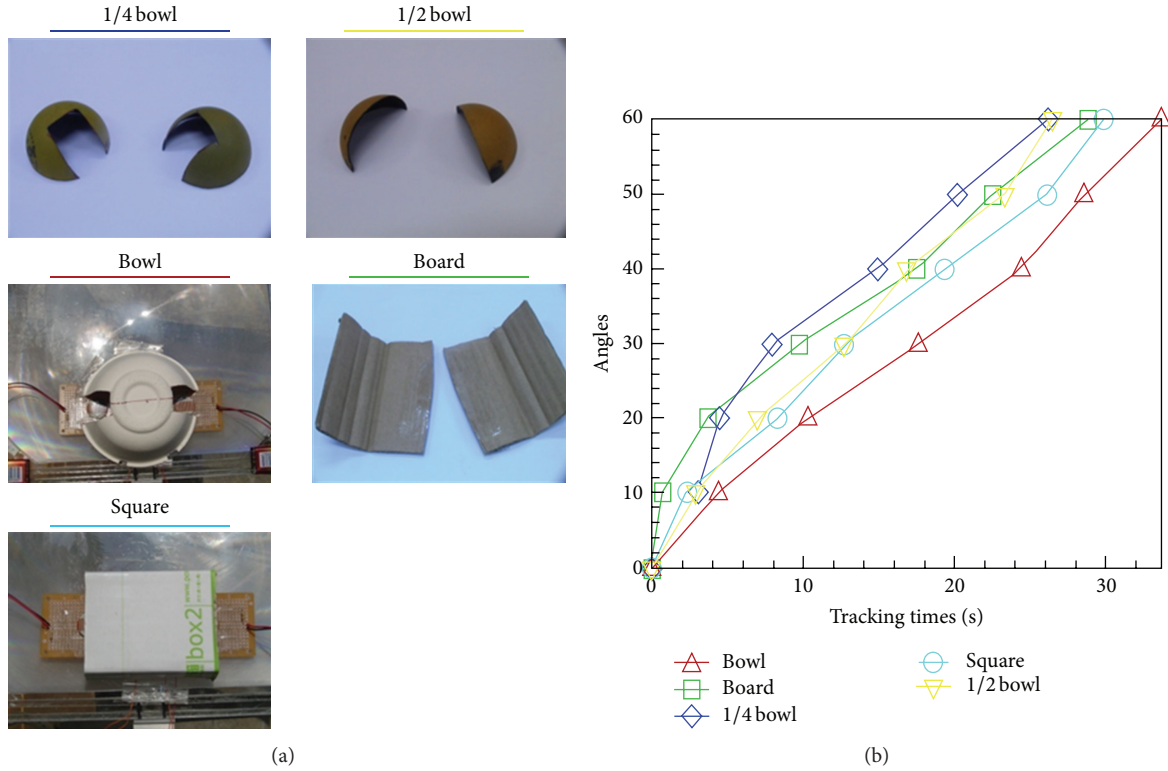


FIGURE 3: (a) The different shadow mask types of LDRs and (b) the tracking speed with different shadow masks.

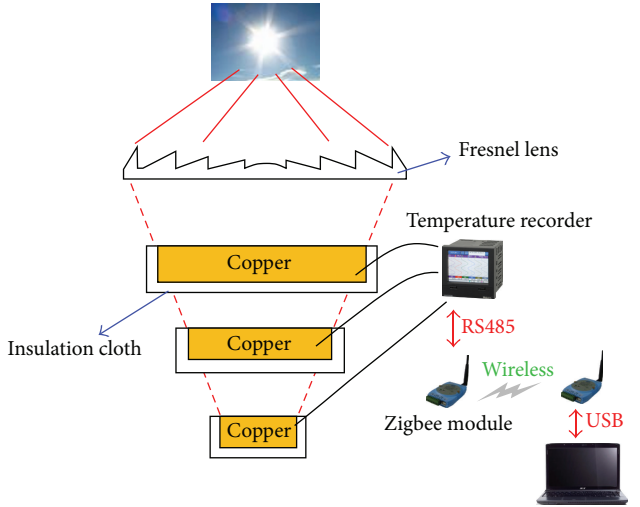


FIGURE 4: The schematic diagram of solar power measurement system.

lens on our two-axis solar tracker. There are three different area coppers, 19.63 mm², 1963.50 mm², and 11309.73 mm², which were used to record the temperature difference by the data recorder system and then used these temperature data to calculate the absorbing power. The asbestos insulation cloth was wrapped around the copper to reduce the heat loss. The power gain per unit area W can be calculated from the following equation:

$$W = \frac{(m \times s \times \Delta T / \Delta t|_{init})}{A}, \quad (1)$$

where m is the mass of the copper, s is the specific heat of the copper, A is the area of the copper plate, ΔT is the range of temperature, and Δt is the time (second) of this experiment. The $\Delta T / \Delta t|_{init}$ is the slope at the initial period in Figure 5(a) and the slope difference between initial period and real period implies the heat loss of copper. As illustrated the schematic diagram in Figure 4, in order to make sure that the sunlight irradiate on the surface of copper totally to avoid the additional energy loss, the less focus length needs larger copper surface area. This method not only measures the power of sun irradiation but also finds the best heating area of stirling engine. As shown in Figure 5(a), the temperature slope at initial periodic means the smallest heat loss and the decrease of temperature slope at real periodic indicated that there are some heat loss such as heat transfer from copper and ambient or the energy storage by copper block. Therefore, the ideal power gain and heat loss of copper can be calculated form (1) at different focal length. The result indicated that at 345 mm, focal length has best heating energy gain but large heat loss. This is because the larger temperature difference between copper and ambient air will cause the larger heat loss. Besides, Figure 5(b) shows the power of copper at different focal length and focal area at different times. The largest power of copper was acquired about 500 W/m² at 12:00 and the focal length was 345 mm. The reason is that the large focal length has small focus range which means that the copper area is smallest. Small copper area which was heated by sunlight irradiation will reduce the heat loss from the copper and decrease the less storage energy of copper block. Therefore, if we want to get more heating power from

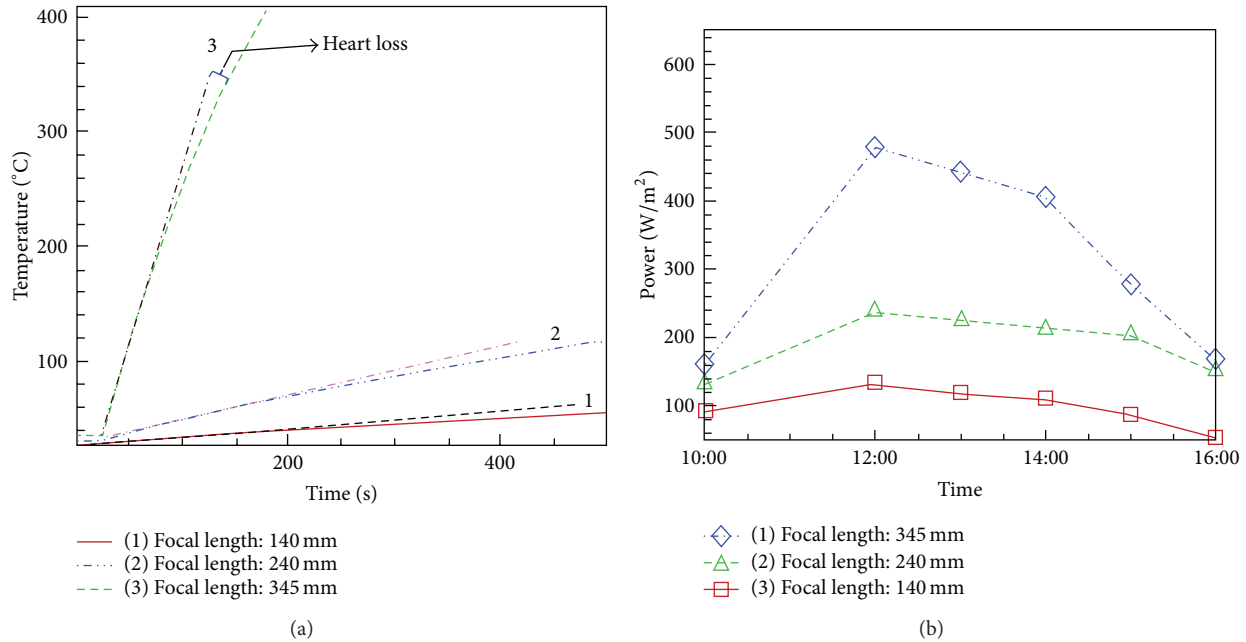


FIGURE 5: (a) The temperature raising rate and (b) the power gain of solar power measurement with different focal lengths.

sunlight, the heating head area of stirling engine should decrease as small as possible. Also shown in Figure 5(b), the solar heating power was larger during 12:00 to 13:00 than other times of the day at February 23 in Kaohsiung, Taiwan. It implied that if we want to get the sun irradiation power more efficiently, the time during 12:00-13:00 of the day is the best time period to get the sun irradiation power.

3.3. Measurements of Two-Axis Tracking System under Normal Weather Conditions. The solar power and the temperature of simulated stirling head experiments took place on 16 June 2012 from 09:00 to 16:00 in Kaohsiung, Taiwan, and the ambient temperature was 28°C, the humidity 65%, and the results are shown in Figure 6. During these experiments the weather conditions were very good and just a little cloudy in the sky at 12:25. The solar power was measured by our power gain measurement system as described earlier. As shown in Figure 6, the temperature response is slower and obtuse than the solar irradiation power. Because the insulation cloth was covered on the copper surface, the temperature is still maintained at a certain value even through the solar input energy decreases due to drifting clouds at 12:08. Moreover, from the data in Figure 6, the results also indicated that the best time to obtain the largest solar irradiation power is during 11:00–13:00.

4. Conclusions

In this paper an experimental study is performed to investigate the effect of closed-loop two-axis tracking on the solar heat energy collected for photo-thermal application. The hardware and software elements of the two-axes sun tracking system were designed and constructed. According to the results of the measurements performed in the present study,

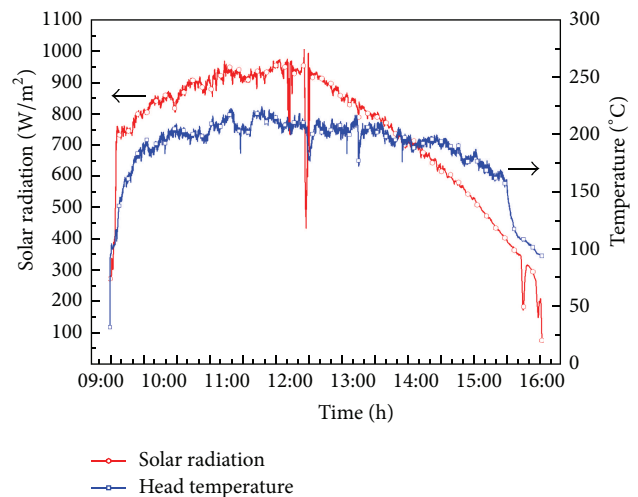


FIGURE 6: Time variation of solar irradiation power collection and heating head temperature by solar tracking system.

it can be concluded that proper shadow mask of LDR sensor will increase the accuracy and reduce the tracking time of tracking sun's radiation. Besides, in our experiment, we also design the heat power measurement system to measure the heat power of solar irradiation. Besides, the hourly values of solar radiation are added to obtain the total daily solar radiation and simulated stirling head temperature. The results indicated that the response of head temperature is slower than solar irradiation power without any heat loss, and if we want to get the solar heat power more efficiently, the time during 11:00–13:00 is the best time periods to get the sun's power. Moreover, in order to totally collect the solar

thermal energy of the sunlight by Fresnel lens, letting the concentrative sunlight to totally illuminate on the heating element without any heat loss is very important.

Acknowledgment

The authors would like to thank the National Science Council of Taiwan, for partially supporting this research under Contract no. NSC 101-2221-E-151-010.

References

- [1] J. A. Beltrán, J. L. González, S. Rubio, and C. D. García-Beltrán, *Fourth Congress of Electronics, Robotics and Automotive Mechanics*, vol. 786, IEEE Computer Society Press, 2007.
- [2] P. Roth, A. Georgiev, and H. Boudinov, "Cheap two axis sun following device," *Energy Conversion and Management*, vol. 46, no. 7-8, pp. 1179–1192, 2005.
- [3] M. J. Clifford and D. Eastwood, "Design of a novel passive solar tracker," *Solar Energy*, vol. 77, no. 3, pp. 269–280, 2004.
- [4] G. Mwithiga and S. N. Kigo, "Performance of a solar dryer with limited sun tracking capability," *Journal of Food Engineering*, vol. 74, no. 2, pp. 247–252, 2006.
- [5] V. Poulek, "Testing the new solar tracker with shape memory alloy actors," in *Proceedings of the 24th IEEE Photovoltaic Specialists Conference*, pp. 1131–1133, December 1994.
- [6] M. Abouzeid, "Use of a reluctance stepper motor for solar tracking based on a programmable logic array (PLA) controller," *Renewable Energy*, vol. 23, no. 3-4, pp. 551–560, 2001.
- [7] Y. Oner, E. Cetin, H. K. Ozturk, and A. Yilanci, "Design of a new three-degree of freedom spherical motor for photovoltaic-tracking systems," *Renewable Energy*, vol. 34, no. 12, pp. 2751–2756, 2009.
- [8] P. Roth, A. Georgiev, and H. Boudinov, "Design and construction of a system for sun-tracking," *Renewable Energy*, vol. 29, no. 3, pp. 393–402, 2004.
- [9] F. R. Rubio, M. G. Ortega, F. Gordillo, and M. López-Martínez, "Application of new control strategy for sun tracking," *Energy Conversion and Management*, vol. 48, no. 7, pp. 2174–2184, 2007.
- [10] M. Alata, M. A. Al-Nimr, and Y. Qaroush, "Developing a multi-purpose sun tracking system using fuzzy control," *Energy Conversion and Management*, vol. 46, no. 7-8, pp. 1229–1245, 2005.
- [11] S.-S. N. Rumala, "A shadow method for automatic tracking," *Solar Energy*, vol. 37, no. 3, pp. 245–247, 1986.
- [12] W. A. Lynch and Z. M. Salameh, "Simple electro-optically controlled dual-axis sun tracker," *Solar Energy*, vol. 45, no. 2, pp. 65–69, 1990.
- [13] V. Poulek and M. Libra, "New solar tracker," *Solar Energy Materials and Solar Cells*, vol. 51, no. 2, pp. 113–120, 1998.
- [14] S. Abdallah and S. Nijmeh, "Two axes sun tracking system with PLC control," *Energy Conversion and Management*, vol. 45, no. 11-12, pp. 1931–1939, 2004.
- [15] R. C. Neville, "Solar energy collector orientation and tracking mode," *Solar Energy*, vol. 20, no. 1, pp. 7–11, 1978.
- [16] C. Sungur, "Multi-axes sun-tracking system with PLC control for photovoltaic panels in Turkey," *Renewable Energy*, vol. 34, no. 4, pp. 1119–1125, 2009.
- [17] B. Barakat, H. Rahab, B. Mohmedi, and N. Naiit, "Design of a tracking system with photovoltaic panels," in *Proceedings of the fourth Jordanian International Mechanical Engineering Conference (JIMEC '01)*, vol. 471, 2001.
- [18] G. C. Bakos, "Design and construction of a two-axis Sun tracking system for parabolic trough collector (PTC) efficiency improvement," *Renewable Energy*, vol. 31, no. 15, pp. 2411–2421, 2006.
- [19] A.-J. N. Khalifa and S. S. Al-Mutawalli, "Effect of two-axis sun tracking on the performance of compound parabolic concentrators," *Energy Conversion and Management*, vol. 39, no. 10, pp. 1073–1079, 1998.
- [20] H. Mousazadeh, A. Keyhani, A. Javadi, H. Mobli, K. Abrinia, and A. Sharifi, "A review of principle and sun-tracking methods for maximizing solar systems output," *Renewable and Sustainable Energy Reviews*, vol. 13, no. 8, pp. 1800–1818, 2009.
- [21] H. Baiga, K. C. Heasman, and T. K. Mallick, "Non-uniform illumination in concentrating solar cells," *Renewable and Sustainable Energy Reviews*, vol. 16, no. 8, pp. 5890–5909, 2012.
- [22] K. K. Chong, F. L. Siaw, C. W. Wong, and G. S. Wong, "Design and construction of non-imaging planar concentrator for concentrator photovoltaic system," *Renewable Energy*, vol. 34, no. 5, pp. 1364–1370, 2009.

Research Article

High Efficiency of Dye-Sensitized Solar Cells Based on Ruthenium and Metal-Free Dyes

Che-Lung Lee,¹ Wen-Hsi Lee,¹ and Cheng-Hsien Yang²

¹ Department of Electrical Engineering, Nation Cheng Kung University, No. 1, Daxue Rd., East Dist., Tainan City 70101, Taiwan

² Nano-Powder and Thin Film Technology Center, ITRI South, Room 603, Buildig. R2, No. 31, Gongye 2nd Road, Annan District, Tainan 70955, Taiwan

Correspondence should be addressed to Cheng-Hsien Yang; jasonyang@fusol-material.com

Received 8 September 2013; Accepted 12 October 2013

Academic Editor: Teen-Hang Meen

Copyright © 2013 Che-Lung Lee et al. This is an open access article distributed under the Creative Commons Attribution License, which permits unrestricted use, distribution, and reproduction in any medium, provided the original work is properly cited.

The influence of using different concentrations of triazoloisoquinoline based small molecule as coadsorbent to modify the monolayer of a TiO₂ semiconductor on the performance of a dye-sensitized solar cell is studied. The co-adsorbent significantly enhances the open-circuit photovoltage (V_{oc}), the short circuit photocurrent density (J_{sc}) the solar energy conversion efficiency (η). The co-adsorbent 4L is applied successfully to prepare an insulating molecular layer with N719 and achieve high energy conversion efficiency as high as 8.83% at 100 mW cm⁻² and AM 1.5 at 1 to 0.25 (N719 : co-adsorbent) molar ratio. The resulting efficiency is about 6% higher than that of a nonadditive device. The result shows that the organic small molecule 4L (2-cyano-3-(5-(4-(3-oxo-[1,2,4]triazolo[3,4-a]isoquinoline-2(3H)-yl)phenyl)thiophene-2-yl)acrylic acid) is the promising candidates for improvement of the performance of dye-sensitized solar cell.

1. Introduction

Dye-sensitized solar cells have attracted considerable academic and industrial research interest since Regan and Grätzel's report in 1991 [1]. Usually these cells consist of a working electrode which is coated with a dye-sensitized mesoporous film of nanocrystalline particles of TiO₂, a Pt-coated counterelectrode, and an electrolyte containing a suitable redox couple. The function of such devices is based on the electron injection from the photoexcited state of the dye molecule into the conduction band of the TiO₂, followed by regeneration of the dye by an iodide/triiodide redox couple. Typically, high power conversion efficiencies (η) of more than 11% have been achieved by using ruthenium complex and acetonitrile based electrolytes [2]. However, organic additives play a key role in the characteristics of both electrolytes and devices and have been explored extensively with regard to improving the efficiency of DSSC [3–5].

A few reports have described the use of organic additives for a compact layer, comprised of the dye and coadsorbent

[6, 7]. Chenodeoxycholic acid (DCA) is frequently added to the dye solution to enhance the open-circuit photovoltage (V_{oc}), the short circuit photocurrent density (J_{sc}), and the efficiency (η) of DSSC [8, 9]. The V_{oc} , J_{sc} , and FF of the DSSC are affected by DCA due to the suppression of dark current at the semiconductor/electrolyte junction, since DCA blocks the surface states Ti(IV) ions that are active in the charge transfer [10]. Due to the insulating molecular layer, the charge recombination process can be shielded, and this increases the V_{oc} , J_{sc} , and η . Several approaches have been developed for this purpose, such as the use of pyridinium additives [11], pyrimidine additives [12], dipolar carboxylic acid derivatives [13], zwitterionic coadsorbents [14], and guanidinium cations [4]. In this paper, we synthesize a new triazoloisoquinoline-based organic small molecule used as co-adsorbents to modify the monolayer of a TiO₂ semiconductor. We discuss the concentration effect of co-adsorbents and investigate the possibility of using triazoloisoquinoline-based organic small molecule as co-adsorbents in DSSC.

2. Experimental

2.1. General Procedure for Preparation of Solar Cells. Fluorine-doped tin oxide (FTO, $10 \Omega \text{ square}^{-1}$) glass plates were cleaned using detergent solution, water, and ethanol in an ultrasonic bath overnight. The screen-printing procedure was repeated with TiO_2 paste (~15–20 nm colloidal particles, Ti-Nanoxide T series, Solaronix SA) to obtain a transparent nanocrystalline film of thickness around $12 \mu\text{m}$. The 100 nm colloidal particles were prepared in a basic environment according to the literature [15] and dispersed in α -terpineol with ethyl cellulose for scattering TiO_2 paste. A scattering layer around $4 \mu\text{m}$ was deposited by using this scattering TiO_2 paste and a final thickness of $16 \mu\text{m}$ was attained. The TiO_2 electrodes were gradually annealed at 450°C for 30 min in an oven in an air atmosphere. After sintering, the electrodes were further treated with 0.2 M TiCl_4 aqueous solution at room temperature for 12 h, then washed with water and ethanol, and annealed at 450°C for 30 min. When the temperature decreased to 70°C after sintering, the electrodes were immersed into dye solution, which included 0.5 mM N719 and different concentrations of co-adsorbent in tert-butanol/acetonitrile (AN) (1:1 in volume). The dye solutions were kept at 25°C for more than 18 h to allow the dye to adsorb to the TiO_2 surface. After the adsorption of the dyes, the electrode was rinsed with the same solvent. The dye-loaded TiO_2 film as the working electrode and Pt-coated TCO as the counterelectrode (about 20 nm) were separated by a hot-melt Surlyn sheet ($25 \mu\text{m}$) and sealed together by pressing them under heat. The electrolytes were introduced into the gap between the working and counterelectrodes from two holes predrilled on the back of the counterelectrode. Finally, the two holes were sealed with a Surlyn film covering a thin glass slide under heat. The cells were evaluated by using 0.6 M [BMI][I], 0.1 M GuNCS, 0.3 M I_2 , and 0.5 M TBP in a AN/VN (85/15, v/v) solvent as the redox electrolyte.

2.2. Photovoltaic Measurement. The current-voltage (I - V) characteristics in the dark and under illumination were measured with a Keithley 2400 sourcemeter. The photocurrent was measured in a nitrogen-filled glove box under a solar simulator (Oriol 96000 150 W) with AM 1.5 G-filtered illumination (100 mW cm^{-2}). The spectra-mismatch factor of the simulated solar irradiation was corrected using a Schott visible-color glass-filtered (KG5 color filter) Si diode (Hamamatsu S1133). The active area of the device was 0.25 cm^2 .

2.3. Dye Loading Measurement. The TiO_2 films were put into the dye solution (N719, 3×10^{-4} M in tert-butanol and acetonitrile, 1:1, v/v) for 24 h. Subsequently, the TiO_2 films were washed with acetonitrile after the adsorption process and then dried in N_2 flow. Dye loading measurements were conducted by desorbing the dye molecules from the dye-anchored films in NaOH ethanolic solution. The loading amount was calculated from the absorbance of the completely desorbed dye solutions by the spectrophotometer.

2.4. Synthesis

2.4.1. Synthesis of 2-(4-(4,4,5,5-Tetramethyl-1,3,2-dioxaborolane-2-yl)phenyl)-[1,2,4]triazolo[3,4-a]isoquinoline-3(2H)-one (2). In a round-bottom flask, compound 1 (5.6 g, 16.3 mmol), 4,4,5,5-tetramethyl-2-(4,4,5,5-tetramethyl-1,3,2-dioxaborolane-2-yl)-1,3,2-dioxaborolane (4.4 g, 17.1 mmol), and potassium acetate (4.8 g, 49.0 mmol) were dissolved in dimethyl sulfoxide (DMSO) under nitrogen atmosphere. After adding a catalyst of dichloro-[1,1'-bis(diphenylphosphino)ferrocenyl]palladium(II) ($\text{Pd}(\text{dppf})\text{Cl}_2$), the mixed solution was heated at 80°C for 6 hours with vigorous stirring. It was then poured into EtOAc-water for extraction. The organic phase was concentrated and adsorbed on silica gel and purified by column chromatography using hexane/EtOAc mixture (5:1) as the eluant: white powder; yield 5.32 g (84.2%); $^1\text{H NMR}$ (300 MHz, d_6 -DMSO): δ 8.31 (d, 1H, $J = 7.53$ Hz), 8.17 (d, 2H, $J = 8.23$ Hz), 7.84 (d, 3H, $J = 8.57$ Hz), 7.77~7.66 (m, 3H), 7.02 (d, 1H, $J = 7.44$ Hz), 1.32 (s, 12H).

2.4.2. Synthesis of 5-(4-(3-Oxo-[1,2,4]triazolo[3,4-a]isoquinoline-2(3H)-yl)phenyl)thiophene-2-carbaldehyde (3). In a three-necked round-bottomed flask (25 mL) equipped with a reflux condenser, compound 2 (1.71 g, 4.4 mmol), 5-bromothiophene-2-carbaldehyde (1.0 g, 5.2 mmol), and 2 M potassium carbonate solution were added to a suspension of $\text{Pd}(\text{PPh}_3)_4$ (3.0 mol%) in tetrahydrofuran (30 mL) at ambient temperature under nitrogen. The reaction mixture was heated to 80°C with rapid stirring for 16 hours. After cooling, the resulting solution was poured into water. The separated solid was filtered and thoroughly washed with water-acetone and dried: pale yellow powder; yield 1.0 g (61.6%); $^1\text{H NMR}$ (300 MHz, d_6 -DMSO): δ 9.23 (s, 1H), 8.32 (d, 1H, $J = 7.56$ Hz), 8.24 (d, 2H, $J = 8.53$ Hz), 8.07 (d, 1H, $J = 3.81$ Hz), 8.01 (d, 2H, $J = 8.60$ Hz), 7.86~7.67 (m, 5H), 7.04 (d, 1H, $J = 7.39$ Hz).

2.4.3. Synthesis of 2-Cyano-3-(5-(4-(3-oxo-[1,2,4]triazolo[3,4-a]isoquinoline-2(3H)-yl)phenyl)thiophene-2-yl)acrylic Acid (4L). In a three-neck bottle, compound 3 (1.2 g, 3.3 mmol), 2-cyanoacetic acid (0.6 g, 6.5 mmol), and piperidine (0.08 g, 0.98 mmol) were dissolved in chloroform. The mixed solution was refluxed for 16 hours with rapid stirring. After cooling, the resulting solution was poured into EtOAc-MeOH. The separated solid was filtered and thoroughly washed with EtOAc and MeOH and dried: pale orange powder; yield 1.2 g (85.0%); $^1\text{H NMR}$ (300 MHz, d_6 -DMSO): δ 8.32 (d, 1H, $J = 7.50$ Hz), 8.23 (s, 1H), 8.20 (d, 2H, $J = 3.20$ Hz), 7.93 (d, 2H, $J = 8.72$ Hz), 7.89~7.67 (m, 6H), 7.03 (d, 1H, $J = 7.46$ Hz); ESI-MS m/z 437 (M-H^+); Anal. Calcd for $\text{C}_{24}\text{H}_{14}\text{N}_4\text{O}_3\text{S}$: C, 65.74; H, 3.22; N, 12.78. Found: C, 65.96; H, 3.28; N, 12.60.

3. Results and Discussion

3.1. Synthesis. The synthetic route of the co-adsorbent is shown in Figure 1. 2-(4-bromophenyl)-[1, 2, 4]triazolo[3,4-a]isoquinoline-3(2H)-one (1) was obtained as reported earlier

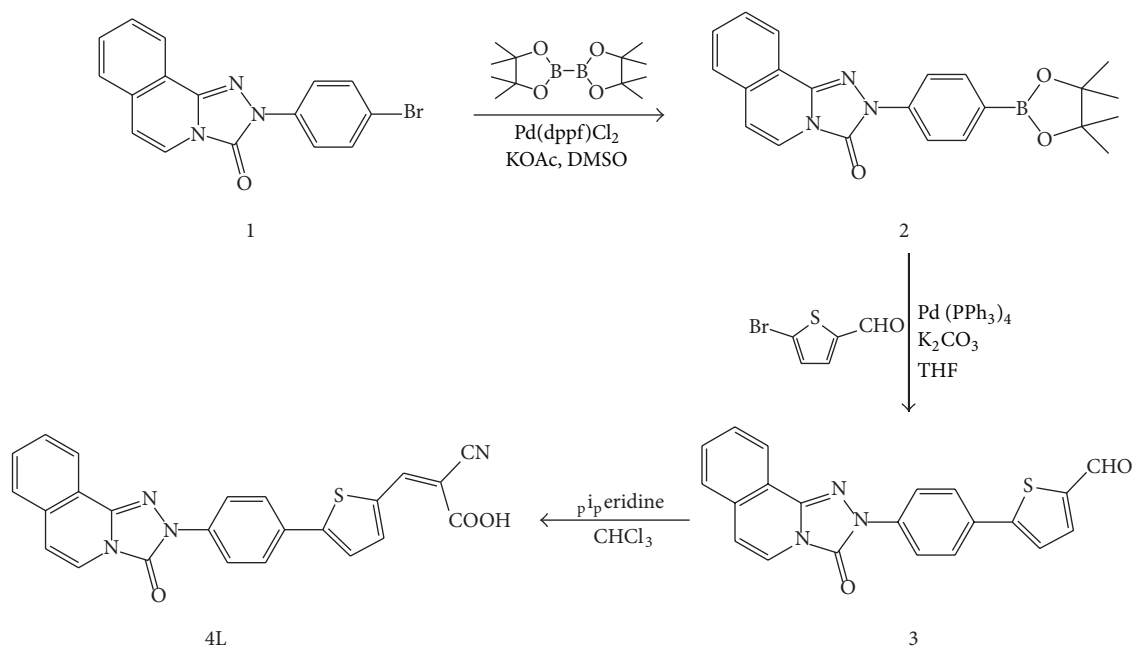


FIGURE 1: Synthetic route of co-adsorbent 4L.

[16]. 4L was synthesized by Suzuki coupling of compound 2 with 5-formylthiophene-2-ylboronic acid, followed by Knoevenagel condensation reaction with cyanoacrylic acid in the presence of piperidine. This product was well characterized by spectroscopic analyses.

3.2. The Double-Layer TiO₂ Film. Recently, an enhancement in light absorption via application of light scattering has been studied for DSSCs [17, 18]. To take advantage of the light-scattering effect of TiO₂ particles, light absorption can be enhanced in TiO₂ films by increasing the absorption path length of photons, which can effectively improve the photocurrent output of cells. In order to obtain a high photoelectric conversion efficiency in DSSCs, a double-layer TiO₂ film was fabricated, composed of a light-scattering layer and a transparent layer. The transparent layer was prepared by commercial TiO₂ paste and the light-scattering layer was deposited by home-made scattering TiO₂ paste. First, TiCl₄ solution was converted to Ti(OH)₄ gel after ammonia neutralization and H₂O₂ was used to hydrolyze Ti(OH)₄ to form TiO₂ sol. Subsequently, the result solution was refluxed 35–40 hours for crystallization, and the anatase type TiO₂ organic sol was obtained. This solution was concentrated by rotary evaporator and dispersed in α -terpineol with ethyl cellulose for scattering TiO₂ paste. After screen-printing, the thickness of the double-layer film was about 16 μ m. Figure 2(a) shows the surface morphology of the light-scattering layer, revealing their well-connected network and the porous nature of TiO₂ film. The average sizes of the nanostructures were about 100 nm in diameter. This results in a good scattering effect because of the elongated optical path length. Figure 2(b) shows the surface morphology of light-scattering layer after TiCl₄ posttreatment. From the SEM image, one can see that

TABLE 1: The amount of adsorbed N719 dye for different TiO₂ structures.

	TiO ₂ structure	Dye adsorption (10 ⁻⁷ mol cm ⁻²)
Film 1	FTO/transparent layer	5.23
Film 2	FTO/transparent layer/light-scattering layer	5.35
Film 3	FTO/transparent layer/light-scattering layer/TiCl ₄ posttreatment	7.02

the necking of the TiO₂ particles and the surface roughness are enhanced and resulting in higher dye adsorption amount. As summarized in Table 1, it was found that the dye amount on a film of Film 3-TiCl₄ posttreatment is higher than those of Films 1 and 2. It is well known that the short-circuit current density is mainly determined by the initial number of photogenerated electrons, and the initial number of photogenerated electrons could be significantly affected by the dye amount on the TiO₂ films. This result agrees well with recent experiments [19, 20]. In order to maximize the light harvesting efficiency, we fabricate the structure of Film 3 for the follow-up discussion of co-adsorbent effect.

3.3. The Concentration Effect of Coadsorbents. After optimization of the devices, the photovoltaic characteristics of the small molecule as co-adsorbent for DSSCs were evaluated with a sandwich DSSC cell (as shown in Figure 3) using 0.6 M [BMI][I], 0.1 M GuNCS, 0.3 M I₂, and 0.5 M TBP in a AN/VN (85/15, v/v) solvent as the redox electrolyte. Details of the device preparation and characterization are described in the experimental section, and all the essential properties of these cells are listed in Figure 3 and Table 2.

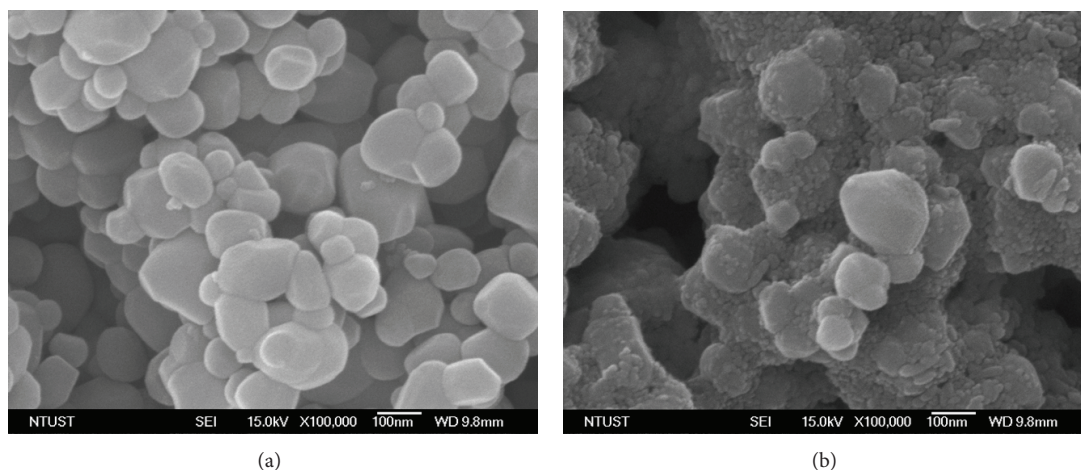


FIGURE 2: SEM images of (a) light-scattering layer of double layer TiO_2 films and (b) TiCl_4 posttreatment of light-scattering layer.

TABLE 2: Photovoltaic parameters of the DSSCs with N719:4L in different molar ratios under AM 1.5 G sunlight^a.

	Dyestuff coadsorbent molar ratio	J_{sc} (mA cm^{-2})	V_{oc} (V)	FF	η (%)
Device A	N719	15.65	0.76	0.70	8.36
Device B	N719-4L 1:0.25	16.39	0.77	0.70	8.83
Device C	N719-4L 1:0.50	15.27	0.76	0.71	8.21
Device D	N719-4L 1:1	15.72	0.75	0.69	8.10

^aPerformances of DSSCs were measured with 0.25 cm^2 working area.

Under the standard AM 1.5 G irradiation, the maximum efficiency (η) for the N719-sensitized solar cell-device B with an active area of 0.25 cm^2 was calculated to be 8.36%, with a J_{sc} of 15.65 mA cm^{-2} , a V_{oc} of 0.76 V, and a fill factor (FF) of 0.70. However, the solar cells based on the $12 + 4 \mu\text{m}$ transparent layer which was sensitized by N719-4L with 1 to 0.25 molar ratio yielded a remarkably high photocurrent density of 16.39 mA cm^{-2} , an open circuit voltage of 0.77 V, and a fill factor of 0.70, corresponding to an overall power conversion efficiency of 8.83%. This result is also in agreement with the observation of the incident photon-to-electron conversion efficiency (IPCE) action spectra of DSSCs presented in Figure 4. With the increase in 4L concentration, the overall power conversion efficiency shows a downward trend. Compared to device A with a single dyestuff-N719, devices C and D based on a high 4L molar ratio exhibit lower η values of 8.21% and 8.10%. It is well known that co-adsorbents will compete with N719 for adsorption on the TiO_2 surface. This result shows that N719 and co-adsorbent 4L are in balance at a 1 to 0.25 molar ratio. In this concentration of cosensitizers, N719 may occupy positions on the TiO_2 surface, and coadsorbent 4L then anchors to the blank to create a perfect insulating molecular layer. Because of this layer, the charge recombination process can be shielded, and the incident photo-to-electron conversion efficiency can be enhanced, and this increases V_{oc} , J_{sc} , and η . On the other

hand, devices C and D show downward trend at V_{oc} and FF values in comparison with device A. This indicates that co-adsorbent 4L has considerable superiority at 1 to 0.50 and 1 to 1 molar ratios, with some N719 molecules having lost their positions on TiO_2 and being replaced by co-adsorbent 4L. This increases the opportunities for π - π stacking of small organic molecule-4L and decreases the contribution of N719 to the incident photon-to-electron conversion efficiency [20–22]. These photovoltaic performance results indicate that coadsorption with 4L and N719 in an appropriate concentration is effective in improving solar cell performance.

4. Conclusions

A new triazoloisoquinoline-based co-adsorbent has been prepared and applied in DSSC. This study demonstrates that coadsorption of N719 sensitizer with triazoloisoquinoline-based organic small molecule onto nanocrystalline TiO_2 films significantly increases the photovoltage and photocurrent, thus enhancing the total conversion efficiency. After optimization of the structure of the TiO_2 layer, the cell produced in this work achieved an energy conversion efficiency as high as 8.83% at 100 mW cm^{-2} and AM 1.5 G at 1 to 0.25 (N719:co-adsorbent) molar ratio. This improved conversion efficiency is attributed to the insulating molecular layer, which was composed of small molecule 4L and N719,

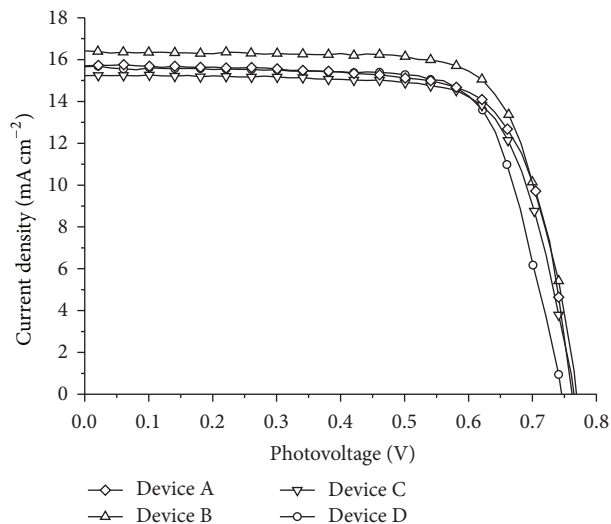


FIGURE 3: Photocurrent density-voltage characteristics of solar cells sensitized by N719 (Device A), N719:4L (1:0.25) (Device B), N719:4L (1:0.5) (Device C), and N719:4L (1:1) (Device D) with 12.0 + 4.0 μm double layers nanocrystalline TiO_2 electrodes.

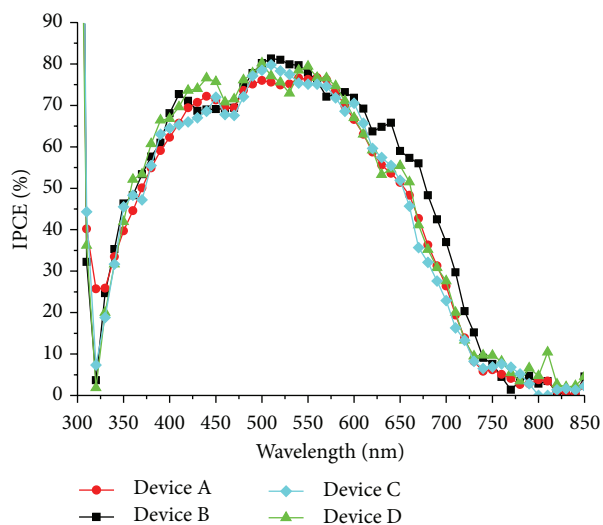


FIGURE 4: IPCE action spectra of solar cells sensitized by N719 (Device A), N719:4L (1:0.25) (Device B), N719:4L (1:0.5) (Device C), and N719:4L (1:1) (Device D) with 12.0 + 4.0 μm double layers nanocrystalline TiO_2 electrodes.

and the charge recombination process can be shielded. This breakthrough will contribute to promoting organic small molecule as co-adsorbents in DSSC.

References

- [1] B. O'Regan and M. Grätzel, "A low-cost, high-efficiency solar cell based on dye-sensitized colloidal TiO_2 films," *Nature*, vol. 353, no. 6346, pp. 737–740, 1991.
- [2] M. Grätzel, "Conversion of sunlight to electric power by nanocrystalline dye-sensitized solar cells," *Journal of Photochemistry and Photobiology A*, vol. 164, pp. 3–14, 2004.
- [3] J. N. de Freitas, A. F. Nogueira, and M.-A. de Paoli, "New insights into dye-sensitized solar cells with polymer electrolytes," *Journal of Materials Chemistry*, vol. 19, no. 30, pp. 5279–5294, 2009.
- [4] M. Gorlov and L. Kloo, "Ionic liquid electrolytes for dye-sensitized solar cells," *Dalton Transactions*, no. 20, pp. 2655–2666, 2008.
- [5] B. Li, L. Wang, B. Kang, P. Wang, and Y. Qiu, "Review of recent progress in solid-state dye-sensitized solar cells," *Solar Energy Materials and Solar Cells*, vol. 90, no. 5, pp. 549–573, 2006.
- [6] M. K. Nazeeruddin, A. Kay, I. Rodicio, and M. Grätzel, "Conversion of light to electricity by cis- X_2 bis(2,2'-bipyridyl-4,4'-dicarboxylate)ruthenium(II) charge-transfer sensitizers ($\text{X} = \text{Cl}^-$, Br^- , I^- , CN^- , and SCN^-) on nanocrystalline TiO_2 electrodes," *Journal of the American Chemical Society*, vol. 115, no. 14, pp. 6382–6390, 1993.
- [7] H. Paulsson, A. Hagfeldt, and L. Kloo, "Molten and solid trialkylsulfonium iodides and their polyiodides as electrolytes in dye-sensitized nanocrystalline solar cells," *Journal of Physical Chemistry B*, vol. 107, no. 49, pp. 13665–13670, 2003.
- [8] J.-H. Yum, P. Walter, S. Huber et al., "Efficient far red sensitization of nanocrystalline TiO_2 films by an unsymmetrical squaraine dye," *Journal of the American Chemical Society*, vol. 129, no. 34, pp. 10320–10321, 2007.
- [9] H. Tian, X. Yang, J. Cong et al., "Tuning of phenoxazine chromophores for efficient organic dye-sensitized solar cells," *Chemical Communications*, no. 41, pp. 6288–6290, 2009.
- [10] S. Ito, H. Miura, S. Uchida et al., "High-conversion-efficiency organic dye-sensitized solar cells with a novel indoline dye," *Chemical Communications*, no. 41, pp. 5194–5196, 2008.
- [11] J.-C. Chang, C.-H. Yang, H.-H. Yang et al., "Pyridinium molten salts as co-adsorbents in dye-sensitized solar cells," *Solar Energy*, vol. 85, no. 1, pp. 174–179, 2011.
- [12] H. Kusama and H. Arakawa, "Influence of pyrimidine additives in electrolytic solution on dye-sensitized solar cell," *Journal of Photochemistry and Photobiology A*, vol. 160, no. 3, pp. 171–179, 2003.
- [13] S. Ruhle, M. Greenshtein, S.-G. Chen et al., "Molecular adjustment of the electronic properties of nanoporous electrodes in dye-sensitized solar cells," *Journal of Physical Chemistry B*, vol. 109, no. 40, pp. 18907–18913, 2005.
- [14] M. Wang, C. Grätzel, S.-J. Moon et al., "Surface design in solid-state dye sensitized solar cells: effects of zwitterionic co-adsorbents on photovoltaic performance," *Advanced Functional Materials*, vol. 19, no. 13, pp. 2163–2172, 2009.
- [15] Y. M. Lin, S. L. Liu, and Y. H. Tseng, "Photocatalytic titanium oxide solution and method for producing the same," TW 130690, 2005.
- [16] C. Y. Chiu, C. N. Kuo, W. F. Kuo, and M. Y. Yeh, "Studies on the reaction of α -chloroformylarylhrazine hydrochloride with N-heterocyclic compounds," *Journal of the Chinese Chemical Society*, vol. 49, p. 239, 2002.
- [17] S. Hore, C. Vetter, R. Kern, H. Smit, and A. Hinsch, "Influence of scattering layers on efficiency of dye-sensitized solar cells," *Solar Energy Materials and Solar Cells*, vol. 90, no. 9, pp. 1176–1188, 2006.
- [18] S. Ito, T. N. Murakami, P. Comte et al., "Fabrication of thin film dye sensitized solar cells with solar to electric power conversion efficiency over 10%," *Thin Solid Films*, vol. 516, no. 14, pp. 4613–4619, 2008.

- [19] P. M. Sommeling, B. C. O'Regan, R. R. Haswell et al., "Influence of a TiCl_4 post-treatment on nanocrystalline TiO_2 films in dye-sensitized solar cells," *Journal of Physical Chemistry B*, vol. 110, no. 39, pp. 19191–19197, 2006.
- [20] M.-S. Wu, C.-H. Tsai, J.-J. Jow, and T.-C. Wei, "Enhanced performance of dye-sensitized solar cell via surface modification of mesoporous TiO_2 photoanode with electrodeposited thin TiO_2 layer," *Electrochimica Acta*, vol. 56, no. 24, pp. 8906–8911, 2011.
- [21] X.-F. Wang, H. Tamiaki, L. Wang et al., "Chlorophyll-a derivatives with various hydrocarbon ester groups for efficient dye-sensitized solar cells: static and ultrafast evaluations on electron injection and charge collection processes," *Langmuir*, vol. 26, no. 9, pp. 6320–6327, 2010.
- [22] F. Gao, Y. Cheng, Q. Yu et al., "Conjugation of selenophene with bipyridine for a high molar extinction coefficient sensitizer in dye-sensitized solar cells," *Inorganic Chemistry*, vol. 48, no. 6, pp. 2664–2669, 2009.

Research Article

Design of High Efficiency Illumination for LED Lighting

Yong-Nong Chang,¹ Hung-Liang Cheng,² and Chih-Ming Kuo¹

¹ Department of Electrical Engineering, National Formosa University, Yunlin County 63201, Taiwan

² Department of Electrical Engineering, I-Shou University, Kaohsiung 84001, Taiwan

Correspondence should be addressed to Yong-Nong Chang; ynchang@nfu.edu.tw

Received 11 September 2013; Accepted 6 October 2013

Academic Editor: Teen-Hang Meen

Copyright © 2013 Yong-Nong Chang et al. This is an open access article distributed under the Creative Commons Attribution License, which permits unrestricted use, distribution, and reproduction in any medium, provided the original work is properly cited.

A high efficiency illumination for LED street lighting is proposed. For energy saving, this paper uses Class-E resonant inverter as main electric circuit to improve efficiency. In addition, single dimming control has the best efficiency, simplest control scheme and lowest circuit cost among other types of dimming techniques. Multiple serial-connected transformers used to drive the LED strings as they can provide galvanic isolation and have the advantage of good current distribution against device difference. Finally, a prototype circuit for driving 112 W LEDs in total was built and tested to verify the theoretical analysis.

1. Introduction

Green energy and high efficiency equipment have been developed rapidly to mitigate to global warming problem. In order to improve the efficiency of lighting equipments, light emitting diode (LED) has been paid attention and adopted as the light source. LED has the highest lighting efficiency among other lighting equipments. Furthermore, it possesses longer life cycle, faster dynamic response, smaller device volume and higher color rendering index. LED lighting equipments are widely used for automobiles [1–4], indoor lightings [5], outdoor lights [6, 7], and street lamps recently. LED lighting equipments are look upon as the main lighting equipment in the future. In order to replace traditional lighting equipments, LED lighting equipments of high output power are developing rapidly in recent years. Performance of LED lighting equipment has been paid attention to, such as efficiency of LED drivers, device reliability, and dimming features. In this paper, multiple serial-connected transformers are used to overcome the problems mentioned above.

In order to drive the multiple serial-connected transformers, an inverter is required. Class-E serial resonant inverter will be used in this paper as main electric circuit. Class-E resonant inverter can achieve higher efficiency than Class-D resonant inverter [8, 9]. In order to lower the usage of

electricity for lightings during daytime, dimming features are seen as a way to save energy of lighting equipments. Conventional ways to achieve dimming feature is to use linear current-regulator to control LED lighting equipments individually [10]. Another way is to use PWM controller to achieve dimming control [11, 12], but PWM controller without current limitation function causes the shrink of life cycle of LED. Dimming switches of both ways do not have the ability of soft switching, which involves switching losses during dimming control. In this paper, integral-cycle control is used to achieve ZCS function of dimming switches, minimizing the power losses during dimming control.

There are several different control schemes to achieve same output power of an LED lighting equipment. This paper proposes three types of different dimming controls for multiple serial-connected transformers. Three types of dimming controls include synchronism dimming control, sequential dimming control, and single dimming control. The efficiency and control scheme are both compared in this paper to find out the best dimming control scheme.

2. Topology and Analysis of Proposed Circuit

To improve the efficiency of street lighting, Class-E resonant inverter is used in this paper. Class-E resonant inverter possesses higher efficiency than other types of inverter.

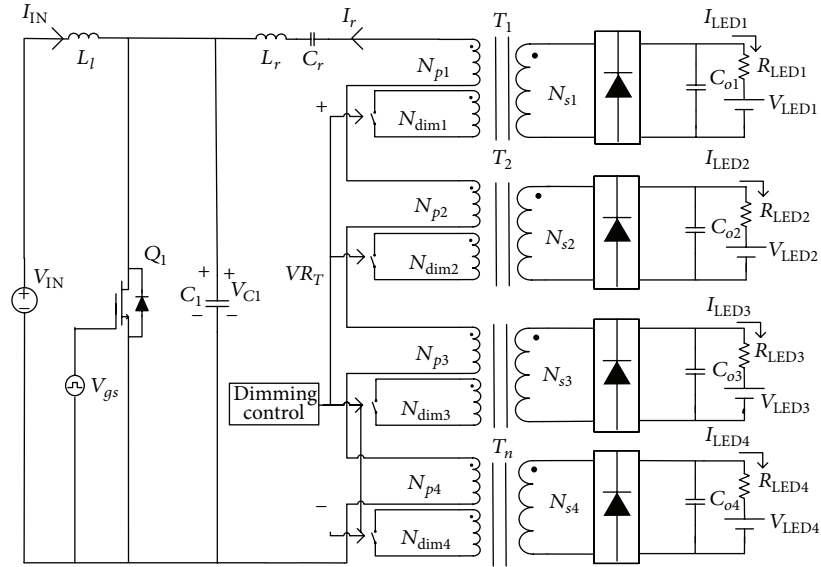


FIGURE 1: Proposed circuit in this paper.

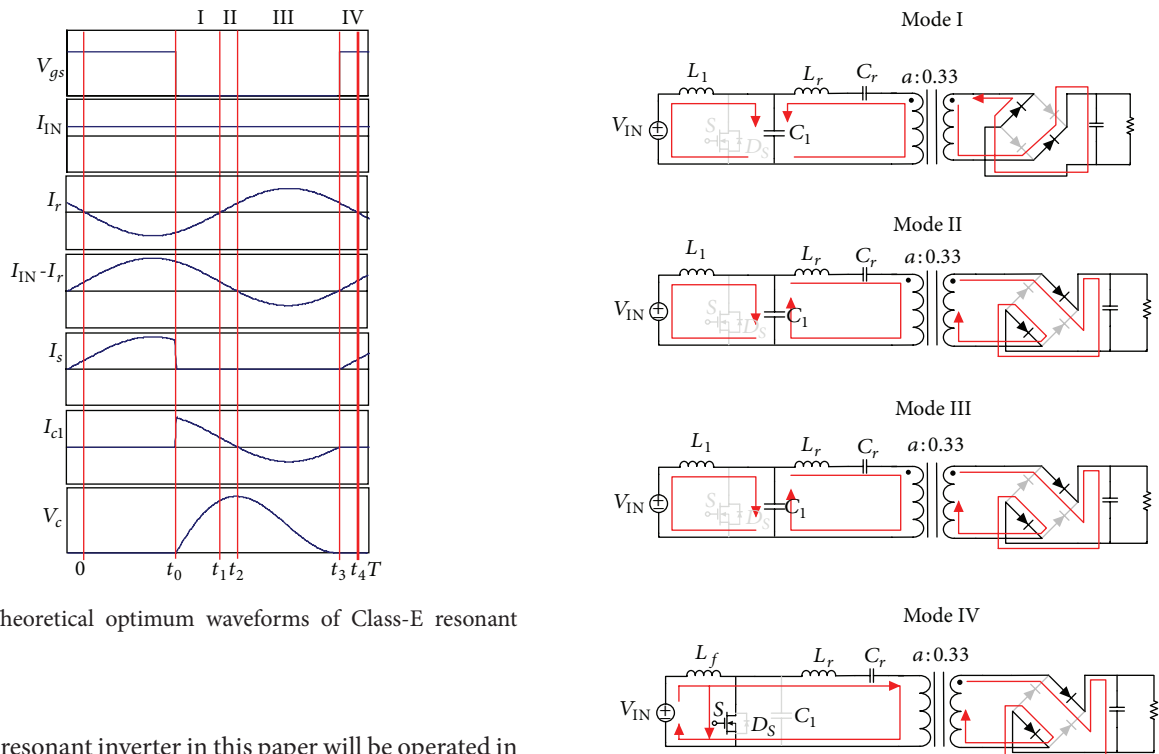


FIGURE 2: Theoretical optimum waveforms of Class-E resonant inverter.

The class-E resonant inverter in this paper will be operated in close to optimum mode to ensure ZVS function of the main switch at all time. Figure 1 shows the proposed circuit in this paper. Figure 2 shows the theoretical optimum waveforms of operating modes of class-E resonant inverter; it can be categorized into 4 modes as shown in Figure 3; the modes are described as follows.

2.1. *Mode I:* $t_0 < t < t_1$. When switch S1 turns off, Mode I starts. As the switch of the resonant inverter turns off, current $I_{IN} - I_r$ is in positive cycle. The current is flowing through the parallel capacitor C_1 and, voltage on C_1 is raised from zero.

Mode I ends when the resonant current passes through zero and the circuit enters the next mode.

2.2. *Mode II:* $t_1 < t < t_2$. Mode II starts when the resonant current enters positive cycle and ends when current of C_1, I_{c1} passes through zero point and then the circuit enters Mode III.

FIGURE 3: Operating modes of proposed circuit.

2.3. *Mode III*: $t_2 < t < t_3$. Mode III starts when the current $I_{IN} - I_r$ passes through zero and enters negative cycle. The main switch of class-E resonant inverter remains off. The current $I_{IN} - I_r$ enters negative cycle and so is the current of capacitor C_1, I_{c1} . The voltage on the parallel capacitor C_1 begins to discharge. This mode ends when current $I_{IN} - I_r$ passes through zero and enters the positive cycle.

2.4. *Mode IV*: $t_3 < t < t_4$. Mode IV starts after current $I_{IN} - I_r$ enters positive cycle. Parallel capacitor C_1 is completely discharged and the main switch turns on. Since the voltage applied on the parallel capacitor drops to zero and so is the voltage applied on the main switch. Therefore, the main switch of Class-E resonant inverter achieves zero-voltage switching (ZVS) function and reduces switching losses. This mode ends when the resonant current becomes negative and the circuit enters Mode I of the next high frequency cycle.

Reactance changes to resonant tank during dimming control might result in current variation. Current variation might result in malfunction of LED street lamp, which influences the safety of drivers, and it is not acceptable. Class-E resonant inverter must be well designed to prevent unacceptable current variation. Therefore, characteristics of proposed circuit are analyzed as follows.

To simplify the analysis, the circuit is simplified as in Figure 4. As shown in Figure 5, in order to simplify the parameters design, the loads are equivalent to the primary side of transformers R_p . The value of the input inductor will influence the ripple of input current which can be expressed as in (1). The value of DC input current can be estimated by (2). With a high load quality factor, almost all the harmonic contents and Dc components will be filtered by the resonant tank. Only the fundamental current at the switching frequency will be present in the load circuit. Therefore, the load resonant circuit can be analyzed using the fundamental component approximation. The fundamental voltage V_{c1} applied on parallel capacitor C_1 can be estimated by (3)

$$\Delta L_{1,pp} = \frac{V_{IN}}{L_1} DT, \quad (1)$$

$$\implies L_1 = \frac{V_{IN}}{\Delta i_{L,PP}} DT,$$

$$I_{IN} = \frac{P}{V_{IN}}, \quad (2)$$

$$V_{c1} \approx \frac{2\sqrt{2} \times V_{IN}}{\pi}. \quad (3)$$

During dimming control, the resonant current is impossible to be kept unchanged, and determination of the maximum loading current is essential. The variation of LED current is proportional to the variation of resonant current, and the resonant current is dominated by Z_{LC} and R_T . The minimum resonant current $I_{r \min}$ will occur at full load; minimum resonant current $I_{r \min}$ can be expressed as in (4), where n is the number of LED lighting sets. When LED lighting sets are shorted during dimming control, the resonant current

will rise to the maximum. The maximum resonant current $I_{r \max}$ occurs when only one equivalent resistance of LED set participates in the resonant tank. $I_{r \max}$ can be expressed as in (5). With T_x being defined as ratio of Z_{LC} and R_p as expressed by (6), the resonant current ratio of $I_{r \min}$ and $I_{r \max}$, K can be expressed as in (7)

$$I_{r \min} = \frac{V_{c1}}{\sqrt{(nR_p)^2 + (Z_{LC})^2}}, \quad (4)$$

$$I_{r \max} = \frac{V_{c1}}{\sqrt{(R_p)^2 + (Z_{LC})^2}}, \quad (5)$$

$$Z_{LC} = |T_x R_p|, \quad (6)$$

$$K \equiv \frac{I_{r \min}}{I_{r \max}} = \sqrt{\frac{(1 + T_x^2)}{n^2 + T_x^2}}, \quad (7)$$

where K is the current ratio of $I_{r \min}$ and $I_{r \max}$.

As shown in (8), according to Kirchhoff's voltage law (KVL), voltage of the resonant tank is equal to the sum of the voltage applied on resonant components and loads, and, wherein, the R_T can be found by (9). Since the ratio of reactance Z_{LC} to R_p has been found, voltage applied on single transformer V_{R_p} with full load can be calculated by (10)

$$(V_{c1})^2 = (VR_T)^2 + (V_{Z_{LC}})^2, \quad (8)$$

$$R_T = n \times R_p, \quad (9)$$

$$V_{R_p} = \sqrt{\frac{V_{c1}^2}{n^2 + T_x^2}}. \quad (10)$$

The specifications of LED lighting sets are given in Table 1. The operating voltage of LED lighting set at rate output, V_{lamp} , will be estimated by (11), where the $I_{LED \min}$ can be estimated by (12)

$$V_{lamp} = V_{LED} + I_{LED \min} \cdot R_{LED}, \quad (11)$$

$$I_{LED \min} = I_{LED} \times K. \quad (12)$$

With the voltages of both sides of transformers being found out, turn ratio N_p/N_s can be estimated by (13)

$$a \equiv \frac{N_p}{N_s} = \frac{\pi \times V_{R_p}}{2\sqrt{2} \times V_{Lamp}}, \quad (13)$$

where a is the turn ratio in this paper.

Moreover, the resonant current during full load can be referred from the secondary side of transformer to the primary side; the RMS value of full load resonant current $I_{r \min}$ can be estimated by (14)

$$I_{r \min} = \frac{\pi \times I_{LED \min}}{2\sqrt{2} \times a}. \quad (14)$$

Since all the components are ideal, there will be no power losses in transformers, and the input power is equal to the

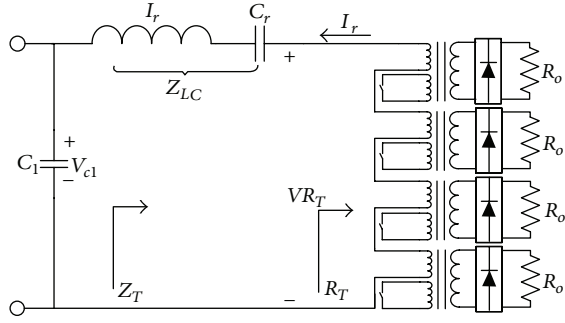
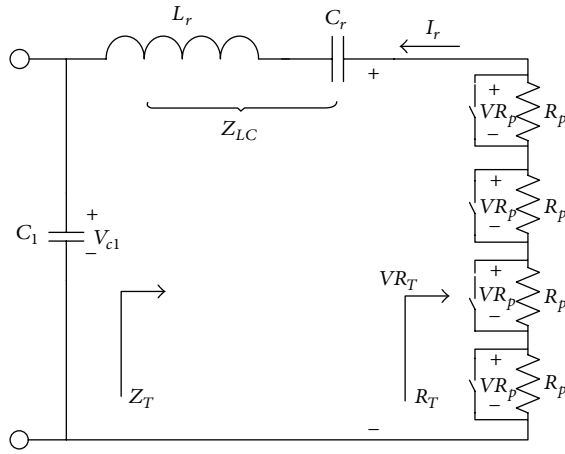


FIGURE 4: Simplified circuit.

FIGURE 5: Equivalent power resistance R_p .

output power; therefore, the input power of primary side can be estimated by (15)

$$P_{R_p} = I_{LED \min} \times V_{Lamp}. \quad (15)$$

With the input power P_{R_p} and the resonant current of primary side $I_{r \min}$, the equivalent power resistance can be estimated by (16)

$$R_p \equiv \frac{P_{R_p}}{(I_{r \min})^2} = \frac{8 \times a^2 \times V_{Lamp}}{\pi^2 \times I_{LED \min}}, \quad (16)$$

where R_p is the equivalent power resistance in the primary side of transformers.

Since the value of C_1 influences whether the main switch of class-E resonant inverter has the capability of zero-voltage switching (ZVS) function or not, analysis of parallel capacitor C_1 is critical in this research. If the resonant current is defined as (17), the output power can be expressed as in (18). If RMS value of resonant current is expressed as in (19), the peak value of resonant current can be expressed as in (20). The current of parallel capacitor C_1 , I_{c1} , is expressed as in (21). The instantaneous voltage of parallel capacitor C_1 , $V_{c1}(t)$, is expressed as in (22). $V_{c1}(t_3)$ will drop to zero at time instant t_3 as expressed by (23). Besides, $V_{c1}(t_3)$ can be expressed as in (24). Therefore, the angle, Φ , by which the resonant voltage

leads the resonant current can be found by deducing (24). The mean voltage of C_1 , V_{c1av} will be equal to the input voltage V_{IN} as in (25). The mean voltage of C_1 , V_{c1av} , can be expressed as in (26). Therefore, the value of C_1 can be rewritten as in (27), and the value can be found by deriving (27)

$$I_r = I_o \sin(\omega t - \Phi), \quad (17)$$

$$P = I_r^2 \times R_T, \quad (18)$$

$$I_{r(rms)} = \sqrt{\frac{4 \times I_{LED \min} \times V_{Lamp}}{R_T}}, \quad (19)$$

$$I_{o(peak)} = \sqrt{\frac{8 \times I_{LED \min} \times V_{Lamp}}{R_T}}, \quad (20)$$

$$i_{c1}(t) = I_{IN} - I_o \sin(\omega t - \Phi), \quad (21)$$

$$\begin{aligned} V_{c1}(t) &= \frac{1}{C_1} \int_{t_0}^t [I_{IN} - I_o \sin(\omega t - \Phi)] dt \\ &= \frac{1}{C_1} \left[I_{IN} \times t + \frac{I_o}{\omega} \cos(\omega t - \Phi) - \frac{I_o}{\omega} \cos \Phi \right], \end{aligned} \quad (22)$$

$$V_{c1}(t_3) = 0, \quad (23)$$

$$\begin{aligned} V_{c1}(t_3) &= \frac{1}{C_1} \int_{t_0}^{t_3} [I_{DC} - I_o \sin(\omega t - \Phi)] dt \\ &= \frac{1}{C_1} \left[(1-D)T \times I_{IN} + \frac{I_o}{\omega} \cos(2D\pi + \Phi) \right. \end{aligned} \quad (24)$$

$$\left. - \frac{I_o}{\omega} \cos \Phi \right],$$

$$V_{c1av} = V_{IN}, \quad (25)$$

$$\begin{aligned} V_{c1av} &= \frac{1}{T} \int_{t_0}^{(1-D)T} V_{c1}(t) dt \\ &= \frac{1}{C_1} \left\{ \frac{(1-D)^2 T}{2} I_{IN} - \frac{(1-D)T}{2\pi} \cos \Phi \times I_o \right. \end{aligned} \quad (26)$$

$$\left. + \frac{T}{4\pi^2} I_o [\sin \Phi - \sin(2D\pi + \Phi)] \right\},$$

$$\begin{aligned} C_1 &= \frac{1}{V_{IN}} \left\{ \frac{(1-D)^2 T}{2} I_{IN} - \frac{(1-D)T}{2\pi} \cos \Phi \times I_o \right. \\ &\quad \left. + \frac{T}{4\pi^2} I_o [\sin \Phi - \sin(2D\pi + \Phi)] \right\}. \end{aligned} \quad (27)$$

Using the parameters of resonant frequency of resonant tank f_r and switching frequency f_s defined in Table 1, the reactance Z_{LC} defined as in (28) and resonant components C_r

TABLE 1: Specifications of proposed circuit.

Input voltage, V_{IN}	140 V
Current ratio, K	0.7
Turn ratio, a	0.30
Turn ratio of dimming circuit	0.125
Switching frequency, f_s	50 kHz
Resonant frequency, f_r	40 kHz
Maximum loading current of LED, I_{LED}	350 mA
Operating voltage of LED, V_{LED}	78.8 V
Total output power, P_o	112 W
Value of output capacitor, C_{on}	330 μ F

TABLE 2: Parameters deduced from design procedures.

Input inductor, L_1	10 mH
Voltage apply on C_1 , V_{c1}	126 V
Magnification of resistance, T_X	3.66
Equivalent power resistance, R_T	118 Ω
Voltage apply on a single transformer, V_{Rp}	23.24 V
Minimum resonant current, I_{rmin}	0.9 A
Minimum loading current of LEDs, I_{LEDmin}	280 mA
Value of parallel capacitor, C_1	20.5 nF
Value of resonant capacitor, C_r	49 nF
Value of resonant inductor, L_r	321 μ H

and L_r can be solved by deducing simultaneous (28), where K is the resonant current ratio of I_{rmin} and I_{rmax}

$$Z_{LC} = \omega_s L_r - \frac{1}{\omega_s C_r}, \quad (28)$$

$$\omega_r = 2\pi f_r = \frac{1}{\sqrt{L_r C_r}}.$$

3. Experimental Results

In this paper, a high efficiency street lighting is proposed. Table 1 shows the specification of the proposed circuit, following the design procedures in the previous section. Parameters can be deduced as in Table 2. Figure 6 shows the waveforms of the Class-E resonant inverter during full load using the parameters listed in Table 2. Experimental waveforms show that the experimental results are in good consistency with the theoretical prediction.

Figures 7 and 8 show the waveforms which indicate that the main switch is able to achieve ZVS function in both full load and single load. Figure 7 shows the voltage waveforms of V_{gs} and V_{c1} during single load and Figure 8 shows the voltage waveforms of V_{gs} and V_{c1} during full load. Resonant current will flow through the body diode of the main switch before it turns on. It can be clearly seen that the main switch of the Class-E resonant inverter has achieved ZVS function in both full load and single load as demanded.

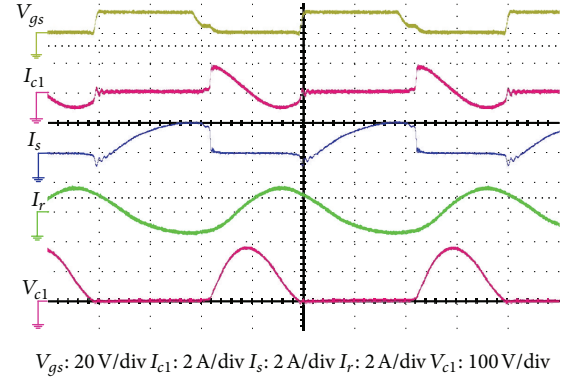


FIGURE 6: Experimental waveforms of Class-E resonant inverter.

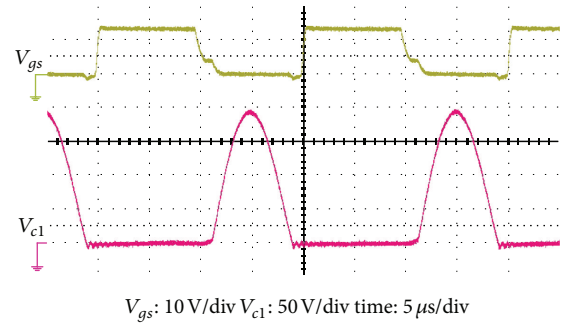


FIGURE 7: Waveforms of ZVS function of the main switch of Class-E resonant inverter during single load.

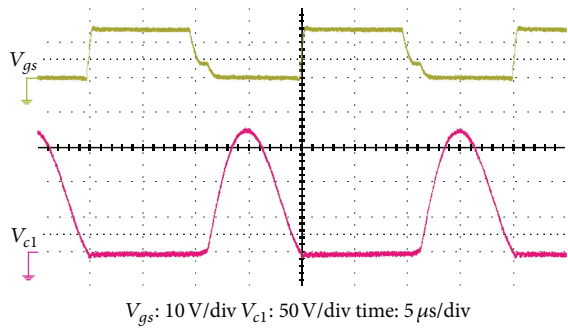


FIGURE 8: Waveforms of ZVS function of the main switch of Class-E resonant inverter during full load.

4. Discussions of Different Types of Dimming Control

With integral-cycle control being used in this paper to implement the dimmer design, wide range and precise dimming control can be achieved. During dimming control, reactance changes will occur. There are several ways to achieve same output effect with different dimming control techniques. The relationship between different dimming techniques and reactance changes will be discussed in this section. The frequency of dimming signal V_{gs-dim} is 500 Hz and switching frequency of the Class-E resonant inverter is 50 kHz. Dimming range is made possible from 0.25% to 100%. Since street lamps are

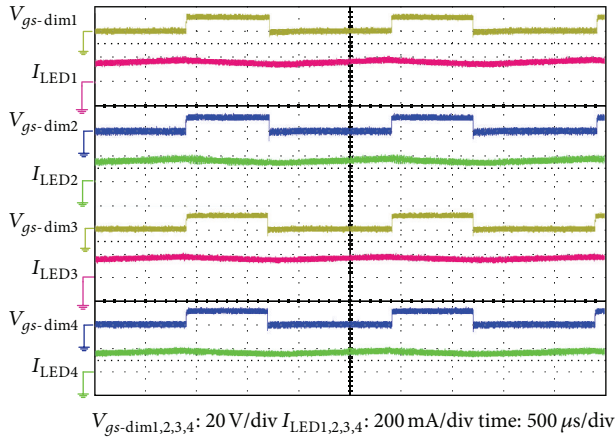


FIGURE 9: 60% output of synchronism dimming control.

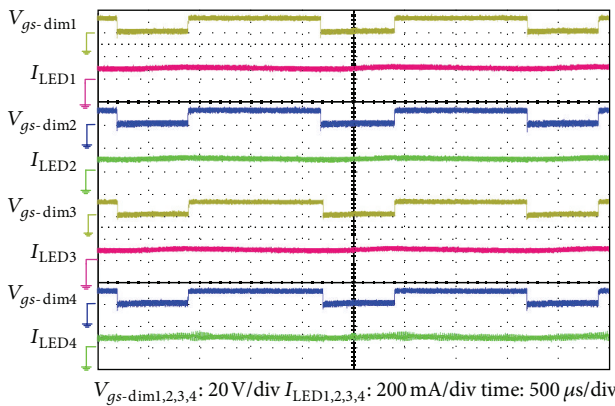


FIGURE 10: 35% output of synchronism dimming control.

operated at rate output, generally, they do not require wide range of dimming control. The dimming control of 35% to 100% rated power is proposed in this paper. Output capacitors with great value are used in this paper to limit the effect of current variation occurrence during dimming control.

4.1. Synchronism Dimming Control. The first way to control the LED lighting set is to control all the lighting sets simultaneously, while the LED lighting sets are able to produce the same amount of output power. But in this way, the reactance will change at any time, leading to a huge reactance change to the whole system during dimming control.

Figure 9 shows 60% rated power; Figure 10 shows 35% rated power. Theoretically, the mean value of loading current I_{LEDn} under 85% output of dimming control is about 238 mA, while it is 168 mA under 60% output of dimming control, 98 mA under 35% output of dimming control, and 56 mA under 20% output of dimming control.

4.2. Sequential Dimming Control. To avoid reactance changes at any time and leading huge reactance to whole system, sequential dimming control is proposed. LED lighting sets are separated into 2 groups, with 1 ms delay of each group.

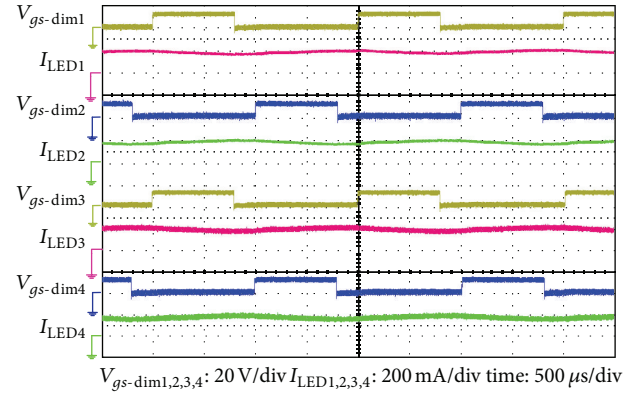


FIGURE 11: 60% output of sequential dimming control.

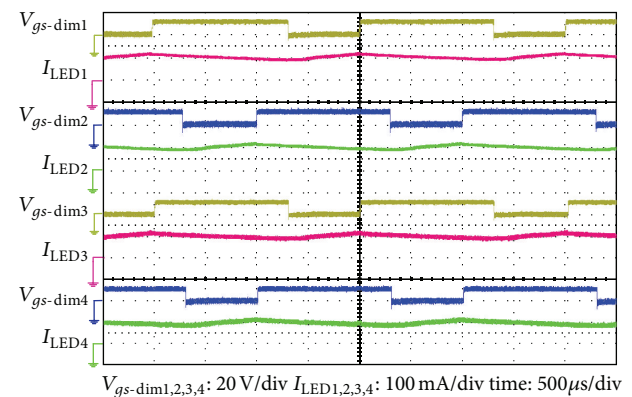


FIGURE 12: 35% output of sequential dimming control.

The reactance changes of each LED lamp can be equally shared in different periods, which lower the reactance changes comparing to synchronism dimming control. Figure 11 shows 60% output of dimming control; Figure 12 shows 35% output of dimming control. In these ways, four sets of integral control circuits must be required, and control scheme is complicated as well.

4.3. Single Dimming Control. Last technique is single dimming control. Only one LED lighting set is in charge of detail dimming control while the rest of the LED lighting sets are kept either on or off. In this way, only one set needs the Integral-Cycle Control circuit, which can reduce the circuit cost and simplify the control scheme, the reactance change is the lowest as well.

Figure 13 shows 60% output of dimming control; Figure 14 shows 35% output of dimming control.

Finally, we compare the efficiency of the three types of dimming controls, Figure 15 shows the efficiency of the three types of dimming controls. Single dimming control has the best efficiency among the three types; it requires one integral-cycle control circuit only, reduces reactance changes during dimming control, and is a comparatively simplified dimming control scheme. Figure 16 shows the lumen curve of single dimming control from 35% to 100% output.

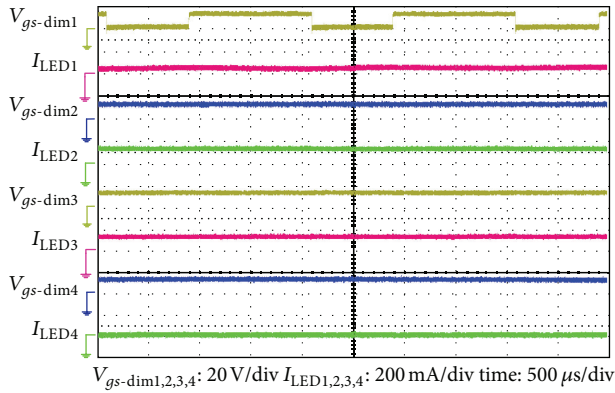


FIGURE 13: 60% output of single dimming control.

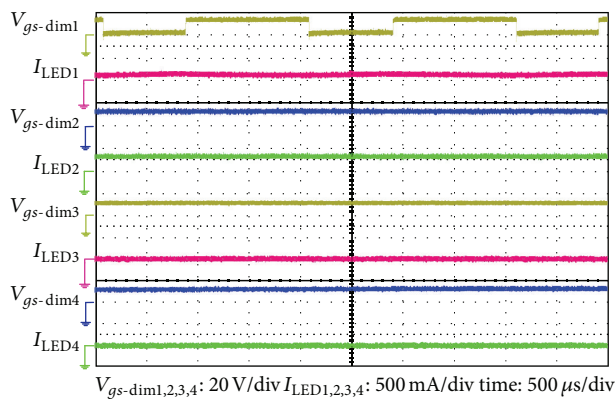


FIGURE 14: 35% output of single dimming control.

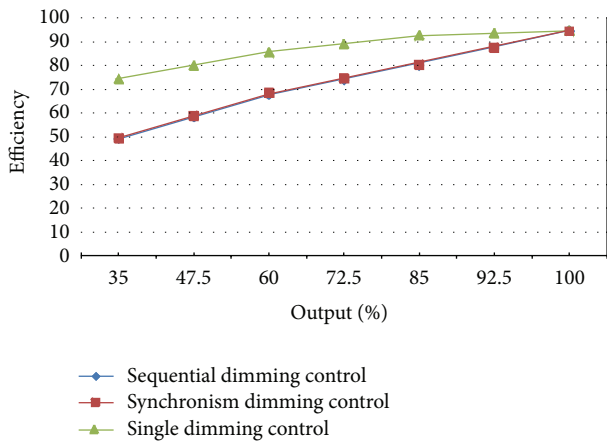


FIGURE 15: Efficiency of three types of dimming controls.

5. Conclusion

Via precise design of the Class-E resonant inverter, LED street lamps can prevent damage from current variation during dimming control. From experimental results, multiple serial-connected transformers have successfully solved the problems of power isolation and current uniformity. Single dimming control is the best way of achieving dimming

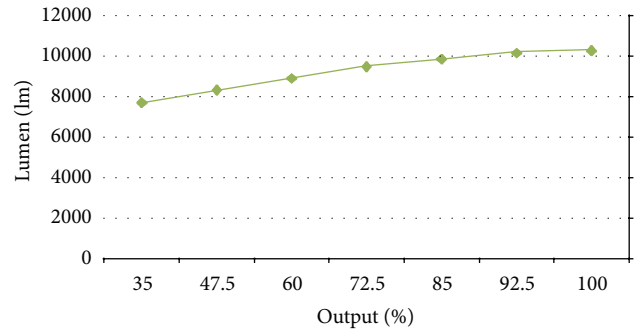


FIGURE 16: Lumen curve of single dimming control.

feature. Not only did it reduce the reactance changes during dimming control, but it also achieves comparatively the highest efficiency as well, leading to curtailing circuit cost and simplifying the control scheme. Finally, an 112 W high efficiency illumination for LED street lighting is developed, and efficiency can maintain 94% and 10270 lm at rate output.

Conflict of Interests

The authors declare that there is no conflict of interests regarding the publication of this paper.

Acknowledgment

This research is supported by the National Science Council, R.O.C., under Contract NSC 101-2221-E-150 -067-MY2.

References

- [1] S. Saponara, G. Pasetti, N. Costantino, F. Tinfena, P. D’Abramo, and L. Fanucci, “A flexible LED driver for automotive lighting applications: IC design and experimental characterization,” *IEEE Transactions on Power Electronics*, vol. 27, no. 3, pp. 1071–1075, 2012.
- [2] S. Jang and M. W. Shin, “Thermal analysis of LED arrays for automotive headlamp with a novel cooling system,” *IEEE Transactions on Device and Materials Reliability*, vol. 8, no. 3, pp. 561–564, 2008.
- [3] D. Gacio, J. Cardesin, E. L. Corominas, J. M. Alonso, M. Dalla-Costa, and A. J. Calleja, “Comparison among power LEDs for automotive lighting applications,” in *Proceedings of the IEEE Industry Applications Society Annual Meeting, (IAS ’08)*, vol. 93, pp. 1204–1223, Alberta, Canada, October 2008.
- [4] I. Takai, S. Ito, K. Yasutomi, K. Kagawa, M. Andoh, and S. Kawahito, “LED and CMOS image sensor based optical wireless communication system for automotive applications,” *IEEE Photonics Journal*, vol. 5, Article ID 6801418, 2013.
- [5] S. Y. Jung, S. Hann, and C. S. Park, “TDOA-based optical wireless indoor localization using LED ceiling lamps,” *IEEE Transactions on Consumer Electronics*, vol. 57, no. 4, pp. 1592–1597, 2011.
- [6] S. Moon, G. B. Koo, and G. W. Moon, “A new control method of interleaved single-stage flyback AC-DC converter for outdoor LED lighting systems,” *IEEE Transactions on Power Electronics*, vol. 28, pp. 4051–4062, 2013.

- [7] M. Wada, T. Yendo, T. Fujii, and M. Tanimoto, "Performance enhancement of outdoor visible-light communication system using selective combining receiver," *IET Optoelectronics*, vol. 3, no. 1, pp. 30–39, 2009.
- [8] T. Suetsugu and M. K. Kazimierczuk, "Design procedure of Class-E amplifier for off-nominal operation at 50% duty ratio," *IEEE Transactions on Circuits and Systems*, vol. 53, no. 7, pp. 1468–1476, 2006.
- [9] I. Boonyaroonate and S. Mori, "Analysis and design of class E isolated dc/dc converter using class E low dv/dt PWM synchronous rectifier," *IEEE Transactions on Power Electronics*, vol. 16, no. 4, pp. 514–521, 2001.
- [10] H. J. Chiu, H. M. Huang, H. T. Yang, and S. J. Cheng, "An improved single-stage flyback PFC converter for high-luminance lighting LED lamps," *International Journal of Circuit Theory and Applications*, vol. 36, no. 2, pp. 205–210, 2008.
- [11] H. J. Chiu and S. J. Cheng, "LED backlight driving system for large-scale LCD panels," *IEEE Transactions on Industrial Electronics*, vol. 54, no. 5, pp. 2751–2760, 2007.
- [12] Y. T. Huang, H. C. Hsiao, Y. H. Liu, C. R. Lee, and L. L. Lee, "A novel constant-power control for metal-halide lamp electronic ballasts with dimming capability," *IEEE Transactions on Plasma Science*, vol. 38, no. 6, pp. 1482–1488, 2010.

Research Article

The Investigation on Color Purity of Blue Organic Light-Emitting Diodes (BOLED) by Hole-Blocking Layer

Kan-Lin Chen,¹ Chien-Jung Huang,² Wen-Ray Chen,³ Chih-Chieh Kang,⁴
Wen-How Lan,⁵ and Yu-Chen Lee²

¹ Department of Electronic Engineering, Fortune Institute of Technology, Kaohsiung 83160, Taiwan

² Department of Applied Physics, National University of Kaohsiung, Kaohsiung 81148, Taiwan

³ Department of Electronic Engineering, National Formosa University, Huwei, Yunlin 63201, Taiwan

⁴ Department of Electro-Optical Engineering, Southern Taiwan University of Science and Technology, Tainan 71005, Taiwan

⁵ Department of Electrical Engineering, National University of Kaohsiung, Kaohsiung 81148, Taiwan

Correspondence should be addressed to Kan-Lin Chen; klchen@fotech.edu.tw and Chien-Jung Huang; chien@nuk.edu.tw

Received 18 October 2013; Accepted 31 October 2013

Academic Editor: Teen-Hang Meen

Copyright © 2013 Kan-Lin Chen et al. This is an open access article distributed under the Creative Commons Attribution License, which permits unrestricted use, distribution, and reproduction in any medium, provided the original work is properly cited.

Organic light-emitting diodes (OLEDs) with triple hole-blocking layer (THBL) structure, which consist of 2,9-dimethyl-4,7-diphenyl-1,10-phenanthroline (BCP), 4,4'-bis(2,2'-diphenyl vinyl)-1,1'-biphenyl (DPVBi), and (4,4'-N,N'-dicarbazole)biphenyl (CBP), have been fabricated. Regardless of applied voltage variation, the luminous efficiency of the OLEDs with THBL structure was increased by 41% as compared with the dual hole-blocking layer (DHBL) structure. The CIE coordinates of (0.157, 0.111) of device with THBL structure are close to pure blue emission than that of other devices of DHBL. There is a coordinate with the slight shift of $\pm\Delta_{x,y} = (0.001, 0.008)$ for the device with THBL structure during the applied voltage of 6–9 V. The results indicate that the excitons can be effectively confined in the emitting layer of device, leading to an enhancement of luminance efficiency and more stable coordinate.

1. Introduction

Recently, organic light-emitting diodes (OLEDs) have attracted much attention due to their superior characteristics such as high luminance, wide range of colors, and wide viewing angles. OLEDs have been regarded as the next generation display technology. Many approaches have been tried to realize full-color displays [1], and it requires three basic emitting colors, red, green, and blue. However, the blue OLEDs still have inherent problems of low efficiency, poor color purity, and short lifetime in comparison with other red or green OLEDs [2]. It is important to keep the color stability with applied voltage in the blue OLEDs. So far, there is still a distance to achieve standard Commission International de l'Éclairage (CIE) coordinates (0.14, 0.08) of blue OLEDs. Generally, there are many structures of emitting layer to obtain blue OLEDs, such as single emitting layer, double emitting layer, blue guest doped layer, or multiple-quantum-well (MQW) layer [3–12]. Shi et al. utilized MQW structure

of [4,4-bis[N-(1-naphthyl)-N-phenylamino]biphenyl (NPB)/2,9-dimethyl-4,7-diphenyl-1,10-phenanthroline (BCP)]_n that makes hole-electron balance in emitting layer, resulting in the CIE coordinates of (0.1747, 0.1059) [11]. Bang et al. used 4,4'-bis(2,2'-diphenyl vinyl)-1,1'-biphenyl (DPVBi) and tris-8-hydroxy-quinoline aluminum (Alq₃) as double emitting layer, leading to CIE coordinates of (0.150, 0.137) at 11 V [2]. However, the CIE coordinates are not stable by using the above structure or method, resulting from the shift of the excitons recombination zone.

In this study, we improved the color purity of OLEDs by using structure of triple-hole blocking layer (THBL), which consisted of alternate (4,4'-N,N'-dicarbazole) biphenyl (CBP) and BCP. Both of them have excellent electron mobility and holes barrier ability. The CBP layer compared with BCP layer has better electron mobility and is $3 \times 10^{-4} \text{ cm}^2/\text{V}^{-1} \text{ s}^{-1}$, which will favor electron injection from BPhen layer to emitting layer [13]. The BCP layer can effectively control the carrier in the emitting layer that will enable an increase

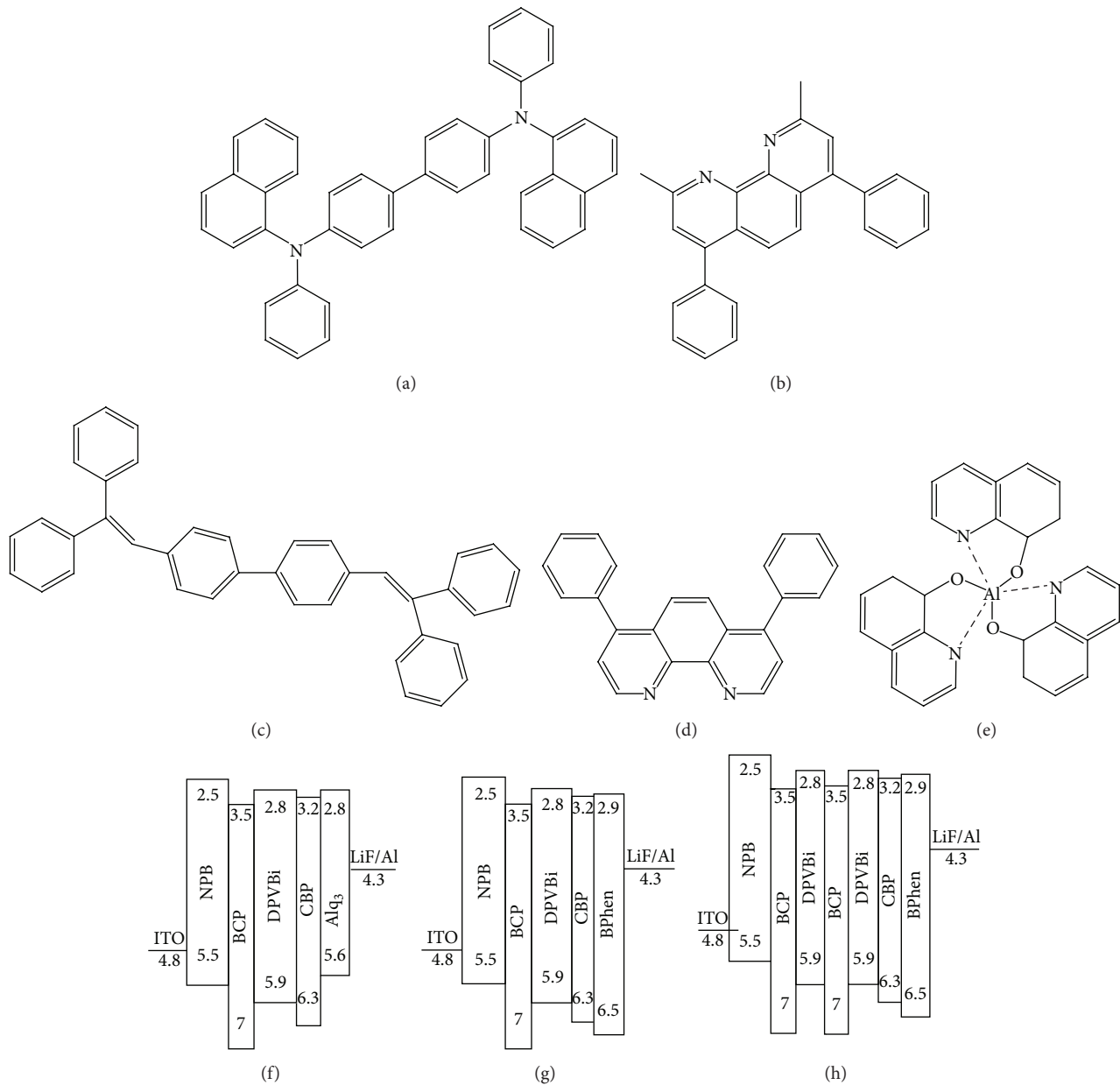


FIGURE 1: The chemical structures of (a) NPB, (b) BCP, (c) DPVBi, (d) BPhen, and (e) Alq₃ and the schematic energy band diagrams of (f) device A, (g) device B, and (h) device C.

in the recombination of emission region. It is due to the fact that there is a higher occupied molecular orbital (HOMO) of 7.0 eV for BCP. However, we used the THBL structure so that the carrier can be effectively confined and controlled in the DPVBi emitting layer, resulting in the fact that the CIE color coordinates of devices can be considerably improved. Simultaneously, the mechanism of the color stability of device with various structures is presented.

2. Experimental

Indium tin oxide (ITO) coated glass with a sheet resistance of approximately $15 \Omega/\square$ was consecutively cleaned in ultrasonic bath containing detergent water, acetone, ethanol, and

deionized (DI) water for 20 min each and then dried with a nitrogen (N₂) flow. The chemical structures of organic materials used and the schematic energy band diagrams of the devices A–C in this study are shown in Figure 1. These structures were as follows:

- (A) ITO/NPB (40 nm)/BCP (8 nm)/DPVBi (40 nm)/CBP (2 nm)/Alq₃ (20 nm)/LiF (0.5 nm)/Al (100 nm);
- (B) ITO/NPB (40 nm)/BCP (8 nm)/DPVBi (40 nm)/CBP (2 nm)/BPhen (10 nm)/LiF (0.5 nm)/Al (100 nm);
- (C) ITO/NPB (40 nm)/BCP (I) (6 nm)/DPVBi (20 nm)/BCP (II) (2 nm)/DPVBi (20 nm)/CBP (2 nm)/BPhen (10 nm)/LiF (0.5 nm)/Al (100 nm).

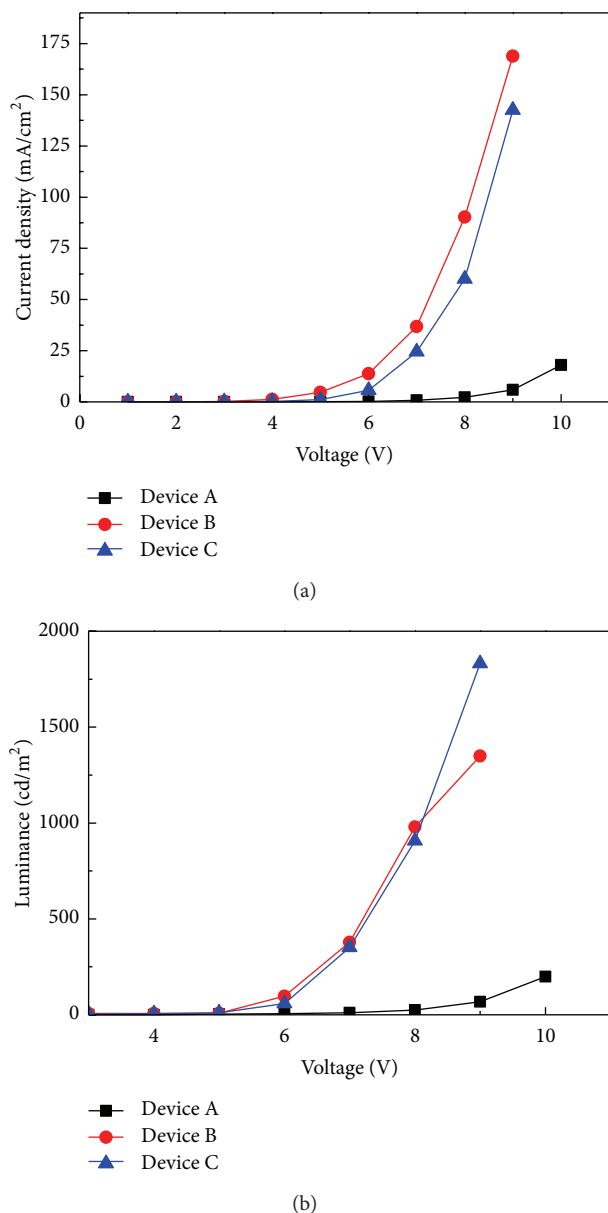


FIGURE 2: The (a) current density-voltage and (b) luminance-voltage characteristics of the devices A-C.

In the device, NPB is used as hole-injecting layer and hole-transport layer. The BCP and CBP are used as hole-blocking layer inserted between DPVBi and HTL. The DPVBi acts as blue-emitting layer. The Alq₃ and 4,7-diphenyl-1,10-phenanthroline (BPhen) are used as a HTL. LiF and Al are used as an electron-injection layer and cathode, respectively. All of the deposition procedures involved thermal evaporation in a vacuum chamber (<10⁻⁶ Torr). The organic layers were sequentially evaporated onto the ITO coated-glass substrate. The deposition rates of all organic materials were monitored by an oscillating quartz thickness monitor (Sigma, SID-142). The deposition rates were about 0.2~0.5 Å/s for organic layers and 5 Å/s for cathode (Al) and LiF. CIE coordinates, electroluminescence (EL) spectra, and luminance were measured by the photospectrometer (Kollmorgen

Instrument PR-655, USA) and the current-voltage characteristics were simultaneously measured by the programmable power source (Keithley SourceMeter 2400, USA), controlled using computer software (Chief I-V-L system, Taiwan). All measurements were carried out at room temperature under ambient.

3. Results and Discussion

Figures 2(a) and 2(b) show the current density-voltage and luminance-voltage characteristics of devices, respectively. Generally, the applied voltage is defined as turn-on voltage when the current density of device reaches the one-tenth of maximum value of the current density. In Figure 2(a), the turn-on voltages of device A-C are 9.5, 5.5, and 6.2 V, respectively. The turn-on voltage of device A is higher than that of devices B-C. It is attributed to the different electron transport layers (Alq₃, BPhen) in the devices. It is well known that the electron mobility of BPhen ($2.4 \times 10^{-4} \text{ cm}^2/\text{V}^{-1} \text{ s}^{-1}$) is higher than that of Alq₃ ($4.7 \times 10^{-6} \text{ cm}^2/\text{V}^{-1} \text{ s}^{-1}$) [14, 15]. However, the ability of electron injection from cathode to the emitting layer can increase via using an electron transport layer with higher electron mobility, resulting in a decrease in the turn-on voltage of device. In addition, from the turn-on voltages of devices B and C, there is a high turn-on voltage in device C due to inserting a thin BCP layer in the emitting layer to form the THBL structure.

By comparing devices A and B, the luminance is greatly improved from 68 cd/m² to 1350 cd/m² at 9 V. It can be ascribed to the fact that more electrons inject from the cathode to the DPVBi and generate more excitons in the DPVBi layer. The luminance of devices B and C are 1350 and 1831 cd/m² at 9 V, respectively. The enhancement of the luminance in device C as compared with device B can be attributed to three factors: (1) THBL has better excitons confinement ability, (2) an increase in excitons formation in EML, and (3) there is formation both emitting layers (DPVBi) in THBL of device C.

In the devices, holes are accumulated and confined in the BCP layers because of the existence of the barrier at the interface of NPB/BCP. Hence, the hole mobility in the multilayer is expected to be decreased, and the performance of device C is expected to be enhanced. The luminous efficiency-current density characteristic is shown in Figure 3. The major parameters are summarized in Table 1. The maximum luminous efficiencies of devices B and C are 1.08 and 1.52 cd/A, respectively. The luminous efficiency of device C is 41% higher than that of device B. It shows that there is a better carrier balance in device C. The electrons are confined and accumulated in the lowest unoccupied molecular orbital (LUMO) level of DPVBi/BCP/DPVBi potential well in device C due to the existence of potential barrier at the DPVBi/BCP (II) and BCP (I)/DPVBi heterointerfaces. As a result, the balance of electron and hole can be improved by inserting a thin BCP layer in device C, forming the THBL structure, and thus more carriers will be confined within both the DPVBi layers.

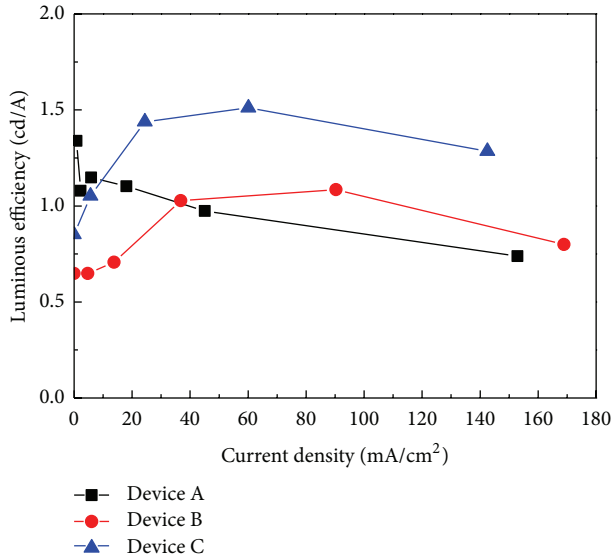


FIGURE 3: The luminance efficiency-current density characteristics of the devices A-C.

TABLE 1: Performance of devices A-C.

	Device A	Device B	Device C
Turn-on voltage (V)	9.5	5.5	6.2
Luminance (cd/m^2)	68	1350	1830
Luminance efficiency (cd/A)	1.15	0.8	1.28
Wavelength peak (nm)	448	444	436
FWHM (nm)	68	65	65
CIE $\pm \Delta_{x,y}$	(0.010, 0.005)	(0.000, 0.004)	(0.001, 0.008)

Figure 4 shows the normalized electroluminescent (EL) spectra of the devices A-C at the same current density of $10 \text{ mA}/\text{cm}^2$. The EL peaks of devices A-C are at 448, 444, and 436 nm, respectively. The EL peaks of devices A and B are near to the PL peak of NPB (446 nm) [16]. It can be directly inferred and demonstrated that major holes were accumulated in the interface of the NPB/BCP and electron-hole recombination occurred in NPB layer, resulting in the blue emission from the NPB layer. The EL peak of the device C is consistent with the PL peak of DPVBi (436 nm) [17]. It is due to the insertion of thin BCP layer in the middle of DPVBi layer, leading to the fact that the major holes were confined in the HOMO level of BCP (I)/DPVBi/BCP (II) potential well in device C and recombined with electron in the DPVBi layer. From the energy level of Figure 1, the LUMO of BCP is -3.5 eV and is higher than that of DPVBi, so the inserted thin BCP (II) layer can confine the electron and prevent it from transporting from blue DPVBi layer to NPB layer. In Figure 4, the full width at half maximum (FWHM) of devices A-C are 68, 65, and 65 nm, respectively. It can be seen in Figure 4 that there is a little color-mixing phenomenon of device A and it emits blue emission because the spectrum has a broad peak.

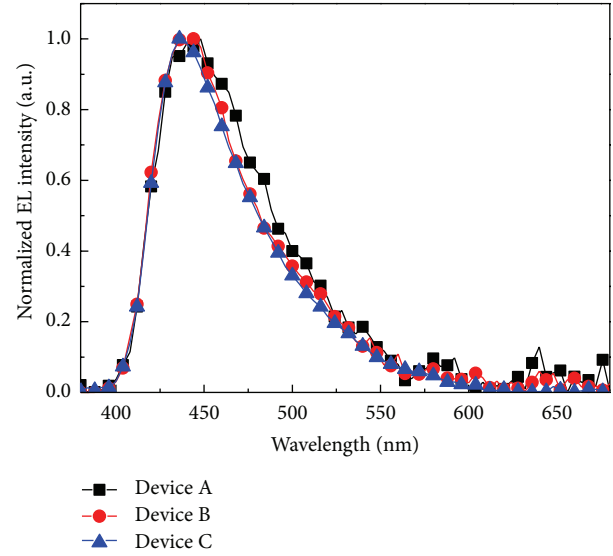


FIGURE 4: The normalized EL intensity spectra characteristics of the devices A-C at the current density of $10 \text{ mA}/\text{cm}^2$.

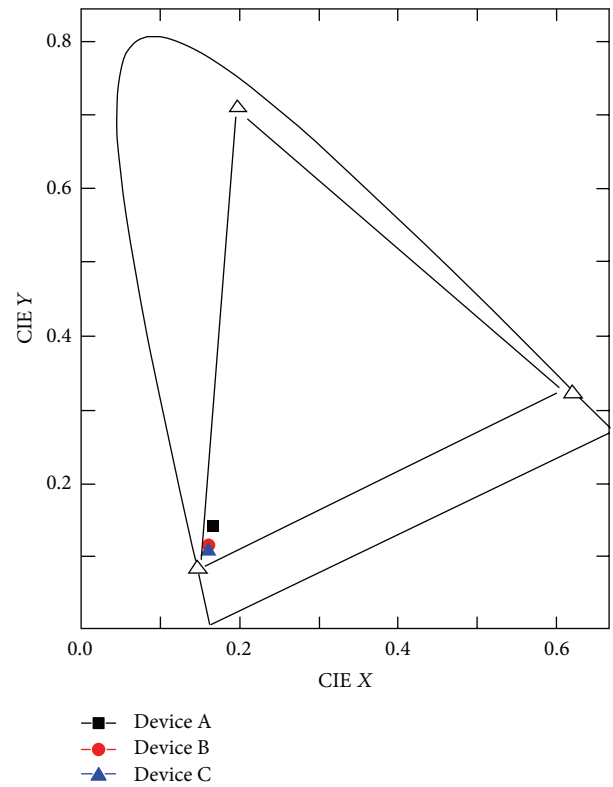


FIGURE 5: The CIE chromaticity coordinates of devices A-C at the applied voltage of 9 V.

That is to say, the blue emission in device C is more pure than that of other devices.

Figure 5 shows the CIE coordinates of devices as a function of applied voltage. The CIE coordinates of device A, device B, and device C at 9 V are (0.166, 0.135), (0.157, 0.113), and (0.157, 0.111), respectively. The CIE coordinates

of device A are far away from the pure blue emission with CIE coordinates of (0.14, 0.08). It is attributed to the portion of carriers recombination at the Alq₃ layer, generating slight green emission. The phenomenon is consistent with the result obtained in Figure 4. Besides, the CIE coordinates of device A are (0.166, 0.135) at 9 V. The difference in CIE coordinates of device A is $\pm\Delta_{x,y} = (0.010, 0.005)$. Thus, the function of BPhen to replace the Alq₃ is not only due to its higher mobility but also due to its higher HOMO energy level which can avoid the hole to cross the CBP barrier layer, keeping off a mix of green light and far CIE coordinates of pure blue light. The CIE coordinates of devices B-C are (0.157, 0.113) and (0.157, 0.111) at 9 V, respectively. By comparison with device A, the color coordinates of the devices B-C are close to the pure blue region. The variation in CIE coordinates of devices B-C is only $\pm\Delta_{x,y} = (0.000, 0.004)$ and (0.001, 0.008), respectively. All the above results reveal that the displacement of the CIE coordinates for the device C at high voltage is obviously small in comparison with that of devices A-B, indicating that there is a better stability and more standard CIE coordinate of blue emission in device C. This is because the emission region of the OLEDs with a THBL consisting of BCP layer and CBP layer is confined within both DPVBi layers. Hence, the performance of near blue emitting devices with a THBL structure of BCP and CBP is greatly improved which is attributed to the improved hole-electron balance and that can be further attributed to hole barrier in the HBL structure. So by adjusting the number of multiple HBL, the amount of hole injection into emitting layer can be controlled. In this study, THBL structure outperforms dual-HBL (DHBL) structure in both luminance and efficiency, enabling electrons to be injected into the device easily and increasing electron-hole pair recombination in EML to achieve carrier effective balance.

4. Conclusions

In summary, the OLEDs with THBL and DHBL structure are fabricated and investigated. With THBL structure, it can efficiently control the holes transport and achieve an electron-hole pair balance, the efficiency of which is improved by 41% as compared with the DHBL. The optimized blue CIE coordinates of (0.157, 0.111) at 9 V and coordinates shift only $\pm\Delta_{x,y} = (0.001, 0.008)$ were obtained. These results indicate that the enhancement of luminance efficiency and the more stable purity of blue color can be achieved by using THBL due to excitons confined in the EML.

Acknowledgment

This work was partially supported by the National Science Council of the Republic of China under Contract no. NSC102-2221-E-390-019-MY2.

References

- [1] H. Aziz, "Degradation mechanism of small molecule-based organic light-emitting devices," *Science*, vol. 283, no. 5409, pp. 1900–1902, 1999.
- [2] H. S. Bang, D. U. Lee, T. W. Kim, S. M. Han, J. H. Seo, and Y. K. Kim, "Efficiency stabilization in deep-blue organic light-emitting devices with a double emitting layer acting as electron and hole trapping layers," *Thin Solid Films*, vol. 516, no. 16, pp. 5649–5653, 2008.
- [3] C. J. Huang, C. C. Kang, T. C. Lee, W. R. Chen, and T. H. Meen, "Improving the color purity and efficiency of blue organic light-emitting diodes (BOLED) by adding hole-blocking layer," *Journal of Luminescence*, vol. 129, no. 11, pp. 1292–1297, 2009.
- [4] C.-J. Huang, T.-H. Meen, K.-C. Liao, and Y.-K. Su, "The mechanism of efficiency enhancement with proper thickness of DPVBi layer for blue organic light-emitting devices (BOLED)," *Journal of Physics and Chemistry of Solids*, vol. 70, no. 3-4, pp. 765–768, 2009.
- [5] D. U. Lee, D. C. Choo, T. W. Kim, J. H. Seo, J. H. Park, and Y. K. Kim, "Enhancement of efficiency in blue organic light-emitting devices with nanoscale barrier and trapping layers embedded in an emitting layer and a hole transport layer," *Thin Solid Films*, vol. 517, no. 17, pp. 5326–5329, 2009.
- [6] W. Song, M. Meng, Y. H. Kim et al., "High efficient and color stable WOLED using double white emissive layer," *Journal of Luminescence*, vol. 132, no. 8, pp. 2122–2125, 2012.
- [7] Khizar-ul-Haq, M. A. Khan, X. Y. Jiang et al., "Blue organic light-emitting diodes with low driving voltage and maximum enhanced power efficiency based on buffer layer MoO₃," *Journal of Luminescence*, vol. 129, no. 10, pp. 1158–1162, 2009.
- [8] H. S. Bang, S. Y. Seo, D. C. Choo et al., "Effect of doped emitting layer on electrical and optical properties in blue organic light-emitting devices," *Thin Solid Films*, vol. 517, no. 17, pp. 5314–5317, 2009.
- [9] H.-P. Lin, F. Zhou, X.-W. Zhang et al., "Enhanced color stability and improved performance in white organic light-emitting devices by utilizing a double-graded structure," *Synthetic Metals*, vol. 161, no. 11-12, pp. 1133–1136, 2011.
- [10] H. Zhu, Z. Xu, S. Zhao et al., "Study on the influences of quantum well structure on the performance of organic light emitting devices," *Displays*, vol. 32, no. 3, pp. 102–105, 2011.
- [11] Y.-M. Shi, Z.-B. Deng, D.-H. Xu, and J. Xiao, "Organic light-emitting diodes with improved hole-electron balance and tunable light emission with aromatic diamine/bathocuproine multiple hole-trapping-layer," *Displays*, vol. 27, no. 4-5, pp. 166–169, 2006.
- [12] Y. Qiu, Y. Gao, P. Wei, and L. Wang, "Organic light-emitting diodes with improved hole-electron balance by using copper phthalocyanine/aromatic diamine multiple quantum wells," *Applied Physics Letters*, vol. 80, no. 15, pp. 2628–2630, 2002.
- [13] J.-W. Kang, S.-H. Lee, H.-D. Park et al., "Low roll-off of efficiency at high current density in phosphorescent organic light emitting diodes," *Applied Physics Letters*, vol. 90, no. 22, Article ID 223508, 2007.
- [14] T. Yasuda, Y. Yamaguchi, D.-C. Zou, and T. Tsutsui, "Carrier mobilities in organic electron transport materials determined from space charge limited current," *Japanese Journal of Applied Physics*, vol. 41, no. 9, pp. 5626–5629, 2002.
- [15] M. A. Khan, W. Xu, K.-U. Khizar-Ul-Haq et al., "Electron mobility of 4,7-diphenyl-1,10-phenanthroline estimated by using space-charge-limited currents," *Journal of Applied Physics*, vol. 103, no. 1, Article ID 014509, 2008.
- [16] H. Xu, Y. Yue, H. Wang, L. Chen, Y. Hao, and B. Xu, "Single-crystal structure, photophysical characteristics and

electroluminescent properties of bis(2-(4-trifluoromethyl-2-hydroxyphenyl)benzothiazolate)zinc,” *Journal of Luminescence*, vol. 132, no. 4, pp. 919–923, 2012.

- [17] M. Zhang, Z. Chen, L. Xiao, B. Qu, and Q. Gong, “High-color-quality blue top-emitting organic light-emitting diodes with enhanced contrast ratio,” *The Japanese Journal of Applied Physics*, vol. 52, Article ID 05DC17, p. 4, 2013.

Research Article

Dye-Sensitized Solar Cells with Optimal Gel Electrolyte Using the Taguchi Design Method

Jenn-Kai Tsai,¹ Wen Dung Hsu,² Tian-Chiuan Wu,¹ Jia-Song Zhou,¹ Ji-Lin Li,¹ Jian-Hao Liao,¹ and Teen-Hang Meen¹

¹ Department of Electronic Engineering, National Formosa University, Yunlin 632, Taiwan

² Department of Materials Science and Engineering, National Cheng Kung University, Tainan City 701, Taiwan

Correspondence should be addressed to Jenn-Kai Tsai; tsaijk@nfu.edu.tw

Received 11 September 2013; Accepted 10 October 2013

Academic Editor: Liang-Wen Ji

Copyright © 2013 Jenn-Kai Tsai et al. This is an open access article distributed under the Creative Commons Attribution License, which permits unrestricted use, distribution, and reproduction in any medium, provided the original work is properly cited.

The Taguchi method was adopted to determine the optimal gel electrolyte used in dye-sensitized solar cells (DSSCs). Since electrolyte is a very important factor in fabrication of high performance and long-term stability DSSCs, to find the optimal composition of gel electrolyte is desired. In this paper, the common ingredients used in the liquid electrolyte were chosen. The ingredients then mixed with cheap ionic liquids and poly(vinylidene fluoride-co-hexafluoropropylene) (PVDF-HFP) was added to form colloidal electrolyte (gel). The optimal composition of each materials in the gel electrolyte determined by Taguchi method consists of 0.03 M I₂, 0.15 M KI, 0.6 M LiI, 0.5 M 4-tertbutylpyridine (TBP), and 10% PVDF-HFP dissolved in the acetonitrile and 3-methoxypropionitrile (MPN) solution with volume ratio of 2 : 1. The short circuit current density of 14.11 mA/cm², the conversion efficiency (η) of 5.52%, and the lifetime of over 110 days was observed for the dye-sensitized solar cell assembled with optimal gel electrolyte. The lifetime increases 10 times when compared with the conventional dye-sensitized solar cell assembled with liquid electrolyte.

1. Introduction

Since the pioneering work of Grätzel and O'Regan in 1991, dye-sensitized solar cells (DSSCs) have become one of the promising devices in photovoltaic application, because of low fabrication cost, good stability, and compatibility with flexible substrates [1–3]. Conventional dye-sensitized solar cell has the structure of porous titanium dioxide layer as the dye adsorbed on the TiO₂ surface and an organic liquid, I⁻/I₃⁻ solution as electrolyte top on the TiO₂ layer, and the two layers are sandwiched in between bottom electrode made of ITO (SnO₂) and top electrode made of platinum thin film. However, due to the loss of liquid electrolyte through the leakage or evaporation, the lifetime of dye-sensitized solar cells is limited, which causes the problem for commercialization. To solve this issue and enhance durability, gel or quasisolid-state electrolytes mixed with ionic liquids were used to improve the sealing and minimize the loss of electrolytes [4–6]. Since the electrolyte is an important

factor affecting the conversion efficiency of DSSC, to find an optimized composition of the mixture is crucial.

The mixture is usually composed of polymers and ionic liquids. In order to determine the optimized composition of each material, Taguchi method which takes multifactors into consideration is the most powerful tool for statistical design of this kind of experiments for improvement of the product and the process. It is a simple, systematic and powerful method to increase the experiment quality. The advantage of this method is to reduce both product cost and number of experiments [7–9]. The method starts from identifying the impact factors in the experiments and then does the experiments by systematically adjusting the quantity of each factor and assuming that the interaction between the factors is orthogonal.

In this study the optimized mixture was determined by Taguchi method. The mixture was composed of seven materials, iodine (I₂), lithium iodide (LI), potassium iodide (KI), 4-tertbutylpyridine (TBP), 3-methoxypropionitrile (MPN), ac-

etonitrile (ACN), and PVDF-HFP. The other common ionic liquids as 1,2-dimethyl-3-propylimidazolium iodide (DMPII) [10] and N-methylimidazole (NMBI) [11] were not employed in this study due to the fact that were more expensive. The quantity of each material was controlled in two levels. The optimized constitute of the most suitable gel electrolyte used in DSSC was identified with minimum number of experiments. DSSC with the best efficiency of 5.52% was observed in AM 1.5 illuminations.

2. Materials and Methods

The gel electrolyte studied in this work containing I_2 (Osaka, Japan), LiI (Aldrich, USA), KI (Hanawa, Japan), TBP (Aldrich, USA), 3-methoxypropionitrile (MPN) (Fluka, China), acetonitrile (Avantor, USA), and PVDF-HFP (Aldrich, USA) was prepared, and the Taguchi method was used to determine the optimized composition of each component. The mixture was then heated to 80°C and became a liquid-type electrolyte.

The 10 wt% TiO_2 paste was prepared by mixing nanocrystalline TiO_2 nanoparticles (NPs) (Degussa, P25, the average nanoparticle diameter was about 25–30 nm), tert-butyl alcohol, and deionized water. The paste then scraped on transparent indium-tin-oxide (ITO) glass by doctor balding process to form TiO_2 thick film. The film was annealed under air at 150°C for 90 min to decompose the organic compounds and then the temperature increased to 350°C for 30 min to assist the interconnection of TiO_2 NPs. After that the TiO_2 thin films were immersed in 0.3 mM N3 dye at 45°C for 90 min. The Pt thin film was grown on ITO glass by an electroplating process prepared for as counter electrode. Then the counter electrode was placed on the top of the TiO_2 thin film and bonded by a 50 μ m-thick hot-melt polymer spacer. Finally, the previously prepared gel electrolyte was injected into the cell by capillary forces through an injecting hole drilled in the counter electrode. Finally, the hole was covered and sealed with a piece of hot-melt polymer to prevent electrolyte leakage. The liquid-type electrolyte then cooled and became a gel electrolyte. The resulting active electrode area was approximately 0.25 cm² (0.5 cm × 0.5 cm). The schematic image of the DSSC structure is shown in Figure 1.

The current-voltage characteristics of samples were measured by Keithley 2400 source meter (Keithley Instruments, Inc., Ohio, USA) under simulated sunlight (SAN-EI XES-40S1, San Ei Brand, Japan), AM 1.5 radiation at 100 mW/cm².

Table 1 shows the composition of gel electrolyte and factor symbols used in the Taguchi method. The reason that the seven materials were chosen for fabrication of the gel electrolytes is explained as follows.

- (1) Iodine (I_2 , factor A), lithium iodide (LiI, factor B), and potassium iodide (KI, factor C) are the most popular materials used as the electrolyte in DSSC to produce the redox I^-/I_3^- , in which the redox energy level matches the highest occupied molecular orbital (HOMO) energy level of the dye, and hence speeds up the carrier diffusion in the organic liquid solvent. In addition LiI would improve the current density

TABLE 1: Gel electrolyte parameters and factors of Taguchi method.

Factor symbol	Parameter	Level 1	Level 2
A	I_2	0.03 M	0.06 M
B	LiI	0.3 M	0.6 M
C	KI	0.15 M	0.1 M
D	TBP	0.5 M	0.8 M
E	MPN	1 mL	2 mL
F	Acetonitrile	1 mL	2 mL
G	PVDF-HFP	10 wt%	5 wt%

of DSSC. The LiI would decompose to Li^+ -e pair while be absorbed on the TiO_2 surface by attracting the conduction band electrons. The Li^+ -e pairs can migrate toward or away from the TiO_2 nanoparticle surface improving the conductivity of TiO_2 layer and enhance the current density of DSSC. Besides, the materials are relatively cheap and easy to obtain.

- (2) 4-Tertbutylpyridine (TBP, factor D) was used to avoid the TiO_2 nanoparticles which are not covered by the dye molecules directly contacted with the electrolyte. The contact would result in high leakage current through transport of excited electrons in TiO_2 layer to electrolyte.
- (3) 3-Methoxypropionitrile (MPN, factor E) and acetonitrile (factor F) are the common solvent used to prepare the electrolyte. Acetonitrile was employed due to its high ionic conductivity and effective electrolyte leakage-proof.
- (4) PVDF-HFP (factor G) is a useful material to gel liquid electrolyte to overcome the electrolyte leakage problem. In addition, it also can improve the dissociation of lithium iodide to enhance the iodide ion concentration [12].

In the Taguchi method, a modified orthogonal array of L_8 is found to be appropriate and hence it was chosen. The orthogonal array (L_8) is shown in Table 2 where the experiments are divided into 8 groups and number 1 represents level 1 shown in Table 1 (so as 2). The experimental design using the orthogonal array L_8 of Taguchi's method provides a simple, efficient, and systematic approach for optimal design of experiments to assess the performance, quality, and cost. The error would be small and the cost of experiments would be economical. Each experiment group was duplicated three times in order to estimate the random error.

3. Results and Discussion

Figure 2 shows the conversion efficiencies of DSSCs of 8 experiment groups. The results demonstrate that the conversion efficiency of the duplicates of each experiment group is very closely indicating that the random errors are small and the fabrication processes of DSSC are reliable. The 1st experiment group has the highest conversion efficiency of 4.37% among all the groups.

TABLE 2: Experimental layout and results using the modified L_8 orthogonal array.

Group	Factor							η_{avg}	S/N_{LTB}
	A	B	C	D	E	F	G		
1	1	1	1	1	1	1	1	4.08	12.20
2	1	1	2	2	2	2	1	2.98	9.49
3	2	2	1	1	2	2	1	3.80	11.56
4	2	2	2	2	1	1	1	2.48	7.76
5	1	2	1	2	2	1	2	3.19	10.06
6	1	2	2	1	1	2	2	3.15	9.95
7	2	1	1	2	1	2	2	2.17	6.70
8	2	1	2	1	2	1	2	2.64	8.39

TABLE 3: The analysis results of each parameter and the optimal design parameters of the electrolyte composition.

Parameter	I_2	LiI	KI	TBP	MPN	ACN	PVDF-HFP
Factor Symbol	A	B	C	D	E	F	G
Level 1 S/N	10.421	9.192	10.129	10.524	9.152	9.599	10.205
Level 2 S/N	8.603	9.833	8.895	8.501	9.872	9.426	8.774
$S/N_{max} - S/N_{min}$	1.82	0.64	1.23	2.02	0.72	0.17	1.44
Ranking	2	6	4	1	5	7	3
Optimum	0.03 M	0.6 M	0.15 M	0.5 M	1 mL	2 mL	10 wt%

Taguchi defined that the optimal operator combination is to minimize variances of quality characteristics resulted from signal-to-noise ratio (S/N ratio). It was used for the larger-the-better (LTB) evaluated by using the following equation:

$$\frac{S}{N_{LTB}} = -10 \log \left[\frac{1}{n} \sum_{i=1}^n \left(\frac{1}{y_i} \right)^2 \right], \quad (1)$$

where n is the number of tests and y_i denotes the respective characteristic, which is the conversion efficiency in this study. Then, the measured values of quality characteristics obtained through the experiments will be transformed into S/N ratio by using (1). Table 2 shows the average conversion efficiencies (η_{avg}) and the S/N ratio of each experiment group. The maximum average conversion efficiency and S/N ratio appear in the 1st experiment group with the value of 4.08 and 12.19, respectively. Since the S/N ratio represents the signal-to-noise ratio of conversion efficiencies, the larger the ratio the higher consistent the data. By comparison of the difference of S/N ratio between level 1 and level 2 of the same material, the degree of the influence of seven materials can be ranked. Table 3 shows the further analysis. The results indicate that the TBP, which is used to avoid the TiO_2 nanoparticles that are not covered by the dye molecules directly contact with the electrolyte, gives the most impact on the performance of conversion efficiency. If the TBP is over added in the mixture, the electronic transport is hindered and lowering the conversion efficiency. The seven materials are

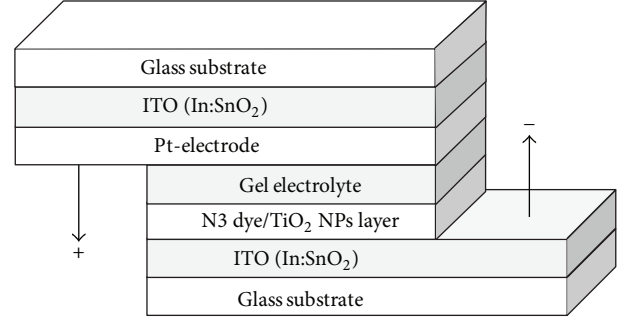
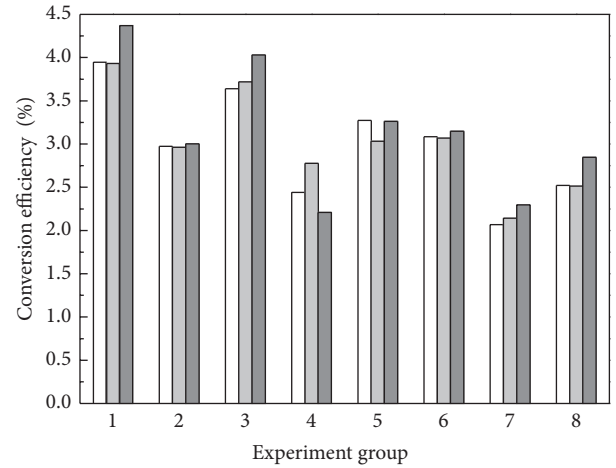
FIGURE 1: The schematic device structure of TiO_2 nanoparticles dye-sensitized solar cell using the gel electrolyte.

FIGURE 2: The conversion efficiency distribution of dye-sensitized solar cells using different gel electrolyte.

ranked as TBP, I_2 , PVDF-HFP, KI, MPN, LiI, and ACN from high to low by the sequence of their degree of influence.

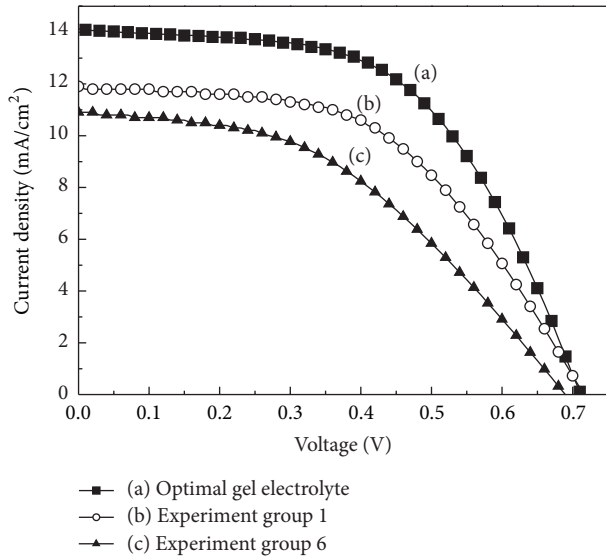
After further analysis, the optimal operator combinations can be located, according to the S/N_{max} ratio. The optimal design of experiment parameters are I_2 of 0.03 M, LiI of 0.6 M, KI of 0.15 M, TBP of 0.5 M, MPN of 1 mL, ACN of 2 mL, and PVDF-HFP of 10 wt%, as arranged and shown in Table 3. Current densities against voltage ($J-V$) characteristics of the DSSCs prepared by the optimal parameters under AM 1.5 sunlight are shown in Figure 3. The photovoltaic properties of the DSSCs using the optimal operator combinations, the gel electrolyte of 1st and 6th experiment groups, are summarized in Table 4. The short-circuit current density is 12.17 mA/cm² and the open-circuit voltage is 0.71 V. The fill factor (F.F.) was calculated using

$$F.F. = \frac{J_{max} \times V_{max}}{J_{SC} \times V_{OC}}, \quad (2)$$

where J_{max} is the current density at maximum power output, J_{SC} the current density at short circuit, V_{max} the voltage at maximum power output, and V_{OC} the voltage at open circuit. The fill factor calculated using (2) for the optimum electrolyte

TABLE 4: Characteristics of DSSCs fabricated using the optimal operator combination, experiment groups 1 and 6 gel electrolyte.

Electrolyte	V_{OC} (V)	J_{SC} (mA/cm ²)	V_m (V)	J_m (mA/cm ²)	F.F. (%)	H (%)
Optimum	0.71	14.11	0.48	11.51	55.14	5.52
Group 1	0.72	11.86	0.45	9.70	51.43	4.37
Group 6	0.69	10.90	0.40	8.241	43.84	3.30

FIGURE 3: J - V curves of DSSCs using (a) the optimal combination and (b) 1st and (c) 6th experiment group gel electrolytes.

DSSC is 55.8%. The photoelectric conversion efficiency (η) is calculated by

$$\eta = \frac{J_{SC} \times V_{OC} \times F.F.}{P_{in}}, \quad (3)$$

where P_{in} is total incident power density. The conversion efficiency for the optimum electrolyte DSSC calculated using (3) is 5.52%. It is enhanced over 26.3% compared to the 1st experiment group. The result demonstrates that the Taguchi experiment design method is very useful in this study.

Figure 4 shows the electrolyte effect on the lifetime of DSSCs characterized by the power conversion efficiency associated with time. The lifetime of DSSC, fabricated by the 6th experiment group, used the gel electrolytes with PVDF-HFP concentration of 5 wt% was about 30 days. On the other hand the lifetime of DSSC, fabricated by the optimal gel electrolyte, of PVDF-HFP concentration of 10 wt% was over 80 days and the lifetime is expected to be 110 days as the conversion efficiency becomes zero. In general the lifetime of the DSSC with liquid electrolyte was about one week to ten days, however, by replacing the liquid electrolyte with the gel electrolyte, the lifetime of DSSC increases over ten times. Therefore, the DSSCs using gel electrolytes present a better performance in lifetime compared to those assembled with classical liquid electrolyte.

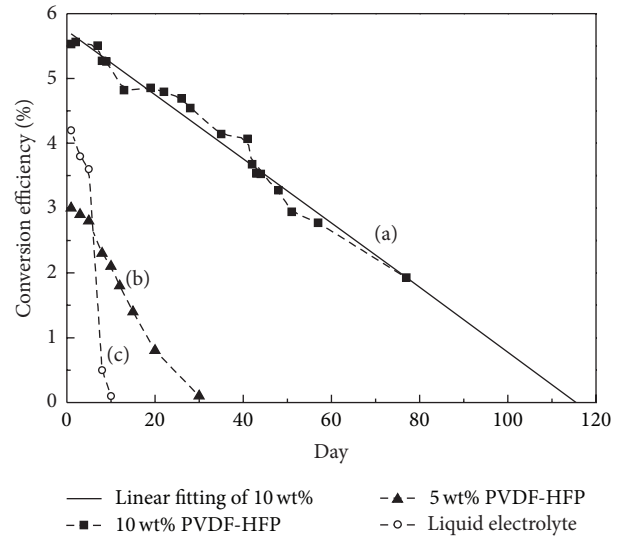


FIGURE 4: The lifetime of DSSCs uses the different concentrations of gel electrolyte, (a) 10 wt% PVDF-HFP (optimal operator combination), (b) 5 wt% PVDF-HFP (6th experiment group), and (c) the common liquid electrolyte comparison chart.

4. Conclusion

In this study, the Taguchi method is adopted to determine the optimal composition of gel electrolyte in the assembly of dye-sensitized solar cells. The development procedure can be more efficient by using Taguchi experimental design method. The lifetime was found ten times longer than conventional DSSC by replacing liquid electrolyte with optimal gel electrolyte. The DSSC with optimal gel electrolyte had the short circuit current density of 12.17 mA/cm², the open-circuit voltage of 0.71 V, fill factor of 55.8%, the conversion efficiency of 5.52%, and the lifetime of over 110 days.

Conflict of Interests

The authors declare that there is no conflict of interests regarding the publication of this paper.

Acknowledgments

The authors are grateful to Tung-Lung Wu and Jun-Hong Shih for their assistance and National Formosa University for providing financial support in this project.

References

- [1] B. O'Regan and M. Grätzel, "A low-cost, high-efficiency solar cell based on dye-sensitized colloidal TiO₂ films," *Nature*, vol. 353, no. 6346, pp. 737–740, 1991.
- [2] M. Grätzel, "Photoelectrochemical cells," *Nature*, vol. 414, pp. 338–344, 2001.
- [3] M. K. Nazeeruddin, A. Kay, I. Rodicio et al., "Conversion of light to electricity by *cis*-X₂bis(2,2'-bipyridyl-4,4'-dicarboxylate)ruthenium(II) charge-transfer sensitizers (X = Cl⁻, Br⁻, I⁻, CN⁻, and SCN⁻) on nanocrystalline TiO₂ electrodes," *Journal of the American Chemical Society*, vol. 115, no. 14, pp. 6382–6390, 1993.
- [4] T. M. W. J. Bandara, M. A. K. L. Dissanayake, and B.-E. Mellander, "Dye sensitized solar cells with poly(acrylonitrile) based plasticized electrolyte containing MgI₂," *Electrochimica Acta*, vol. 55, no. 6, pp. 2044–2047, 2010.
- [5] D. Kuang, P. Wang, S. Ito, S. M. Zakeeruddin, and M. Grätzel, "Stable mesoscopic dye-sensitized solar cells based on tetracyanoborate ionic liquid electrolyte," *Journal of the American Chemical Society*, vol. 128, no. 24, pp. 7732–7733, 2006.
- [6] J. E. Benedetti, A. D. Gonçalves, A. L. B. Formiga et al., "A polymer gel electrolyte composed of a poly(ethylene oxide) copolymer and the influence of its composition on the dynamics and performance of dye-sensitized solar cells," *Journal of Power Sources*, vol. 195, no. 4, pp. 1246–1255, 2010.
- [7] C. Chan, W. Hsu, C. Chang, and C. Hsu, "Preparation and characterization of gasochromic Pt/WO₃ hydrogen sensor by using the Taguchi design method," *Sensors and Actuators B*, vol. 145, no. 2, pp. 691–697, 2010.
- [8] T. Tsai, "Improving the fine-pitch stencil printing capability using the Taguchi method and Taguchi fuzzy-based model," *Robotics and Computer-Integrated Manufacturing*, vol. 27, no. 4, pp. 808–817, 2011.
- [9] H. Lee, C. Han, Y. Sung, S. S. Sekhon, and K. Kim, "Gel electrolyte based on UV-cured polyurethane for dye-sensitized solar cells," *Current Applied Physics*, vol. 11, no. 1, pp. 158–162, 2011.
- [10] H. Chen, C. Lin, Y. Lai et al., "Electrophoretic deposition of ZnO film and its compression for a plastic based flexible dye-sensitized solar cell," *Journal of Power Sources*, vol. 196, no. 10, pp. 4859–4864, 2011.
- [11] H. Yang, J. Liu, Y. Lin, J. Zhang, and X. Zhou, "PEO-imidazole ionic liquid-based electrolyte and the influence of NMBI on dye-sensitized solar cells," *Electrochimica Acta*, vol. 56, no. 18, pp. 6271–6276, 2011.
- [12] J. H. Kim, Y. S. Chi, and T. J. Kang, "Optimization of quasi-solid-state dye-sensitized photovoltaic fibers using porous polymer electrolyte membranes," *Journal of Power Sources*, vol. 229, pp. 84–94, 2013.

Research Article

Triazoloisoquinoline-Based/Ruthenium-Hybrid Sensitizer for Efficient Dye-Sensitized Solar Cells

Che-Lung Lee,¹ Wen-Hsi Lee,¹ and Cheng-Hsien Yang²

¹ Department of Electrical Engineering, Nation Cheng Kung University, No. 1, Daxue Road, East District, Tainan City 70101, Taiwan

² ShiFeng Technology Co., Ltd., Room 603, Building. R2, No. 31, Gongye 2nd Road, Annan District, Tainan 70955, Taiwan

Correspondence should be addressed to Cheng-Hsien Yang; jasonyang@fusol-material.com

Received 8 September 2013; Accepted 12 October 2013

Academic Editor: Teen-Hang Meen

Copyright © 2013 Che-Lung Lee et al. This is an open access article distributed under the Creative Commons Attribution License, which permits unrestricted use, distribution, and reproduction in any medium, provided the original work is properly cited.

Triazoloisoquinoline-based organic dyestuffs were synthesized and used in the fabrication of dye-sensitized solar cells (DSSCs). After cosensitization with ruthenium complex, the triazoloisoquinoline-based organic dyestuffs overcame the deficiency of ruthenium dyestuff absorption in the blue part of the visible spectrum. This method also fills the blanks of ruthenium dyestuff sensitized TiO₂ film and forms a compact insulating molecular layer due to the nature of small molecular organic dyestuffs. The incident photon-to-electron conversion efficiency of N719 at shorter wavelength regions is 49%. After addition of a triazoloisoquinoline-based dyestuff for co-sensitization, the IPCE at 350–500 nm increased significantly. This can be attributed to the increased photocurrent of the cells, which improves the dye-sensitized photoelectric conversion efficiency from 6.23% to 7.84%, and the overall conversion efficiency increased by about 26%. As a consequence, this low molecular weight organic dyestuff is a promising candidate as coadsorbent and cosensitizer for highly efficient dye-sensitized solar cells.

1. Introduction

To date, there are two kinds of dyestuff used in DSSCs, one is based on metal-free organic materials and the other on ruthenium metal complexes [1–3]. In 1993, Nazeeruddin et al. successfully used the ruthenium complex-*cis*-bis(isothiocyanato)bis(2,2'-bipyridyl-4,4'-dicarboxylato)-ruthenium(II) (N3) as a sensitizer, with the photoelectric conversion efficiency, η , reaching about 10% [4]. However, in view of their lower cost and greater diversity of molecular structures, organic dyestuffs are now attracting more attention than ruthenium complexes.

Although many studies focus on ruthenium complexes for the dyeing of TiO₂ photoelectrodes, the related molar absorption coefficient is lower than that for the metal-free organic dyestuffs [5–7]. In order to combine the advantages of ruthenium complexes (i.e., high photoelectric conversion efficiency) and metal-free organic dyestuffs (i.e., high molar absorption coefficient), many studies examine cosensitized DSSCs [8–10]. For example, Miao et al. obtained a high efficiency of 11.05%

by using (tri(isothiocyanato)(2,2':6',2''-terpyridyl-4,4',4''-tricarboxylic acid)ruthenium(II)) (BD) to overcome the deficient areas in the NIR absorption spectra of *cis*-dithiocyanate-N,N'-bis-(4-carboxylate-4-tetrabutyl ammonium-carboxylate-2,2'-bipyridine)ruthenium(II) (N719) [8]. However, to the best of our knowledge, few studies examine the use of cosensitization to broaden the light absorption spectra of N719 in the blue part of the visible spectrum. In this work, we report a new triazoloisoquinoline-based dyestuff, which can be used in a cosensitized dyestuff to absorb the blue part of the visible spectrum. By combining the triazoloisoquinoline-based dyestuff and the N719 sensitizer, greater efficiency is obtained than seen with the individual dye cells.

2. Experimental Procedure

2.1. Fabrication of Photovoltaic Devices. Twelve-micrometer nanocrystalline TiO₂ photoelectrodes were prepared from a titania paste (Ti-Nanoxide T series, Solaronix SA). The paste was applied to a transparent conducting oxide by doctor-blading techniques and annealed at 450°C for 30 min

in air. The thickness of the TiO₂ films was measured with an Alpha-Step 300 profiler. When the TiO₂ electrodes cooled down to around 100°C, the electrodes were dipped in dye solutions, which included 0.5 mM N719 and different concentrations of dyestuff 4L in tert-butanol/acetonitrile (AN) (1:1 in volume). The TiO₂ electrodes were immersed in the dye solutions, then kept at 25°C for more than 18 h to allow the dye to adsorb to the TiO₂ surface, and rinsed with the same solvents. The dye-loaded TiO₂ film as the working electrode and Pt-coated TCO as the counter electrode were separated by a hot-melt Surlyn sheet (25 μm) and sealed together by pressing them under heat. The electrolytes were introduced into the gap between the working and the counter electrodes from two holes predrilled on the back of the counter electrode. Finally, the two holes were sealed with a Surlyn film covering a thin glass slide under heat. The cells were evaluated by using 0.6 M [BMI][I], 0.1 M GuNCS, 0.3 M I₂, and 0.5 M TBP in an MPN (3-Methoxypropionitrile) solvent as the redox electrolyte.

2.2. Photovoltaic Measurement. Absorption spectra were recorded on a Agilent 8453 spectrophotometer. The current density-voltage (*J-V*) characteristics in the dark and under illumination were measured with a Keithley 2400 sourceme-ter. The photocurrent was measured in a nitrogen-filled glove box under a solar simulator (Oriel 96000 150 W) with AM 1.5G-filtered illumination (100 mW cm⁻²). The spectramismatch factor of the simulated solar irradiation was corrected using a Schott visible-color glass-filtered (KG5 color filter) Si diode (Hamamatsu S1133). The active area of the device was 0.25 cm².

3. Results and Discussion

Metal-free organic dyestuffs have been extensively studied in DSSCs, but few reports discuss triazoloisoquinoline-based ones. Triazoloisoquinoline contains electron-rich nitrogen and oxygen heteroatoms in a heterocyclic structure with high electron-donating ability, and it is a good candidate for metal-free organic dyestuffs for use in DSSCs. This study is the first report of the use of triazoloisoquinoline dyestuffs as a cosensitizer to absorb the blue part of the visible spectrum. The synthesis of organic dyestuff 4L is depicted in Figure 1. They consist of treating triazoloisoquinolines substituted tetramethyl-dioxaborolane (2) with 5-formyl-2-bromothiophene under conditions for Suzuki coupling to produce 5-(4-(3-oxo-[1, 2, 4]triazolo[3,4-a]isoquinolin-2(3H)-yl)phenyl)thiophene-2-carbaldehyde (3). Knoevenagel condensation of compound 3 with cyanoacrylic acid is carried out in the presence of piperidine, and after precipitation and purification with silica gel chromatography, the final dyestuff 4L is obtained as a yellow powder. This product has been characterized by spectroscopic analyses (¹H NMR (300 MHz, d₆-DMSO): δ 8.32 (d, 1H, *J* = 7.50 Hz), 8.23 (s, 1H), 8.20 (d, 2H, *J* = 3.20 Hz), 7.93 (d, 2H, *J* = 8.72 Hz), 7.89~7.67 (m, 6H), 7.03 (d, 1H, *J* = 7.46 Hz); ESI-MS *m/z* 437 (M-H⁺); Anal. Calcd for C₂₄H₁₄N₄O₃S: C, 65.74; H, 3.22; N, 12.78.

TABLE 1: Photovoltaic parameters of the DSSCs with N719:4L sensitizers in different molar ratios under AM 1.5G sunlight^a.

	Dyestuffs molar ratio	<i>J</i> _{sc} (mA cm ⁻²)	<i>V</i> _{oc} (V)	FF	<i>η</i> (%)
Device A	4L	7.14	0.71	0.64	3.21
Device B	N719	12.55	0.78	0.64	6.23
Device C	N719-4L 1:0.05	12.71	0.76	0.66	6.37
Device D	N719-4L 1:0.15	14.63	0.78	0.65	7.38
Device E	N719-4L 1:0.25	15.29	0.78	0.66	7.84
Device F	N719-4L 1:0.35	15.11	0.74	0.66	7.35

^aPerformances of the DSSCs were measured with a 0.25 cm² working area.

% Found: C, 65.96; H, 3.28; N, 12.60; λ_{max}/nm (ε/M⁻¹ cm⁻¹): 277 (19435), 380 (29651)).

The absorption spectra of the dyestuffs 4L and N719 in DMF (Dimethylformamide) solutions are shown in Figure 2. The absorption spectrum of 4L shows two major bands at ca. 250–350 nm and ca. 350–500 nm. UV absorption is attributed to localized aromatic π-π* transitions. In the visible region, this may be attributed to intramolecular charge transfer (ICT) absorption, because an efficient charge-separated excited state could be produced between the triazoloisoquinoline and the cyanoacrylic acid moieties. The ICT absorption (λ_{max}) appeared at 380 nm for 4L, and the molar extinction coefficients in the visible region were 29651 M⁻¹ cm⁻¹. The molar extinction coefficient is twice as high as that of the ruthenium complexes. Interestingly, the maximum absorption peaks and absorption bands of dyestuffs were red-shifted compared to their spectra in DMF solution, which can be ascribed to the electronic coupling of the dyes on the TiO₂ surface. The interaction between the COOH group and the surface Ti⁴⁺ ions can lead to the increased delocalization of the π* orbital of the conjugated framework, and thus, the energy of the π* level was decreased by this delocalization, resulting in the red-shifted absorption spectra. However, 4L shows a good potential to broaden the light absorption spectra of N719 in the blue part of the visible spectrum.

The photovoltaic characteristics of these dyes with regard to their use as sensitizers for DSSCs have been evaluated with a sandwich DSSC cell using 0.6 M [BMI][I], 0.1 M GuNCS, 0.3 M I₂, and 0.5 M TBP in an MPN solvent as the redox electrolyte. Details of the preparation and characterization of the device are described in the experimental section of this work in the supporting information, and all the essential properties of these cells are listed in Figure 3 and Table 1. Under the standard AM 1.5G irradiation, the maximum efficiency (*η*) for the N719-sensitized solar cell-device B with an active area of 0.25 cm² was calculated to be 6.23%, with a *J*_{sc} of 12.55 mA cm⁻², a *V*_{oc} of 0.78 V, and a fill factor (FF) of 0.64. However, device A, based on dyestuff 4L,

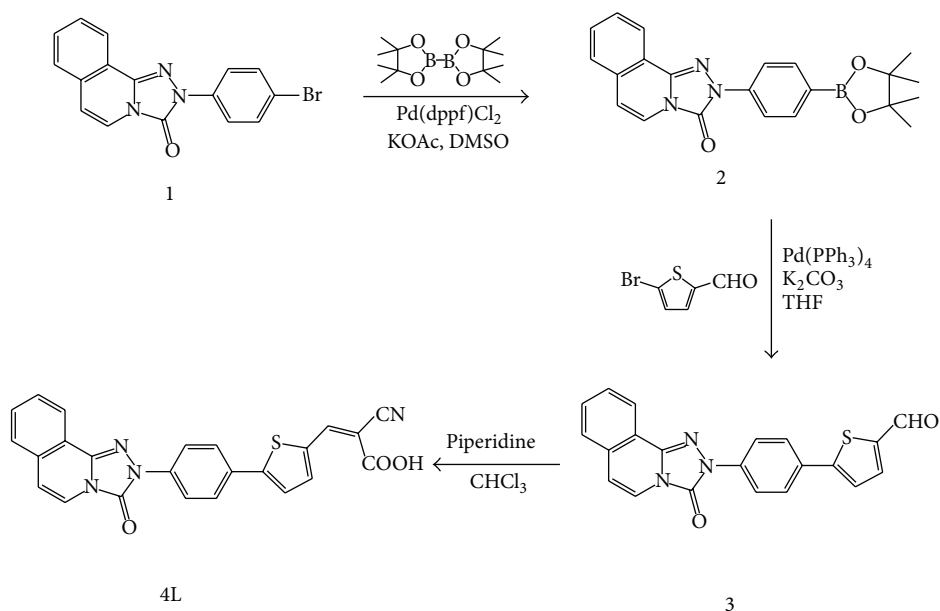
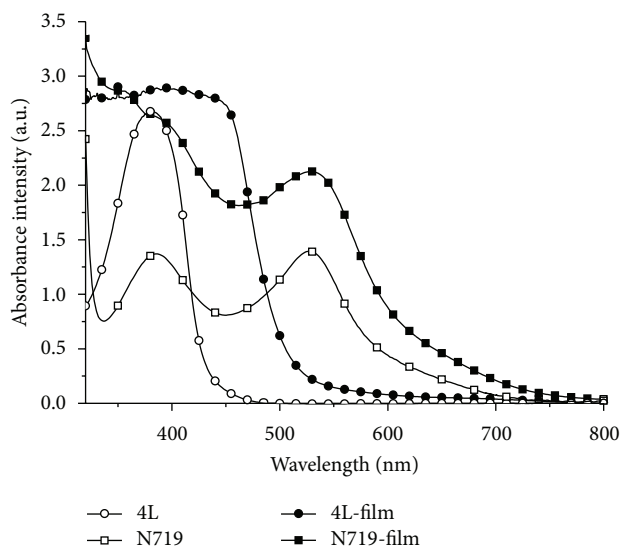


FIGURE 1: Synthesis of organic dyestuff 4L.

FIGURE 2: Absorption spectra of dyestuffs in DMF and spectra of dyestuffs adsorbed on TiO_2 film.

showed relatively low J_{sc} - 7.14 mA cm^{-2} , V_{oc} - 0.71 V , and FF- 0.64 , leading to a lower η value of 3.21% . This is reasonable, as dyestuff 4L has narrower absorption in the blue part of the visible region (as shown in Figures 2 and 4), and hence could not capture enough solar radiation energy in comparison with N719. In addition, the large π -conjugated system of triazoloisoquinoline causes stronger intermolecular π - π interaction, leading to unfavorable π -stacked dye aggregation on TiO_2 in the single sensitizer dyeing device A. Generally, close π -stacked dye aggregation leads to inefficient electron injection, resulting in a low η value due to the formation of excited triplet states [11]. Based on these physical properties, dyestuff 4L was used as cosensitizer to overcome the deficiency of N719 absorption in the 350 – 500 nm range.

Cosensitized solar cells based on the $12 \mu\text{m}$ transparent layer yielded a remarkably high photocurrent density of 12.71 , 14.63 , and 15.29 . The best cosensitized solar cell, which was sensitized by N719-4L with a 1 to 0.25 molar ratio, showed an open circuit voltage of 0.78 V and a fill factor of 0.66 , corresponding to an overall power conversion efficiency of 7.84% . This result is also in agreement with the observation of the incident photon-to-electron conversion efficiency (IPCE) action spectra of the DSSCs presented in Figure 4. On the other hand, device A, sensitized with dyestuff 4L, exhibited a lower V_{oc} - 0.71 V , while devices C, D, and E cosensitized with dyestuffs 4L and N719 showed only small changes in the V_{oc} value. These values are very close to that of device B, based on N719, which is 0.78 V . This result is attributed to

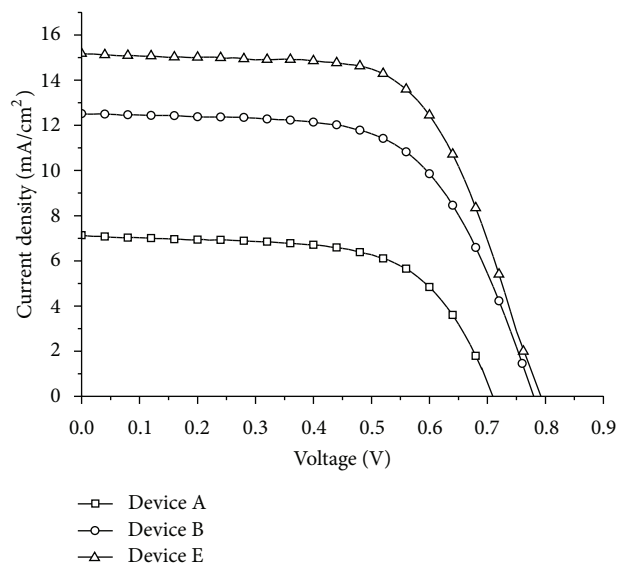


FIGURE 3: J - V curves of solar cells sensitized by 4L (device A), N719 (device B), and N719 : 4L (1 : 0.25) (device E) with $12.0 \mu\text{m}$ single layer nanocrystalline TiO_2 electrodes.

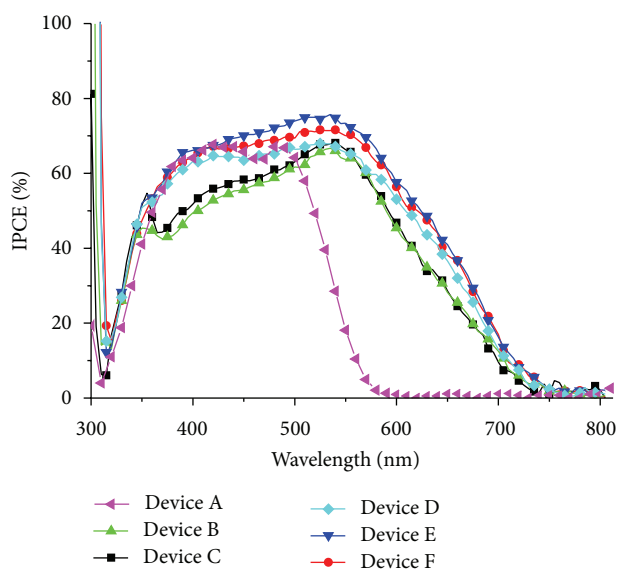


FIGURE 4: IPCE action spectra of solar cells sensitized by 4L (device A), N719 (device B), N719 : 4L (1 : 0.05) (device C), N719 : 4L (1 : 0.15) (device D), N719 : 4L (1 : 0.25) (device E), and N719 : 4L (1 : 0.35) (device F) with $12.0 \mu\text{m}$ single layer nanocrystalline TiO_2 electrodes.

the coadsorbent effect of dyestuff 4L, which has been applied successfully to prepare an insulating molecular layer with N719 [12, 13].

IPCE as a function of wavelength was measured to evaluate the photoresponse of the photoelectrodes in the whole spectra region. As shown in Figure 4, the maximum IPCE of the dyestuff 4L based device A was ca. 67% at 420 nm. This indicates that dyestuff 4L has good light harvesting effects at shorter wavelength regions. Device B exhibited the maximum IPCE of ca. 66% at 550 nm for the N719 sensitized solar

cell. The incident photon-to-electron conversion efficiency of N719 at shorter wavelength regions (ca. 52% at 420 nm) is thus not as good as at longer ones [14]. This is a niche for organic dyestuffs, such as dyestuff 4L, which can enhance absorption at shorter wavelength regions. When dyestuff 4L was added to the dye solution, the IPCE of devices D and E at 350–500 nm increased significantly. The maximum IPCE increased from 52% to 64% when 0.15 molar ratio dyestuff 4L was added to the dye solution. After increasing the concentration of 4L to a 0.25 molar ratio, the maximum IPCE increased from 52% to 67%. Upon dyestuff 4L coadsorption, the maximum IPCE improved significantly, compared to that seen with device B, which can be attributed to the increased photocurrent of the DSSCs. Cosensitization broadens the photocurrent action spectrum covering the visible domain at 350–500 nm. The related experimental data are in line with the results in Table 1 and Figure 3.

It is well known that organic dyestuffs will compete with N719 for adsorption on the TiO_2 surface. As shown in Figure 4 and Table 1 for devices C, D, and E, there is a balanced relationship between dyestuff 4L and N719 cosensitizers. The IPCE spectra of device C have a similar response to those of device B, which indicates that the concentration of 4L (a 0.05 molar ratio) was not enough to anchor the blank of the insulating molecular layer. This caused the performance of device C to rise slightly and produced $\eta = 6.37\%$, $J_{\text{sc}} = 12.71 \text{ mA cm}^{-2}$, $V_{\text{oc}} = 0.76 \text{ V}$, and $\text{FF} = 0.66$. Obviously, when the concentration of 4L was increased to a 0.15 and 0.25 molar ratio, this led to greater efficiency, which is attributed to the significant enhancement of J_{sc} , mainly due to the perfect insulating molecular layer and good incident photo-to-electron conversion efficiency at shorter wavelengths. Because of this layer, the best cell performance was achieved, with $\eta = 7.84\%$, $J_{\text{sc}} = 15.29 \text{ mA cm}^{-2}$, $V_{\text{oc}} = 0.78 \text{ V}$, and $\text{FF} = 0.66$. When the concentration of 4L was increased to a 0.35 molar ratio, the performance of

the device began to deteriorate and produced $\eta = 7.35\%$, $J_{sc} = 15.11 \text{ mA cm}^{-2}$, $V_{oc} = 0.74 \text{ V}$, and $FF = 0.66$. These results indicate that cosensitization with 4L in a 0.25 molar ratio is very effective in improving solar cell performance.

4. Conclusions

This study investigated the role of triazoloisoquinoline dyestuffs as a cosensitizer with N719. The results show that coadsorption of N719 sensitizer with dyestuff 4L onto nanocrystalline TiO_2 films significantly increased the photocurrent in a 1 to 0.25 molar ratio, thus enhancing the total conversion efficiency. The cell produced in this work achieved an energy conversion efficiency as high as 7.84% at 100 mW cm^{-2} and AM 1.5G. This improved conversion efficiency is attributed to the insulating molecular layer, which was composed of the small molecular organic dyestuff 4L and N719, and the better light harvesting effect at shorter-wavelength regions. It is anticipated that the findings of this work will contribute to the development of a cosensitizer which absorbs at shorter-wavelength regions in DSSCs.

References

- [1] B. O. Regan and M. Gratzel, "A low-cost, high-efficiency solar cell based on dye-sensitized colloidal TiO_2 films," *Nature*, vol. 353, pp. 737–740, 1991.
- [2] A. Mishra, M. K. R. Fischer, and P. Bauerle, "Metal-free organic dyes for dye-sensitized solar cells: from structure: property relationships to design rules," *Angewandte Chemie*, vol. 48, no. 14, pp. 2474–2499, 2009.
- [3] A. Hagfeldt, G. Boschloo, L. Sun, L. Kloo, and H. Pettersson, "Dye-sensitized solar cells," *Chemical Reviews*, vol. 110, no. 11, pp. 6595–6663, 2010.
- [4] M. K. Nazeeruddin, A. Kay, L. Rodicio et al., "Conversion of light to electricity by cis-X2bis(2,2'-bipyridyl-4,4'-dicarboxylate)ruthenium(II) charge-transfer sensitizers (X = Cl-, Br-, I-, CN-, and SCN-) on nanocrystalline titanium dioxide electrodes," *Journal of the American Chemical Society*, vol. 115, p. 6382, 1993.
- [5] J. He, W. Wu, J. Hua et al., "Bithiazole-bridged dyes for dye-sensitized solar cells with high open circuit voltage performance," *Journal of Materials Chemistry*, vol. 21, pp. 6054–6062, 2011.
- [6] Y. Numata, I. Ashraful, Y. Shirai, and L. Han, "Preparation of donor-acceptor type organic dyes bearing various electron-withdrawing groups for dye-sensitized solar cell application," *Chemical Communications*, vol. 47, no. 21, pp. 6159–6161, 2011.
- [7] L.-Y. Lin, C.-H. Tsai, K.-T. Wong et al., "Organic dyes containing coplanar diphenyl-substituted dithienosilole core for efficient dye-sensitized solar cells," *The Journal of Organic Chemistry*, vol. 75, no. 14, pp. 4778–4785, 2010.
- [8] Q. Miao, L. Wu, J. Cui, M. Huang, and T. Ma, "A new type of dye-sensitized solar cell with a multilayered photoanode prepared by a film-transfer technique," *Advanced Materials*, vol. 23, no. 24, pp. 2764–2768, 2011.
- [9] J. H. Yum, S. R. Jang, P. Walter et al., "Efficient co-sensitization of nanocrystalline TiO_2 films by organic sensitizers," *Chemical Communications*, no. 44, pp. 4680–4682, 2007.
- [10] Y. Hong, J. Liao, D. Cao et al., "Organic dye bearing asymmetric double donor- π -acceptor chains for dye-sensitized solar cells," *The Journal Organic Chemistry*, vol. 76, p. 8015, 2011.
- [11] B. Liu, W. Zhu, Q. Zhang et al., "Conveniently synthesized isophorone dyes for high efficiency dye-sensitized solar cells: tuning photovoltaic performance by structural modification of donor group in donor- π -acceptor system," *Chemical Communications*, no. 13, pp. 1766–1668, 2009.
- [12] S. Rühle, M. Greenshtein, S.-G. Chen et al., "Molecular adjustment of the electronic properties of nanoporous electrodes in dye-sensitized solar cells," *Journal of Physical Chemistry B*, vol. 109, no. 40, pp. 18907–18913, 2005.
- [13] J. H. Yum, P. Walter, S. Huber et al., "Efficient far red sensitization of nanocrystalline TiO_2 films by an unsymmetrical squaraine dye," *Journal of the American Chemical Society*, vol. 129, pp. 10320–10321, 2007.
- [14] A. Mishra, N. Pootrakulchote, M. K. R. Fischer et al., "Design and synthesis of a novel anchoring ligand for highly efficient thin film dye-sensitized solar cells," *Chemical Communications*, no. 46, pp. 7146–7148, 2009.

Research Article

To Enhance Performance of Light Soaking Process on ZnS/CuIn_{1-x}Ga_xSe₂ Solar Cell

Yu-Jen Hsiao,¹ Chung-Hsin Lu,² and Te-Hua Fang³

¹ National Nano Device Laboratories, Tainan 741, Taiwan

² Department of Chemical Engineering, National Taiwan University, Taipei 617, Taiwan

³ Department of Mechanical Engineering, National Kaohsiung University of Applied Sciences, Kaohsiung 807, Taiwan

Correspondence should be addressed to Yu-Jen Hsiao; yujenhsiao.tw@gmail.com

Received 20 September 2013; Accepted 13 October 2013

Academic Editor: Teen-Hang Meen

Copyright © 2013 Yu-Jen Hsiao et al. This is an open access article distributed under the Creative Commons Attribution License, which permits unrestricted use, distribution, and reproduction in any medium, provided the original work is properly cited.

The ZnS/CuInGaSe₂ heterojunction solar cell fabricated on Mo coated glass is studied. The crystallinity of the CIGS absorber layer is prepared by coevaporated method and the ZnS buffer layer with a band gap of 3.21 eV. The MoS₂ phase was also found in the CuInGaSe₂/Mo system from HRTEM. The light soaking effect of photoactive film for 10 min results in an increase in F.F. from 55.8 to 64%, but series resistivity from 7.4 to 3.8 Ω. The efficiency of the devices improved from 8.12 to 9.50%.

1. Introduction

Various photovoltaic (PV) devices have received a lot of attention as a renewable energy source [1]. These devices are made based on inorganic or organic materials, such as silicon-based thin film solar cells [2], multijunction solar cells [3], and dye-sensitized solar cells [4]. However, most of these devices suffer from either high cost or relatively low energy conversion efficiency. CuIn_{1-x}Ga_xSe₂ (CIGS)-based thin films have received considerable attention as one of the most promising materials for thin film solar cells due to their high absorption coefficient, the potential for low cost manufacturing, and high conversion efficiency for inorganic solar cell application, although Mo/CuInGaSe₂ (CIGS) thin film solar cells have been extensively studied [5].

A high efficiency CIGS is usually fabricated by a coevaporation method, but this is a complex process to scale up to large areas due to the problem of nonuniformity. Several low cost and promising alternatives to coevaporation suitable for large scale production, such as sputtering [6], electrodeposition [7], and screen printing [8], have been investigated. In particular, sputtering of CuInGa precursors followed by selenization appears to be a favored process for thin film deposition [9]. In this study, a three-stage

co-evaporation deposition technology was adopted to grow CIGS photovoltaic/electronic films to realize efficient solar cells. To avoid the Cd-induced pollution to environment, the n-type ZnS buffer layer for forming CIGS PVs was introduced [10].

In this paper, we report ZnS/CuIn_{1-x}Ga_xSe₂ heterojunction solar cells fabricated on Mo coated glass. The crystallinity of the CIGS and ZnS buffer layer were studied. The microstructure phase was investigated in the CuInGaSe₂/Mo system by HRTEM. The light soaking and electrical properties of the fabricated p-CIGS/n-ZnS solar cells will also be discussed.

2. Experimental

The soda-lime glasses were carefully cleaned in isopropanol-acetone ultrasonic bath to remove electrostatic charges. An approximately 0.7 μm thick Mo back contact was directly deposited by RF sputtering on glass substrate. CIGS absorber layers were deposited by evaporation of elemental Cu, In, Ga, and Se onto Mo by three-stage co-evaporation. During the 1st stage of the absorber growth the substrate temperature was kept at 400°C, while during the 2nd and 3rd stages

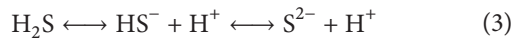
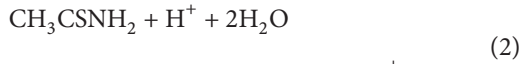
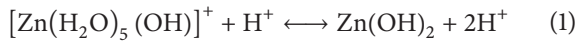
the substrate temperature increased up to 600°C. The 100–300 nm thick ZnS buffer layer was deposited on CIGS film by chemical bath deposition at 80°C. The solar cells were finished by deposition of a ZnS buffer layer, RF sputtering of ZnO:Al front contacts (~400 nm thick), and electron beam evaporation of 1 μm thick Al contact grids for better current collection. No antireflection (AR) coating was applied.

The phase identification was performed by X-ray powder diffraction (XRD, Rigaku Dmax-33). The surface microstructure was examined by scanning electron microscopy (SEM, Hitachi S4200). The morphology and microstructure were examined by transmission electron microscopy (HRTEM, HF-2000, Hitachi). The absorption spectra were obtained using an optical spectrometer (Hitachi, U-4100), and current-voltage measurements (Keithley 2410 SourceMeter) were obtained using a solar simulator (TELTEC) with an AM 1.5 filter under an irradiation intensity of 100 mW/cm².

3. Results and Discussion

The CIGS quaternary alloy absorber layer coevaporated exhibits the characteristic peaks of chalcopyrite structure in X-ray diffraction (XRD) analysis, as shown in Figure 1(a). XRD spectra also indicate that the CIGS film presents a strong (112) preferred orientation at $2\theta = 26.68$ corresponding to chalcopyrite phases. The other prominent peaks corresponded to the (220) and (312) directions. The full width at half maximum (FWHM) of the diffraction peak is rather small, which indicates that the film crystallinity is fairly good.

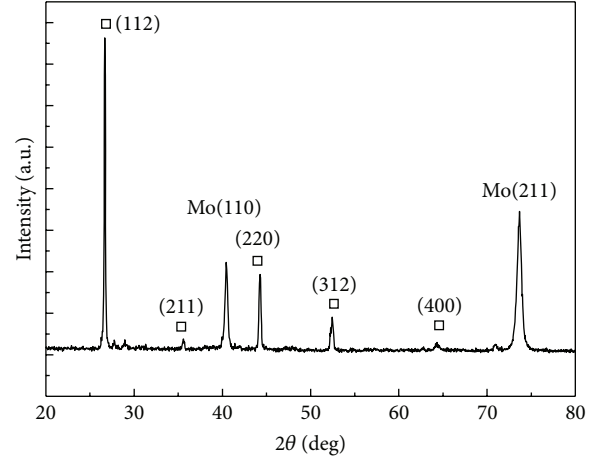
XRD patterns of ZnS with various deposition thicknesses are shown in Figure 1(b). The possible chemical reactions for the synthesis of ZnS films are as follows:



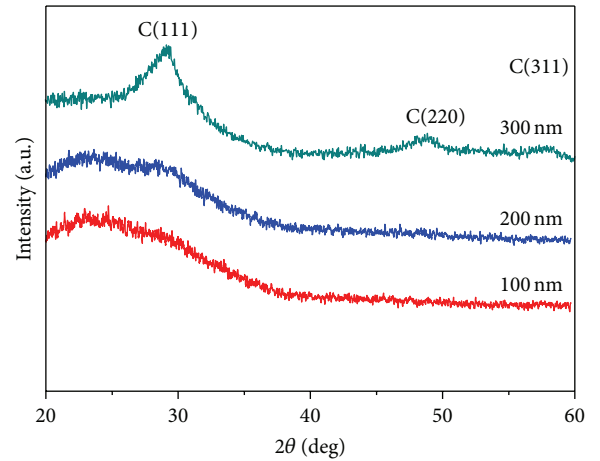
During the reaction processes, sulfide ions are released slowly from CH₃CSNH₂ and react with zinc ions. It indicates that ZnS is produced by reaction of S²⁻ and Zn²⁺ in (4). All of the peaks were identified to be those of the cubic ZnS phase (JCPDS card number 79-0043) [11]. The crystallinity of ZnS increased along with deposition thickness. When the thickness was increased from 100 to 300 nm, the peaks of (111), (220), and (311) were obviously shown.

Figure 2(a) has shown the UV-vis absorption spectra of 200 nm ZnS film on glass and estimated the band gap. For a direct band gap semiconductor, the absorbance in the vicinity of the onset due to the electronic transition is given by the following equation:

$$\alpha = \frac{C(h\nu - E_g)^{1/2}}{h\nu}, \quad (5)$$



(a)



(b)

FIGURE 1: (a) XRD spectra of CIGS film on Mo electrode. (b) XRD spectra of ZnS film synthesized using a chemical bath deposition method at various thicknesses.

where α is the absorption coefficient, C is the constant, $h\nu$ is the photon energy, and E_g is the band gap. The visible light absorption edge of 200 nm ZnS film was at 386 nm. Extrapolation of the linear region gives a band gap of 3.21 eV. Therefore, the direct band gap energy obtained from our experiment is 3.21 eV. As known, hydrothermal process may transform some elemental S species to sulfur dioxides. It has defect states like S vacancies in the band gap of ZnS [12]. Therefore, the sample had lower band gap than ideal crystal structure of ZnS with 3.68 eV. It has shown actual sample of ZnS film before and after being deposited on CIGS/Mo substrate in Figure 2(b). The color of CIGS/Mo was gray on the surface, and then we can see brown color as ZnS film deposited on CIGS/Mo substrate. Therefore, we can determine ZnS film on CIGS by color variability.

Figure 3(a) shows the cross-sectional bright field TEM image of the Mo/CIGS/ZnS stacked layers. In contrast to the relatively large grains of the CIGS layer (0.2 to 0.7 μm),

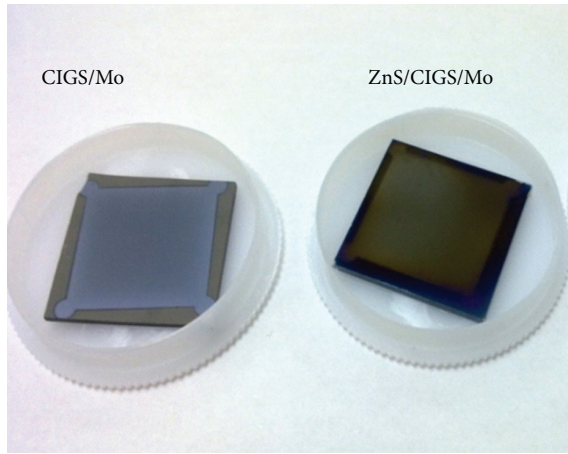
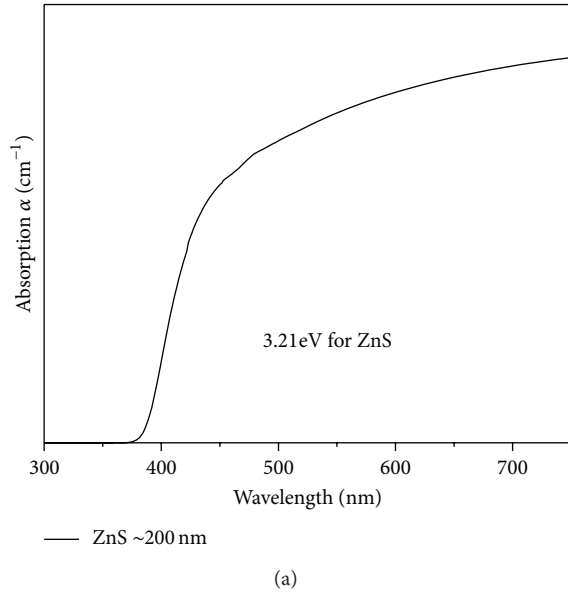


FIGURE 2: (a) Absorption spectra are as the function of photon energy for the 200 nm ZnS film. (b) Realized sample of ZnS film deposited on CIGS/Mo substrate.

the ZnS layer consists of very small grains. Although the CIGS layer exhibits substantial surface roughness (~ 80 nm in average), the ZnS layer grown on top of CIGS has a uniform thickness (~ 200 nm) that was prepared for TEM by the focused ion beam (FIB). Each one of the layers constituting the Mo/CIGS/ZnS system was investigated in order to know the formation of defects as well as to get information regarding crystalline structure and grain size. On the other hand, two different regions are identified in the ZnS and CIGS/Mo films as is observed in the micrograph of Figures 3(b)-3(c). The crystalline ZnS films are identified by the high resolution lattice images. A representative HRTEM image enlarging a round part of the structure in Figure 3(b) is given. The interplanar distances of the crystal fringes are about 0.31 nm.

The microstructure of the Mo/CuInGaSe₂ interfaces was investigated in order to visualize defects and the formation

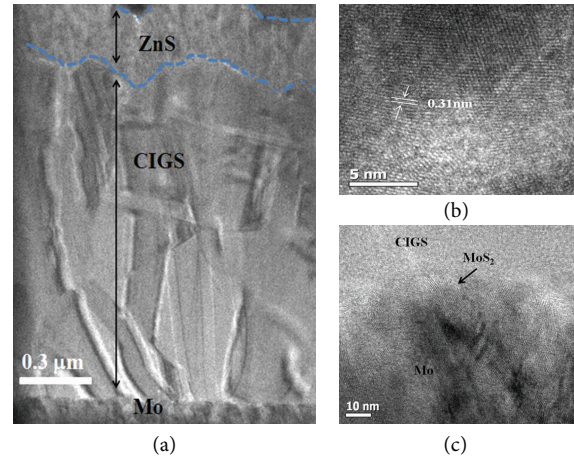


FIGURE 3: (a) TEM cross-section images of ZnS/CIGS/Mo, (b) high-resolution TEM image of the cubic ZnS film, and (c) the interface of CIGS and Mo.

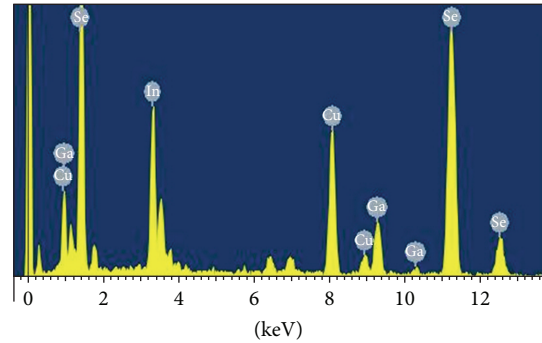


FIGURE 4: EDX analysis of the CIGS film.

of secondary phases as a result of possible chemical reactions occurring during the deposition of the stacked layers. Figure 3(c) shows a typical cross-sectional HRTEM image of the Mo/CIGS interface. The formation of a very thin layer (10–40 nm) of a new compound is observed around the Mo/CIGS interface. It seems that the new compound corresponds to the MoS₂ phase due to the similarity with the CuInGaSe₂/Mo system in which an interlayer of MoS₂ is usually formed [13]. This result makes sure that the metallic Mo thin layer is converted into MoS₂ during the initial minutes of CIGS deposition. The MoS₂ layer gives rise to a small conduction band offset with respect to the CIGS bulk material and a small Schottky barrier at the Mo back contact [14]. Both features are good for device performance, because the conduction band offset diminishes the back surface recombination, and then arrow Schottky barrier gives no substantial resistance to holes between CIGS and the metallic back contact. The EDS line profiles indicate that the CIGS film consists of Cu, In, Ga, and Se, as shown in Figure 4. In addition, the atomic concentrations of Cu = 23%, In = 21%, Ga = 10%, and Se = 46% are calculated from the EDS spectrum.

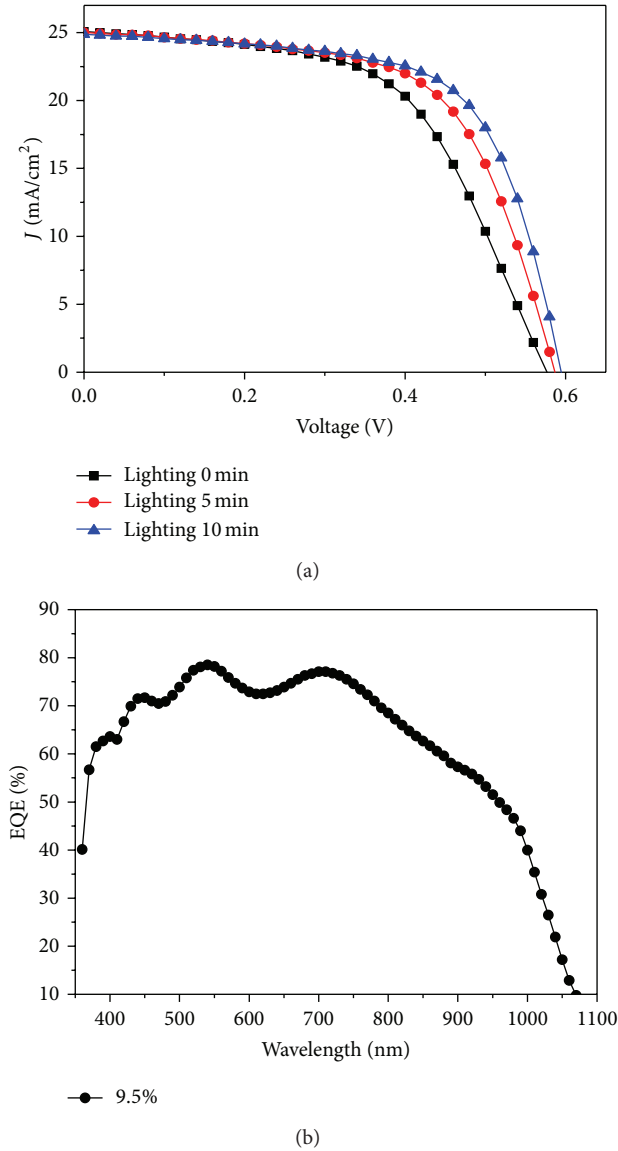


FIGURE 5: (a) J - V characteristics of ZnS/CIGS heterojunction solar cell with various light soaking times and (b) the IPCE spectrum of CIGS solar cell with efficiency of 9.5%.

TABLE 1: Photovoltaic performance of the AZO/ZnS/CIGS heterojunction solar cell with various light soaking times, under AM1.5G at 100 mW/cm² illumination.

Light soaking	V_{oc} (V)	J_{sc} (mA/cm ²)	F.F. (%)	R_s (Ω)	R_{sh} (Ω)	η (%)
0 min	0.58	25.07	55.8	7.4	995	8.12
5 min	0.58	25.02	61.8	5.6	1023	8.97
10 min	0.60	24.88	64.0	3.8	1087	9.50

Before light soaking the AZO/ZnS/CIGS heterojunction solar cell generally suffered from poor one-diode behaviour, a characteristic especially marked at low temperatures. The situation is considerably improved after light soaking with various times, under AM1.5G at 100 mW/cm² illumination.

The solar cell parameters of the cells used in photovoltaic measurements in Table 1. The time needed for the parameters to saturate under illumination is also shown. Before light soaking the problem with the cells was the low fill factor and high series resistivity. The fill factor increased significantly with light soaking for ZnS buffer layer, while V_{oc} remains stable. In Figure 5(a), J - V curves obtained in the light soaked states for the lighting 5 and 10 min.

The measurements reveal that lighting into the photoactive film results in an increase in F.F. from 55.8 to 64%, but series resistivity from 7.4 to 3.8 Ω. The η value of the devices improved from 8.12 to 9.50%. The effect of F.F. value is attributed to the positive conduction band offsets (CBO) between the CIGS layer and the buffer layer, and it has been suggested that this barrier is lowered by illumination due to persistent photoconductivity (PPC) in the buffer layer [15]. In this work white light-induced metastable changes to the F.F. are only observed for cells with buffer layers having a lighting time 10 min. In addition, the quantum efficiencies are measured after light soaking in Figure 5(b). The EQE spectra are similar in shape, consistent with the almost unchanged short circuit current density.

4. Conclusions

In summary, the ZnS/CuInGaSe₂ heterojunction solar cell with the light soaking process has been investigated. The crystallinity of the CIGS absorber layer is fairly good by coevaporated method. ZnS buffer layer with a band gap of 3.21 eV was deposited on CIGS/Mo sample. The MoS₂ phase was found in the CuInGaSe₂/Mo system from HRTEM. The light soaking effect of photoactive film for 10 min results in an increase in F.F. from 55.8 to 64%, but series resistivity from 7.4 to 3.8 Ω. The η value of the devices improved from 8.12 to 9.50%.

Acknowledgment

This research is supported by the National Science Council, Taiwan under contract no. NSC 102-3113-P-002-026.

References

- [1] N. S. Lewis, "Toward cost-effective solar energy use," *Science*, vol. 315, no. 5813, pp. 798–801, 2007.
- [2] K. L. Chopra, P. D. Paulson, and V. Dutta, "Thin-film solar cells: an overview," *Progress in Photovoltaics*, vol. 12, pp. 69–92, 2004.
- [3] M. Konagai, "Deposition of new microcrystalline materials, μ -SiC, μ -GeC by HWCVD and solar cell applications," *Thin Solid Films*, vol. 516, no. 5, pp. 490–495, 2008.
- [4] L. Lu, R. Li, K. Fan, and T. Peng, "Effects of annealing conditions on the photoelectrochemical properties of dye-sensitized solar cells made with ZnO nanoparticles," *Solar Energy*, vol. 84, pp. 844–853, 2010.
- [5] I. Repins, M. A. Contreras, B. Egaas et al., "19.9%-efficient ZnO/CdS/CuInGaSe₂ solar cell with 81.2% fill factor," *Progress in Photovoltaics*, vol. 16, pp. 235–239, 2008.

- [6] G. S. Chen, J. C. Yang, Y. C. Chan, L. C. Yang, and W. Huang, "Another route to fabricate single-phase chalcogenides by post-selenization of Cu-In-Ga precursors sputter deposited from a single ternary target," *Solar Energy Materials and Solar Cells*, vol. 93, pp. 1351–1355, 2009.
- [7] Y. Lai, F. Liu, Z. Zhang et al., "Cyclic voltammetry study of electrodeposition of Cu(In,Ga)Se₂ thin films," *Electrochimica Acta*, vol. 54, no. 11, pp. 3004–3010, 2009.
- [8] S. J. Ahn, C. W. Kim, J. H. Yun et al., "CuInSe₂ (CIS) thin film solar cells by direct coating and selenization of solution precursors," *Journal of Physical Chemistry C*, vol. 114, no. 17, pp. 8108–8113, 2010.
- [9] M. S. Hanssen, H. Efstathiadis, and P. Haldar, "Development of smooth CuInGa precursor films for CuIn_{1-x}Ga_xSe₂ thin film solar cell applications," *Thin Solid Films*, vol. 519, no. 19, pp. 6297–6301, 2011.
- [10] T. Nakada and M. Mizutani, "18% Efficiency Cd-free Cu(In,Ga)Se₂ thin-film solar cells fabricated using chemical bath deposition (CBD)-ZnS buffer layers," *Japanese Journal of Applied Physics*, vol. 41, pp. L165–L167, 2002.
- [11] M. Scocioreanu, M. Baibarac, I. Baltog, I. Pasuk, and T. Velula, "Photoluminescence and Raman evidence for mechanochemical interaction of polyaniline-emeraldine base with ZnS in cubic and hexagonal phase," *Journal of Solid State Chemistry*, vol. 186, pp. 217–223, 2012.
- [12] W. Chen, Z. G. Wang, Z. J. Lin, and L. Y. Lin, "Absorption and luminescence of the surface states in ZnS nanoparticles," *Journal of Applied Physics*, vol. 82, no. 6, pp. 3111–3115, 1997.
- [13] X. Zhu, Z. Zhou, Y. Wang, L. Zhang, A. Li, and F. Huang, "Determining factor of MoSe₂ formation in Cu(In,Ga)Se₂ solar cells," *Solar Energy Materials and Solar Cells*, vol. 101, pp. 57–61, 2012.
- [14] D. Abou-Ras, G. Kostorz, D. Bremaud et al., "Formation and characterisation of MoSe₂ for Cu(In,Ga)Se₂ based solar cells," *Thin Solid Films*, vol. 480–481, pp. 433–438, 2005.
- [15] I. L. Eisgruber, J. E. Granata, J. R. Sites, J. Hou, and J. Kessler, "Blue-photon modification of nonstandard diode barrier in CuInSe₂ solar cells," *Solar Energy Materials and Solar Cells*, vol. 53, no. 3–4, pp. 367–377, 1998.

Research Article

Fabrication and Characterization of CuInSe_2 Thin Film Applicable for a Solar Energy Light Absorption Material via a Low Temperature Solid State Reaction

Kuo-Chin Hsu,¹ Yaw-Shyan Fu,² Pei-Ying Lin,³ I-Tseng Tang,² and Jiunn-Der Liao¹

¹ Department of Materials Science and Engineering, National Cheng Kung University, Tainan 701, Taiwan

² Department of Greenery, National University of Tainan, 701, Taiwan

³ Department of Photonics, National Cheng Kung University, Tainan 701, Taiwan

Correspondence should be addressed to Jiunn-Der Liao; jdliao@mail.ncku.edu.tw

Received 15 September 2013; Accepted 7 October 2013

Academic Editor: Teen-Hang Meen

Copyright © 2013 Kuo-Chin Hsu et al. This is an open access article distributed under the Creative Commons Attribution License, which permits unrestricted use, distribution, and reproduction in any medium, provided the original work is properly cited.

The chalcopyrite CuInSe_2 thin film synthesized via a low temperature solid state reaction from CuSe and InSe powders was investigated using X-ray diffractometry (XRD), scanning electron microscope (SEM), energy dispersive spectrometer (EDS), transmission electron microscopy (TEM), and UV-vis absorption spectroscopy. CuSe and InSe phases react and directly transform into CuInSe_2 without the occurrence of any intermediate phase. The morphology of the newly formed CuInSe_2 crystalline was close to that of the CuSe reactant particle based on the TEM results, which indicate that the solid state reaction kinetics may be dominated by the In^{3+} ions diffusion. The CuInSe_2 thin film prepared from the solid state reaction did not use the selenide process; its band gap might reach 1.06 eV, which is competent and suitable to be used for a thin film solar cell light absorption layer.

1. Introduction

For the new type-energy materials, the group IV quantum dot nanostructures for future generation solar cell applications [1] and next generation ionic conducting membranes for photochemical materials (i.e., fuels from light), batteries (i.e., electricity storage), fuel cells (i.e., electricity from fuels), and other applications [2] are highly promising. Successful results have been increasingly converted into products, and more and more organizations have developed novel advanced materials for renewable energy for the future. Many efforts have also been focused on photovoltaic cells. Among them, the ternary I-III-VI₂ semiconductor of CuInSe_2 (CIS) is one of the most important semiconductor materials used in thin film photovoltaic cells. Because of its high absorption coefficient, suitable band gap, good radiation stability, and the thickness of the absorption layers can be reduced to several micrometers [3].

High efficiency CIS solar cells are commonly prepared via the physical vapor deposition method [4–6]. This kind of

process requires a complicated facility, thereby leading to the high fabrication cost. However, the general vacuum methods have drawbacks such as the complexity in process and high production costs and are difficult to be made on a large scale, which need to be solved before the mass production of CIS solar cells. To avoid these drawbacks, nonvacuum processes have been extensively investigated in recent years, such as ink printing method [7], electrodeposition process [8, 9], spray pyrolysis method [10], chemical deposited method [11], and combustion method and nonvacuum spin-coating process [12].

A potential nonvacuum method for CIS formation is developed in this work. In the experiment, the CuSe and InSe powders are prepared by wet chemical method, which is one of the simplest and cheapest methods. The CIS thin film is thereafter obtained by spin coating from CuSe and InSe powders on the glass and then heated at 350°C for 3 h under nitrogen gas. The structure and the optical properties of the precursors and the CIS films are investigated and discussed.

TABLE 1: Experimental conditions and results.

No.	Materials	Precursors ratio	Measured by EDS (Cu : In : Se)	Time (h)	Temp (°C)	Products
1 ^a	InCl ₃ + Se	1:1	0:1:1.06	5	220	InSe
2 ^a	InCl ₃ + Se	2:3	0:2:3.01	5	280	In ₂ Se ₃
3 ^a	CuCl + Se	1:1	1:0:0.99	2	220	CuSe
4 ^a	CuCl + Se	2:1	1.74:0:1	2	220	Cu ₂ Se
5 ^b	InSe + CuSe	1:1	1:0.79:1.86	3	350	CuInSe ₂
6 ^b	In ₂ Se ₃ + Cu ₂ Se	1:1	1:1.32:1.94	3	350	CuInSe ₂ + In ₂ Se ₃

^aSamples no. 1~4 were reaction via wet chemical process using OLA as solvent.

^bThe precursors were prepared by samples no. 1~4 and reaction through low temperature solid state reaction.

2. Experimental

2.1. Materials. The copper (I) chloride (99.99%, Alfa Aesar, Ward Hill, MA, USA) and indium (III) chloride (99.99%, Acros, Geel, Belgium) used were analytical grade reagents. Selenium powder (99.99%, Sigma-Aldrich, St. Louis, Missouri, USA) was a high purity reagent. Oleylamine (70%, Kanto Chemical Co., Inc., Tokyo, Japan), hexane (99%, Acros, Geel, Belgium), and ethanol (95%, Acros, Geel, Belgium) were used as received, without further purification. The deionized water (DI water) used in this work was obtained from EMD Millipore Corporation-Direct-Q 3 system (Billerica, MA, USA).

2.2. Synthesis of InSe Particles. A typical synthesis of InSe particles was modified from Park et al.'s procedure [13]; 0.45 mmol InCl₃ and 0.50 mmol Se powder were added into 10 mL of oleylamine (OLA) at room temperature. The reaction mixture was heated to 220°C and kept at that temperature under nitrogen gas with magnet stirring for 5 h. The product was then centrifuged and washed with hexane, ethanol and DI water several times and then dried at 80°C for 3 h in a vacuum oven.

2.3. Synthesis of In₂Se₃ Particles. The In₂Se₃ particles were synthesized by annealing the reaction mixture containing 0.45 mmol InCl₃ and 0.70 mmol Se powder in 10 mL of OLA at 280°C under nitrogen gas for 5 h. The product was then centrifuged and washed with hexane, ethanol, and DI water several times and then dried at 80°C for 3 h in a vacuum oven.

2.4. Synthesis of CuSe Particles. The CuSe particles were synthesized by annealing the reaction mixture containing 0.50 mmol Se powder and 10 mL of OLA (OLA/Se) firstly mixed at room temperature, and the resulting solution was heated to 180°C. 0.46 mmol CuCl and was then quickly added into the hot OLA/Se solution; the reaction mixture was annealed at 220°C for 2 h under nitrogen gas. The product was then centrifuged and washed with hexane, ethanol, and DI water several times and then dried at 80°C for 3 h in a vacuum oven.

2.5. Synthesis of Cu₂Se Particles. The Cu₂Se particles were synthesized by annealing the reaction mixture containing 0.91 mmol CuCl and 0.50 mmol Se powder in 10 mL of OLA at

220°C for 2 h under nitrogen gas. All the products were then centrifuged and washed with hexane, ethanol, and DI water several times and then dried at 80°C for 3 h in a vacuum oven.

2.6. Synthesis of CuInSe₂ Films. The CuInSe₂ films were prepared using the as-prepared metal Se compounds as precursors in two reaction paths. In the reaction path A, the as-prepared InSe (0.25 mmol) and CuSe (0.25 mmol) were dispersed in ethanol and spin-coated on the glass with 500 rev. min⁻¹ for 20 s in air, then dried at 100°C for 1 h to remove residual solvent. The glass was transferred into closed graphite box and heated at 350°C for 3 h under nitrogen gas. In the reaction path B, the as-prepared In₂Se₃ (0.25 mmol) and Cu₂Se (0.25 mmol) were also dispersed in ethanol and spin-coated on the glass with 500 rev. min⁻¹ for 20 s in air, then dried at 100°C for 1 h to remove residual solvent. The glass was transferred into closed graphite box and heated at 350°C for 3 h under nitrogen gas. The experimental parameters were summarized in Table 1.

2.7. Material Characterization. The X-ray powder diffraction (XRD, operating at 8 kV) patterns of the as-prepared samples were recorded on Shimadzu XRD-6000 X-ray diffractometer (Kyoto, Japan) with Cu K α radiation ($\lambda = 0.15418$ nm). The morphologies and micro-/nanostructure were investigated by Hitachi 4200A (Tokyo, Japan) scanning electron microscope (SEM, operating at 10 kV) and JEOL JEM-2000EX (Tokyo, Japan) transmission electron microscope (TEM, operating at 160 kV). The measurements using energy dispersive spectrometer (EDS) were performed on Horiba EX220 (Kyoto, Japan), which was attached to TEM for compositional analyses. Thermal analysis was carried out with Perkin Elmer Pyris Diamond TG/DTA thermal analyzer (Boston, MA, USA) in nitrogen atmosphere at a heating rate of 20°C/min. UV-vis absorption spectra were recorded by Hitachi U-3010 spectrophotometer (Tokyo, Japan).

3. Results and Discussion

The phase and crystallographic structure of the as-prepared metal Se compounds were determined by XRD. Figure 1 showed XRD patterns of the as-prepared (a) InSe, (b) In₂Se₃, (c) CuSe, and (d) Cu₂Se particles, which corresponded to the cubic phase, consistent with the literature [13], the hexagonal structure (JCPDS no. 89-0658) [14], the klockmannite

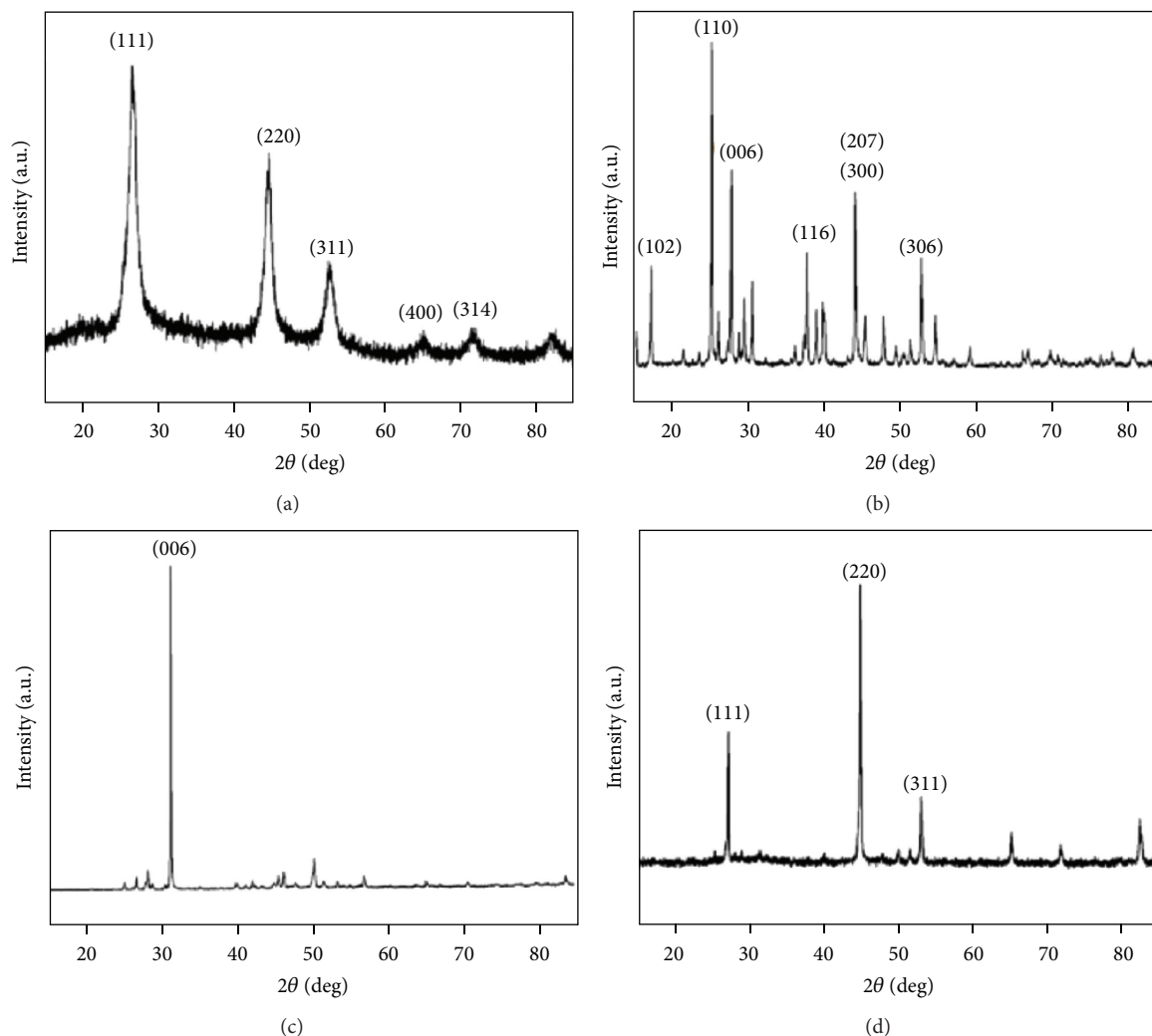


FIGURE 1: XRD patterns of as-prepared (a) InSe [13], (b) In_2Se_3 [14], (c) CuSe [14], and (d) Cu_2Se [14] particles.

structure (JCPDS no. 49-1457) [14], and the cubic structure (JCPDS no. 88-2044) [14], respectively. Figure 2 showed XRD patterns of the CIS films synthesized from (a) the as-prepared metal Se compounds: InSe and CuSe, and (b) the as-prepared metal Se compounds: In_2Se_3 and Cu_2Se , respectively. The chemical composition of the as-prepared metal Se compounds and other products was analyzed with EDS and given in Table 1.

Figure 2(a) showed XRD pattern obtained from the annealed thin film made by CuSe and InSe, which exhibited a single crystalline structure composed of CIS that corresponds to the peaks at (112), (211), (204)/(220), (116)/(312), (008)/(400), (316)/(332), and (228)/(424). The chalcopyrite phase of CIS (JCPDS no. 40-1487) was then synthesized. Figure 2(b) showed XRD pattern obtained from the annealed thin film made by Cu_2Se and In_2Se_3 , which exhibited a multicrystalline structure composed of CuInSe_2 and In_2Se_3 that corresponds to the chalcopyrite CIS and the hexagonal In_2Se_3 .

Figure 3 showed various images of the as-prepared CIS thin film from path A: (a) cross-sectioned SEM image for

the as-synthesized CIS before annealing and (b) that after annealing, (c) LR-TEM, and (d) HR-TEM and SAED (the insert) images for the as-prepared CIS. In Figure 3(a), the upper layer was identified as InSe particles with irregular shapes. The lower layer was identified as CuSe particles with a regular hexagonal shape of around $2\ \mu\text{m}$ in diameter. In Figure 3(b), the CIS thin film exhibited a regular shape of hexagonal chalcopyrite particles. The insert image was the dispersed CIS particles from its film. Figure 3(c) showed the LR-TEM image of CIS particle. Its morphology and particle size were consistent with those observed by SEM. Figure 3(d) showed the HR-TEM and inserted SAED image of CIS particle. The spacing of the crystal lattice was measured around $3.3\ \text{\AA}$, which is consistent with the crystal lattice plane of CIS under (112). The EDS analysis expected an average composition of $\text{Cu}_{1.0}\text{In}_{0.79}\text{Se}_{1.86}$, which estimated an element ratio for copper, indium, and selenium of 1.27:1.00:2.36. The CIS structure prepared through the solid state reaction showed a Cu- and Se-rich structure, but roughly correlated with the composition of CuInSe_2 .

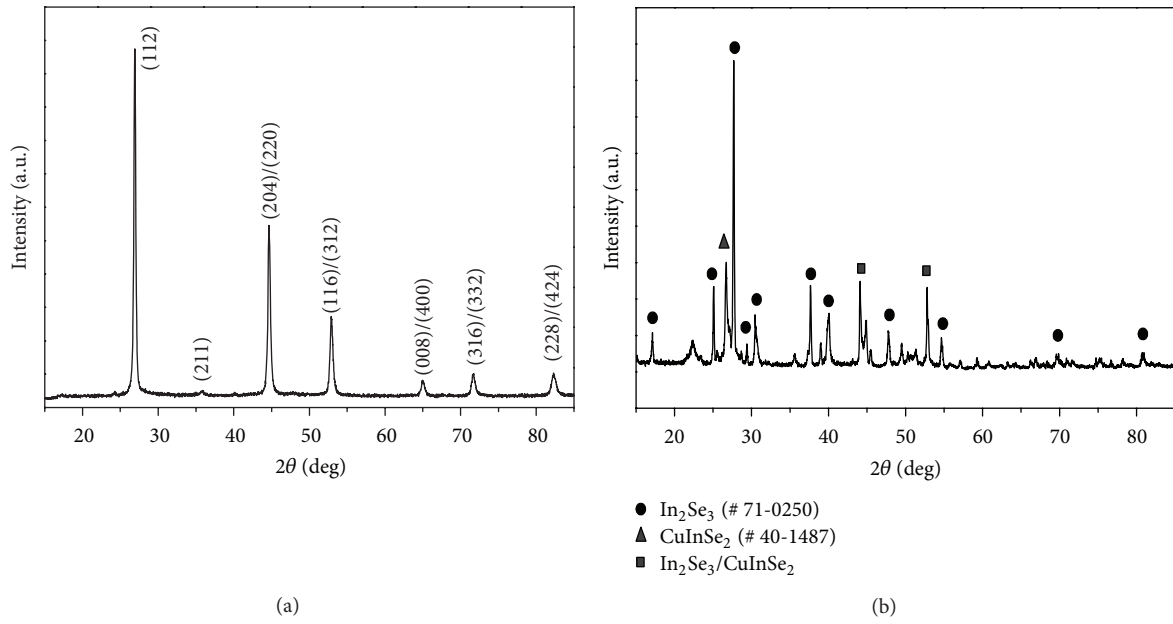


FIGURE 2: XRD patterns obtained from the annealed thin film made by (a) CuSe and InSe and (b) Cu_2Se and In_2Se_3 .

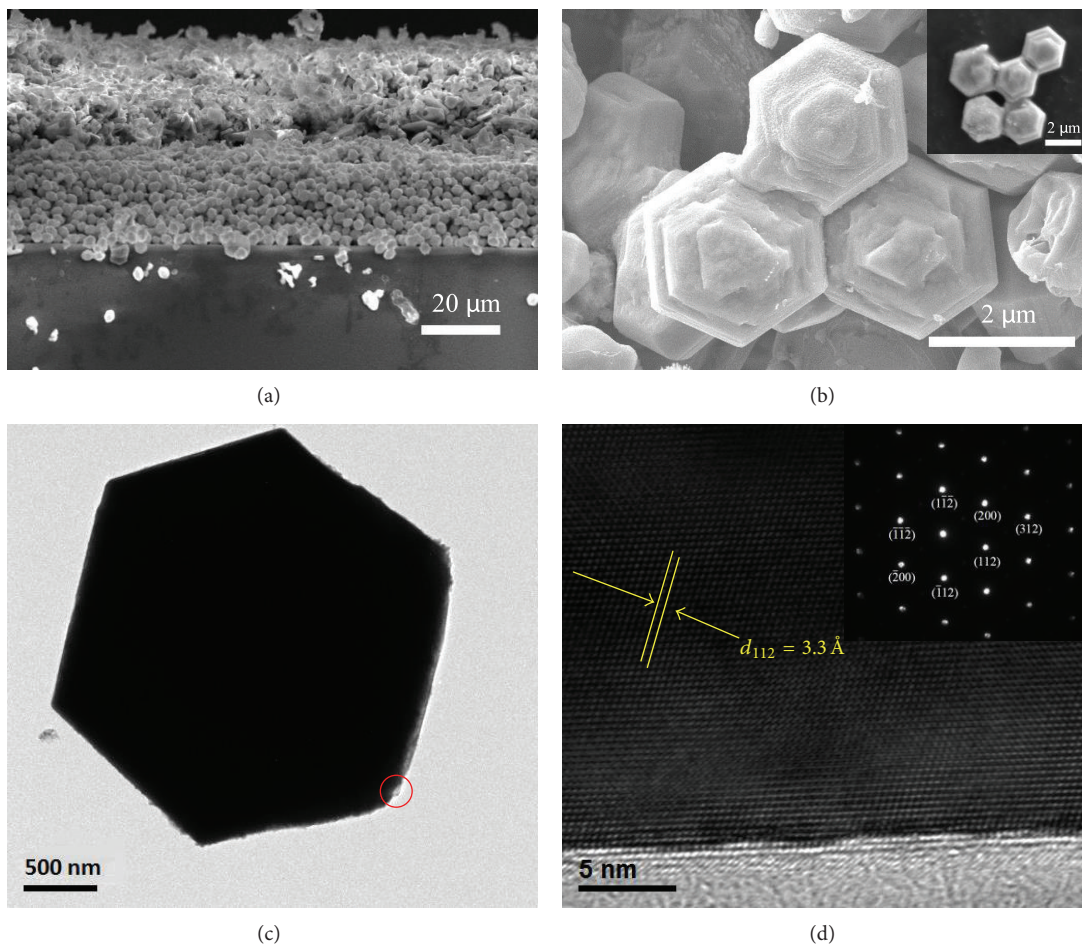


FIGURE 3: Various images of the as-prepared CIS thin film from path A: (a) cross-sectioned SEM image for the as-synthesized CIS before annealing and (b) that after annealing, (c) LR-TEM, and (d) HR-TEM and SAED (the insert) images for the as-prepared CIS.

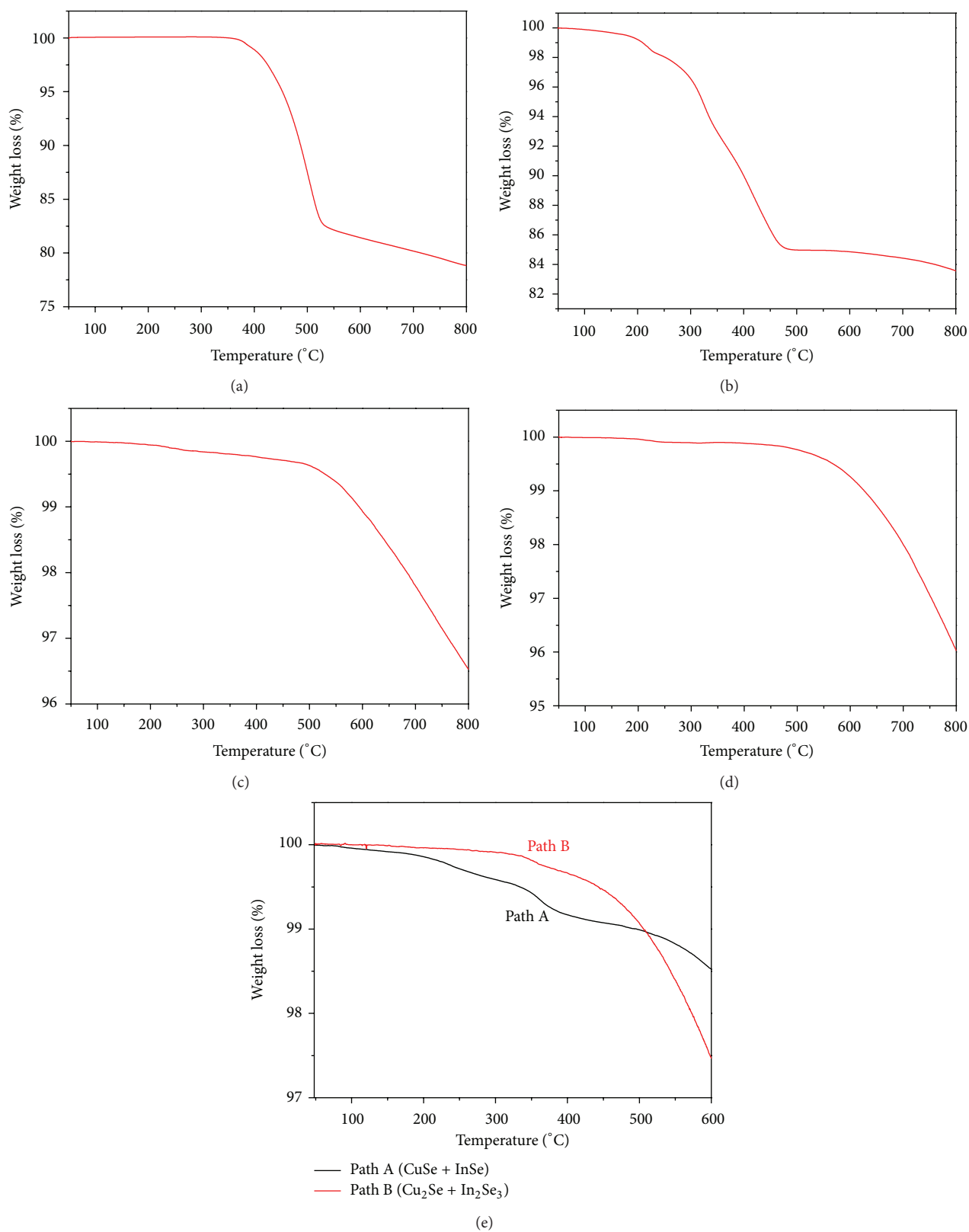


FIGURE 4: TGA curves of (a) CuSe, (b) InSe, (c) Cu₂Se, (d) In₂Se₃, and (e) CIS particles prepared by the reaction path A or B via solid state reaction.

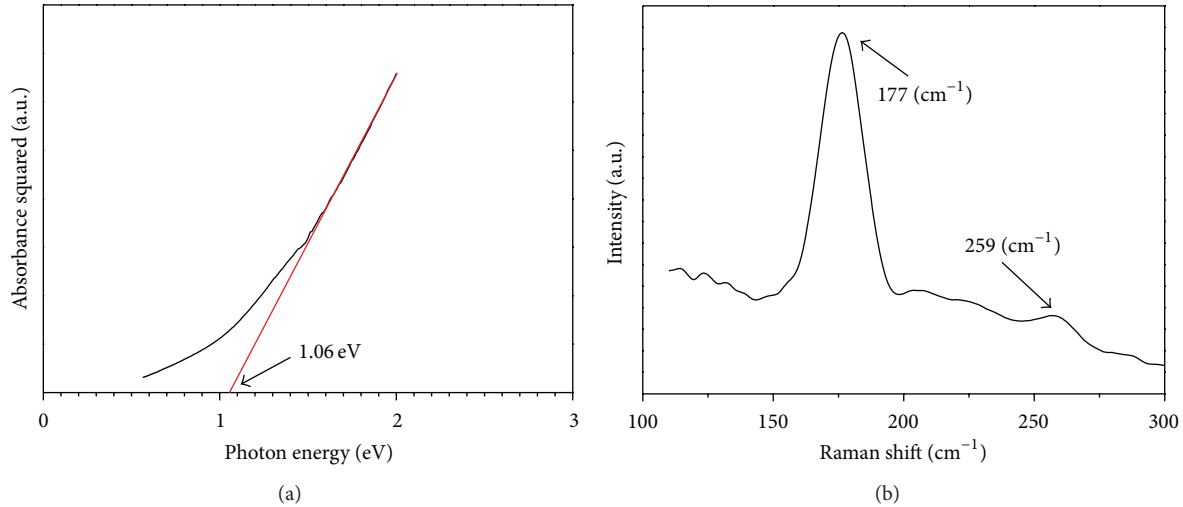


FIGURE 5: The (a) UV-vis absorption spectrum and (b) Raman spectrum of CIS thin films synthesized from the reaction path A.

Hsiang et al. [15] investigated that the CIS crystalline reaction from Cu_2Se and In_2Se_3 was close to that from the Cu_2Se reactant particle, based on the TEM result. It indicates that the solid state reaction kinetics may be dominated by the In^{3+} ions diffusion. The same situation also occurred in the experiment of path A. From TEM images, the solid state reaction kinetics of path A was most probably dominated by the In^{3+} ions diffusion. On the other hand, the reaction kinetics using solid state reaction from CuSe and InSe precursors was lower than that from Cu_2Se and In_2Se_3 precursors [16, 17]. Figure 4 showed TGA curves of (a) CuSe , (b) InSe , (c) Cu_2Se , (d) In_2Se_3 , and (e) CIS particles prepared by the reaction path A or B via solid state reaction. The figures showed the total percentage of weight loss as the increasing temperatures till 800°C . According to Figures 4(a)–4(d), only InSe had 7% weight loss, whereas almost no weight loss measured till 350°C for CuSe , Cu_2Se , and In_2Se_3 was found. Figure 4(e) showed that the weight loss of path A was about 1.5% at 600°C . The result indicated that CIS particles prepared by solid state reaction exhibited good thermal stability. In addition, the weight loss of path B was about 0.1% at 350°C and about 2.5% at 600°C , which indicated that the path B might require higher reaction temperature to form CIS phase. As a result, the path B for synthesizing CIS phase was relatively difficult at 350°C , while the solid state reaction kinetics of path A was presumably dominated by In^{3+} ions diffusion [15].

Furthermore, Figure 5(a) showed the UV-vis absorption spectrum of CIS particles prepared by reaction path A. The sample was dispersed in absolute ethanol under intense sonication for 20 min, while ethanol was used as a reference. The band gap of CIS particles was calculated using the direct band gap method from its optical absorption spectrum [7]; the value was determined as 1.06 eV, which is consistent with the reported value of 1.04 eV for the bulk CIS [18]. Figure 5(b) showed Raman spectrum of CIS thin films synthesized from the reaction path A. The main peak at around 177 cm^{-1} could be identified as the A_1 vibrational mode from chalcopyrite ordered CIS. A relatively small peak at around 240 cm^{-1}

was related to the characteristic mode from the elemental Se [19, 20]; however, scarcely Se could not be found in the form of CIS thin film. The Cu and Se binary phase were difficult to be identified in the measured spectral range: the peak at 259 cm^{-1} was the most intense one observed on Raman spectrum of CuSe [21].

4. Conclusions

In this work, CIS thin film is successfully fabricated by using CuSe and InSe binary precursors via a low temperature solid state reaction. The XRD results indicate that CIS thin film has a chalcopyrite structure with good crystallinity, which exhibits (112) prefer orientation. Particularly, CIS thin film can be preferably obtained by path A with the reaction of $\text{CuSe} + \text{InSe} \rightarrow \text{CuInSe}_2$ at relatively low temperature (350°C) and short preparation time (3 h). Besides, the weight loss indicated by TGA pattern is only 1.5% at 600°C . The value of band gap for the as-prepared CIS is calculated to be 1.06 eV, which demonstrates that this material is suitable to be used for a thin film solar cell light absorption material. Its good absorption in the visible light region also suggests that such photovoltaic material is promising for sustainable energy related applications.

Acknowledgment

The authors thank the National Sciences Council of Taiwan for the financial support, Grant nos. NSC102-2113-M-024-001 and 101-2321-B-006-01.

References

- [1] G. Conibeer, M. Green, E.-C. Cho et al., "Silicon quantum dot nanostructures for tandem photovoltaic cells," *Thin Solid Films*, vol. 516, no. 20, pp. 6748–6756, 2008.
- [2] B. Levy, "Photochemistry of nanostructured materials for energy applications," *Journal of Electroceramics*, vol. 1, pp. 239–272, 1997.

- [3] D. Cahen, J.-M. Gilet, C. Schmitz, L. Chernyak, K. Gartsman, and A. Jakubowicz, "Room-temperature, electric field-induced creation of stable devices in CuInSe_2 crystals," *Science*, vol. 258, no. 5080, pp. 271–274, 1992.
- [4] I. Repins, M. A. Contreras, B. Egaas et al., "19.9%-efficient $\text{ZnO/CdS/CuInGaSe}_2$ solar cell with 81.2% fill factor," *Progress in Photovoltaics*, vol. 16, no. 3, pp. 235–239, 2008.
- [5] W. Liu, Y. Sun, W. Li, C.-J. Li, F.-Y. Li, and J.-G. Tian, "Influence of different precursor surface layers on $\text{Cu}(\text{In}_{1-x}\text{Ga}_x)\text{Se}_2$ thin film solar cells," *Applied Physics A*, vol. 88, no. 4, pp. 653–656, 2007.
- [6] F. Kurdesau, M. Kaelin, V. B. Zaleski, and V. I. Kovalevsky, "In situ resistivity measurements of Cu-In thin films during their selenization," *Journal of Alloys and Compounds*, vol. 378, no. 1–2, pp. 298–301, 2004.
- [7] Q. Guo, S. J. Kim, M. Kar et al., "Development of CuInSe_2 nanocrystal and nanoring inks for low-cost solar cells," *Nano Letters*, vol. 8, no. 9, pp. 2982–2987, 2008.
- [8] L. Kaupmees, M. Altosaar, O. Volubujeva, and E. Mellikov, "Study of composition reproducibility of electrochemically co-deposited CuInSe_2 films onto ITO," *Thin Solid Films*, vol. 515, no. 15, pp. 5891–5894, 2007.
- [9] F. Kang, J. Ao, G. Sun, Q. He, and Y. Sun, "Structure and photovoltaic characteristics of CuInSe_2 thin films prepared by pulse-reverse electrodeposition and selenization process," *Journal of Alloys and Compounds*, vol. 478, no. 1–2, pp. L25–L27, 2009.
- [10] S. L. Castro, S. G. Bailey, R. P. Raffaele, K. K. Banger, and A. F. Hepp, "Nanocrystalline chalcopyrite materials (CuInS_2 and CuInSe_2) via low-temperature pyrolysis of molecular single-source precursors," *Chemistry of Materials*, vol. 15, no. 16, pp. 3142–3147, 2003.
- [11] R. H. Bari, L. A. Patil, P. S. Sonawane, M. D. Mahanubhav, V. R. Patil, and P. K. Khanna, "Studies on chemically deposited CuInSe_2 thin films," *Materials Letters*, vol. 61, no. 10, pp. 2058–2061, 2007.
- [12] P. F. Luo, R. Z. Zuo, and L.T. Chen, "The preparation of CuInSe_2 films by combustion method and non-vacuum spin-coating process," *Solar Energy Materials and Solar Cells*, vol. 94, no. 6, pp. 1146–1151, 2010.
- [13] K. H. Park, K. Jang, S. Kim, J. K. Hae, and U. S. Seung, "Phase-controlled one-dimensional shape evolution of InSe nanocrystals," *Journal of the American Chemical Society*, vol. 128, no. 46, pp. 14780–14781, 2006.
- [14] P.-Y. Lin and Y.-S. Fu, "Fabrication of CuInSe_2 light absorption materials from binary precursors via wet chemical process," *Materials Letters*, vol. 75, pp. 65–67, 2012.
- [15] H.-I. Hsiang, L.-H. Lu, Y.-L. Chang, D. Ray, and F.-S. Yen, " CuInSe_2 nano-crystallite reaction kinetics using solid state reaction from Cu_2Se and In_2Se_3 powders," *Journal of Alloys and Compounds*, vol. 509, no. 24, pp. 6950–6954, 2011.
- [16] S. Kim, W. K. Kim, R. M. Kaczynski et al., "Reaction kinetics of CuInSe_2 thin films grown from bilayer InSe/CuSe precursors," *Journal of Vacuum Science and Technology A*, vol. 23, no. 2, pp. 310–315, 2005.
- [17] J. S. Park, Z. Dong, S. Kim, and J. H. Perepezko, " CuInSe_2 phase formation during $\text{Cu}_2\text{Se}/\text{In}_2\text{Se}_3$ interdiffusion reaction," *Journal of Applied Physics*, vol. 87, no. 8, pp. 3683–3690, 2000.
- [18] H. S. Soliman, M. M. El-Nahas, O. Jamjoum, and K. A. Mady, "Optical properties of CuInSe_2 thin films," *Journal of Materials Science*, vol. 23, no. 11, pp. 4071–4075, 1988.
- [19] V. V. Poborchii, A. V. Kolobov, and K. Tanaka, "An in situ Raman study of polarization-dependent photocrystallization in amorphous selenium films," *Applied Physics Letters*, vol. 72, no. 10, pp. 1167–1169, 1998.
- [20] P. Nagels, E. Sleetckx, R. Callaerts, and L. Tichy, "Structural and optical properties of amorphous selenium prepared by plasma-enhanced CVD," *Solid State Communications*, vol. 94, no. 1, pp. 49–52, 1995.
- [21] M. Ishii, K. Shibata, and H. Nozaki, "Anion distributions and phase transitions in $\text{CuS}_{1-x}\text{Se}_x$ ($x = 0 - 1$) studied by raman spectroscopy," *Journal of Solid State Chemistry*, vol. 105, no. 2, pp. 504–511, 1993.

Research Article

Preparation of Vertically Aligned ZnO/TiO₂ Core-Shell Composites for Dye-Sensitized Solar Cells

Lung-Chuan Chen, Shuei-Feng Tsai, Jean-Hong Chen, and Gaun-Wen Wang

Department of Materials Engineering, Kun-Shan University, Yung Kang, Tainan 710, Taiwan

Correspondence should be addressed to Lung-Chuan Chen; lcchen@mail.ksu.edu.tw

Received 13 September 2013; Accepted 6 October 2013

Academic Editor: Teen-Hang Meen

Copyright © 2013 Lung-Chuan Chen et al. This is an open access article distributed under the Creative Commons Attribution License, which permits unrestricted use, distribution, and reproduction in any medium, provided the original work is properly cited.

Vertically aligned ZnO/TiO₂ (VA-ZnO/TiO₂) core-shell composites deposited on ZnO-seeded indium tin oxide (ITO) glasses have been synthesized by a chemical bath deposition approach for growing one-dimensional ZnO structure followed by a spin procedure for coating TiO₂ on the surface of ZnO structure. The influences of the cycles of spin coating of TiO₂ (CSCT) on the properties of VA-ZnO/TiO₂ and performances of the assembled DSSCs were studied. The power conversion efficiency of the VA-ZnO/TiO₂-based DSSC measured under illumination of 100 mW/cm² and AM 1.5 can reach 0.81%, representing 93% improvement when compared with that of the pristine VA-ZnO electrode (0.42%). The intensity-modulated photocurrent spectroscopy (IMPS) and electrochemical impedance spectroscopy (EIS) were applied to study the kinetics and interfacial transfer of the photogenerated electrons. Both the photocurrent and power conversion efficiency correlate well with the steady state electron density. Enlargement in surface area and dye adsorption, suppression of dissolution of Zn²⁺, diminishment in electron recombination, and fast transfer of injected electrons from excited dyes to TiO₂ conduction bands arising from coating TiO₂ on VA-ZnO are regarded as the predominant causes for this improvement.

1. Introduction

Regarded as a promising alternative to conventional silicon-based solar cells, DSSCs have attracted worldwide attention in both academia and industry because of the inherent characteristics of low production cost, simple processing, less toxic manufacturing, and moderate energy conversion efficiency [1–5]. The common architecture of DSSCs consists of a dye-sensitized semiconductor film deposited on transparent conducting oxide (TCO) glass as a photoanode, the redox couples (usually I⁻/I₃⁻) in organic solvent as electrolyte, and a counter electrode usually made from platinum or carbon materials on TCO [2, 6]. Photoexcitation of the adsorbed-dyes generates photoelectrons, which are then transferred to the conduction bands of semiconductors where they infiltrate to the back contact, and then to the counter electrode through the external circuit. The oxidized dyes are regenerated by capturing electrons from the reducing ions in the electrolyte, accompanying the formation of oxidizing ions which are then reduced by the electrons donated from the counter electrode.

Inevitably, the property and morphology of the semiconductor films must substantially affect the performance of DSSCs.

Lin et al. [3] indicated that strategies to boost the photo-to-electricity conversion efficiency included the enhancement of electron transport within the semiconductor film and reduction of recombination between injected electrons and I₃⁻ ions in electrolytes. Up to now, TiO₂ nanoparticles with sizes of 10–20 nm have been widely employed as the materials for fabricating mesoporous photoanodes in DSSCs. Although this construction can feature with high dye loads and light harvesting as a result of high surface area, however, it may create a plenty of grain boundary, which in turn reduces the electron transport efficiency and increases the recombination probability [2, 7, 8]. Vertically aligned (VA) one-dimensional (1D) nanostructures such as nanotubes and nanorods have been considered to provide straight routes to facilitate electron transfer and suppress the recombination rate by reducing the grain boundaries and traveling length of photoelectrons before reaching the back contact [9–11].

The electron diffusion coefficient and electron mobility of ZnO film are reported to be $1.2 \times 10^{-4} \text{ cm}^2/\text{s}$ and $10^{-1}-10^{-3} \text{ cm}^2 \text{ V}^{-1} \text{ s}^{-1}$, which are both higher than those of $5 \times 10^{-5} \text{ cm}^2/\text{s}$ and $10^{-6}-10^{-4} \text{ cm}^2 \text{ V}^{-1} \text{ s}^{-1}$, respectively, of TiO_2 [12–18]. These characteristics imply that ZnO can be a potential candidate as the photoanode of DSSC in addition to TiO_2 semiconductor [3]. Although the pristine 1D structure of ZnO can raise the transport rate of electron, however, the DSSC's energy conversion efficiency is low when compared with nanoparticulate TiO_2 . For example, Jung et al. [19] reported a light-harvesting efficiency of 0.26% based on a ZnO nanowire photoanode by optimizing the synthesis parameters, and Gan et al. [20] revealed an overall power conversion efficiency of 0.79% by a ZnO nanowire/ TiO_2 nanoparticle photoanode prepared by the ultrasonic irradiation assisted dip-coating method.

Commercially available ruthenium polypyridine complexes dyes such as N3 and N719 have been widely used in the TiO_2 -based DSSCs and demonstrate superior performance than other dye molecules. However, these Ru-dyes are not suitable to be directly employed in the ZnO-based DSSCs because ZnO crystals may be destroyed by protons releases from dye molecules, causing the formation of $\text{Zn}^{2+}/\text{dye}$ complexes when they are soaked in an acidic solution containing Ru-dyes over an appropriate soaking time. Furthermore, the formed $\text{Zn}^{2+}/\text{dyes}$ complexes can agglomerate on the surface of ZnO to generate a thick covering layer instead of a monolayer, and is intrinsically inactive for electron injection [21–23]. Therefore, utilization of core-shell construction to coating a chemically-inert shell layer on ZnO core structure can efficiently avoid dissolution of ZnO crystals and enhance their performance of DSSCs.

Law et al. [24] prepared ZnO nanowires coated with thin shells of Al_2O_3 or TiO_2 by atomic layer deposition and indicated significant improved efficiencies in power conversion of the DSSCs based on the core-shell architectures. In this report, we presented a simpler spin coating method to obtain a shell layer of TiO_2 coated on VA-ZnO arrays, which then acted as photoanodes assembled in DSSCs in an attempt to improve photovoltaic performance by combining the advantages of high surface area and chemical inertness of TiO_2 and high electron transport rate of 1D ZnO nanostructures. The properties of the prepared VA-ZnO/ TiO_2 structures and their influences on the performance of the DSSCs were investigated.

2. Experimental

2.1. Preparation of VA-ZnO/ TiO_2 . A revised version of chemical bath deposition (CBD) established by Ku et al. [25, 26] and a spin coating procedure were employed to prepare VA-ZnO/ TiO_2 grown on indium tin oxide (ITO) ($7 \Omega \text{ sq}^{-1}$, 0.7 mm). The substrates were first deposited with a TiO_2 compact layer; then they were seeded with ZnO layers from a solution of 0.05 M zinc acetate and 0.05 M hexamethylenetetramine (HMTA) by a spin coating technique followed by thermal decomposition at 350°C for 30 min.

An aqueous solution containing 0.02 M zinc acetate and 0.02 M HMTA was applied to grow VA-ZnO structures on the ZnO-seeded ITO substrates by CBD at 95°C for 3 h. The as-prepared VA-ZnO structures were washed with deionized water and ethanol. The CBD procedure was repeated several cycles (1–5) to elucidate its impact on the properties of VA-ZnO/ TiO_2 . Finally, the prepared VA-ZnO samples were calcined at 400°C for 30 min [27].

For the synthesis of VA-ZnO/ TiO_2 core-shell structures, the TiO_2 shell layer was deposited on the surface of ZnO by spin coating a solution containing 0.05 M TTIP and 0.15 M HCl in isopropanol. The spin rate was controlled at 1000 rpm for 30 s. Such procedure was duplicated several times (1–6) to increase the TiO_2 load on VA-ZnO. The prepared VA-ZnO/ TiO_2 composites on ITO substrates were annealed in air at 450°C for 30 min to increase crystallization.

The prepared samples were denoted as ZaTb, where a and b represented the cycles of chemical bath deposition of ZnO (CCBDZ) and spin coating of TiO_2 (CSCT), respectively.

2.2. Characterization of the VA-ZnO/ TiO_2 Composites on ITO Substrates. Crystal phases of the prepared VA-ZnO/ TiO_2 samples were determined by an X-ray diffractometer (XRD) (Rigaku D/MAX 2500) using a grazing incident diffraction model. The morphology of the VA-ZnO/ TiO_2 on ITO substrates was decided by field emission scanning electron microscopy (FESEM, JEOL, JSM-6700F) equipped with an energy dispersive spectrometer (EDS) to quantitatively and qualitatively determine the elements of the prepared samples. The threshold wavelengths and photoabsorbance of the VA-ZnO/ TiO_2 samples were obtained using a UV-Vis spectrophotometer (Jasco, V-550). Photoluminescence (PL) spectra were measured on a spectrofluorophotometer (Jasco, V670) with exciting wavelength of 320 nm.

2.3. Device Fabrication and Measurements. After being heated at 80°C for 1 h, the prepared VA-ZnO/ TiO_2 electrodes were immersed into an 0.5 mM ruthenium (II) 535 bis-TBA (N-719, Solaronix) dye solution in ethanol for 24 h at room temperature under dark condition. The as-obtained dye-sensitized electrodes were rinsed with absolute ethanol and dried in a vacuum oven at 40°C . Afterwards, they were assembled with a Pt counter electrode using a 60 μm thick hot melt ring as the spacer (Surlyn, Solaronix) and sealed by heating to form a sandwich structure. The cell internal space was filled with a I_3^-/I^- liquid electrolyte comprised of 0.05 M I_2 , 0.5 M 4-tert-butylpyridine (TBP), and 0.1 M LiI in 3-methoxypropionitrile (MPN), through a predrilled hole using a vacuum pump.

The photoelectrochemical performances of DSSCs were measured using a source meter (Keithley 2400) and a 300 W xenon lamp (PerkinElmer, PS300BUV). The incident light intensity (AM 1.5 , $100 \text{ mW}/\text{cm}^2$) was calibrated using a power meter (Oriel, 70310) equipped with a photodiode detector (Newport 818UV). Electrochemical impedance spectra (EIS) were measured using an impedance analyzer (PGSTAT 302N, Autolab) equipped with an FRA2 module at an open-circuit potential under illumination intensity

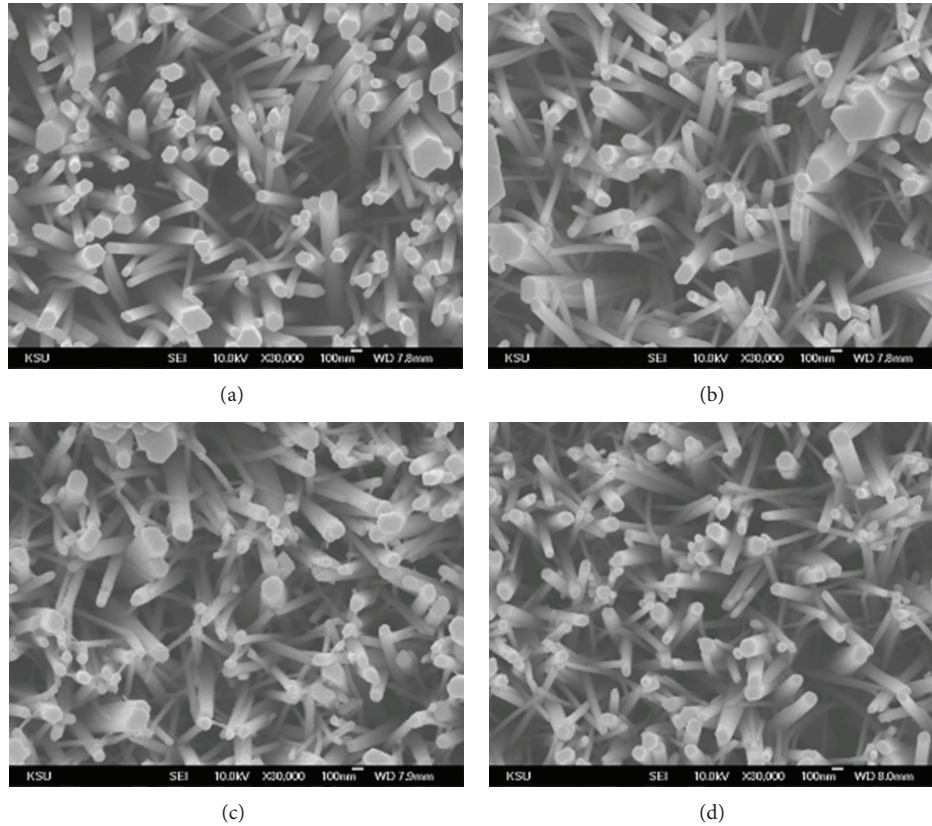


FIGURE 1: Top view FESEM images of (a) VA-ZnO and VA-TiO₂/ZnO samples with CSCTs of (b) 1, (c) 3, and (d) 5.

of 100 mW/cm². The AC amplitude was 10 mV and the frequency evaluated was in the range of 0.1 to 10⁵ Hz. The impedance spectroscopy was fitted with an equivalent circuit using Z-view software. Intensity-modulated photocurrent spectroscopy (IMPS) was operated under short-circuit status using the above-mentioned impedance analyzer with a light emitting diode (LED, 625 nm).

3. Results and Discussion

The morphologies of the prepared VA-ZnO and VA-ZnO/TiO₂ were observed by FESEM. Figure 1 displays the top view FESEM images of the VA-ZnO and VA-ZnO/TiO₂ structures. The results indicate that both ZnO and ZnO/TiO₂ composites grow in the vertically aligned direction forming array structure with hexagonal faces and diameters roughly ranging from 50 to 350 nm. The thickness of the TiO₂ layer cannot be significantly observed to increase with spin coating cycles of TiO₂, which seems to indicate that the TiO₂ layer is much thinner than ZnO nanorod. However, the surface of VA-ZnO is smoother than that of VA-ZnO/TiO₂ by the high resolution image (not shown here), which can be attributed to the adherence of TiO₂ on ZnO surface, supporting the formation of TiO₂ shell layer [27]. Figure 2 demonstrates cross-sectional FESEM image of the VA-ZnO and VA-ZnO/TiO₂ films, confirming one-dimensional array structures. The thickness of VA-ZnO and VA-ZnO/TiO₂ films

with spin coating cycles of 1, 3, and 5 are 7.2, 5.2, 5.1, and 5.5 μm, respectively. The shortness of the VA-ZnO length with initial coating TiO₂ can be accounted by the dissolution of ZnO by hydrogen chloride acid present in the TiO₂ sol. The TiO₂ coating layer on ZnO can avoid this dissolution with further TiO₂ deposition and slightly lengthen the film thickness. According to the energy dispersion spectroscopy (EDS) measurement, the Ti/Zn atomic ratio of the VA-ZnO/TiO₂ increases from 0.022 to 0.23 as the CSCT increases from 1 to 5. This result verifies the formation of TiO₂ on VA-ZnO, and its content increases with CSCT.

Figure 3 depicts the XRD patterns of the VA-ZnO and VA-ZnO/TiO₂ with CSCT under a grazing incident diffraction model. Obviously, the ITO substrate exhibits significant diffraction peaks at 30.4° (222), 35.3° (400), and 50.6° (440) (JCPDS #89-4598). In addition, XRD peaks at 2θ = 31.8° (100), 34.4° (002), 36.2° (101), 47.5° (102), and 56.5° (110) occurs, representing a wurtzite structure of ZnO (JCPDS #89-1397). The strongest peak of ZnO at 34.4° indicates that the (002) direction is the most preferential crystal plane for the aligned ZnO array to grow with good crystallinity along c-axis, which is perpendicular to the surface of the ITO substrate. On the other hand, the crystal peaks of TiO₂ are all absent after calcination at 450°C even when the CSCT increases to 6 (sample Z3T6). In general, calcination at 450°C can cause crystallization of TiO₂. Hence, it is some reasons, rather than calcination temperature, that give rise to this

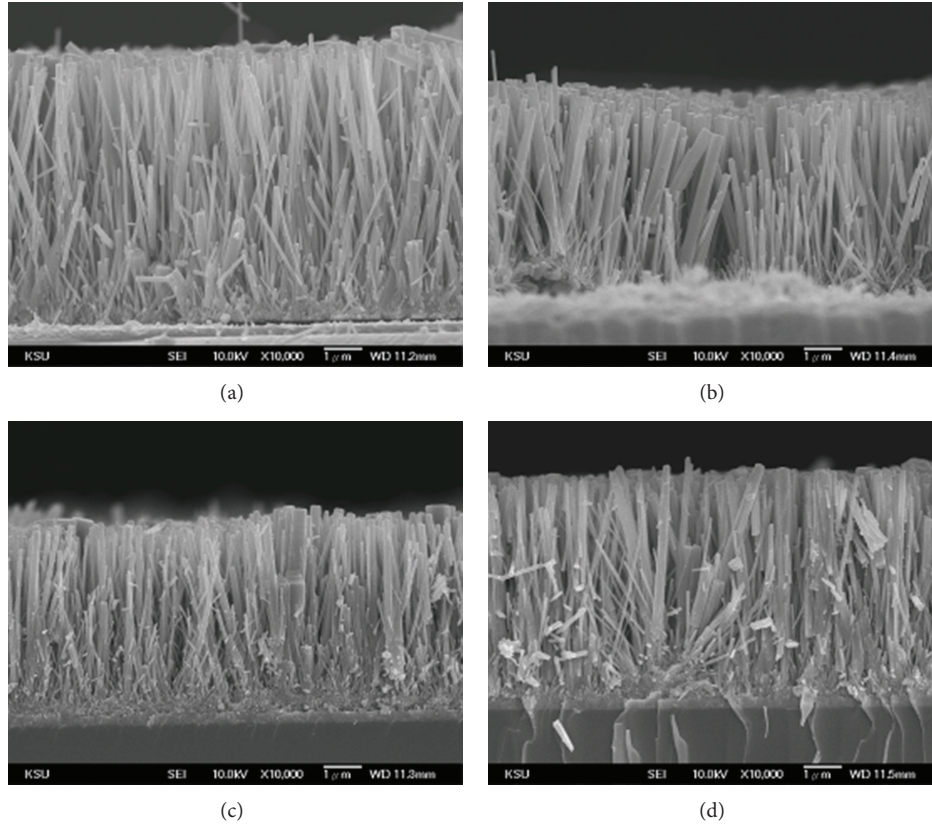


FIGURE 2: Cross-sectional FESEM images of (a) VA-ZnO and VA-TiO₂/ZnO samples with CSCTs of (b) 1, (c) 3, and (d) 5.

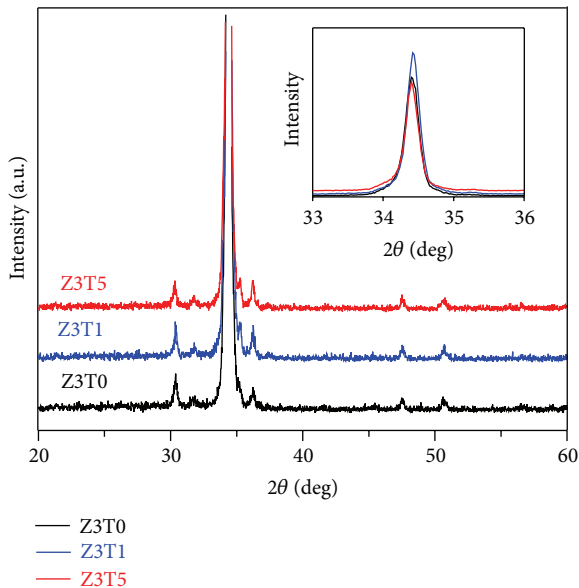


FIGURE 3: XRD patterns of VA-ZnO and VA-TiO₂/ZnO samples with CSCTs of 1 and 5.

result. Law et al. [24] mentioned that a TiO₂ shell film with thickness less than 5 nm appeared amorphous. Therefore, the thickness of the TiO₂ layer may be a cause for the XRD results.

Figure 4 represents the effect of CSCT on the optical absorption spectra of VA-ZnO/TiO₂ samples. In the visible light region, the optical absorption exhibits insignificant increase with the cycles of spin coating, which is probable due to the remained trace carbon species in the ZnO/TiO₂ samples after calcination at 450°C for 30 min. In the ultraviolet region, on the contrary, CSCT exerts distinct influence on the optical absorption intensity, which increases in order of Z3T6 < Z3T5 < Z3T4 < Z3T1 < Z3T0 < Z3T3 < Z3T2. Apparently, the changing tendency of photoabsorbance in the ultraviolet region does not coincide with CSCT; conversely, the moderate CSCT (Z3T2) provides the highest absorbance. This phenomenon is suspected to result from the competitive absorption of the UV light between TiO₂ and ZnO, and/or morphology variation with CSCT.

Figure 5 illustrates the photoluminescence spectra (PL) of the VA-ZnO/TiO₂ samples with CSCT. In general, PL is composed of two types of electron transitions. The one, originated from direct transition of electron from conduction band to valence band, is band PL, while the other one, resulted from the indirect transition of electron to the surface state, oxygen vacancy, or crystal defect state, and then to valence band, is excitonic PL [27–30]. Therefore, the band PL can be estimated as the band gap energy of semiconductor, and the excitonic PL can be used to evaluate the density of oxygen vacancy, surface state, crystal defects, and so forth. Figure 5 demonstrates that the predominant PL peaks of

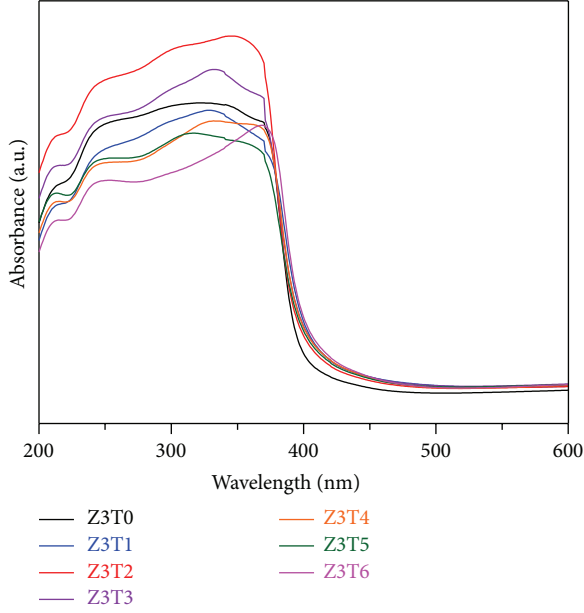


FIGURE 4: Optical absorbances of VA-ZnO and VA-TiO₂/ZnO samples with CSCTs of 1, 2, 3, 4, 5, and 6.

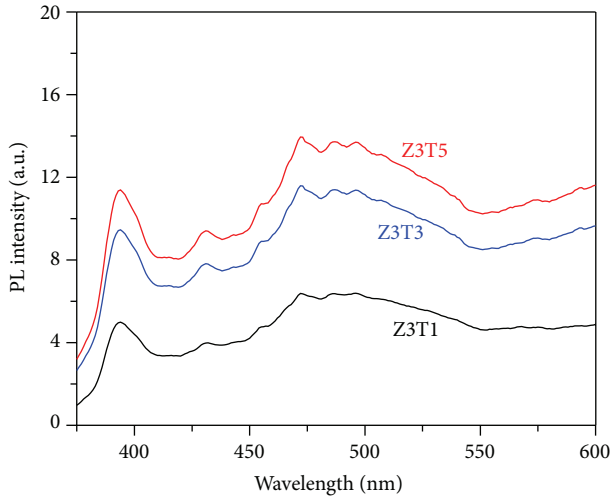


FIGURE 5: PL intensities of Z3T1, Z3T3, and Z3T5 samples with an incident irradiation of wavelength 320 nm.

the VA-ZnO/TiO₂ located at 394, 432, 454, 472, 486, and 496 nm. The peak at 395 nm is considered as the band PL, indicating a band gap energy of about 3.1 eV, which is consistent with the band gap energy of TiO₂ and/or ZnO [27]. In addition, the peak at 430 nm is likely due to the emission of free excitons near conduction band, while the PL peaks in the range of 470–550 nm are probably from the emission of bound excitons [27, 28]. It is inferred that increasing CSCT can increase the thickness of TiO₂ shell layer, and then increases the penetration length of electrons travelling to the ZnO core region, enhancing the probability of electron recombination, leading to the result that increasing CSCT increases both the band and excitonic PLs. In addition, the

TABLE 1: Photovoltaic parameters of the DSSCs based on VA-TiO₂/ZnO as photoanodes with CCBZ under illumination of 100 mW/cm² and AM 1.5.

Sample	CCBDZ	V_{OC} (V)	J_{SC} (mA/cm ²)	F.F.	η (%)
BIS4Z1T1	1	0.64	2.85	0.25	0.47
BIS4Z2T1	2	0.64	3.42	0.29	0.65
BIS4Z3T1	3	0.66	4.00	0.3	0.81

TABLE 2: Photovoltaic parameters of the DSSCs based on VA-TiO₂/ZnO samples with CSCT under illumination of 100 mW/cm² and AM 1.5.

Samples	V_{OC} (V)	J_{SC} (mA/cm ²)	F.F.	η (%)	R_2 (Ω)	W_1 (Ω)
Z3T0	0.61	2.46	0.27	0.42	401.7	19.2
Z3T1	0.66	4.00	0.3	0.81	303.4	22.8
Z3T3	0.64	3.06	0.29	0.58	360.4	35.2
Z3T5	0.62	2.53	0.27	0.43	369.4	42.7

amorphous structure and heterogeneous dispersion of TiO₂ over ZnO may also raise PL emission. These PL behaviors are similar to those that appeared in our previous report concerning the etched VA-TiO₂/ZnO [27].

The CCBZ can affect the property and length of VA-ZnO/TiO₂, which in turn makes a great impact on the DSSC's performance. Figure 6(a) shows the I - V curves of the DSSCs fabricated with various CCBZ under a constant CSCT of 1, and their photovoltaic parameters are summarized in Table 1. Both the short circuit current (J_{sc}) and fill factor (FF) increase from 2.85 to 4.0 mA/cm² and 0.25 to 0.30, respectively; in contrast, open circuit voltage (V_{oc}) varies little and is in the region of 0.64 V to 0.66 V, as the CCBZ increases from 1 to 3 (the corresponding length of VA-ZnO increased from 3.1 to 7.2 μ m). The power conversion efficiency (PCE) exhibits an enhancement from 0.47 to 0.81% as the CCBZ increased from 1 to 3, primarily due to the increment in J_{sc} and secondarily from the FF. The J_{sc} enhancement arising from the increase of CCBZ is suspected to strongly depend on the increase of length and diameter and on the decrease of crystal defect of VA-ZnO structures, which allow a high dye-loading and facilitate the transport of injected electrons, respectively. These two factors are also expected to account for the alteration of FF. Figure 6(b) displays the onset potentials of the dark current with CCBZ. The dark current is indicative of the level of recombination between electrons in the semiconductor films and the oxidized I₃⁻ ions in electrolyte. A higher onset potential usually correlates to a lower dark current and a higher efficiency. In this study, the onset potential of the dark current decreases in order of Z3T1 > Z2T1 > Z1T1, which is consistent with the photovoltaic efficiency.

Figure 7 depicts the characteristic of photocurrent versus voltage of DSSCs made with different CSCT, and Table 2 summaries the corresponding photovoltaic parameters. It can be seen that J_{sc} , V_{oc} , FF, and PCE increase firstly as CSCT increases from 0 to 1 and then decrease as CSCT further increases. The sample Z3T0 (i.e., without coating TiO₂) demonstrates the least activity, while the sample with

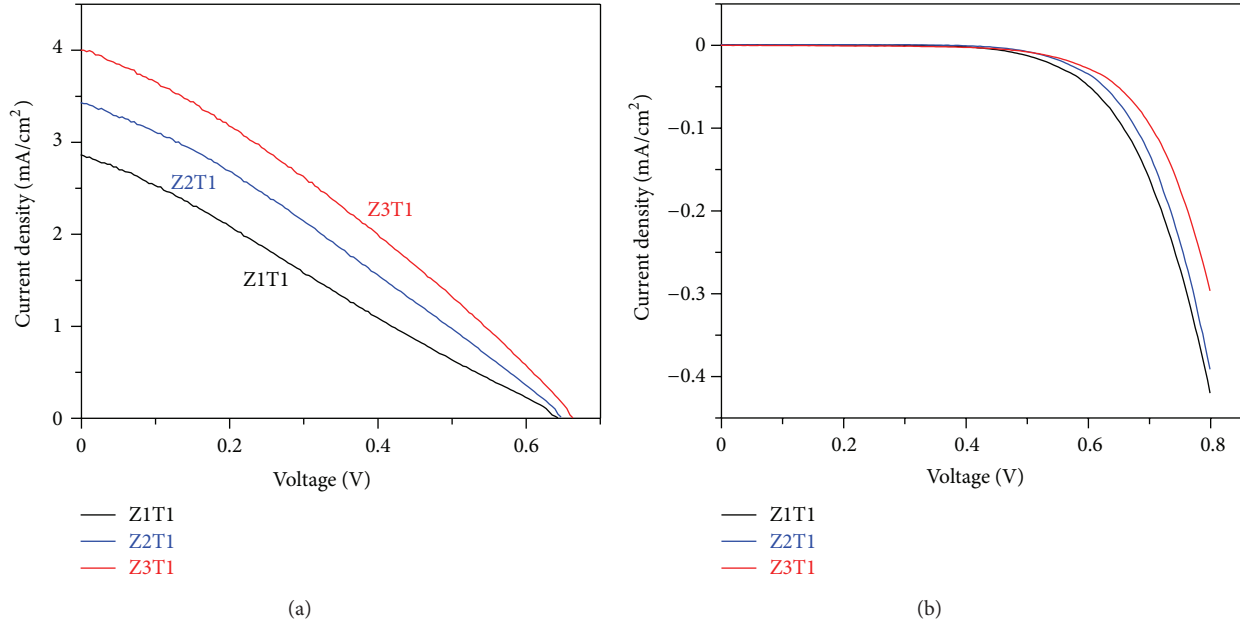


FIGURE 6: Influences of CCBDZ on the current-voltage characteristics of VA-TiO₂/ZnO (a) under illumination of 100 mW/cm² (AM 1.5) and (b) in the dark.

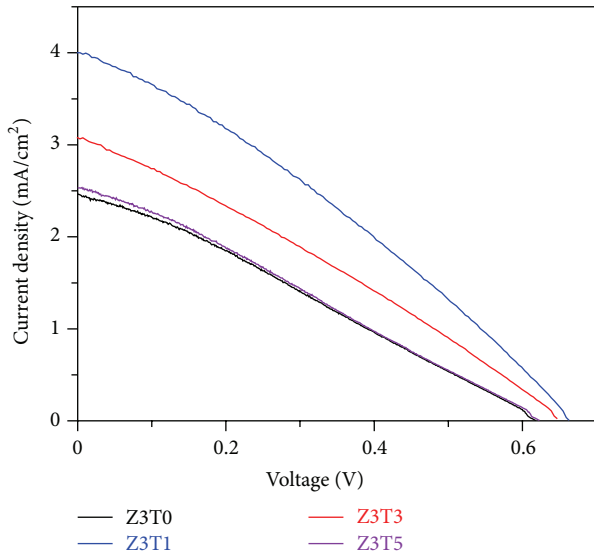


FIGURE 7: The current-voltage characteristics of DSSCs based on VA-TiO₂/ZnO samples with various CSCTs as photoanodes under illumination of 100 mW/cm² (AM 1.5).

CSCST of 1 explores the highest efficiency. Coating TiO₂ onto ZnO can create high surface area and inhibit the dissolution of ZnO, which then suppress the formation of Zn²⁺/dye complex. In addition, a faster electron-injection efficiency can be expected for the TiO₂-coated ZnO nanorods when compared with bared ZnO nanorods, because the ZnO conduction bands are largely composed of empty s and p orbitals from Zn²⁺, while those of TiO₂ consist predominantly of empty 3d orbitals of Ti⁴⁺ [22, 31]. These factors are suggested

to be responsible for the increase in efficiency with coating TiO₂ layer on ZnO. The results also indicate that all the V_{oc} , J_{sc} , and FF decrease with further increasing the coating of TiO₂ over 1 layer, and thereby causing the decrease of PCE. Upon increasing the coating layer of TiO₂, the thickness of the shell layer became excessively thick, which raises the resistance to transfer injected electrons from the shell layer of TiO₂ to core region of ZnO nanorods because both the electron mobility and diffusivity within TiO₂ are much lower than those of ZnO. The insignificant crystalline characteristic of the coated TiO₂, as indicated by XRD, may develop a high recombination probability of the injected electrons during transportation within the TiO₂ layer. As indicated by PL measurement, increasing CSCST can promote electron quenching within the semiconductor film, which is also an important reason for the decrease of PCE with increasing CSCST. In addition, TiO₂ features a lower conduction band energy (-4.2 eV versus vacuum) than ZnO (-4.0 eV versus vacuum) [22], which is considered to reduce the efficiency for the injected electrons transferred from TiO₂ to ZnO. It is also possible that TiO₂ may agglomerate on the surface or within the interstitial space due to incomplete dispersion of TiO₂ precursor by a spin method, which reduces the PCE by hampering transport of electrolyte.

Electrochemical impedance spectra (EIS) can be adopted to investigate the electron kinetics in DSSCs. Usually three semicircles can be observed as the frequency starts from 100 k to 0.01 Hz. The high-frequency semicircle (1 k–100 k Hz) is related to the capacitance (CPE1) and charge transfer resistance (R_1) between counter electrode and electrolyte, while the low-frequency semicircle (in the mHz range) corresponded to the Warburg diffusion of electrolyte (W_1). The impedance in the middle frequency region is associated

TABLE 3: The parameters of electron kinetics of DSSCs based on the VA-ZnO/TiO₂ samples as photoanodes.

Samples	τ_T (ms)	τ_R (ms)	D (cm ² /s)	L (μ M)	n_s (cm ⁻³)
Z3T0	0.179	118.3	1.23×10^{-3}	120.6	6.6×10^{16}
Z3T1	0.179	118.3	6.41×10^{-4}	87.1	1.2×10^{17}
Z3T3	0.225	100.9	4.92×10^{-4}	70.5	8.8×10^{16}
Z3T5	0.282	86.2	4.57×10^{-4}	62.7	6.8×10^{16}

with the capacitance (CPE2) and interfacial charge transfer resistance (R_2) between TiO₂/dyes and electrolyte. Figure 8 provides the impedance spectra of the DSSCs with Z3T0, Z3T1, Z3T3, and Z3T5. The corresponding R_2 and W_1 values by fitting the impedance spectra based on the equivalent circuit shown in the inset of Figure 8 are listed in Table 3. The interfacial charge transfer resistance (R_2) increases in the order of Z3T1 < Z3T3 < Z3T5 < Z3T0. This result is in good agreement with the changing trends of PCE and the amount of dye loading as shown in Figure 9, which is demonstrated by the optical absorbance with wavelength by dissolving out the adsorbed dye molecules from the photoanode in 10 mL NaOH. The probable reason is that low dye loading on the VA-ZnO/TiO₂ may generate low electron density and interfacial charge transfer rate, causing a high R_2 value. With appropriate coating of TiO₂ on ZnO, the amount of adsorbed dye increases and significantly reduced the R_2 value. In contrast, coating TiO₂ over 3 times increased the R_2 values. This fact may be partly attributed to the penetration limitation of dye molecules due to the blocking effect induced by the coated TiO₂. The EIS results also indicate that increasing TiO₂ coating cycles increases the Warburg diffusion resistance (W_1) which reflects that over coating and/or improperly dispersion of TiO₂ may block the penetration channels of electrolytes.

Intensity-modulated photocurrent spectroscopy (IMPS) was used to calculate the charge-transport time (τ_T) according to the formula of $\tau_T = 1/(2\pi f_{\text{IMPS}})$, where the f_{IMPS} represent the frequency of the minimum current of the imaginary part of IMPS [32–34]. Figure 10 provides the IMPS of the DSSCs based on ZnO/TiO₂ photoanodes. The electron diffusion coefficient (D) can be obtained from the expression of $\chi^2/2.35\tau_T$, with χ indicating the film thickness. The electron recombination lifetime (τ_R) can be estimated from the reciprocal of the peak frequency of the central semicircle in the Nyquist plot of the EIS spectroscopy [35]. Following these parameters, the electron diffusion length (L) can be determined by the expression of $(D\chi)^{1/2}$. Furthermore, the steady state electron density (n_s) in the conduction band of VA-ZnO/TiO₂ can be calculated by the term of $k_B T \tau_R / (q^2 A R_2 \chi)$, where k_B , T , q , and A are the Boltzmann constant, absolute temperature, elementary charge, and surface area of the anode film [35]. Table 3 summarizes the parameters of τ_T , τ_R , D , L , and n_s for Z3T0, Z3T1, Z3T3, and Z3T5. The dependence of τ_T on CSCT can be expressed as Z3T0 = Z3T1 < Z3T3 < Z3T5, while the relation of τ_R can be noted as Z3T0 = Z3T1 > Z3T3 > Z3T5. The samples of Z3T0 and Z3T1 exhibit the smallest and largest τ_T

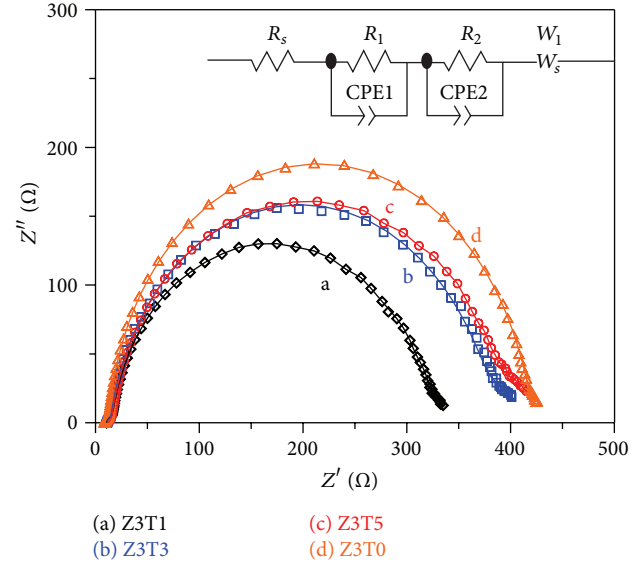


FIGURE 8: Nyquist plots of DSSCs based on Z3T0, Z3T1, Z3T3, and Z3T5 samples as the photoanodes under illumination of 100 mW/cm² (AM 1.5) and AC amplitude of 10 mV. The data points are from experiments, and the solid lines are the fitting results according to the equivalent circuit shown in the inset.

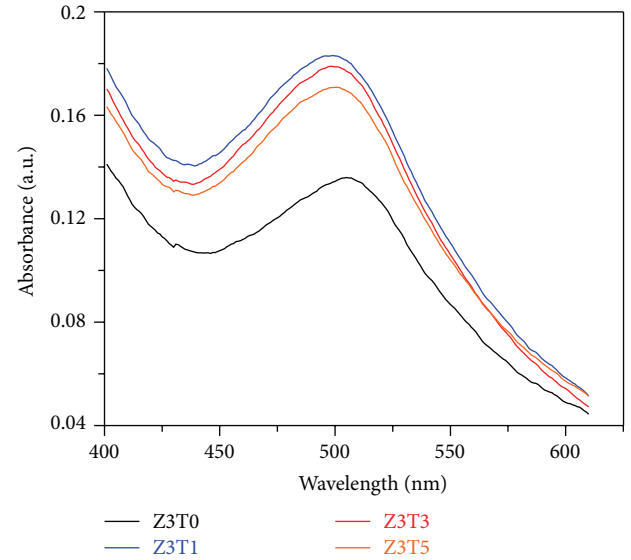


FIGURE 9: Optical absorbances of the dissolved-out dyes of the Z3T0, Z3T1, Z3T3, and Z3T5 samples in 10 mL NaOH solution (0.1 M).

and τ_R . Increasing spin coating cycles of TiO₂ increases τ_T , and decreases τ_R , electron diffusion coefficient, and electron diffusion length, which can be originated from the fact that ZnO possesses higher electron diffusion coefficient and electron mobility than that of TiO₂. In addition, coating TiO₂ shell layers over ZnO nanorods would increase the lateral diffusion of electrons and then increase the transport time and recombination probability of electron captured by redox species in electrolyte, causing a short recombination lifetime. Furthermore, ZnO nanostructures feature less population of

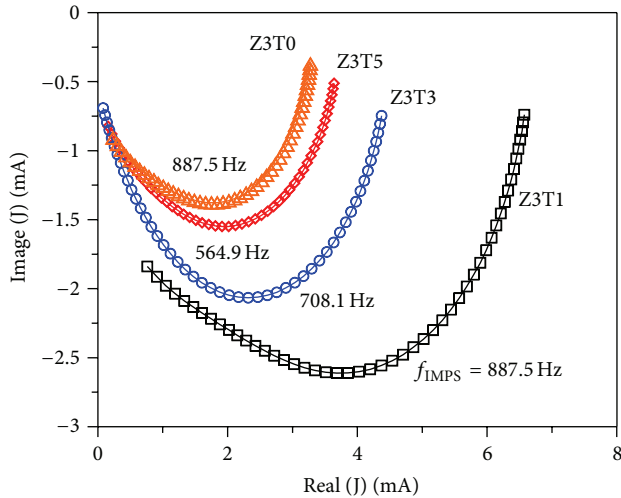


FIGURE 10: Intensity-modulated photocurrent spectroscopy (IMPS) of the DSSCs based on the Z3T0, Z3T1, Z3T3, and Z3T5 as the photoanodes.

deep traps and are then expected to possess a longer electron lifetime when compared with TiO_2 [23]. The results also exhibit that the changing tendency of n_s with CSCT is similar to that of the amount of adsorbed dye on VA-ZnO/ TiO_2 . Enhancing n_s is likely to reduce both the interfacial charge resistance (R_2) and transport resistance of electrons within the photoanode films, which coincides with the results of EIS and IMPS. Similar results have also been reported previously [35]. Overall, the obtained n_s in this work is significantly lower than the averaged one reported in the literature for the DSSCs with TiO_2 nanoparticle-based anodes [35, 36]. It indicates that increasing the surface area of VA-ZnO/ TiO_2 with appropriate pore structure is crucial to further raise the power conversion efficiency.

4. Conclusions

VA-ZnO/ TiO_2 core-shell structure can be successfully deposited on ITO glasses acting as photoanodes in DDSCs by a chemical bath deposition for growing ZnO and a spin method for coating TiO_2 in sequence. Increasing CCBDZ can increase the length of 1D ZnO on ITO substrates, and thereby increase the energy conversion efficiency. The Ti/Zn atomic ratio of VA-ZnO/ TiO_2 raises with increasing CSCT, however, XRD results indicate that TiO_2 on VA-ZnO appears as amorphous. Increasing CSCT over 1 can extend PL intensity and then boosts the electron recombination rate, causing reduced energy conversion efficiency. Coating 1 layer of TiO_2 on VA-ZnO can significantly enhance the energy conversion efficiency, mainly due to the suppression of dissolution of ZnO, the enlargement of surface area, and fast transfer of injected electrons from excited dye to TiO_2 conduction band. However, the energy conversion efficiency gradually decreases with increasing CSCT over 1. The Z3T1 and Z3T0 samples exhibit the less interfacial charge transfer resistance between TiO_2 /dyes and electrolyte, and the smaller transport time than the other samples.

The changing tendency of power conversion efficiency is similar to that of the steady state electron density in the conduction band.

Acknowledgment

This work was financially supported by the National Science Council of Taiwan, Taiwan, under Grant nos. of NSC 100-2221-E-168-037 and NSC 100-2632-E-168-001-MY3.

References

- [1] P. Charoensirithavorn, Y. Ogomi, T. Sagawa, S. Hayase, and S. Yoshikawa, "Improvement of dye-sensitized solar cell through TiCl_4 -Treated TiO_2 nanotube arrays," *Journal of the Electrochemical Society*, vol. 157, no. 3, pp. B354–B356, 2010.
- [2] J. Chae and M. Kang, "Cubic titanium dioxide photoanode for dye-sensitized solar cells," *Journal of Power Sources*, vol. 196, no. 8, pp. 4143–4151, 2011.
- [3] L.-Y. Lin, M.-H. Yeh, C.-P. Lee, C.-Y. Chou, R. Vittal, and K.-C. Ho, "Enhanced performance of a flexible dye-sensitized solar cell with a composite semiconductor film of ZnO nanorods and ZnO nanoparticles," *Electrochimica Acta*, vol. 62, pp. 341–347, 2012.
- [4] L.-L. Li, C.-W. Chang, H.-H. Wu, J.-W. Shiu, P.-T. Wu, and E. Wei-Guang Diao, "Morphological control of platinum nanostructures for highly efficient dye-sensitized solar cells," *Journal of Materials Chemistry*, vol. 22, no. 13, pp. 6267–6273, 2012.
- [5] M. Giannouli, "Nanostructured ZnO, TiO_2 , and composite ZnO/ TiO_2 films for application in dye-sensitized solar cells," *International Journal of Photoenergy*, vol. 2013, Article ID 612095, 8 pages, 2013.
- [6] D. Zhao, T. Peng, L. Lu, P. Cai, P. Jiang, and Z. Bian, "Effect of annealing temperature on the photoelectrochemical properties of dye-sensitized solar cells made with mesoporous TiO_2 nanoparticles," *Journal of Physical Chemistry C*, vol. 112, no. 22, pp. 8486–8494, 2008.
- [7] J. T. Park, R. Patel, H. Jeon, D. J. Kim, J.-S. Shin, and J. Hak Kim, "Facile fabrication of vertically aligned TiO_2 nanorods with high density and rutile/anatase phases on transparent conducting glasses: high efficiency dye-sensitized solar cells," *Journal of Materials Chemistry*, vol. 22, no. 13, pp. 6131–6138, 2012.
- [8] J. Dewalque, R. Cloots, F. Mathis, O. Dubreuil, N. Krins, and C. Henrist, " TiO_2 multilayer thick films (up to 4 μm) with ordered mesoporosity: influence of template on the film mesostructure and use as high efficiency photoelectrode in DSSCs," *Journal of Materials Chemistry*, vol. 21, no. 20, pp. 7356–7363, 2011.
- [9] K. Lee, D. Kim, and P. Schmuki, "Highly self-ordered nanochannel TiO_2 structures by anodization in a hot glycerol electrolyte," *Chemical Communications*, vol. 47, no. 20, pp. 5789–5791, 2011.
- [10] X. Feng, K. Shankar, O. K. Varghese, M. Paulose, T. J. Latempa, and C. A. Grimes, "Vertically aligned single crystal TiO_2 nanowire arrays grown directly on transparent conducting oxide coated glass: synthesis details and applications," *Nano Letters*, vol. 8, no. 11, pp. 3781–3786, 2008.
- [11] W.-Y. Kim, S.-W. Kim, D.-H. Yoo, E. J. Kim, and S. H. Hahn, "Annealing effect of ZnO seed layer on enhancing photocatalytic activity of ZnO/ TiO_2 nanostructure," *International Journal of Photoenergy*, vol. 2013, Article ID 130541, 7 pages, 2013.

- [12] J. Chung, J. Lee, and S. Lim, "Annealing effects of ZnO nanorods on dye-sensitized solar cell efficiency," *Physica B: Condensed Matter*, vol. 405, no. 11, pp. 2593–2598, 2010.
- [13] L. Dloczik, O. Ileperuma, I. Lauermaann et al., "Dynamic response of dye-sensitized nanocrystalline solar cells: characterization by intensity-modulated photocurrent spectroscopy," *Journal of Physical Chemistry B*, vol. 101, no. 49, pp. 10281–10289, 1997.
- [14] N. Kopidakis, K. D. Benkstein, J. Van De Lagemaat, A. J. Frank, Q. Yuan, and E. A. Schiff, "Temperature dependence of the electron diffusion coefficient in electrolyte-filled TiO₂ nanoparticle films: evidence against multiple trapping in exponential conduction-band tails," *Physical Review B*, vol. 73, no. 4, Article ID 045326, 2006.
- [15] M. Quintana, T. Edvinsson, A. Hagfeldt, and G. Boschloo, "Comparison of dye-sensitized ZnO and TiO₂ solar cells: studies of charge transport and carrier lifetime," *Journal of Physical Chemistry C*, vol. 111, no. 2, pp. 1035–1041, 2007.
- [16] E. M. Kaidashev, M. Lorenz, H. Von Wenckstern et al., "High electron mobility of epitaxial ZnO thin films on c-plane sapphire grown by multistep pulsed-laser deposition," *Applied Physics Letters*, vol. 82, no. 22, pp. 3901–3903, 2003.
- [17] M. Law, L. E. Greene, J. C. Johnson, R. Saykally, and P. Yang, "Nanowire dye-sensitized solar cells," *Nature Materials*, vol. 4, no. 6, pp. 455–459, 2005.
- [18] L.-T. Yan, F.-L. Wu, L. Peng et al., "Photoanode of dye-sensitized solar cells based on a ZnO/TiO₂ composite film," *International Journal of Photoenergy*, vol. 2012, Article ID 613969, 4 pages, 2012.
- [19] J. Jung, J. Myoung, and S. Lim, "Effects of ZnO nanowire synthesis parameters on the photovoltaic performance of dye-sensitized solar cells," *Thin Solid Films*, vol. 520, no. 17, pp. 5779–5789, 2012.
- [20] X. Gan, X. Li, X. Gao, F. Zhuge, and W. Yu, "ZnO nanowire/TiO₂ nanoparticle photoanodes prepared by the ultrasonic irradiation assisted dip-coating method," *Thin Solid Films*, vol. 518, no. 17, pp. 4809–4812, 2010.
- [21] Q. Zhang, C. S. Dandeneau, X. Zhou, and C. Cao, "ZnO nanostructures for dye-sensitized solar cells," *Advanced Materials*, vol. 21, no. 41, pp. 4087–4108, 2009.
- [22] H. Horiuchi, R. Katoh, K. Hara et al., "Electron injection efficiency from excited N3 into nanocrystalline ZnO films: effect of (N3-Zn²⁺) aggregate formation," *Journal of Physical Chemistry B*, vol. 107, no. 11, pp. 2570–2574, 2003.
- [23] M. M. Rahman, N. C. D. Nath, K.-M. Noh, J. Kim, and J.-J. Lee, "A facile synthesis of granular ZnO nanostructures for dye-sensitized solar cells," *International Journal of Photoenergy*, vol. 2013, Article ID 563170, 6 pages, 2013.
- [24] M. Law, L. E. Greene, A. Radenovic, T. Kuykendall, J. Liphardt, and P. Yang, "ZnO-Al₂O₃ and ZnO-TiO₂ core-shell nanowire dye-sensitized solar cells," *Journal of Physical Chemistry B*, vol. 110, no. 45, pp. 22652–22663, 2006.
- [25] C.-H. Ku and J.-J. Wu, "Chemical bath deposition of ZnO nanowire-nanoparticle composite electrodes for use in dye-sensitized solar cells," *Nanotechnology*, vol. 18, no. 50, Article ID 505706, 2007.
- [26] C.-H. Ku, H.-H. Yang, G.-R. Chen, and J.-J. Wu, "Wet-chemical route to ZnO nanowire-layered basic zinc acetate/ZnO nanoparticle composite film," *Crystal Growth and Design*, vol. 8, no. 1, pp. 283–290, 2008.
- [27] L. C. Chen, J.-H. Chen, S.-F. Tsai, and G. W. Wang, "Effect of ZnO seed layer and TiO₂ coating treatments on aligned TiO₂/ZnO nanostructures for dye-sensitized solar cells," *Integrated Ferroelectrics*, vol. 143, pp. 107–114, 2013.
- [28] M. Zhou, J. Yu, S. Liu, P. Zhai, and L. Jiang, "Effects of calcination temperatures on photocatalytic activity of SnO₂/TiO₂ composite films prepared by an EPD method," *Journal of Hazardous Materials*, vol. 154, no. 1–3, pp. 1141–1148, 2008.
- [29] J. Liqiang, Q. Yichun, W. Baiqi et al., "Review of photoluminescence performance of nano-sized semiconductor materials and its relationships with photocatalytic activity," *Solar Energy Materials and Solar Cells*, vol. 90, no. 12, pp. 1773–1787, 2006.
- [30] J.-G. Yu, H.-G. Yu, B. Cheng, X.-J. Zhao, J. C. Yu, and W.-K. Ho, "The effect of calcination temperature on the surface microstructure and photocatalytic activity of TiO₂ thin films prepared by liquid phase deposition," *Journal of Physical Chemistry B*, vol. 107, no. 50, pp. 13871–13879, 2003.
- [31] N. A. Anderson and T. Lian, "Ultrafast electron injection from metal polypyridyl complexes to metal-oxide nanocrystalline thin films," *Coordination Chemistry Reviews*, vol. 248, no. 13–14, pp. 1231–1246, 2004.
- [32] K. Zhu, N. R. Neale, A. Miedaner, and A. J. Frank, "Enhanced charge-collection efficiencies and light scattering in dye-sensitized solar cells using oriented TiO₂ nanotubes arrays," *Nano Letters*, vol. 7, no. 1, pp. 69–74, 2007.
- [33] Q. Wang, J.-E. Moser, and M. Grätzel, "Electrochemical impedance spectroscopic analysis of dye-sensitized solar cells," *Journal of Physical Chemistry B*, vol. 109, no. 31, pp. 14945–14953, 2005.
- [34] D. Hwang, D. Y. Kim, S.-Y. Jang, and D. Kim, "Superior photoelectrodes for solid-state dye-sensitized solar cells using amphiphilic TiO₂," *Journal of Materials Chemistry A*, vol. 1, no. 4, pp. 1228–1238, 2013.
- [35] M. Adachi, M. Sakamoto, J. Jiu, Y. Ogata, and S. Isoda, "Determination of parameters of electron transport in dye-sensitized solar cells using electrochemical impedance spectroscopy," *Journal of Physical Chemistry B*, vol. 110, no. 28, pp. 13872–13880, 2006.
- [36] Q. Zhang and G. Cao, "Nanostructured photoelectrodes for dye-sensitized solar cells," *Nano Today*, vol. 6, no. 1, pp. 91–109, 2011.

Research Article

Low Cost Amorphous Silicon Intrinsic Layer for Thin-Film Tandem Solar Cells

Ching-In Wu,¹ Shoou-Jinn Chang,¹ Kin-Tak Lam,² Shuguang Li,³ and Sheng-Po Chang¹

¹ Institute of Microelectronics & Department of Electrical Engineering, Advanced Optoelectronic Technology Center, Research Center for Energy Technology and Strategy, National Cheng Kung University, Tainan 70101, Taiwan

² College of Physics and Information Engineering, Fuzhou University, Fuzhou, Fujian 350108, China

³ College of Science, China University of Petroleum (East China), Qingdao, Shandong 266555, China

Correspondence should be addressed to Shoou-Jinn Chang; changsj@mail.ncku.edu.tw

Received 19 September 2013; Accepted 2 October 2013

Academic Editor: Teen-Hang Meen

Copyright © 2013 Ching-In Wu et al. This is an open access article distributed under the Creative Commons Attribution License, which permits unrestricted use, distribution, and reproduction in any medium, provided the original work is properly cited.

The authors propose a methodology to improve both the deposition rate and SiH₄ consumption during the deposition of the amorphous silicon intrinsic layer of the a-Si/ μ c-Si tandem solar cells prepared on Gen 5 glass substrate. It was found that the most important issue is to find out the saturation point of deposition rate which guarantees saturated utilization of the sourcing gas. It was also found that amorphous silicon intrinsic layers with the same k value will result in the same degradation of the fabricated modules. Furthermore, it was found that we could significantly reduce the production cost of the a-Si/ μ c-Si tandem solar cells prepared on Gen 5 glass substrate by fine-tuning the process parameters.

1. Introduction

In recent years, silicon-based thin-film solar cells have been studied extensively due to their potential benefits in low cost, high efficiency, and low pollution during production. It has been shown that these silicon-based thin-film solar cells are scalable for full-sized commercial production [1]. However, the fundamental challenge of silicon thin-film solar cells is light-induced degradation known as the Staebler-Wronski Effect (SWE) [2]. There are currently two major types of silicon thin-film solar cells in the market. One is the amorphous silicon (a-Si) only module, which could achieve an approximately 7% energy conversion efficiency with a degradation ratio of around 23%. The other is the amorphous silicon tandem microcrystalline silicon (a-Si/ μ c-Si) tandem device, which could achieve more than 10% energy conversion efficiency with a smaller degradation ratio of around 15%.

It is generally believed that increasing the ratio of hydrogen gas in the process of forming the intrinsic layers could improve the module stability. However, increasing hydrogen dilution ratio during the formation of the intrinsic layers suffers from two major drawbacks. First, hydrogen treatment

could easily compromise p-layer interface in front of the intrinsic layer. Second, increasing the hydrogen dilution ratio of the total process gas also means decreasing the ratio of SiH₄ used for forming the silicon film. This could result in a reduction in deposition rate. It has been reported previously that one can tune the distance of the electrodes to increase both the utilization of the depositing gas and the deposition rate [3]. However, it is necessary to adjust the hardware of the deposition system which depends strongly on the system used. It has also been reported that one can introduce triode to control the dissociation of reacting gas and the deposition rate [4]. However, adding one more electrode could increase the system cost and degrade the uniformity of the deposited layers. In this study, we propose a methodology to improve both the deposition rate and SiH₄ consumption during the deposition of the amorphous silicon intrinsic layer of the a-Si/ μ c-Si tandem solar cells prepared on Gen 5 glass substrate.

2. Experiments

In this work, amorphous silicon thin-film tandem solar cells with amorphous intrinsic layer prepared under different

TABLE 1: A more detailed comparison between samples with two different hydrogen dilution ratios (i.e., 3 and 1).

Intrinsic layer (FR = 20.8 slm, $P = 0.5$ mbar, Dilu = 2.5)	Dilu = 3	Dilu = 1
Depo. rate (A/sec)	2	3.35
k	0.619	0.618
Uniformity	9.95%	15.72%

conditions were fabricated on Gen 5 glass substrate. The silicon active layer and the transparent conductive oxide (TCO), ZnO:B, and electrodes with a large area (1300 mm \times 1100 mm) in tandem were fabricated by very high frequency plasma-enhanced chemical vapor deposition (PECVD) with an excitation frequency of 40.68 MHz and a low-pressure chemical vapor deposition (LPCVD) coater for anode and cathode, respectively. The current density-voltage (J - V) characteristics of the produced module were then measured under a pulsed solar simulator system (Berger system). The system includes a solar simulator device (PSS 8HS) under 500–1200 W/m² light intensity at 25°C and a load measuring device (PSL 8) with a power supply of 230 V-50 Hz, 1000 Watt or 110 V-60 Hz, and 1100 Watt. It should be noted that the J - V measurement system used in this study was designed for fully automated module production lines. In some cases, we study a silicon single film by depositing the silicon single film directly on the front glass by PECVD. The full-sized single film sample was then measured by a large-area ellipsometer (J. A. Woollam, AccuMap-SE VI-1500). Deposition rate, spatial uniformity, refraction index (n), and extinction coefficient (k) were determined by fitting the optical raw data with a suitable optical model Cody-Lorentz.

We adjusted four major process parameters when forming the amorphous silicon intrinsic layer. These parameters include (1) total flow rate, FR \equiv SiH₄ flow + hydrogen flow, (2) pressure, P , (3) process power, Pw, and (4) hydrogen dilution ratio, Dilu \equiv [H₂]/[SiH₄]. It is known that the total flow rate and pressure were mainly correlated with “radical residence time,” while the process power and the hydrogen dilution ratio were mainly correlated with the “dissociation rate of radical” [5]. The basic approach that we took could be summarized as follows: first, we find the onset point of saturation for deposition rate (limited by radical dissociation) at a fixed “radical residence time.” Second, we enhanced “residence time” to further raise the deposition rate.

After choosing potential fitting conditions, we used these specific parameters to form modules. To check the module stability, the fabricated modules were moved outdoors to soak in sunlight in Tainan, Taiwan. After soaking in enough sunlight according to the rules defined by the international electrotechnical commission (IEC) (>43 kw/hr) in one cycle, the modules were moved inside to measure their efficiencies. If the measured modules were unstable in efficiency as defined by IEC (<2% degradation within three cycles), they were moved outdoors again for the next sunlight soaking cycle. The cycles were repeated until the efficiency became stable. Each module was then moved inside and put in room temperature in the dark for at least one day to prevent outdoor environmental influences before module power was measured.

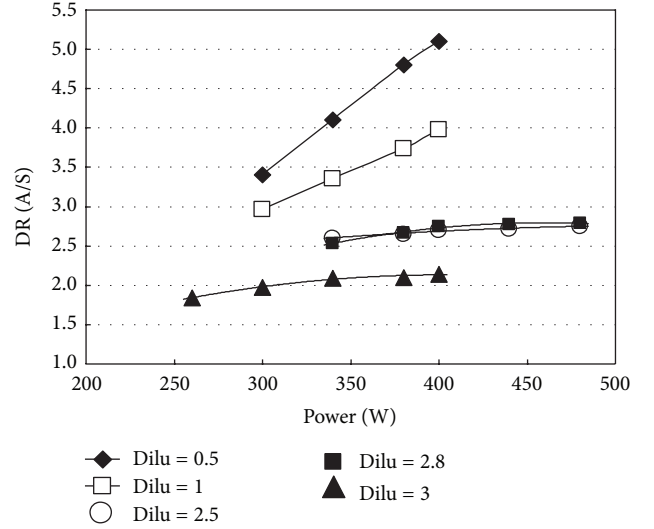


FIGURE 1: Deposition rate of the amorphous silicon intrinsic layer as a function of Dilu and Pw. FR and P are kept at 20.8 slm and 0.5 mbar, respectively.

3. Results and Discussion

An original sample was first prepared. For this sample, the amorphous silicon intrinsic layer was deposited using total flow rate FR = 20.8 slm, pressure $P = 0.5$ mbar, process power Pw = 340 Watt, and hydrogen dilution ratio, Dilu = 3. It was found that the deposition rate was 2 A/sec using these process parameters. We then studied deposition rate of the amorphous silicon intrinsic layer as a function of hydrogen dilution ratio, Dilu, and process power, Pw, while keeping the total flow rate, FR, and pressure, P , at 20.8 slm and 0.5 mbar, respectively. As shown in Figure 1, it can be seen that increasing the plasma power during deposition will lead to an increased deposition rate (DR). This should be attributed to the higher chance for SiH₄ gas to dissociate. However, it was also found that such an enhancement was significantly suppressed as we increased the hydrogen dilution ratio. Table 1 summaries these results. With 340 Watt plasma power, 0.5 mbar pressure, and 20.8 slm total flow rate, it was found that we could increase the deposition rate from 2 to 3.35 A/sec, as we decreased the hydrogen dilution ratio from 3 to 1. This suggests that we could easily achieve a >40% enhancement in deposition rate of the amorphous silicon intrinsic layer by decreasing the hydrogen dilution ratio.

Figure 2 shows outdoor soaking results of the fabricated modules with two different hydrogen dilution ratios (i.e., 3 and 1). It was found that lower hydrogen dilution ratio (Dilu = 1) could provide us a higher deposition rate of the amorphous

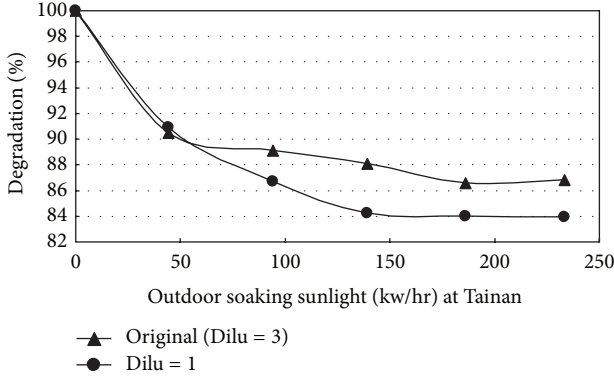


FIGURE 2: Outdoor soaking results of the fabricated modules with two different hydrogen dilution ratios (i.e., 3 and 1).

intrinsic layer. However, it was found from Figure 2 that the degradation ratio became higher, as compared to the original sample with Dilu = 3. Table 1 lists a more detailed comparison between these two samples. It can be seen that the dielectric constant, k , of the amorphous silicon intrinsic layer measured from these two samples was about the same. However, it was also found that thickness uniformity (i.e., 9.95%) was much better for the sample prepared with Dilu = 3, as compared to that prepared with Dilu = 1 (i.e., 15.72%). It is possible that the high degradation observed from the sample prepared with Dilu = 1 was directly related to the thickness nonuniformity.

It has been shown previously that controlling the dissociation of reacting gas (SiH_4 and H_2) is a key factor in achieving good stability of the amorphous silicon intrinsic layer [6, 7]. It has also been shown that we could tune the process parameters to achieve similar crystal size of microcrystalline silicon layer [8]. Thus, we also tried to tune different gas resident time by changing total flow rate, deposition pressure, and plasma power so as to achieve different hydrogen dilution ratios during the deposition of the amorphous silicon intrinsic layer. As we modify different parameters in the experiment, this formula always remains constant:

$$PV = NRT, \quad (1)$$

where P is the pressure in the chamber, V is the total chamber volume, N is the number of moles, R is the gas constant, and T is the absolute temperature of the gas. It should be noted that V , R , and T are constants for the same process chamber. In the experiment, we also kept the value of P as a constant. Since only SiH_4 and H_2 were introduced into the process chamber, we could derive the following formula:

$$P_{(\text{total})}V = P_{(\text{SiH}_4)}V + P_{(\text{H}_2)}V. \quad (2)$$

With P as a constant, we can simplify the formula to

$$P_{(\text{total})} = P_{(\text{SiH}_4)} + P_{(\text{H}_2)}. \quad (3)$$

By keeping $P_{(\text{total})}$ constant, the partial pressure of SiH_4 would have to decrease if we increase the hydrogen flow rate with a fixed flow rate of SiH_4 gas. In other words, the resident time of

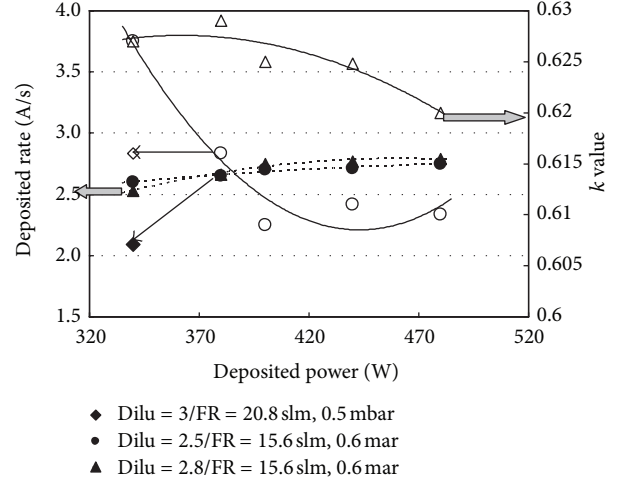


FIGURE 3: Deposition rate and k values as functions of deposition power under three different conditions.

SiH_4 has to decrease. The decreased partial pressure of SiH_4 should result in a lower deposition rate of the silicon film. This could be used to explain why the deposition rate is inversely correlated with the dilution ratio of the hydrogen gas. For better usage of source gas, we should decrease the total flow rate and increase the resident time of the source gas in the chamber while maintaining the same pressure and the same ratio for H_2 and SiH_4 .

To maximize the utilization of source gases, we should also optimize the deposition power. Figure 3 shows deposition rate and k values as functions of deposition power under three different conditions. It can be seen that the deposition rate increased rapidly, reached a saturation point, and then increased slowly. The much slower increase in deposition rate after saturation point should be attributed to the saturation of dissociation. The saturation point in deposition rate also suggests the best composition of the specific ratio of source gas at the same dilution ratio, total flow rate, and pressure. It should be noted that undesired SiH_4 polymer or dangling bond in intrinsic layer could occur easily in the unsaturated region. This could result in serious SWE and severe light-induced degradation. Other than choosing the proper process parameters, we also need to check the k value so as to know if the deposited amorphous silicon intrinsic layer exhibits the same absorption as that of the original sample. As shown in Figure 3, it can be seen that we could achieve a k value matching that of the original sample (i.e., $k = 0.618$) by choosing power = 380 W, FR = 15.6 slm, pressure = 0.6 mbar, and Dilu = 2.5. With this matched k value, we could use the deposited amorphous silicon intrinsic layer in our tandem module. As also shown in Figure 3, it was found that thickness uniformity of the sample prepared with these parameters was 11.12%, which was reasonably good.

Figure 4 shows outdoor soaking results of the fabricated modules with two kinds of amorphous silicon intrinsic layer after tuning (i.e., Dilu = 2.5 and Dilu = 3). These modules were used for the deep top-limited tandem device with the same 1600 nm thick $\mu\text{c-Si}$ device. For comparison, we only

TABLE 2: The results of modulates fabricated with these three kinds of amorphous silicon intrinsic layer.

Condition (FR, P , P_w , Dilu)	SiH_4 consumption	Tact time (s)	Initial module power (W)
20.8, 0.5, 380, 1	100.00%	835	138.85
15.6, 0.5, 380, 2.5	102.60%	1076	138.57
20.8, 0.5, 340, 3 (original)	182.00%	1400	138.75

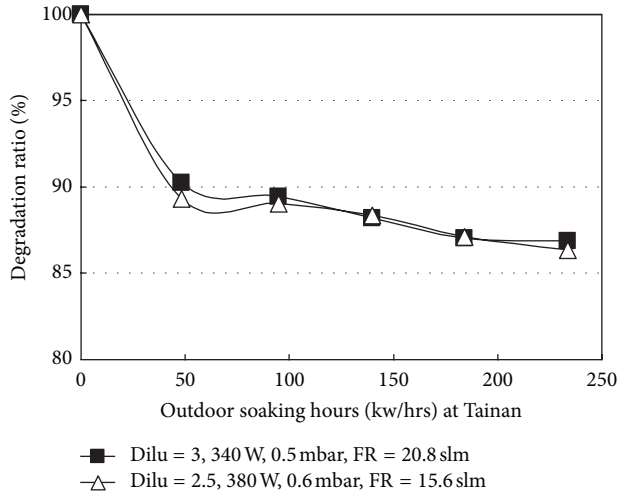


FIGURE 4: Outdoor soaking results of the fabricated modulates with two kinds of amorphous silicon intrinsic layer after tuning (i.e., Dilu = 2.5 and Dilu = 3).

changed the amorphous silicon intrinsic layer. The amount of sunlight was measured by SMA Sunny Web Box. It can be seen from Figure 4 that the degradation behaviors were similar for these two modules. After soaking for 240 kW/hr, it was found that these two modules both became stable with a degradation ratio of around 86%, following the IEC61646 10.19.3 standard. We further fine-tuned the four parameters during the deposition of the amorphous silicon intrinsic layer. Other than the original sample, we also prepared two samples with two different process parameters during the deposition of the amorphous silicon intrinsic layer. One sample was prepared using total flow rate $FR = 20.8$ slm, pressure $P = 0.5$ mbar, process power $P_w = 380$ Watt, and hydrogen dilution ratio $Dilu = 1$. The other sample was prepared using total flow rate $FR = 15.6$ slm, pressure $P = 0.5$ mbar, process power $P_w = 380$ Watt, and hydrogen dilution ratio $Dilu = 2.5$. Table 2 lists the results of modulates fabricated with these three kinds of amorphous silicon intrinsic layer. It can be seen that the initial powers measured from these three modules were similar (i.e., ~ 139 Watt). However, it was found that the amounts of SiH_4 consumed during the deposition of the amorphous silicon intrinsic layers were very different. Assuming that the SiH_4 consumption for the sample prepared with $FR = 20.8$ slm, $P = 0.5$ mbar, $P_w = 380$ Watt, and $Dilu = 1$ was 100%, it was found that the SiH_4 consumption for the sample prepared with $FR = 15.6$ slm, $P = 0.5$ mbar, $P_w = 380$ Watt, and $Dilu = 2.5$ was around 102%. Furthermore, it was found that the SiH_4 consumption for the original sample prepared with $FR = 20.8$ slm, $P = 0.5$ mbar, $P_w = 340$ Watt,

and $Dilu = 3$ was higher than 180%. Furthermore, it was found that tact times observed from the sample prepared with $FR = 20.8$ slm, $P = 0.5$ mbar, $P_w = 380$ Watt, and $Dilu = 1$ was 835 sec, while that observed from the sample prepared with $FR = 15.6$ slm, $P = 0.5$ mbar, $P_w = 380$ Watt, and $Dilu = 2.5$ was 1076 sec. In contrast, it was found that tact time observed from the original sample was as long as 1400 sec. Compared with the original sample, the much smaller SiH_4 consumptions and the shorter tact times observed from the two fine-tuned samples suggest that we could significantly reduce the production cost of the a-Si/ μ c-Si tandem solar cells prepared on Gen 5 glass substrate.

4. Conclusion

In summary, we propose a methodology to improve both the deposition rate and SiH_4 consumption during the deposition of the amorphous silicon intrinsic layer of the a-Si/ μ c-Si tandem solar cells prepared on Gen 5 glass substrate. It was found that the most important issue is to find out the saturation point of deposition rate which guarantee saturated utilization of the sourcing gas. It was also found that amorphous silicon intrinsic layers with the same k value will result in the same degradation of the fabricated modules. Furthermore, it was found that we could significantly reduce the production cost of the a-Si/ μ c-Si tandem solar cells prepared on Gen 5 glass substrate by fine-tuning the process parameters.

Acknowledgment

The authors would like to thank the Bureau of Energy, Ministry of Economic Affairs of Taiwan, R.O.C. for the financial support under Contract no. 102-E0603.

References

- [1] M. Kondo, T. Matsui, Y. Nasuno, H. Sonobe, and S. Shimizu, "Key issues for fabrication of high quality amorphous and microcrystalline silicon solar cells," *Thin Solid Films*, vol. 501, no. 1-2, pp. 243-246, 2006.
- [2] D. L. Staebler and C. R. Wronski, "Reversible conductivity changes in discharge-produced amorphous Si," *Applied Physics Letters*, vol. 31, no. 4, pp. 292-294, 1977.
- [3] Y. Nakano, S. Goya, T. Watanabe, N. Yamashita, and Y. Yonekura, "High-deposition-rate of microcrystalline silicon solar cell by using VHF PECVD," *Thin Solid Films*, vol. 506-507, pp. 33-37, 2006.
- [4] S. Shimizu, H. Miyahara, M. Kondo, and A. Matsuda, "Fabrication of hydrogenated amorphous silicon films exhibiting higher stability against light soaking," *Journal of Non-Crystalline Solids*, vol. 338-340, no. 1, pp. 47-50, 2004.

- [5] A. Gordijn, A. Pollet-Villard, and F. Finger, "At the limit of total silane gas utilization for preparation of high-quality microcrystalline silicon solar cells at high-rate plasma deposition," *Applied Physics Letters*, vol. 98, no. 21, Article ID 211501, 2011.
- [6] A. Matsuda, M. Takai, T. Nishimoto, and M. Kondo, "Control of plasma chemistry for preparing highly stabilized amorphous silicon at high growth rate," *Solar Energy Materials and Solar Cells*, vol. 78, no. 1-4, pp. 3-26, 2003.
- [7] T. Nishimoto, M. Takai, H. Miyahara, M. Kondo, and A. Matsuda, "Amorphous silicon solar cells deposited at high growth rate," *Journal of Non-Crystalline Solids*, vol. 299-302, no. 2, pp. 1116-1122, 2002.
- [8] A. Matsuda, "Thin-film silicon—growth process and solar cell application," *Japanese Journal of Applied Physics*, vol. 43, no. 12, pp. 7909-7920, 2004.

Research Article

Improved Efficiency of Flexible Organic Light-Emitting Diodes by Insertion of Ultrathin SiO₂ Buffer Layers

Chien-Jung Huang,¹ Kan-Lin Chen,² Po-Wen Sze,³ Wen-Ray Chen,⁴
Teen-Hang Meen,⁴ and Shi-Lun Wu⁵

¹ Department of Applied Physics, National University of Kaohsiung, Kaohsiung 81148, Taiwan

² Department of Electronic Engineering, Fortune Institute of Technology, Kaohsiung 83160, Taiwan

³ Department of Electro-Optical Science and Engineering, Kao Yuan University, Kaohsiung 82151, Taiwan

⁴ Department of Electronic Engineering, National Formosa University, Hu-Wei, Yunlin 63201, Taiwan

⁵ Department of Electrical Engineering, Southern Taiwan University of Technology, Tainan 71005, Taiwan

Correspondence should be addressed to Chien-Jung Huang; chien@nuk.edu.tw and Kan-Lin Chen; klchen@fotech.edu.tw

Received 15 September 2013; Accepted 3 October 2013

Academic Editor: Liang-Wen Ji

Copyright © 2013 Chien-Jung Huang et al. This is an open access article distributed under the Creative Commons Attribution License, which permits unrestricted use, distribution, and reproduction in any medium, provided the original work is properly cited.

An ultrathin hole-injection buffer layer (HBL) using silicon dioxide (SiO₂) by electron beam evaporation in flexible organic light-emitting diode (FOLED) has been fabricated. While the current of the device at constant driving voltage decreases as increasing SiO₂ thickness. Compared to the different thicknesses of the buffer layer, the FOLED with the buffer layer of 4 nm showed the highest luminous efficiency. The atomic force microscopy (AFM) investigation of indium tin oxide (ITO)/SiO₂ topography reveals changes at the interface between SiO₂ and N,N'-bis-(1-naphthyl)-diphenyl-1,1'-biphenyl-4,4'-diamine (NPB), resulting in ultrathin SiO₂ layers being a clear advantage for a FOLED. However, the SiO₂ can be expected to be a good buffer layer material and thus enhance the emission performance of the FOLED.

1. Introduction

In the recent years, organic light-emitting diodes (OLED) have gained great interest in the last decade due to their potential application in efficient, large-area, and full-color displays [1–4], especially for flexible displays application [5–8]. The quantum efficiency, photons emitted per electron injected, is dependent upon the current balance between electrons and holes and therefore upon the charge injection rates at cathode and anode interfaces. Current balance is especially difficult to achieve in devices with only a single organic layer since there are no energy barriers to block carrier transit from electrode to electrode. It, therefore, becomes critical to achieve the best possible current balance by suitable choice of materials [9, 10]. The injection currents depend primarily on Schottky barrier heights at each electrode. Furthermore, corroborating evidence for the important injection rate using physical hole-injection buffer layer (HBL) deposited on the anode. Recently, few studies

have reported that an ultrathin film of oxide is employed as an anode buffer layer in organic light-emitting devices to enhance the hole transport and power efficiency of OLED [11–13]. In other words, the buffer layer enhances most of the holes injected from the anode and improves the balance of the hole and electron injections. Although these studies can improve their efficiency, to accurately control the evaporation rate and the concentration of two or more materials, such as molybdenum oxide (MoO₃), zinc oxide (ZnO), and silicon dioxide (SiO₂), in the doping codeposition process is very difficult.

Among these materials, the cost of SiO₂ material is cheaper than that of the other two materials. However, if a thin insulating layer such as silicon dioxide (SiO₂) with a wide bandgap (8 eV, compared to 2.9 eV for 8-hydroxyquinoline aluminum (Alq₃)) is added between the indium tin oxide (ITO) anode and N,N'-bis-(1-naphthyl)-diphenyl-1,1'-biphenyl-4,4'-diamine (NPB) layer, the accumulation of holes can occur at the ITO/NPB interface; hence, the improvement

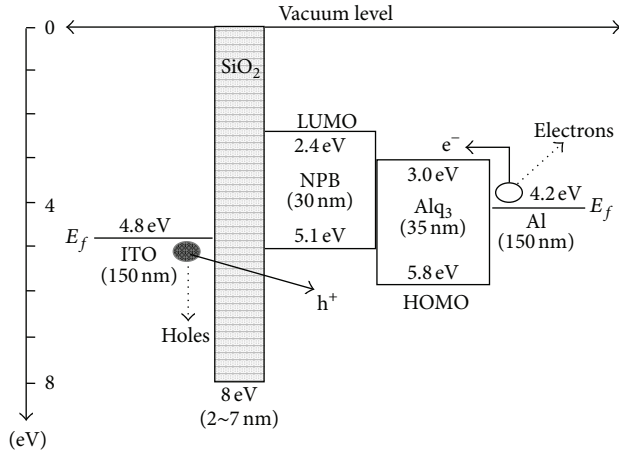


FIGURE 1: The schematic energy level diagram of ITO/SiO₂/NPB/Alq₃/Al.

is of current balance between the injected electrons and holes. The inserted buffer layer has not yet been studied. In this paper, a detailed investigation of an ultrathin SiO₂ layer as the HBL and the effect of SiO₂ on the device efficiency is presented.

2. Experimental

For the fabrication of flexible organic light-emitting diode (FOLED), the devices were performed on 150 nm thickness of indium tin oxide (ITO)-coated plastic substrate. The schematic energy level diagram of the FOLED with the SiO₂ layer inserted between ITO/NPB interface structures is shown in Figure 1. The sheet resistance of ITO was obtained at 50 Ω/sq. The plastic substrate used in this study is a transparent polymer named ARTON (ARTON F, JSR Co., Ltd., Japan). The ITO film is streaked with the photolithography processing via etching and is as an anode electrode. The device configuration was adopted as shown in Figure 2. The multilayer structure consists of an ITO-coated plastic substrate, ultrathin SiO₂ as an HBL, NPB as a hole-transporting layer (HTL), Alq₃ as an electron-transporting layer (ETL), and aluminum (Al) cathode electrode manufactured by shadow mask. The thickness of ITO, NPB, Alq₃, and Al was performed at 150, 30, 35, and 150 nm, respectively. The emitting area of devices is 2.25 mm². After the previously mentioned multilayer structure, the SiO₂ layer is fabricated by using the electron beam deposition (EBD) system. The evaporation onto the ITO-covered plastic substrate is performed in a high vacuum system with a base pressure of 1.0 × 10⁻⁶ torr. The Al was deposited by EBD system at rates of 1 nm/sec. The brightness is measured by spectrophotometer (Photo Research, PR655 SpectraScan, USA). The characterization was carried out by using the power source (Keithley Source Meter 2400, USA). The present study also presents a complementary study of the topography of the surfaces by atomic force microscopy (AFM, Burleigh, METRIS-3345, USA).

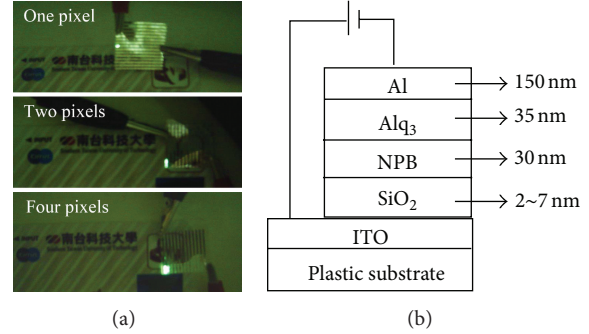


FIGURE 2: Photographs (a) of flexible organic light-emitting diode at an applied voltage of 6 V and schematic diagram of device configuration (b).

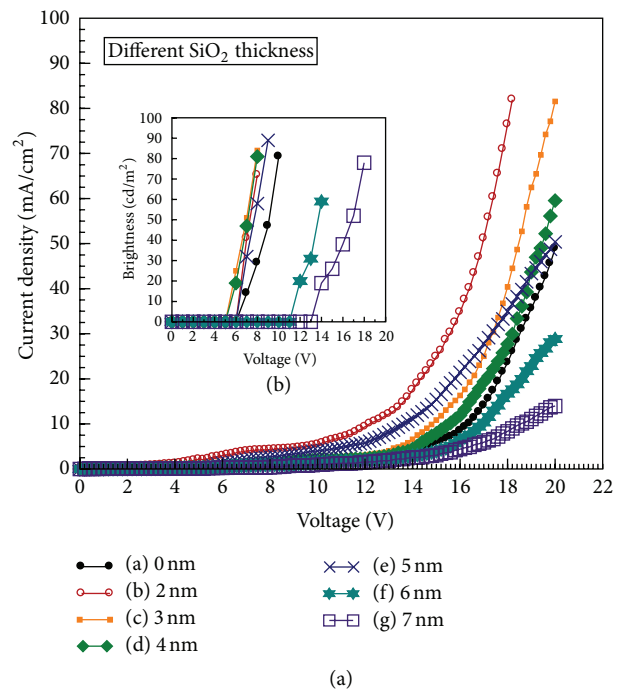


FIGURE 3: (a) J - V characteristics of the devices with different silicon dioxide thicknesses. (b) The inset shows the B - V characteristics of the devices.

3. Results and Discussion

Figure 3(a) shows typical current density versus applied voltage (J - V) characteristics of the studied devices fabricated with different thicknesses of SiO₂ (0, 2, 3, 4, 5, 6, and 7 nm). The current density of the devices is almost zero under negative voltage. As expected, the current density decreases as the buffer layer thickness increases when the buffer layer of SiO₂ is larger than 5 nm at a constant applied voltage of 14 V. On the other hand, there is a tendency that current density increases with the decrease of the thickness of the buffer layer (2~4 nm). This suggests that the buffer layer is as a block layer and has an effect of blocking the hole in movement, leading to more balance. In other words, this barrier impedes hole

injection from ITO, preventing the accumulation of excess holes in the luminance layer, thus increasing the probability of e-h⁺ pair combination.

It is known that holes are the major charge carrier in FOLED, and luminous efficiency strongly depends on charge balance. Luminous intensity therefore increases with the increase of barrier height and with the thickness of the buffer layer (2~4 nm) when the applied voltage is less than 8 V. It shows that the bias voltage to obtain the same current density of 20 mA/cm² is obviously lowered for the FOLED with 2 nm SiO₂ buffer layer compared with the devices without SiO₂. Furthermore, the light onset voltage (V_{L-on} ; defined as the voltage required to drive a luminance of 10 cd/m²) of the device with SiO₂ of 4 nm is as low as 5.2 V, as shown in the inset of Figure 3(b). In other words, the V_{L-on} in Figure 3(b) is estimated to be 7.1, 6.2, 5.1, 5.2, and 6.5 V for devices with buffer layer in 0 nm, 2 nm, 3 nm, 4 nm, and 5 nm, respectively. Thus, the V_{L-on} of 2 nm, 3 nm, 4 nm, and 5 nm is to be lower than that of the device without buffer layer. However, there is a tendency that the V_{L-on} increases with the increase of oxide thickness (2~7 nm) because a larger voltage is dropped across the oxide [14]. When the oxide layer is more than 5 nm, the effective barrier is as (1) [15]

$$\Phi'_B = \Phi_B - \left(q \frac{|E_S|}{4\pi\epsilon\epsilon_0} \right)^{1/2} - \alpha |E_S|, \quad (1)$$

$$D_m = \left[\frac{q}{16\pi\epsilon_0 E} \right]^{1/2}, \quad (2)$$

$$\Delta\Phi = \left[\frac{qE}{4\pi\epsilon_0} \right]^{1/2}, \quad (3)$$

where E_S is the NPB surface field and Φ_B is the potential barrier height when $E_S = 0$. The image force exerted by ITO proximity and the thermally assisted tunneling through the barrier lowers the effective barrier height. Equations (2) and (3) show the relationship between $\Delta\Phi$ and D_m , where D_m is the distance from the ITO. From the previous equation and viewpoints, there is an image force at smaller D_m which results from increasing oxide thickness and lowers considerably the barrier. In other words, the barrier height is inversely proportional to oxide thickness. With lowered barrier, there follows an excess of hole injection and accumulation. However, improved hole/electron injection balance is a consequence one may expect from the inclusion of SiO₂ ultrathin film as HBL. Besides, the electrons possess much lower mobility than holes in organic materials. This gives rise to an accumulation of excess holes at SiO₂-NPB boundary. The electron-hole pair combination is decreased, so the luminous efficiency is decreased.

Figure 4(a) shows the brightness versus applied voltage ($B-V$) characteristics of the FOLED with the SiO₂ buffer layer. In contrast with the value of only 2300 cd/m² without SiO₂ buffer layer, an impressive brightness of more than 3300 cd/m² was measured when the SiO₂ thickness was 2 nm at 20 V. Similarly, the luminous efficiency of the FOLED was increased due to the introduction of the thin SiO₂ layer (Figure 5). Figure 4(b) shows the brightness versus current

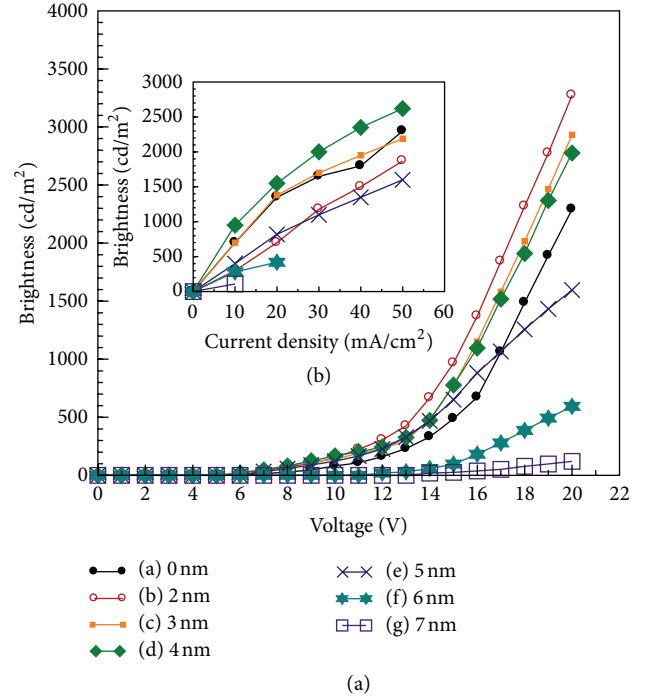


FIGURE 4: (a) $B-V$ characteristics for the devices with different SiO₂ buffer layer thicknesses. (b) The inset shows the $B-J$ characteristics of the devices.

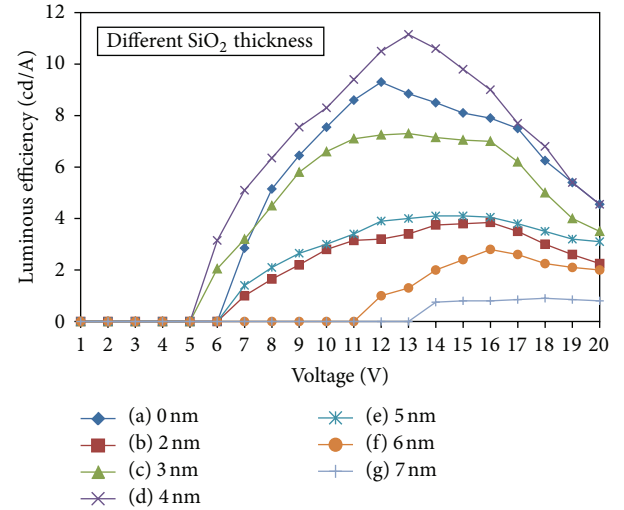


FIGURE 5: Luminous efficiency versus applied voltage curves of the devices with different buffer layer thicknesses.

density ($B-J$) on the SiO₂ thickness for the devices. At a given constant current density of 20 mA/cm², the device with buffer layer of 4 nm displayed the highest luminance of 1550 cd/m² among the seven samples which corresponded to a luminous efficiency of 7.6 cd/A. In contrast, the device without the SiO₂ buffer layer only shows the luminous efficiency of 6.4 cd/A at the current density of 20 mA/cm². Table 1 showed the luminance and efficiency characteristics for the devices with different thicknesses of SiO₂ at the

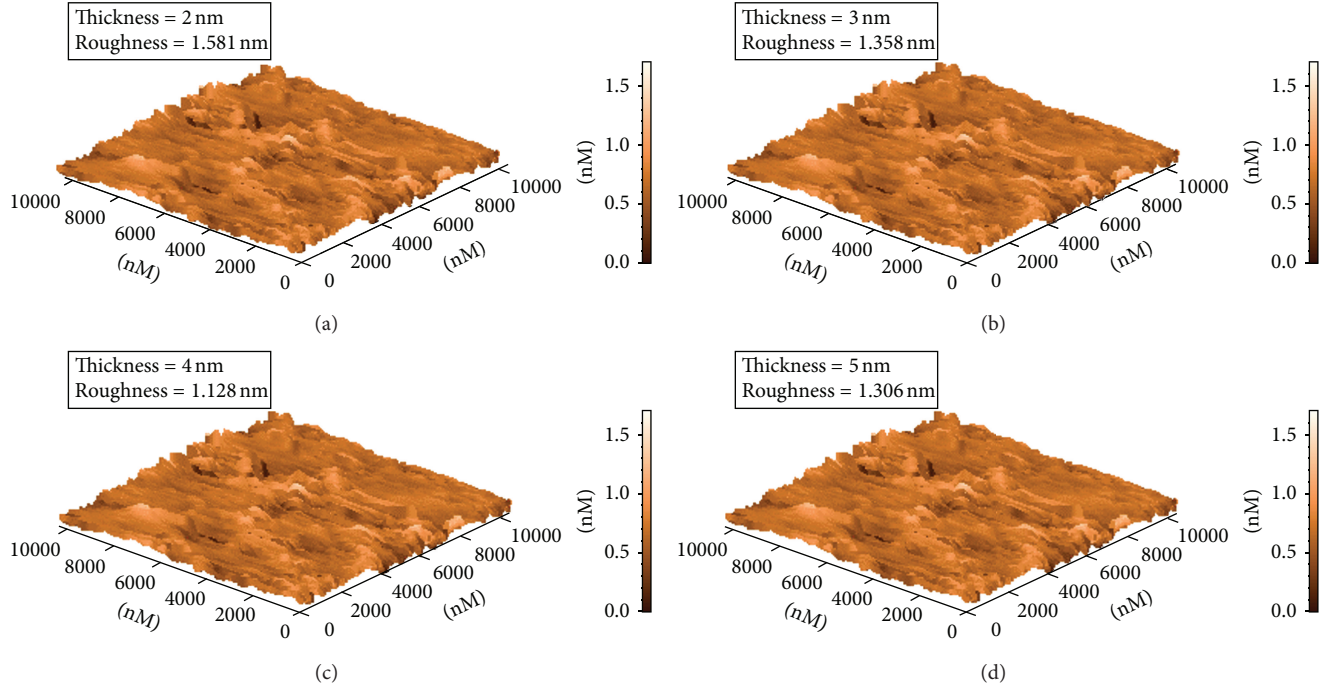


FIGURE 6: Images of atomic force microscopy of the ITO surface after depositing (a) 2, (b) 3, (c) 4, and (d) 5 nm SiO₂ buffer layers.

TABLE 1: Luminance and efficiency characteristics for the devices with different SiO₂ buffer layer thicknesses at the current density of 20 mA/cm².

SiO ₂ thickness (nm)	Luminance (cd/m ²)	Voltage (V)	Luminous efficiency (cd/A)
0	1310	17.8	6.4
2	700	14.2	3.8
3	1380	16.8	6.5
4	1550	17.1	7.6
5	820	15.8	4.1
6	420	18.2	2.2
7	78	18	0.72

current density of 20 mA/cm². The voltages are obtained from Figure 3(a) at a constant current density of 20 mA/cm². Furthermore, the luminance and the luminous efficiency are got and corresponded from above various voltages via Figures 4(a) and 5, respectively. And then it is obvious that the efficiency of the device with buffer layer of 4 nm is better than that of the one without buffer layer. The brightness and efficiency of electroluminescent (EL) devices increased with the thickness of the SiO₂ buffer layer, but those drop after the maximum brightness and efficiency of EL devices, which can be attributed to excessively blocking the hole by the thick buffer layer. However, a good EL device should possess not only the high brightness but also the high luminous efficiency.

Shown in Figure 5 is luminous efficiency versus applied voltage curves for seven different devices, derived from the data shown in Figure 4. There is an optimization thickness of

SiO₂ (4 nm) for the luminous efficiency of the devices. At a given constant voltage of 13 V, obviously the device with the 4 nm thick buffer layer was the most efficient one. In contrast, the device without the SiO₂ buffer only showed a luminous efficiency of 8.8 cd/A at the voltage of 13 V. An increase in the thickness of the SiO₂ buffer beyond 4 nm resulted in a gradual decrease in brightness and efficiency. No EL emission could be findable when the thickness of the layer exceeded 8 nm. Device performance was improved by the use of a buffer layer consisting of SiO₂. Although the exact role of the SiO₂ buffer layer in the hole-injecting transporting process is not completely clear, the enhancements in brightness and efficiency of the devices may tentatively be attributed to an improved balance of the hole and electron injections, which results in enhancements of carrier recombination efficiency. In addition, some groups believe that the deposition of an ultrathin oxide layer prior to the organic material deposition may smooth the interface and lead to a more homogeneous adhesion of the HBL to the anode [16–19].

The topography of SiO₂ on ITO was acquired *ex situ* using atomic force microscopy (AFM). Figures 6(a)–6(d) show the topographical images that present the surface root mean square (RMS) roughness for ITO and surfaces obtained after depositing SiO₂ of 2, 3, 4, 5 nm on ITO. The RMS roughness is 1.581, 1.358, 1.128, and 1.306 nm, respectively. That reveals that ITO has a relatively smooth surface. In the 2 and 3 nm thickness, the surface morphologies are island structure and small quantity of spikes; a few nanometers in height on bare ITO surfaces indicate that the grains coalesce and fill in the channel between the grain and the poor surface uniformity. In addition, there is an optimization thickness of SiO₂ (4 nm) for the low RMS roughness of surface; the structure of island

and spikes have fallen away little by little. In fact, the smooth uniformity of film surface for improving interface contact of the ultrathin SiO₂ layer with organic layer is important for the injection and transmission properties of carrier. Therefore, carrier can be easy to inject through from ITO to organic mediums when the device is properly biased.

4. Conclusions

In summary, the devices with the insertion of an ultrathin SiO₂ buffer layer between ITO and NPB showed enhanced hole-injection efficiency, higher EL efficiency, and operational stability that may be attributed to an improved current balance of the hole and electron injections, resulting mainly from the blocking of the injected holes by the buffer layer. In other words, this buffer layer improves FOLED efficiency without modifying the electrode work function or requiring additional organic layers. Various techniques, including physical and electrical characterizations, show that a smoother SiO₂ (4 nm)/NPB interface versus ultrathin SiO₂ layers is a clear advantage for a FOLED. However, the buffer layer can be to control the emission performance of the FOLED, offering further promise for innovation optoelectronic application.

Conflict of Interests

The authors declare that there is no conflict of interests regarding the publication of this paper.

Acknowledgment

This work was partially supported by the National Science Council of Taiwan under Contract no. NSC102-2221-E-390-019-MY2.

References

- [1] C. Hosokawa, M. Eida, M. Matsuura, K. Fukuoka, H. Nakamura, and T. Kusumoto, "Organic multi-color electroluminescence display with fine pixels," *Synthetic Metals*, vol. 91, no. 1-3, pp. 3-7, 1997.
- [2] Y. Kijima, N. Asai, N. Kishii, and S.-I. Tamura, "RGB luminescence from passive-matrix organic LED's," *IEEE Transactions on Electron Devices*, vol. 44, no. 8, pp. 1222-1228, 1997.
- [3] J. Y. Lee, J. H. Kwon, and H. K. Chung, "High efficiency and low power consumption in active matrix organic light emitting diodes," *Organic Electronics*, vol. 4, no. 2-3, pp. 143-148, 2003.
- [4] T. Dobbertin, E. Becker, T. Benstem et al., "OLED matrix displays: in-line process technology and fundamentals," *Thin Solid Films*, vol. 442, no. 1-2, pp. 132-139, 2003.
- [5] P. E. Burrows, G. L. Graff, M. E. Gross et al., "Ultra barrier flexible substrates for flat panel displays," *Displays*, vol. 22, no. 2, pp. 65-69, 2001.
- [6] Z. Xie, L.-S. Hung, and F. Zhu, "A flexible top-emitting organic light-emitting diode on steel foil," *Chemical Physics Letters*, vol. 381, no. 5-6, pp. 691-696, 2003.
- [7] P. Melpignano, S. Sinesi, G. Rotaris et al., "Optical coupling of flexible microstructured organic light sources for automotive applications," *Synthetic Metals*, vol. 139, no. 3, pp. 913-916, 2003.
- [8] F. Papadimitrakopoulos, X.-M. Zhang, and K. A. Higginson, "Chemical and morphological stability of aluminum tris(8-hydroxyquinoline) (Alq3): effects in light-emitting devices," *IEEE Journal on Selected Topics in Quantum Electronics*, vol. 4, no. 1, pp. 49-57, 1998.
- [9] Y. Qiu, Y. Gao, L. Wang, and D. Zhang, "Efficient light emitting diodes with teflon buffer layer," *Synthetic Metals*, vol. 130, no. 3, pp. 235-237, 2002.
- [10] S. M. Tadayyon, H. M. Grandin, K. Griffiths, P. R. Norton, H. Aziz, and Z. D. Popovic, "CuPc buffer layer role in OLED performance: a study of the interfacial band energies," *Organic Electronics*, vol. 5, no. 4, pp. 157-166, 2004.
- [11] L. Li, M. Guan, G. Cao, Y. Li, and Y. Zeng, "Low operating-voltage and high power-efficiency OLED employing MoO₃-doped CuPc as hole injection layer," *Displays*, vol. 33, no. 1, pp. 17-20, 2012.
- [12] H.-H. Huang, S.-Y. Chu, P.-C. Kao, Y.-C. Chen, M.-R. Yang, and Z.-L. Tseng, "Enhancement of hole-injection and power efficiency of organic light emitting devices using an ultra-thin ZnO buffer layer," *Journal of Alloys and Compounds*, vol. 479, no. 1-2, pp. 520-524, 2009.
- [13] B. J. Chen, X. W. Sun, Y. Divayana, and B. K. Tay, "Improving organic light-emitting devices by modifying indium tin oxide anode with an ultrathin tetrahedral amorphous carbon film," *Journal of Applied Physics*, vol. 98, no. 4, Article ID 046107, pp. 1-3, 2005.
- [14] H. H. Kim, T. M. Miller, E. H. Westerwick et al., "Silicon compatible organic light emitting diode," *Journal of Lightwave Technology*, vol. 12, no. 12, pp. 2107-2113, 1994.
- [15] J. M. Shannon, "Reducing the effective height of a schottky barrier using low-energy ion implantation," *Applied Physics Letters*, vol. 24, no. 8, pp. 369-371, 1974.
- [16] G. Cao, L. Li, M. Guan, J. Zhao, Y. Li, and Y. Zeng, "Stable organic solar cells employing MoO₃-doped copper phthalocyanine as buffer layer," *Applied Surface Science*, vol. 257, no. 22, pp. 9382-9385, 2011.
- [17] L. Hou, P. Liu, Y. Li, and C. Wu, "Enhanced performance in organic light-emitting diodes by sputtering TiO₂ ultra-thin film as the hole buffer layer," *Thin Solid Films*, vol. 517, no. 17, pp. 4926-4929, 2009.
- [18] C. O. Poon, F. L. Wong, S. W. Tong, R. Q. Zhang, C. S. Lee, and S. T. Lee, "Improved performance and stability of organic light-emitting devices with silicon oxy-nitride buffer layer," *Applied Physics Letters*, vol. 83, no. 5, pp. 1038-1040, 2003.
- [19] H. Youn and M. Yang, "Solution processed polymer light-emitting diodes utilizing a ZnO/organic ionic interlayer with Al cathode," *Applied Physics Letters*, vol. 97, no. 24, Article ID 243302, 2010.

Research Article

Using Flexible Polyimide as a Substrate to Deposit ZnO:Ga Thin Films and Fabricate p-i-n α -Si:H Thin-Film Solar Cells

Fang-Hsing Wang,¹ Cheng-Fu Yang,² and Min-Chu Liu¹

¹ Department of Electrical Engineering and Graduate Institute of Optoelectronic Engineering,
National Chung Hsing University, Taichung 402, Taiwan

² Department of Chemical and Materials Engineering, National University of Kaohsiung, Kaohsiung 81148, Taiwan

Correspondence should be addressed to Cheng-Fu Yang; cfyang@nuk.edu.tw

Received 18 September 2013; Accepted 3 October 2013

Academic Editor: Teen-Hang Meen

Copyright © 2013 Fang-Hsing Wang et al. This is an open access article distributed under the Creative Commons Attribution License, which permits unrestricted use, distribution, and reproduction in any medium, provided the original work is properly cited.

The GZO thin films were deposited on the polyimide (PI) substrates to investigate their properties for the possibly flexible applications. The effects of substrate temperature (from room temperature to 200°C) on the surface and cross-section morphologies, X-ray diffraction pattern, optical transmission spectrum, carrier concentration, carrier mobility, and resistivity of the GZO thin films on PI substrates were studied. The measured results showed that the substrate temperature had large effect on the characteristics of the GZO thin films. The cross-section observations really indicated that the GZO thin films deposited at 200°C and below had different crystalline structures. The value variations in the films' optical band gap (E_g) of the GZO thin films were evaluated from plots of $(\alpha h\nu)^2 = c(h\nu - E_g)$, revealing that the measured E_g values increased with increasing deposition temperature. Finally, the prepared GZO thin films were also used as the transparent electrodes to fabricate the α -Si amorphous silicon thin-film solar cells on the flexible PI substrates, and the properties of which were also measured. We would also prove that substrate temperature of the GZO thin films had large effect on the characteristics of the fabricated α -Si amorphous silicon thin-film solar cells.

1. Introduction

Tin doped indium oxide (ITO) thin films are widely used as a transparent conducting oxide (TCO) electrode in optoelectronic devices because they have high performance in the visible region, including very low resistivity and high transmittance. However, the price of indium is increasing due to the high demand of ITO in the rapid development of flat panel displays (FPDs) industry. In addition, the toxic nature and high cost due to the scarcity of indium have led researchers to seek an alternative candidate for ITO. Recently, impurity doped zinc oxide is a possible alternative to ITO due to its unique electrical and optical properties. Zinc oxide (ZnO) is a novel II-VI compound n-type oxide semiconductor with various electrical, optical, acoustic, and chemical properties because of its wide direct band gap (E_g) value of 3.37 eV at room temperature (RT) [1]. Because of the good properties

of thin films, ZnO-based thin films could be used as a transparent electrode in optoelectronic applications such as solar cells [2], and undoped ZnO thin films could be used as a buffer layer of solar cells [3] and the active layer of transparent thin films transistor [4]. Alternatively, the effects of different dopant of In_2O_3 [5], Al_2O_3 [6], and Ga_2O_3 [7] in ZnO films have also been explored and are also regarded as the ideal candidates for replacing ITO as TCO electrodes owing to their promising optical and electrical properties as well as its low cost, nontoxicity, and long-term environmental stability.

Many researchers have reported about the Ga_2O_3 -doped ZnO thin films according to a different doping concentrations of Ga_2O_3 [8]. The highly conductive and transparent Ga_2O_3 -doped ZnO thin films had been deposited at high growth rates by radio frequency magnetron sputtering [9]. The thin films processed at room temperature on soda lime glass substrates using a ceramic Ga_2O_3 -doped ZnO target; a low

resistivity of $2.6 \times 10^{-4} \Omega\text{-cm}$ was obtained. In the present paper, a compound of ZnO with 3 wt% Ga_2O_3 ($\text{ZnO}:\text{Ga}_2\text{O}_3 = 97:3$ in wt%, GZO) was prepared by solid-state reaction method. For the possibly flexible applications, the polyimides (PI) were used as substrates and the GZO thin films were deposited on them to investigate their physical, optical, and electrical properties. However, there is a still controversy about the effects of substrate temperature of the Ga_2O_3 -doped ZnO thin films depositing on PI substrates. For that, the GZO thin films were deposited on PI substrates by changing substrate temperature from RT to 200°C . We would show that substrate temperature played an important role in nucleation, relatively diffraction intensity of orientations, lattice constant, crystalline size, optical E_g value, carrier mobility, carrier concentration, and resistivity of the GZO thin films. In the past, GZO thin films were used as the electrodes of the p-i-n $\alpha\text{-Si:H}$ thin-film solar cells [10], produced in a modified single chamber reactor, and the fabricated solar cells exhibited very good electrical characteristics [11]. In the past, the GZO thin films were also deposited on the polyethylene naphthalate (PEN) substrates by RF magnetron sputtering at room temperature [12]. In this paper, the GZO thin films were deposited on polyimide (PI) substrates by RF magnetron sputtering under different substrate temperatures (from RT to 200°C) to investigate their characteristics for the possible applications in flexible photo devices. Finally, the investigated GZO thin films on PI substrates were also used as the transparent electrodes to fabricate the $\alpha\text{-Si}$ thin-film solar cells. The current-voltage characteristics were measured to determine the effects that substrate temperature of the GZO thin films had on the fabricated $\alpha\text{-Si}$ solar cells.

2. Experimental Details

In this work, GZO with the composition of $\text{ZnO} = 97.0$ wt% (99.999% purity) and $\text{Ga}_2\text{O}_3 = 3.0$ wt% (99.99% purity) was used to prepare 2-inch (in diameter) target. The weighted composition was mixed, ground, calcined at 1000°C for 5 h, and sintered at 1400°C for 4 h to prepare the GZO ceramic target for sputtering process. RF (13.56 MHz) magnetron sputtering process was used, and the used substrate was $33 \text{ mm} \times 33 \text{ mm} \times 2 \text{ mm}$ polyimide (abbreviated as PI). Before deposition process was started, base chamber pressure was pumped to less than 1×10^{-6} Torr; then deposition pressure was controlled at 5×10^{-2} Torr and the GZO thin films were deposited at different temperatures (from RT to $\sim 200^\circ\text{C}$). In case of the GZO thin films, RF power was controlled as 50 W and substrate temperatures as from room temperature (RT) to 200°C , and distance between the target and polyimide substrate was 8 cm. Before deposition process was started, base chamber pressure was pumped to 5×10^{-6} Torr (detected by using MKS Baratron gauge) and substrate temperature was changed from RT to 200°C ; then deposition pressure was controlled at 5×10^{-3} Torr. During deposition process, only argon was introduced in the chamber; the flow rate of pure argon (99.999%) was 20 sccm. Film thickness of the GZO thin films was determined by

averaging five data obtained by FESEM, and deposition rates were calculated from measured thickness of the deposited GZO thin films. Film thickness was measured using a Nano-View SEMF-10 ellipsometer and confirmed by field emission scanning electron microscopy (FESEM); the films' thicknesses were about 260 nm by controlling the deposition time. While the crystalline structure of the GZO thin films was identified by X-ray diffraction (XRD) patterns and the Hall-effect coefficient was measured using a Bio-Rad Hall set-up, the optical transmission spectrum was recorded using a Hitachi U-3300 UV-Vis spectrophotometer in the 300–1400 nm wavelength range. Superstrate p-i-n $\alpha\text{-Si:H}$ thin film solar cells were fabricated using a single-chamber plasma-enhanced chemical vapor deposition unit at 200°C , with a working pressure of 700×10^{-3} Torr and a deposition power of 20 W. The p-type $\alpha\text{-Si}$ thin films (thickness was about 20 nm) were deposited by controlling the gas flowing rates for $\text{H}_2 = 100$ sccm, $\text{SiH}_4 = 20$ sccm, $\text{CH}_4 = 10$ sccm, and $\text{B}_2\text{H}_6 = 40$ sccm; the i-type $\alpha\text{-Si}$ thin films (400 nm) were deposited by using $\text{H}_2 = 100$ sccm and $\text{SiH}_4 = 10$ sccm; and the p-type $\alpha\text{-Si}$ (50 nm) thin films were deposited by using $\text{H}_2 = 100$ sccm, $\text{SiH}_4 = 20$ sccm, and $\text{PH}_3 = 20$ sccm, respectively. The current-voltage characteristic of the fabricated solar cells was measured under an illumination intensity of 300 mW/cm^2 and an AM 1.5 G spectrum.

3. Results and Discussion

XRD patterns of the GZO thin films as a function of substrate temperature are shown in Figure 1. Even though all the GZO thin films exhibited the (002) peak, they really had different diffraction results. The RT- and 100°C -deposited GZO thin films exhibited only a weak (002) peak, and the diffraction intensity of (002) peak had no apparent increase as substrate temperature increased from RT to 100°C . The 200°C -deposited GZO thin films exhibited a strong (002) peak and a weak (004) peak, which indicate that the c -axis is predominantly oriented parallel to the substrate normal. Those results prove that the GZO thin films have different morphologies in the cross-section and they have differently crystalline orientation. The absence of additional peaks in the XRD patterns excludes the possibility of any extra phases and/or large-size precipitates in the GZO thin films. The results in the XRD patterns match the variation in the morphology of the SEM observations that the different morphologies having in the surface (Figure 3) and cross section (Figure 4) of the GZO thin films will lead to different crystallization results. The (002) peaks of the GZO thin films prepared at substrate temperature = RT, 100°C , and 200°C were situated at $2\theta = 34.14^\circ$, 34.18° , and 34.36° , respectively. The lattice constant c was calculated by using the 2θ value; the calculated lattice constants (c) were 0.5249, 0.5243, and 0.5221 as substrate temperatures were RT, 100°C , and 200°C , respectively. All the lattice constant c of the GZO thin films being smaller than that of the ZnO thin films is considerable, because the radius of Ga^{3+} ions (62 pm) is smaller than that of Zn^{2+} ions (72 pm). As substrate temperature is raised from RT to 200°C , the more Ga^{3+} ions will substitute the sites of Zn^{2+} ions, because the radius of Ga^{3+} ions is shorter than that of

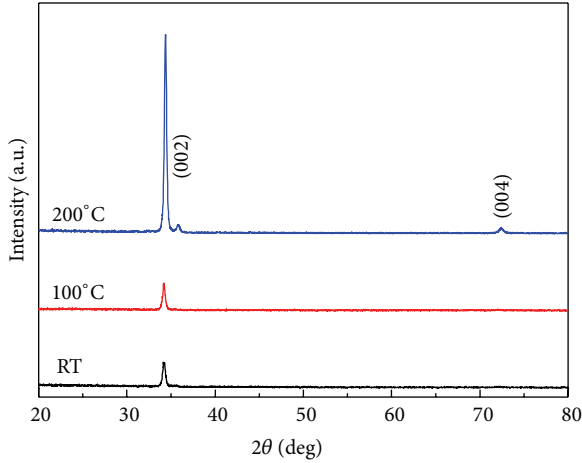


FIGURE 1: XRD patterns of the GZO thin films as a function of substrate temperature.

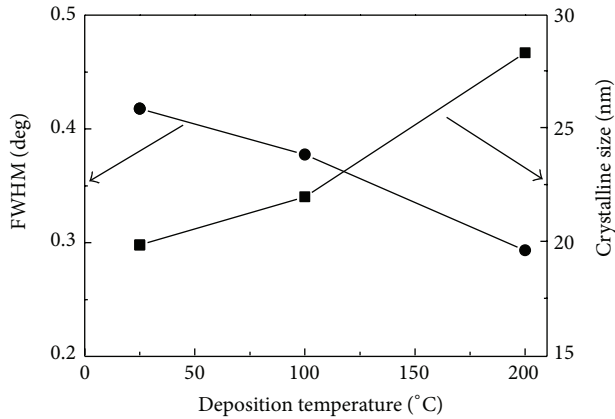


FIGURE 2: FWHM value and crystalline size of the GZO thin films as a function of substrate temperature.

Zn²⁺ ions; for that the lattice constant c of the GZO thin films becomes shorter as substrate temperature is raised.

As Figure 2 shows, the full widths at half maximum (FWHM) values for the (002) peak of the GZO thin films were 0.412, 0.360, and 0.296 for substrate temperature were RT, 100°C, and 200°C, respectively. These results suggest that the GZO thin films deposited at higher temperature have the better crystalline structure. The morphologies of the GZO thin films deposited at different substrate temperatures are shown in Figure 3, which indicates that as deposition temperature is changed, the surface morphologies apparently changed as well. As deposited at room temperature, morphology of the GZO thin films exhibited a roughness surface, which showed the nanocrystalline structure of the GZO grains. As Figure 3 shows, the grain size distributions were around the range of 8~40 nm, 10~43 nm, and 15~55 nm. However, the variations of average crystallization sizes are dependent on substrate temperature and are not easily calculated from the surface observation. We will illustrate the variations of grain sizes

from the XRD patterns and the following [13], and the results are also shown in Figure 2:

$$D = \frac{(0.9\lambda)}{(\beta \cos \theta)}. \quad (1)$$

As Figure 2 shows, the average crystallization sizes were 20.2 nm, 23.1 nm, and 28.1 nm as substrate temperatures were RT, 100°C, and 200°C, respectively.

Even the substrate temperature is raised from RT to 100°C, only a little increase in the active energy of plasma GZO molecules to improve the crystallinity and grain growth, for that the diffraction intensity of (002) peak has no apparent change and the crystallization size increases slightly; as substrate temperature is raised from 100°C to 200°C, the plasma GZO molecules will have enough active energy during deposition process and the chance for growth of the GZO crystallization sizes increases; for that the diffraction intensity of the (002) peak and the crystallization size increases. The number of thin film defects also will decrease and the crystallization of the GZO thin films will be improved; then the crystallization of the GZO thin films is also improved and the FWHM value decreases. From the results in Figures 1–3, as substrate temperature is raised from RT to 200°C, a smoother surface morphology and a more uniform c -axis orientation were obtained in the 200°C-deposited GZO thin films. Thus, better crystallinity resulting from a stronger c -axis orientation and smoother surface morphology could be achieved in the 200°C-deposited GZO thin films prepared on PI substrates.

Figure 4 shows the cross-section observations of the GZO thin films deposited at different substrate temperatures. Calculating the results in Figure 4, thicknesses of both 100°C- and 200°C-deposited GZO thin films were about 260 nm. The cross-section observation of the RT-deposited GZO thin films was not shown here because it had the same thickness and the same cross-section morphology as those of the 100°C-deposited GZO thin films. As the cross-section micrographs shown in Figure 4 are compared, there are different results as the substrate temperature is changed. As RT (not shown here) and 100°C were used as substrate temperatures, the GZO thin films grew like an irregular plate with no specific direction. But depositing at 200°C, the plate-shaped growths were transformed into the nanobar along the up direction. These results prove that the 200°C-deposited GZO thin films and the 100°C-deposited GZO thin films have no the highly oriented parallel to the substrate normal.

Figure 5(a) shows the transmission ratios of the GZO thin films plotted against wavelengths in the region of 300–1400 nm, with substrate temperature as the parameter. As substrate temperature was raised from RT to 200°C, the transmittance ratios of the GZO thin films were almost unchanged. The optical transmission ratios in the visible light region (400–700 nm) were more than 94% for all GZO thin films, regardless of substrate temperature. For the transmission spectra shown in Figure 5(a), as substrate temperature was raised, the optical band edge shifted to a shorter wavelength was observable and a greater sharpness was noticeable in the curves of the absorption edge, which suggest an increase

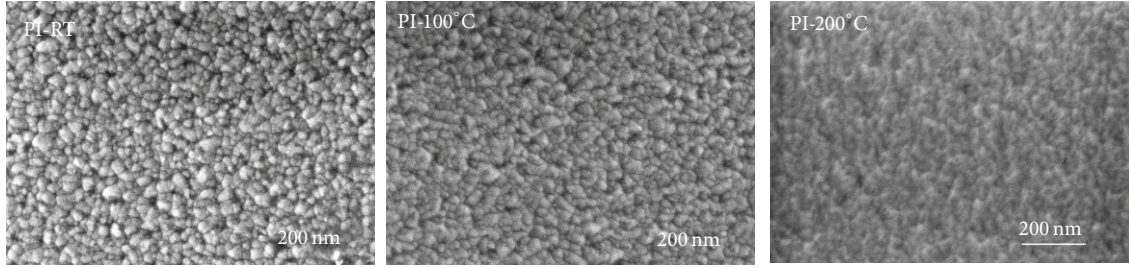


FIGURE 3: Surface observations of the GZO thin films as a function of substrate temperature.

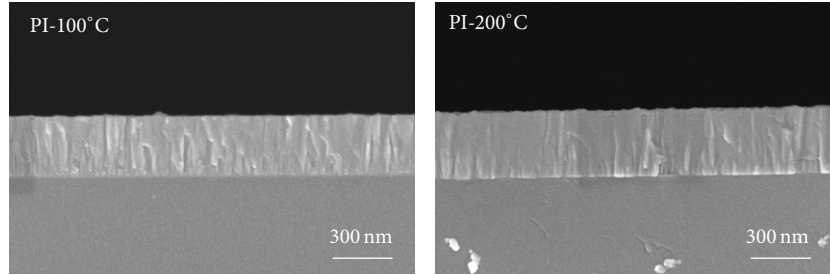


FIGURE 4: Cross-section observations of the 100°C- and 200°C-deposited GZO thin films.

in the E_g values. Also, the GZO thin films deposited on PI substrates had high transmittance ratio of over 89.6% in the near-infrared region (750 nm~1400 nm).

In the past, determination of the optical band gap (E_g) was often necessary to develop the electronic band structure of the thin-film materials for investigating them as a transparent electrode of the thin-film solar cells. However, using extrapolation methods, the E_g values of thin films can be determined from the absorption edge for direct interband transition, which can be calculated using the relation in the following equation:

$$(\alpha h\nu)^2 = c(h\nu - E_g), \quad (2)$$

where α is the optical absorption coefficient, c is the constant for direct transition, h is Planck's constant, and ν is the frequency of the incident photon [14]. Figure 5(b) plots $(\alpha h\nu)^2$ against $h\nu$ (photo energy) in accordance with (2), and the E_g values can be found by extrapolating a straight line at $(\alpha h\nu)^2 = 0$; the calculated E_g values of the GZO thin films are shown. The linear dependence of $(\alpha h\nu)^2$ on $h\nu$ indicates that GZO thin films are direct transition type semiconductors. As the substrate temperature increases from RT to 200°C, the E_g values increase from 3.524 eV to 3.595 eV. Many factors will affect the transmission spectra of the GZO thin films. The increase in the optical band is caused by the increase in carrier concentration because of the decreasing of the lattice defects. The improvement in the electrical properties of the GZO thin films (will be shown in Figure 6) will prove the results. Because the E_g values of the GZO thin films are larger than the energy of visible light, the high transmittance ratio in the visible light region is expected.

The results of the carrier mobility, carrier concentration, and resistivity shown Figure 6 indicate that the electrical

properties of the GZO thin films were dependent on substrate temperature. When plasma molecules are deposited on a glass substrate, many defects result and inhibit electron movement. As different substrate temperatures are used during the deposition process, two factors are believed to cause an increase in the carrier mobility of the GZO thin films. First, higher substrate temperature provides more energy and thus enhances the motion of plasma molecules, which will improve the crystallization and grain size growth of the GZO thin films; also the defects in the thin films will be decreased. Second, as substrate temperature was raised, the defects in the GZO thin films decrease, and that will cause the decrease in the inhibiting of the barriers electron transportation [15]. As Figure 7 shows, both the carrier concentration and carrier mobility of the GZO thin films linearly increased with raising substrate temperature and reached the maximum concentration and carrier mobility at 200°C. The carrier mobility increased from 8.74 cm²/V-s to 11.6 cm²/V-s and the carrier concentration increased from 14.2×10^{20} cm⁻³ to 22.8×10^{20} cm⁻³, respectively, as substrate temperature was raised from RT to 200°C. The resistivity of the TCO thin films is proportional to the reciprocal of the product of carrier concentration N and mobility μ :

$$\rho = \frac{1}{Ne\mu}. \quad (3)$$

Both the carrier concentration and the carrier mobility contribute to the conductivity. As substrate temperature was raised from RT to 200°C, the resistivity decreased from 2.44×10^{-3} Ω-cm to 0.65×10^{-3} Ω-cm. The minimum resistivity of the GZO thin films at a substrate temperature of 200°C is mainly caused by the carrier concentration and mobility being at their maximum.

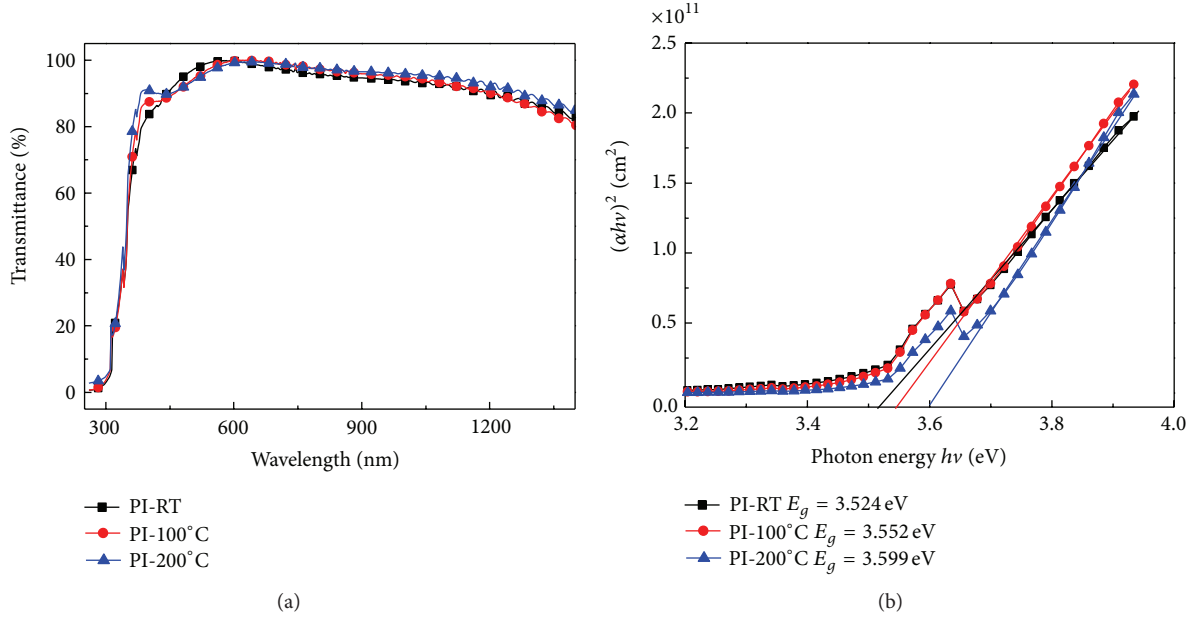
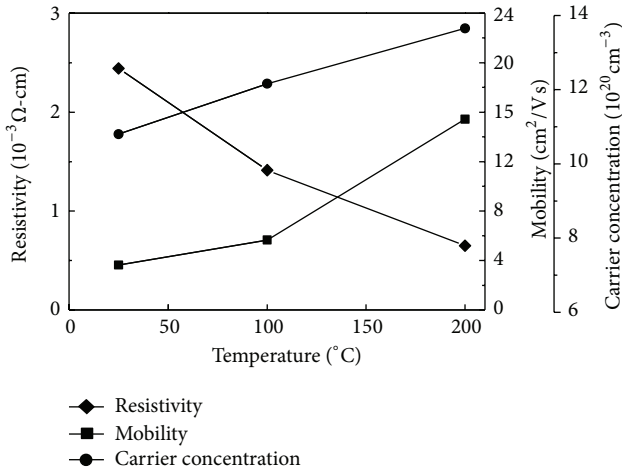

 FIGURE 5: (a) Transmittance and (b) $(\alpha h\nu)^2$ versus $h\nu - E_g$ plots of the GZO thin films as a function of substrate temperature.


FIGURE 6: Carrier mobility, carrier concentration, and resistivity of the GZO thin films as a function of substrate temperature.

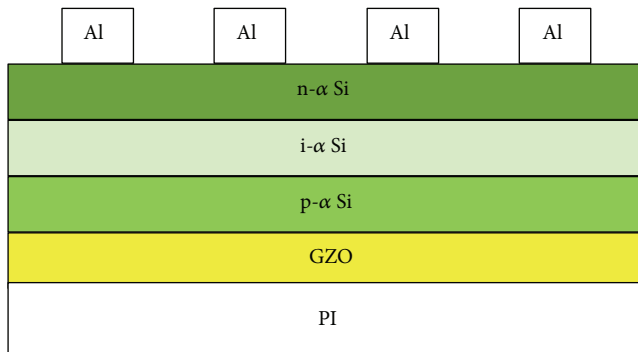

 FIGURE 7: Structure of the superstrate p-i-n α -Si:H thin-film solar cells.

 TABLE 1: Values of open-circuit voltage (V_{oc}), short-circuit current density (J_{sc}), fill factor (F.F.), and efficiency (η) for solar cells with RT-deposited, 100°C-deposited, and 200°C-deposited GZO thin films.

	V_{oc} (mV)	J_{sc} (mA/cm ²)	F.F.	η (%)
PI-RT	0.797	9.11	0.578	4.15 \pm 0.13
PI-100°C	0.790	9.13	0.580	4.20 \pm 0.19
PI-200°C	0.785	10.13	0.588	4.65 \pm 0.10

Superstrate p-i-n α -Si:H thin-film solar cells were fabricated using a single-chamber plasma-enhanced chemical vapor deposition unit at 200°C to demonstrate the optoelectrical properties of the GZO thin film. Figure 7 shows the structure of the fabricated α -Si amorphous silicon thin-film solar cells; no antireflective coatings were deposited on the cells. Figure 8 shows the measured current-voltage characteristics of the solar cells under illumination. Table 1 lists the values of open-circuit voltage (V_{oc}), short-circuit current density (J_{sc}), fill factor (F.F.), and efficiency (η) for the devices using the developed GZO thin films as the front transparent conductive thin films. However, the V_{oc} value had no apparent change and the J_{sc} value apparently increased as substrate temperature of the GZO thin films increased from 100°C to 200°C. The efficiency of the solar cells increased from 4.15% to 4.20% as substrate temperature of the GZO thin films increased from RT to 100°C. Moreover, the efficiency was raised to 4.65% as the GZO thin film was deposited at 200°C. The efficiency of the fabricated solar cells apparently depends on substrate temperature of the GZO thin films. Many reasons will cause the improvement in the efficiency of the α -Si:H thin-film solar cells. In this study, the greater efficiency is mainly ascribable to the results in Figures 2, 5, and 6.

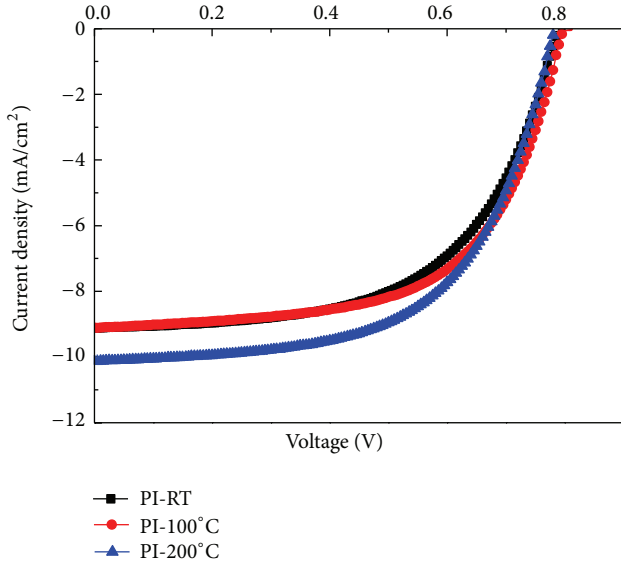


FIGURE 8: Current-voltage characteristics of the p-i-n α -Si:H thin-film solar cells under illumination.

From the cross-section (Figure 2) of the GZO thin films, the nanobar along the up direction will have the more optical waveguide function than the irregular plate with no specific direction, which may scatter the photons in any direction. As 200°C-deposited GZO thin films are used as the electrodes, more photons will reach the solar cells' optical absorption layer to generate more electron-hole pairs and improve the efficiency of the solar cells. As the GZO thin films have the higher transmittance ratio (Figure 5), also the more photons will improve the efficiency of the solar cells. The third reason from Figure 6 is that the smaller value of resistivity of the contact electrodes (GZO thin films) can cause the fabricated solar cells having more short-circuit current density; then the efficiency of the fabricated solar cells increases. This is proved by the I - V curves shown in Figure 8 and Table 1, where the J_{sc} value increases with decreasing in the resistivity of the GZO thin films.

4. Conclusion

In this study, the GZO thin films were deposited on flexible PI substrates and their properties were well developed. As substrate temperatures increased from RT to 200°C, the FWHM values for the (002) peak of the GZO thin films decreased from 0.412 to 0.296; the crystallization sizes increased from 20.2 nm to 28.1 nm; the carrier mobility 8.74 $\text{cm}^2/\text{V}\cdot\text{s}$ to 11.6 $\text{cm}^2/\text{V}\cdot\text{s}$; the carrier concentration increased from $14.2 \times 10^{20} \text{ cm}^{-3}$ to $22.8 \times 10^{20} \text{ cm}^{-3}$; and the resistivity decreased from $2.44 \times 10^{-3} \Omega\cdot\text{cm}$ to $0.65 \times 10^{-3} \Omega\cdot\text{cm}$, respectively. The Burstein-Moss shift theorem was used to prove that as substrate temperatures increased from RT to 200°C, the E_g value shifting from 3.524 eV to 3.599 eV was caused by the increase of carrier concentration increasing from $14.2 \times 10^{20} \text{ cm}^{-3}$ to $22.8 \times 10^{20} \text{ cm}^{-3}$. Finally, the α -Si thin-film solar cells were successfully fabricated on the GZO-deposited

PI substrates. As substrate temperatures increased from RT to 200°C, the J_{sc} value increased from 9.11 mA/cm^2 to 10.13 mA/cm^2 and the η value increased from 4.15 to 4.65, respectively.

Acknowledgments

The authors acknowledge financial supports of NSC 102-2622-E-390-002-CC3 and NSC 102-2221-E-390-027.

References

- [1] U. Ozgur, Y. I. Alivov, C. Liu et al., "A comprehensive review of ZnO materials and devices," *Journal of Applied Physics*, vol. 98, no. 4, Article ID 041301, 2005.
- [2] J.-I. Nomoto, T. Hirano, T. Miyata, and T. Minami, "Preparation of Al-doped ZnO transparent electrodes suitable for thin-film solar cell applications by various types of magnetron sputtering depositions," *Thin Solid Films*, vol. 520, no. 5, pp. 1400–1406, 2011.
- [3] Y. Tokita, S. Chaisitsak, A. Yamada, and M. Konagai, "High-efficiency Cu(In,Ga)Se₂ thin-film solar cells with a novel In(OH)₃:Zn²⁺ buffer layer," *Solar Energy Materials and Solar Cells*, vol. 75, no. 1-2, pp. 9–15, 2003.
- [4] E. Fortunato, A. Gonçalves, A. Pimentel et al., "Zinc oxide, a multifunctional material: from material to device applications," *Applied Physics A*, vol. 96, no. 1, pp. 197–205, 2009.
- [5] R. Martins, P. Almeida, P. Barquinha et al., "Electron transport and optical characteristics in amorphous indium zinc oxide films," *Journal of Non-Crystalline Solids*, vol. 352, no. 9–20, pp. 1471–1474, 2006.
- [6] C. C. Huang, F. H. Wang, and C. F. Yang, "Effects of deposition temperature and hydrogen flow rate on the properties of the Al-doped ZnO thin films and amorphous silicon thin-film solar cells," *Applied Physics A*, vol. 112, no. 4, pp. 877–883, 2013.
- [7] C.-C. Chen, C.-C. Tsao, Y.-C. Lin, and C.-Y. Hsu, "Optimization of the sputtering process parameters of GZO films using the Grey-Taguchi method," *Ceramics International*, vol. 36, no. 3, pp. 979–988, 2010.
- [8] S. Liang and X. Bi, "Structure, conductivity, and transparency of Ga-doped ZnO thin films arising from thickness contributions," *Journal of Applied Physics*, vol. 104, no. 11, Article ID 113533, 2008.
- [9] V. Assunção, E. Fortunato, A. Marques et al., "Influence of the deposition pressure on the properties of transparent and conductive ZnO:Ga thin-film produced by r.f. sputtering at room temperature," *Thin Solid Films*, vol. 427, no. 1-2, pp. 401–405, 2003.
- [10] F. H. Wang, C. C. Huang, C. F. Yang, and H. T. Tzeng, "Optical and electrical properties of the different magnetron sputter power 300°C deposited-ZnO thin films and applications in p-i-n α -Si:H thin-film solar cells," *International Journal of Photoenergy*, vol. 2013, Article ID 270389, 7 pages, 2013.
- [11] R. Martins, L. Raniero, L. Pereira et al., "Nanostructured silicon and its application to solar cells, position sensors and thin film transistors," *Philosophical Magazine*, vol. 89, no. 28–30, pp. 2699–2721, 2009.
- [12] E. Fortunato, A. Gonçalves, A. Marques et al., "New developments in gallium doped Zinc oxide deposited on polymeric substrates by RF magnetron sputtering," *Surface and Coatings Technology*, vol. 180–181, no. 1, pp. 20–25, 2004.

- [13] L. V. Azaroff, *Element of X-Ray Crystallography*, McGraw-Hill, New York, NY, USA, 1968.
- [14] N. Serpone, D. Lawless, and R. Khairutdinov, "Size effects on the photo physical properties of colloidal anatase TiO_2 particles: size quantization or direct transitions in this indirect semiconductor," *Journal of Physical Chemistry*, vol. 99, no. 45, pp. 16646–16654, 1995.
- [15] Y. Igasaki and H. Saito, "Substrate temperature dependence of electrical properties of ZnO:Al epitaxial films on sapphire (1210)," *Journal of Applied Physics*, vol. 69, no. 4, pp. 2190–2195, 1991.

Research Article

Optimal Color Stability for White Organic Light-Emitting Diode (WOLED) by Using Multiple-Ultra-Thin Layers (MUTL)

Kan-Lin Chen,¹ Chien-Jung Huang,² Wen-Ray Chen,³ Fong-Yi Lin,²
Teen-Hang Meen,³ and Chih-Chieh Kang⁴

¹ Department of Electronic Engineering, Fortune Institute of Technology, Kaohsiung 83160, Taiwan

² Department of Applied Physics, National University of Kaohsiung, Kaohsiung 81148, Taiwan

³ Department of Electronic Engineering, National Formosa University, Hu-Wei, Yunlin 63201, Taiwan

⁴ Department of Electro-Optical Engineering, Southern Taiwan University of Science and Technology, Tainan 71005, Taiwan

Correspondence should be addressed to Kan-Lin Chen; klchen@fotech.edu.tw and Chien-Jung Huang; chien@nuk.edu.tw

Received 15 September 2013; Accepted 3 October 2013

Academic Editor: Liang-Wen Ji

Copyright © 2013 Kan-Lin Chen et al. This is an open access article distributed under the Creative Commons Attribution License, which permits unrestricted use, distribution, and reproduction in any medium, provided the original work is properly cited.

The work demonstrates the improvement of color stability for white organic light-emitting diode (WOLED). The devices were prepared by vacuum deposition on ITO-glass substrates. These guest materials of 5,6,11,12-tetraphenylnaphthacene (Rubrene) were deposited in 4,4'-bis(2,2-diphenyl vinyl)-1,1'-biphenyl (DPVBi), resulting in an emitting layer. Experimental results reveal that the properties in the multiple-ultra-thin layer (MUTL) are better than those of the emitting layer with a single guest material, reaching the commercial white-light wavelength requirement of 400–700 nm. The function of the MUTL is as the light-emitting and trapping layer. The results show that the MUTL has excellent carrier capture effect, leading to high color stability of the device at various applied voltages. The Commissions Internationale De L'Eclairage (CIE) coordinate of this device at 3~7 V is few displacement and shows a very slight variation of (0.016, 0.009). The CIE coordinates at a maximal luminance of 9980 cd/m² are (0.34, 0.33).

1. Introduction

Since Tang and Vanslyke first reported on a multilayer organic light-emitting diode (OLED), OLEDs have been widely investigated for their potential application in flat-panel displays [1]. OLED has attracted attention owing to its advantageous emission over a wide visible range and its application in flat-panel displays that are driven at low voltage [2–4]. Furthermore, the development of white organic light-emitting diode (WOLED) with high brightness and good color purity is necessary, because these devices can be employed not only as illumination light source but also as backlight source candidate for next generation flat-panel displays. However, the WOLED lighting technology has been extensively studied. To achieve white emission from OLEDs, various several methods have been tried to obtain optimal WOLEDs, for example, using two complementary colors (blue and yellow), multi-layer stack of three primary colors (red, green, and blue) and

two or three colors of the dye doped into single host material [5–7]. In the co-deposition process, accurately controlling the evaporation rate and the concentration of the two or more materials is not easy, resulting in its poor performance. However, non-doped technique can accurately control to avoid the above problems in the fabrication processes.

In this work, we use nondoped method to fabricate WOLEDs with a multiple-ultra-thin layer (MUTL) structure. The 5,6,11,12-tetraphenylnaphthacene (Rubrene) material was used as yellow light sources in MUTL structure. In addition, the quantum efficiency of the Rubrene can be close to 100% [8–11]. And then the material of 4,40-bis (2,20-diphenyl vinyl)-1,10-biphenyl (DPVBi) is well-known blue fluorescent material. However, DPVBi is not only emitting but also transferring the incomplete energy from DPVBi to the Rubrene. So far the study of fluorescence WOLED (FWOLED) based on the non-doped multiple-ultra-thin layer (MUTL) has not yet

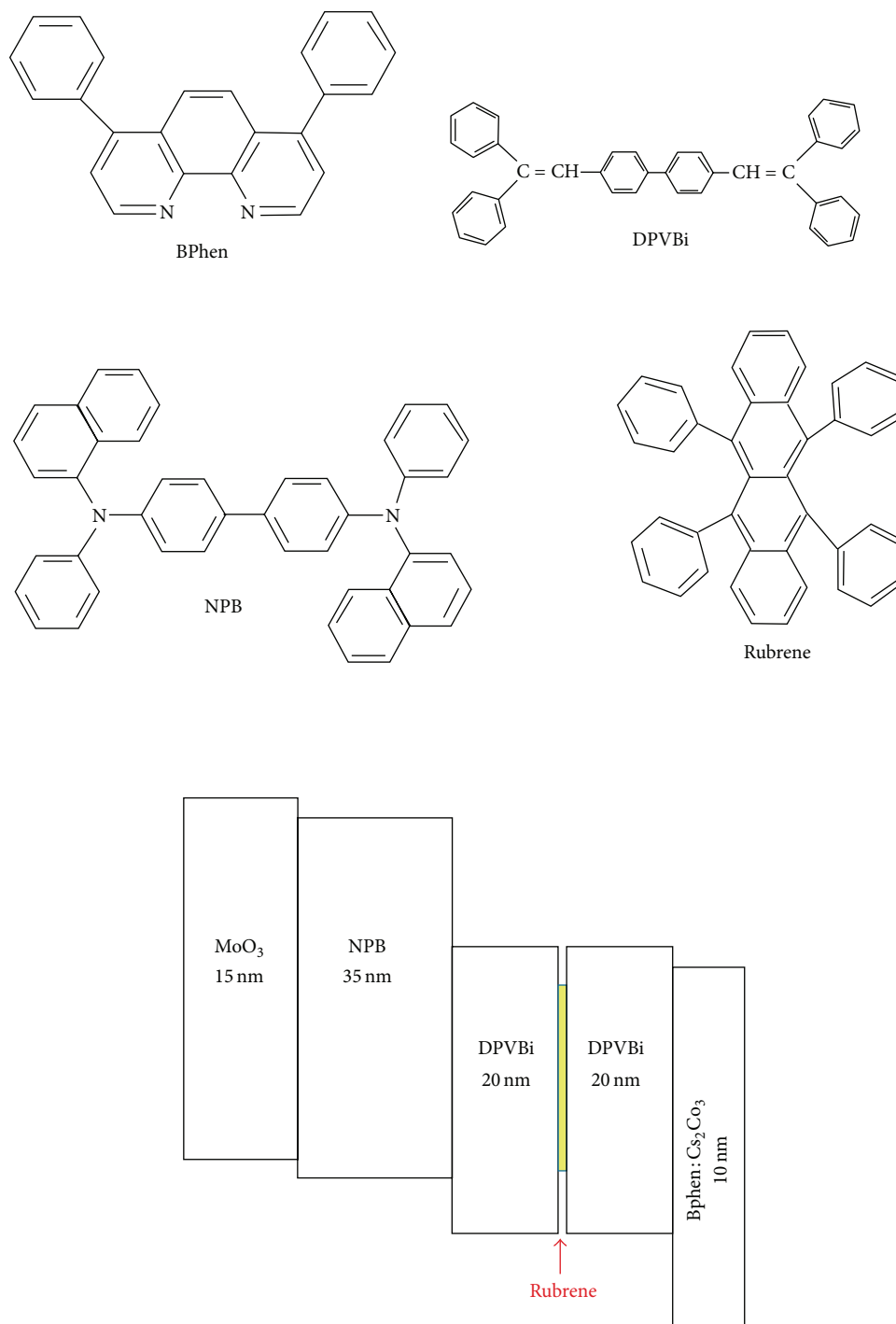


FIGURE 1: The chemical structures of organic materials and the structures of the device in the energy band diagrams of the multilayer (Rubrene = 0.1, 0.2 and 0.3 nm) for WOLEDs.

been established. Therefore, this paper concerns a simple process for the non-doped FWOLEDs with a MUTL structure, ensuring that the improvement of FWOLEDs performance was highly efficient due to the good capture efficiency of charge carrier for the guest material. Besides, a detailed investigation of the transmission mechanism for the MUTL structure on the electroluminescence (EL) and the color stability of FWOLEDs is presented.

2. Experimental

Figure 1 shows the chemical structures of organic materials and the structures of the device that are used in this study. Indium tin oxide (ITO) coated glass with a sheet resistance of approximately $15 \Omega/\text{sq}$ was consecutively cleaned in ultrasonic bath containing detergent water, acetone, ethanol and deionized (DI) water for 20 min each and then dried with

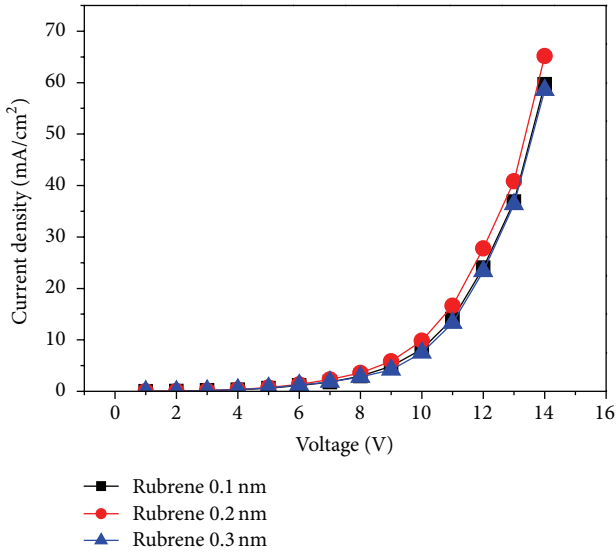


FIGURE 2: The current density-voltage (J-V) characteristics of the devices with various thicknesses of Rubrene layer.

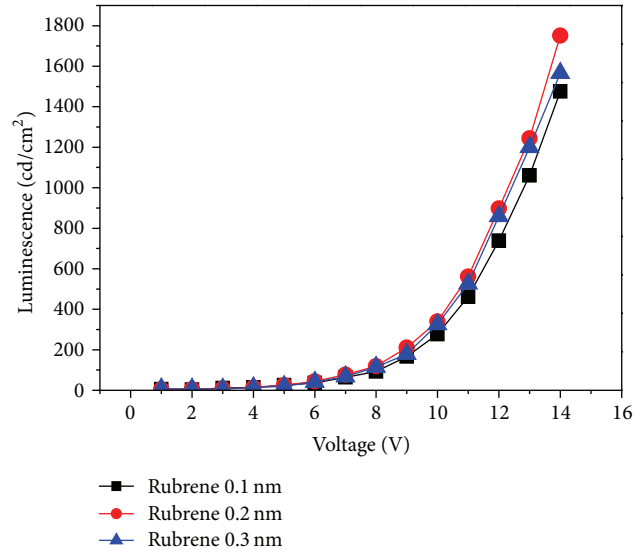


FIGURE 3: The luminance-voltage curves of the devices with various thicknesses of Rubrene layer.

a nitrogen (N_2) flow. All organic layers were sequentially evaporated onto the ITO coated-glass substrate at high-vacuum (1×10^{-6} Torr) thermal evaporation. Thermal deposition rates for organic materials, inorganic materials, and Al were about $1 \text{ \AA}/\text{sec}$, $1 \text{ \AA}/\text{sec}$, and $10 \text{ \AA}/\text{sec}$, respectively. The evaporation rate and thickness of the thin films were controlled using a quartz-crystal monitor system (Sigma, SID-142) in this work.

The active area of the device was 0.6 cm^2 . To measure the properties of the device, a voltage was applied by using a Keithley 2400 programmable voltage-current source (Keithley SourceMeter 2400, USA). EL spectra and Commissions Internationale De L'Eclairage (CIE) coordination of the devices were measured by PR655 spectra scan spectrometer (Kollmorgen Instrument PR655, USA). All measurements were made at room temperature without encapsulating the devices.

3. Results and Discussion

In order to fabricate WOLED, we first attempted to obtain the optimizing thicknesses of Rubrene. Generally, yellow light is required as one of the two-color complementary to obtain white light. The structure of the device in energy band diagrams of the multilayer for WOLEDs is shown in Figure 1. The thicknesses of Rubrene layer change from 0.1 to 0.3 nm at fixing other organic layers. Figure 2 shows the current density-voltage (J-V) characteristics of the devices with various thicknesses of Rubrene layer. The current density of the devices at 14 V, whose thicknesses of Rubrene layer are 0.1–0.3 nm are 59.6, 65.1 and $58.5 \text{ mA}/\text{cm}^2$, respectively. It can be observed that the device whose thickness of Rubrene layer is 0.2 nm has the best J-V characteristics as compared with other devices. Figure 3 shows the luminance-voltage (L-V) curves of the devices with various thicknesses of Rubrene

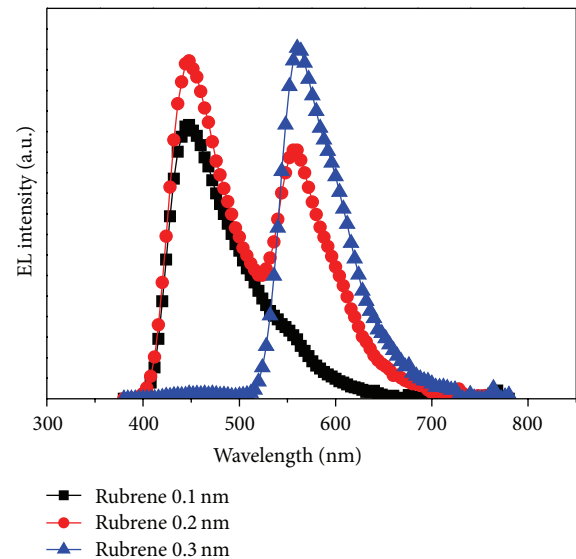


FIGURE 4: The electroluminescence spectra of the devices with various thicknesses of Rubrene layer at 14 V.

layer. The maximum luminance of devices is 1476, 1806, and $1566 \text{ cd}/\text{m}^2$, respectively. The maximum luminance is $1806 \text{ cd}/\text{m}^2$ at 14 V and the CIE coordinate is (0.270, 0.286) when Rubrene layer is 0.2 nm. Besides, the luminance of the device with Rubrene layer of 0.2 nm is higher than other devices at the same voltage. The phenomenon tells us that proper thickness of Rubrene layer results in better luminance for WOLED. The device with Rubrene layer of 0.2 nm is ideal because of the best luminance in other devices at the same applying voltage. However, the device with proper thickness of Rubrene layer can produce a high luminance. Figure 4 shows normalized electroluminescence spectra of the devices at 14 V with various thicknesses of

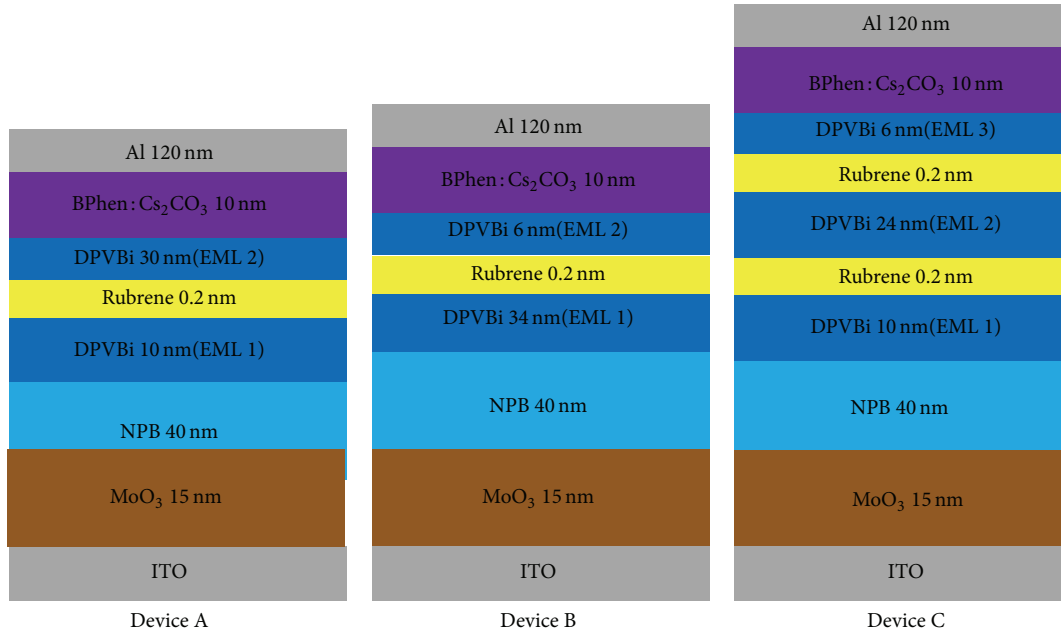


FIGURE 5: The structure of WOLEDs.

Rubrene layer at 0.1, 0.2 and 0.3 nm, respectively. It is well known that the peak wavelengths of the DPVBi layer and the Rubrene layer were 436 nm and 556 nm, respectively [12, 13]. It can be observed that light emission of three devices is composed of yellow light emission and blue light emission. In addition, it can be found that the devices whose thicknesses of Rubrene layer are 0.1 and 0.3 nm all have an EL peak without the balances of blue and yellow emission intensity. The device with Rubrene layer of 0.2 nm has a CIE coordinate of (0.270, 0.286) which lies in about the blue color zone. However, the device with 0.2 nm Rubrene layer at 14 V has better luminance of 1806 cd/m^2 . In this study, the white light emission of device consists of the blue emission layer and the yellow emission layer. The yellow emission of the device was caused by the Rubrene layer, which was inserted in the light-emitting layer of DPVBi to form the structure of DPVBi (10 nm EML1)/Rubrene (0.2 nm)/DPVBi (30 nm EML2). If the intensity of blue emission was higher than that of the yellow emission, then the CIE coordinates of the device were unstable. This is due to the fact that the Rubrene layer in the device cannot trap enough electrons and holes to generate exciton. Therefore, optimum complementary color of the blue and the yellow emission intensity was not achieved. According to the results obtained above, the best recombination zone was in the EML2 of the device. To achieve an objective of the optimal color stability, three structures of devices, as shown in Figure 5, are promoted and fabricated as follows.

(a) ITO/Molybdenum trioxide (MoO_3 ; 15 nm)/N,N0-bis-(1-naphthyl)-N,N0-biphenyl-1,10-biphenyl-4,40-diamine (NPB; 40 nm)/DPVBi (10 nm)/Rubrene

(0.2 nm)/DPVBi (30 nm)/4,7-Diphenyl-1,10-phenanthroline: cesium carbonate (BPhen: Cs_2CO_3 = 4:1; 10 nm)/Aluminum (Al; 120 nm).

(b) ITO/ MoO_3 (15 nm)/NPB (40 nm)/DPVBi (34 nm)/Rubrene (0.2 nm)/DPVBi (6 nm)/BPhen: Cs_2CO_3 = 4:1 (10 nm)/Al (120 nm).

(c) ITO/ MoO_3 (15 nm)/NPB (40 nm)/DPVBi (10 nm)/Rubrene (0.2 nm)/DPVBi (24 nm)/Rubrene (0.2 nm)/DPVBi (6 nm)/BPhen: Cs_2CO_3 = 4:1 (10 nm)/Al (120 nm).

The current density-voltage-luminance characteristics of devices A~C are shown in Figures 6(a) and 6(b). The maximum current density of devices A, B, and C is 203 mA/cm^2 , 298 mA/cm^2 and 355 mA/cm^2 at 7 V, respectively. It can be seen that current density of device C exceeds the other two devices at the same voltage. This is the reason why device C has larger luminance. The maximum luminance of the devices A~C is 6010 cd/m^2 , 7768 cd/m^2 , and 9980 cd/m^2 , respectively. It can be explained that the holes were accumulated at the Rubrene/EML3 interface and that the electrons were accumulated at the BPhen: Cs_2CO_3 layer, indicating that the electric field can be formed in EML3. The electric field is favorable for electron injection into the emission layer. However, it is expected that the holes were trapped and confined in the Rubrene/EML3 interface and electron injection thus enhanced, resulting that an improved carrier balance was achieved.

EL spectra and CIE coordinates during the applied voltage of 3~7 V are shown in Figure 7. It can be found that there is a balance or complementary color between blue emission and yellow emission, as shown in Figure 7(a). Besides, a pure white light emission with CIE coordinates of (0.331, 0.332) is observed at the applied voltage of 5 V. When the applied

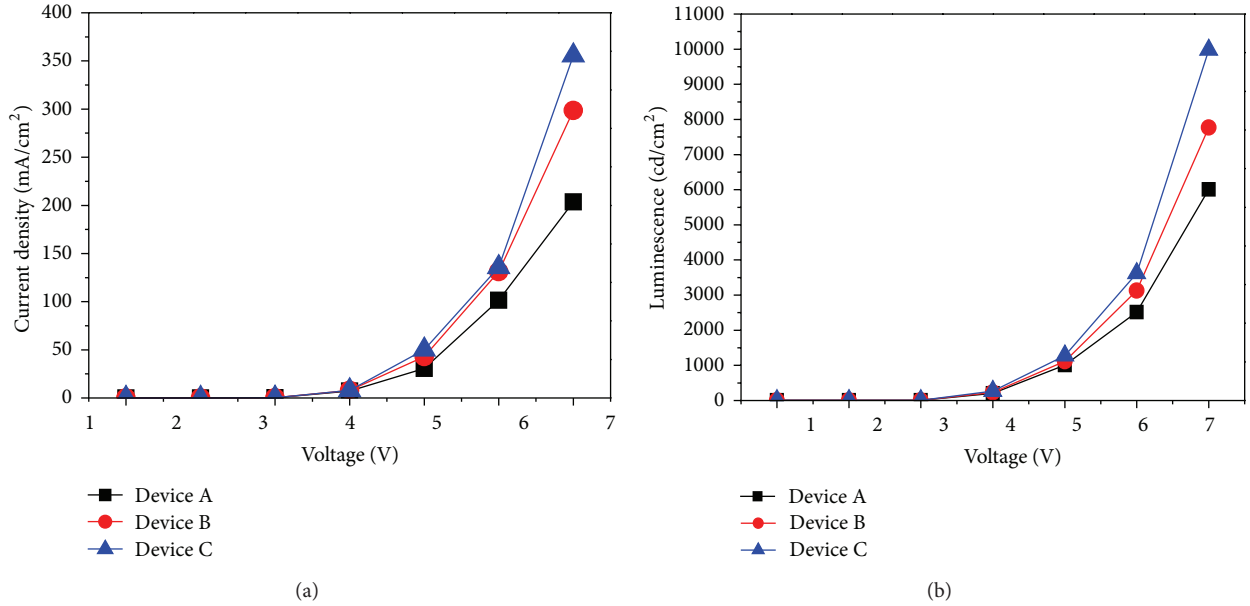


FIGURE 6: (a) The current density versus bias voltage (J-V) characteristics of devices A~C. (b) The luminance versus voltage (L-V) characteristics of devices A~C.

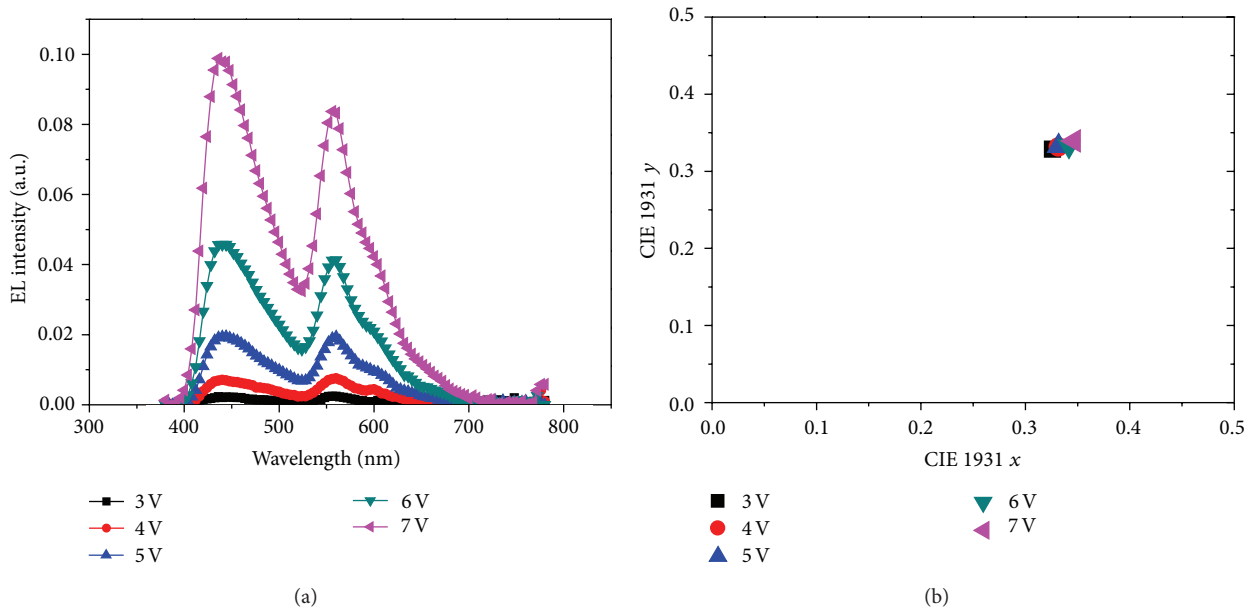


FIGURE 7: (a) The EL spectra of device C at 3~7 V applied voltage. (b) The CIE coordinates of device C at 3~7 V applied voltage.

voltage increases from 6 V to 7 V, the CIE coordinates were, respectively, (0.341, 0.332) and (0.346, 0.339), and showed a little change. This is owing to the fact that the intensity for the ratio of blue and yellow emission from EL spectra of Figure 7(a) is almost the same and about unit. Furthermore, this improvement in chromaticity can be attributed to the MUTL structure of the emission layer, resulting in a balance in the relative intensity of blue and yellow emission. Thus, by introducing a MUTL structure in the emission layer, the WOLED has more stable spectra characteristics than that of devices A and B with the increase of bias voltage.

This is due to the reason that the injection of holes and electrons was enhanced by the MUTL structure and that the MUTL structure can enhance charge carrier trapping in the EML1/Rubrene, EML2/Rubrene and Rubrene/EML3 interfaces. And then the enhanced carrier injection was because of electric fields induced by the accumulated carrier between interfaces of the MUTL. This result is similar to the result discussed in other literature [14–17]. In other words, the excitons formed from electrons and holes can widely distribute in the entire emission layer. As is expected, the excitons of Rubrene and DPVBi layers will increase and

TABLE 1: Various characteristics of devices A–C.

	Device A	Device B	Device C
Turn-on voltage (V)	3.5	3.2	3
Operating voltage (V)	4.1	3.9	3.5
Maximum luminance (cd/m ²)	6010	7768	9980
Maximum Current density (cd/m ²)	203	298	355

reach balance, indicating that the MUTL can enhance color stability of CIE coordinates and chromaticity of pure white emission. However, the displacement of the CIE coordinates during the applied voltage of 3~7 V is almost null.

All the above data, can be summarized in Table 1. From Table 1, it is found that the MUTL structure can enhance color stability of CIE coordinates and chromaticity of pure white emission. Furthermore, these results show that a high luminance can be achieved with improved carrier balance in the emission zone. Besides, the operating voltage of device C is lower than that of other devices due to the presence of the MUTL structure, resulting in more electron injection and balance.

4. Conclusions

In summary, white light emission was achieved by inserting the MUTL structure in the emission layer of WOLED. Experimental results reveal that the properties in the multiple-ultrathin layer (MUTL) are better than those of the emitting layer with a single guest material. The carrier trapping of the MUTL structure can more effectively confine electrons and holes in the emission layer. Consequently, the excitons of Rubrene and DPVBi layers will increase and reach balance; that is, there is a balance or complementary color in blue emission and yellow emission, resulting in good color stability characteristics of WOLED at various applied voltages. A pure white emission CIE coordinates of (0.331, 0.332) can be obtained and show a little change at the applied voltage of 3~7 V. It is demonstrated that EL emission is less dependent on the applied voltage. Thus, the carrier recombination zone must be properly controlled by limiting the exciton zone to prevent the mixing of colors. However, device with a MUTL structure increased carrier tapping probability to improve carrier recombination and luminous efficiency.

Acknowledgment

This work was partially supported by the National Science Council of the Republic of China under Contract no. NSC 102-2221-E-390-019-MY2.

References

- [1] C. W. Tang and S. A. Vanslyke, "Organic electroluminescent diodes," *Applied Physics Letters*, vol. 51, no. 12, pp. 913–915, 1987.
- [2] C. J. Huang, T. H. Meen, S. L. Wu, and C. C. Kang, "Improvement of color purity and electrical characteristics by co-doping method for flexible red-light organic light emitting devices," *Displays*, vol. 30, no. 4-5, pp. 164–169, 2009.
- [3] Y. Sun, N. C. Giebink, H. Kanno, B. Ma, M. E. Thompson, and S. R. Forrest, "Management of singlet and triplet excitons for efficient white organic light-emitting devices," *Nature*, vol. 440, no. 7086, pp. 908–912, 2006.
- [4] C. J. Huang, C. C. Kang, T. C. Lee, W. R. Chen, and T. H. Meen, "Improving the color purity and efficiency of blue organic light-emitting diodes (BOLED) by adding hole-blocking layer," *Journal of Luminescence*, vol. 129, no. 11, pp. 1292–1297, 2009.
- [5] J. Kido, H. Shionota, and K. Nagai, "Single-layer white light-emitting organic electroluminescent devices based on dye-dispersed poly(N-vinylcarbazole)," *Applied Physics Letters*, vol. 67, no. 16, pp. 2281–2283, 1995.
- [6] K. Okumoto, H. Kanno, Y. Hamada, H. Takahashi, and K. Shibata, "High efficiency red organic light-emitting devices using tetraphenyl-dibenzoperiflanthene-doped rubrene as an emitting layer," *Applied Physics Letters*, vol. 89, no. 1, Article ID 013502, 2006.
- [7] G. Li and J. Shinar, "Combinatorial fabrication and studies of bright white organic light-emitting devices based on emission from rubrene-doped 4,4'-bis(2,2'-diphenylvinyl)-1,1'-biphenyl," *Applied Physics Letters*, vol. 83, no. 26, pp. 5359–5361, 2003.
- [8] H. Mattoussi, H. Murata, C. D. Merritt, Y. Iizumi, J. Kido, and Z. H. Kafafi, "Photoluminescence quantum yield of pure and molecularly doped organic solid films," *Journal of Applied Physics*, vol. 86, no. 5, pp. 2642–2650, 1999.
- [9] Y.-M. Wang, F. Teng, Z. Xu, Y.-B. Hou, S.-Y. Yang, and X.-R. Xu, "Trap effect of an ultrathin DCJTb layer in organic light-emitting diodes," *Materials Chemistry and Physics*, vol. 92, no. 2-3, pp. 291–294, 2005.
- [10] M. Matsumura and T. Furukawa, "Efficient electroluminescence from a rubrene sub-monolayer inserted between electron- and hole-transport layers," *Japanese Journal of Applied Physics I*, vol. 40, no. 5, pp. 3211–3214, 2001.
- [11] T. Li, X. Li, W. Li et al., "Tunable red emission by incorporation of a rubrene derivative in p-type and n-type hosts in organic light emitting devices," *Thin Solid Films*, vol. 517, no. 16, pp. 4629–4632, 2009.
- [12] C.-J. Huang, T.-H. Meen, K.-C. Liao, and Y.-K. Su, "The mechanism of efficiency enhancement with proper thickness of DPVBi layer for blue organic light-emitting devices (BOLED)," *Journal of Physics and Chemistry of Solids*, vol. 70, no. 3-4, pp. 765–768, 2009.
- [13] Q. Xue, S. Zhang, G. Xie et al., "Efficient fluorescent white organic light-emitting devices based on a ultrathin 5,6,11,12-tetraphenyl-naphthalene layer," *Solid-State Electronics*, vol. 57, no. 1, pp. 35–38, 2011.
- [14] L. Li, J. Yu, X. Tang, T. Wang, W. Li, and Y. Jiang, "Efficient bright white organic light-emitting diode based on non-doped ultrathin 5,6,11,12-tetraphenyl-naphthalene layer," *Journal of Luminescence*, vol. 128, no. 11, pp. 1783–1786, 2008.
- [15] X. Tang, J. Yu, L. Li, L. Zhang, and Y. Jiang, "White organic light-emitting diodes with improved performance using phosphorescent sensitizer and ultrathin fluorescent emitter," *Displays*, vol. 30, no. 3, pp. 123–127, 2009.
- [16] S.-H. Yang, B.-C. Hong, and S.-F. Huang, "Luminescence enhancement and emission color adjustment of white organic light-emitting diodes with quantum-well-like structures," *Journal of Applied Physics*, vol. 105, no. 11, Article ID 113105, 2009.
- [17] Z. Ma, J. Yu, L. Li, and Y. Jiang, "Non-doped white organic light-emitting diodes consisting of three primary colors based on a bipolar emitter," *Displays*, vol. 33, no. 1, pp. 42–45, 2012.

Research Article

Study of Small Molecule Organic Solar Cells Performance Based on Boron Subphthalocyanine Chloride and C₆₀

Jhong-Ciao Ke,¹ Yeong-Her Wang,¹ Kan-Lin Chen,²
Pao-Hsun Huang,³ and Chien-Jung Huang³

¹ Institute of Microelectronics, Department of Electrical Engineering, National Cheng Kung University, Tainan 70101, Taiwan

² Department of Electronic Engineering, Fortune Institute of Technology, Kaohsiung 83160, Taiwan

³ Department of Applied Physics, National University of Kaohsiung, Nanzih, Kaohsiung 81148, Taiwan

Correspondence should be addressed to Chien-Jung Huang; chien@nuk.edu.tw

Received 15 September 2013; Accepted 3 October 2013

Academic Editor: Teen-Hang Meen

Copyright © 2013 Jhong-Ciao Ke et al. This is an open access article distributed under the Creative Commons Attribution License, which permits unrestricted use, distribution, and reproduction in any medium, provided the original work is properly cited.

The small molecule organic solar cells based on boron subphthalocyanine chloride (SubPc) and C₆₀ by varying the SubPc layer thickness from 3 nm to 21 nm were fabricated. The maximum power conversion efficiency (PCE) of 1.47% was obtained at the 9 nm SubPc layer under 100 mW/cm² AM1.5G illumination, which is attributed to reach the optimal balance between the light absorption efficiency and the carrier collection efficiency in the device. To increase the open-circuit voltage (V_{oc}) of device, the molybdenum oxide (MoO₃) and poly(3,4-ethylenedioxythiophene):poly(styrene sulfonate) were inserted between the indium tin oxide and the SubPc layer, respectively. Finally, the V_{oc} of device increased from 0.46 V to 1 V by using MoO₃ buffer layer, resulting in the fact that the PCE of device increased from 1.47% to 2.52%.

1. Introduction

Solar cells are considered as an important source of renewable energy to solve the shortage of energy today. Various solar cells have been developed and one of the most promising solar cells is organic solar cells (OSCs). OSCs have received much attention recently due to several potential applications, including compatibility with flexible substrates, low-manufacturing cost, and roll-to-roll fabrication process [1–3]. In organic materials, light absorption leads to the formation of excitons (bound electron-hole pairs) rather than the free electron-hole pairs. The excitons dissociation occurred at the donor-acceptor interfaces, using the difference of energy level to overcome the binding energy of excitons, leading to the free electron and hole in device which can be extracted to the electrodes. Since Tang reported the first two-layer heterojunction OSC [4], the power conversion efficiency of OSCs had increased steadily in the recent years by using new materials and the different device structures [5–8]. The shortage of organic materials is narrow absorption range in visible region, which leads to the low short-circuit current

density (J_{sc}). Therefore, to get the highest J_{sc} for the best performance, optimizing the device structure is necessary [9, 10].

Boron subphthalocyanine chloride (SubPc) is a promising donor material for the small molecule OSCs due to its deep highest occupied molecular orbital (HOMO) energy level, which can get the higher V_{oc} of device. In this paper, we used SubPc as donor and changed the thickness of SubPc layer to investigate the influences on performance and to obtain the optimal thickness of SubPc for the best efficiency. In addition, the V_{oc} variation of device with different SubPc layer thicknesses and anode buffer layers is also investigated in detail.

2. Experimental

The indium tin oxide (ITO)/glass substrates (with a sheet resistance of 7 Ω /sq) are sequentially cleaned by ultrasonic treatment in acetone, isopropyl alcohol, and deionized water and blown by N₂ gas before deposition. The layer of poly(3,4-ethylenedioxythiophene):poly(styrene sulfonate)

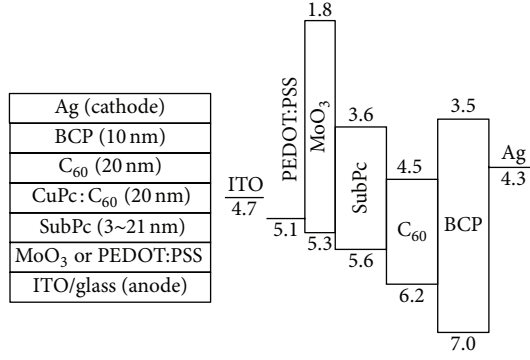


FIGURE 1: The configuration of device and the energy level diagram in the study.

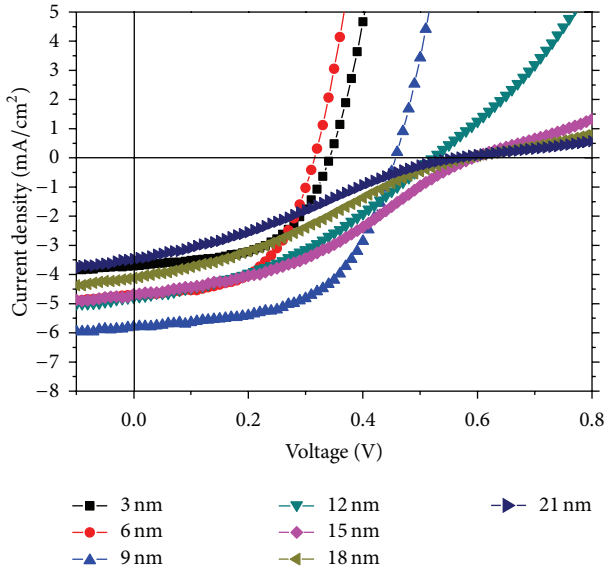


FIGURE 2: The J - V characteristics of devices (ITO/SubPc/ C_{60} (30 nm)/BCP (10 nm)/Ag) with different SubPc layer thicknesses (3~21 nm).

(PEDOT:PSS) was formed by a spin-coating method. The spin coatings were performed at a rotation rate of 3500 rpm for 20s. The organic materials in the device were MoO₃ (99%), SubPc (99%), C₆₀ (99.95%), and BCP (99%), which were used without further purification. All layers in OSC were deposited at a deposition rate of 0.02~0.04 nm/s below the pressure of 6.4×10^{-4} Pa. The Ag as a cathode was deposited at a deposition rate of 0.2~0.3 nm/s by thermal evaporation through a shadow mask, giving an active area of 6 mm². The thickness of thin film was monitored by an oscillating quartz thickness monitor. The configurations of device and the energy level in this study are shown in Figure 1.

The current-voltage characteristics are measured with a Keithley 2400 sourcemeeter, under an illumination of 100 mW/cm² with an AM1.5G sun simulator. The intensity of irradiation was measured by an optical power meter. All measurements were carried out in air without any encapsulation.

TABLE 1: Photovoltaic performance parameters of devices (ITO/SubPc (3~21 nm)/C₆₀ (30 nm)/BCP (10 nm)/Ag) with different SubPc layer thicknesses.

SubPc thickness (nm)	J_{sc} (mA/cm ²)	V_{oc} (V)	FF	R_s (Ω·cm ²)	η (%)
3	3.70	0.34	0.55	17.8	0.69
6	4.70	0.32	0.54	13.0	0.82
9	5.79	0.46	0.55	14.4	1.47
12	4.77	0.52	0.38	62.8	0.95
15	4.68	0.59	0.37	127.9	1.04
18	4.12	0.58	0.30	233.9	0.72
21	3.47	0.57	0.27	326.9	0.55

3. Results and Discussion

Figure 2 showed the current density-voltage (J - V) characteristics of device (ITO/SubPc (3~21 nm)/C₆₀ (30 nm)/BCP (10 nm)/Ag) with different SubPc layer thicknesses. The performance parameters and the series resistance (R_s) were listed in Table 1. The SubPc layer thickness of device has not only influence on the amount of light absorption but also influence on the ability of carrier transportation in device. Both of light absorption and the R_s increased as the SubPc layer thickness increased. In Table 1, the J_{sc} of device increased from 3.70 mA/cm² to 5.79 mA/cm² when the SubPc layer thickness from 3 nm to 9 nm, which is attributed to the more light absorption with thicker SubPc layer. However, the advantage of SubPc as an electron donor in device was not revealed, high V_{oc} value, which will be discussed later. It was found that the R_s of device with 12 nm SubPc layer is nearly four times than that of device with 9 nm SubPc layer, indicating that the carrier extracted from SubPc to ITO became hard as the thickness of SubPc layer exceeds 9 nm. It might result from the short diffusion length of SubPc which is only about 8 nm [11]. As a result, the J_{sc} of device continually decreased from 5.79 mA/cm² to 3.47 mA/cm² corresponding to the SubPc layer thickness from 9 to 21 nm. The fill factor (FF) of device is associated with the R_s , and the change of FF is consistent with the R_s variation. As the R_s of device increased, the FF of device decreased. Finally, the optimal balance between light absorption and carrier transportation was obtained at 9 nm SubPc, resulting in higher efficiency of 1.47% at 9 nm SubPc than that of device with other SubPc layer thicknesses.

The V_{oc} of device increased as the SubPc layer thickness increased from 3 nm to 15 nm and then saturation at 0.58 ± 0.1 V from 15 nm to 21 nm. The tendency of V_{oc} variation is in agreement with the result obtained by Kim and Yim [12]. To investigate the origin of V_{oc} which varied as a function of SubPc layer thickness, the surface morphologies of different SubPc layer thicknesses deposited on ITO/glass substrate were measured. Figure 3 showed the height profiles of bare ITO, 3 nm SubPc, 6 nm SubPc, and 9 nm SubPc deposited on ITO, respectively. It can be seen that the roughness of bare ITO is as high as 7 nm, resulting in that the vacancy of ITO cannot be fully covered by the 3 nm or 6 nm SubPc layer

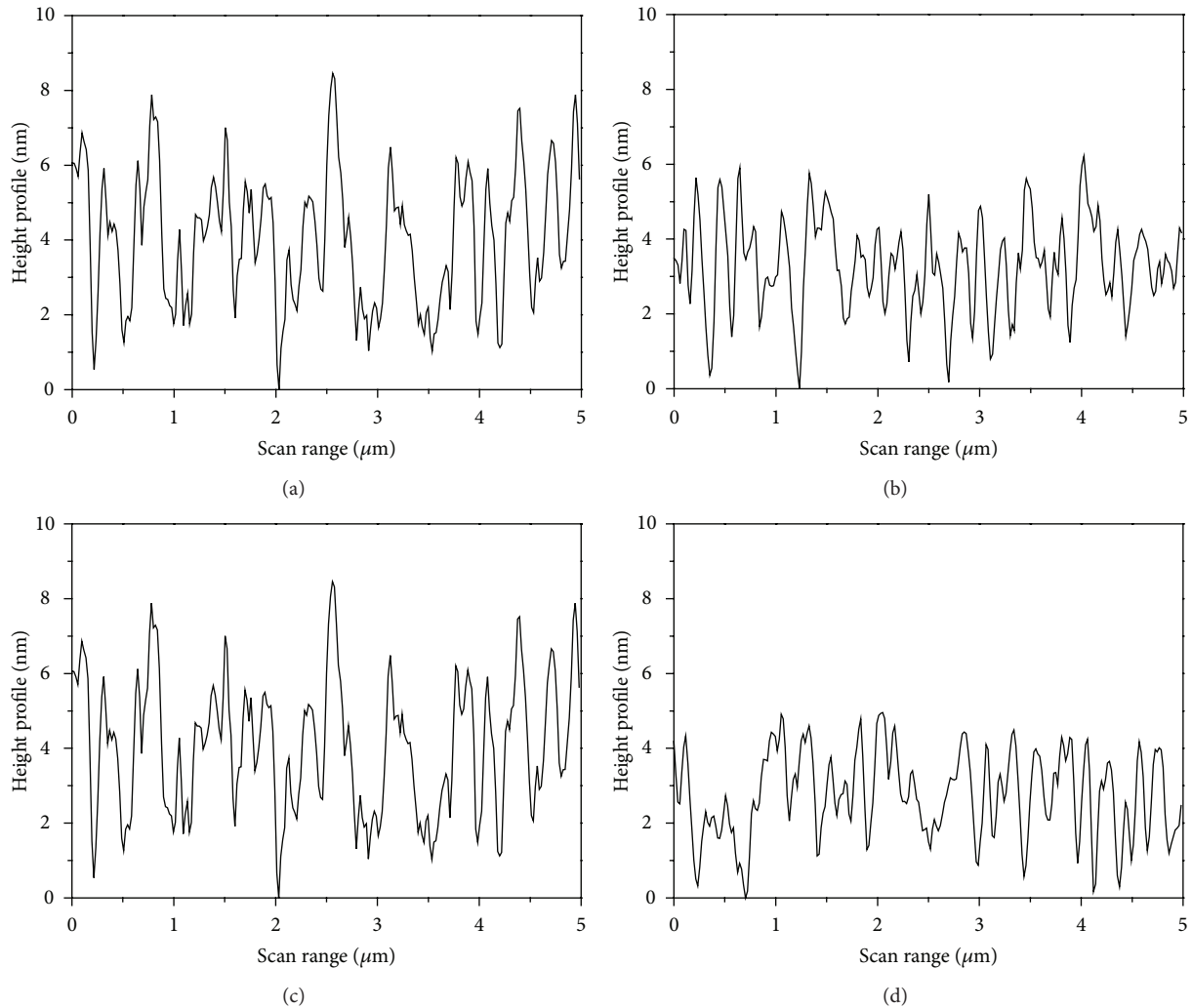


FIGURE 3: The height profiles of (a) bare ITO, (b) ITO/SubPc (3 nm), (c) ITO/SubPc (6 nm), and (d) ITO/SubPc (9 nm).

(as shown in Figures 3(b) and 3(c)). As a result, the contact between the ITO and the C_{60} after depositing C_{60} on SubPc layer cannot be avoided, causing that the V_{oc} of device with 3 nm and 6 nm SubPc is only at 0.34 V and 0.32 V, respectively. In contrast, the 9 nm SubPc layer is thicker enough to cover the roughness of ITO, which can avoid the contact between ITO and C_{60} , resulting in that the V_{oc} of device with 9 nm SubPc layer is enhanced to 0.46 V. However, the V_{oc} of device still continually increased from 0.46 V to 0.59 V as the SubPc layer thickness increased from 9 nm to 15 nm. It results from the carrier accumulation in SubPc layer, which can be realized from the R_s which dramatically increased, resulting in the increase of electric potential in SubPc layer. The V_{oc} of device was maintained in a value at SubPc layer thickness from 15 nm to 21 nm, and it is due to the fact that the amount of carrier accumulated in SubPc layer is saturated. That is to say, the balance of carrier generation and recombination was achieved at SubPc layer thickness above 15 nm, leading to that the amount of carrier is the same in SubPc layer.

However, the V_{oc} of device based on SubPc and C_{60} is still lower than that of other studies which also used the

same materials. In theorem, the maximum V_{oc} of OSCs is limited by the energy difference between the HOMO energy level of donor and the lowest unoccupied molecular orbital (LUMO) energy level of acceptor [13], and the V_{oc} in device is determined by difference of work function of electrodes within the maximum V_{oc} [14]. From Figure 1, the energy level difference between HOMO of SubPc and the LUMO of C_{60} is 1.1 V. The V_{oc} of devices with different SubPc layer thicknesses ranges from 0.32 V to 0.59 V, which is far from 1.1 V. The results were attributed to the low work function of ITO typically at 4.7 V. To improve the work function of ITO, the MoO_3 layer and the PEDOT:PSS inserted between the ITO and the SubPc layer in the device with optimal SubPc layer thickness of 9 nm, respectively. The performance parameters were summarized in Table 2. The V_{oc} of device was enhanced to 0.77 V and 1 V by inserting the PEDOT:PSS and the MoO_3 layer, respectively. The surface morphologies of bare ITO, ITO/PEDOT:PSS, and ITO/ MoO_3 were measured to further clarify whether the V_{oc} enhancement is attributed to the roughness of ITO. Figure 4 showed the AFM images of bare ITO, ITO/PEDOT:PSS, and ITO/ MoO_3 corresponding to

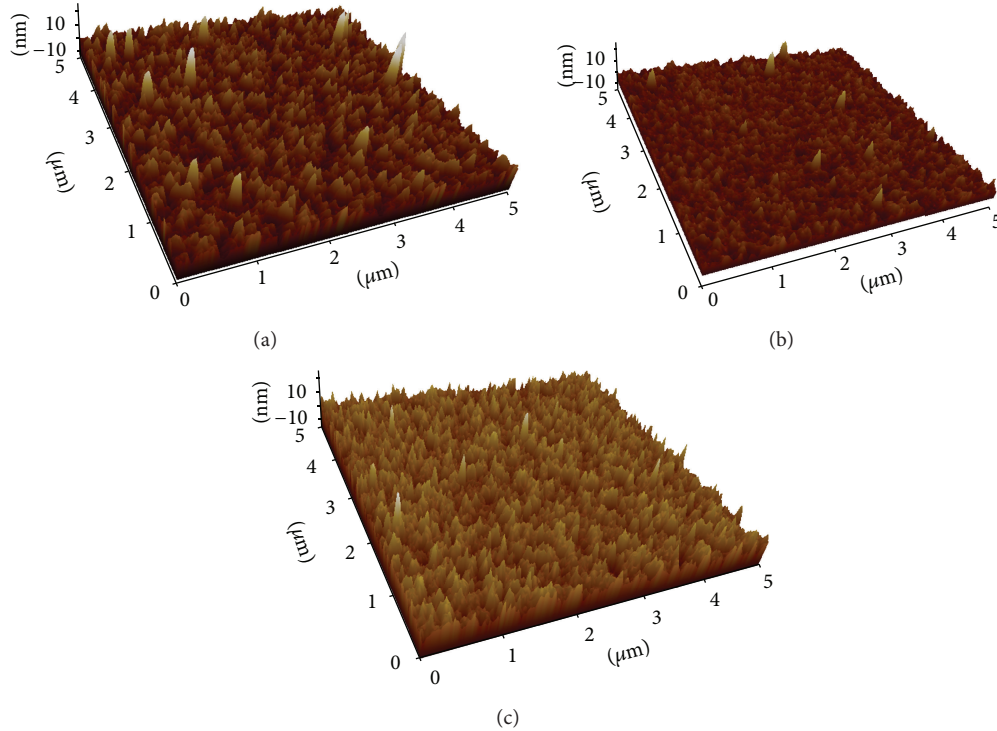


FIGURE 4: The surface morphologies of (a) bare ITO, (b) ITO/PEDOT: PSS, and (c) ITO/MoO₃.

TABLE 2: Photovoltaic performance parameters of device (ITO/PEDOT:PSS or MoO₃/SubPc (9 nm)/C₆₀ (30 nm)/BCP (10 nm)/Ag) with different buffer layers.

Buffer layer	J_{sc} (mA/cm ²)	V_{oc} (V)	FF	R_s (Ω·cm ²)	η (%)
PEDOT:PSS	4.12	0.77	0.35	20.06	1.13
MoO ₃	4.56	1	0.55	31.7	2.52

the root mean square roughness of 3.73 nm, 2.08 nm, and 3.92 nm, respectively. It can be seen that the MoO₃ cannot smooth the ITO surface, indicating that the enhancement of V_{oc} was not related to the roughness of ITO. As a result, the improvement of V_{oc} can be ascribed to the work function of ITO modification by the PEDOT:PSS and the MoO₃. In addition, the V_{oc} of device using MoO₃ as a buffer layer is higher than that of device with PEDOT:PSS buffer layer due to the fact that the HOMO energy level of MoO₃ is deeper than that of PEDOT:PSS. The PEDOT:PSS layer was not optimized here, causing that the efficiency of device decreased from 1.47% to 1.13% by using PEDOT:PSS buffer layer. Eventually, the advantage of small molecule OSC based on the SubPc and the C₆₀, high V_{oc} , was achieved by depositing the MoO₃ layer on the ITO, resulting in the efficiency improvement from 1.47% to 2.56%.

4. Conclusions

The performances of devices with different SubPc layer thicknesses have been investigated. The maximum J_{sc} and FF were achieved simultaneously at 9 nm SubPc, which is

attributed to reach the optimal balance between the light absorption efficiency and the carrier collection efficiency in device, resulting in the efficiency of 1.47%. In addition, to obtain the highest V_{oc} of device not only needs the deepest HOMO level of donor but also needs the highest work function of anode. The V_{oc} of device by using MoO₃ as a buffer layer is better than that of device using PEDOT:PSS. As a result, the V_{oc} is greatly improved from 0.46 V to 1 V by inserting the MoO₃ layer between the ITO and SubPc layer, leading to an increase in efficiency of device from 1.47% to 2.52%.

Acknowledgment

This work was partially supported by the National Science Council of China under Contract No. NSC102-2221-E-390-019-MY2.

References

- [1] J. Y. Kim, K. Lee, N. E. Coates et al., "Efficient tandem polymer solar cells fabricated by all-solution processing," *Science*, vol. 317, no. 5835, pp. 222–225, 2007.
- [2] F. C. Krebs, S. A. Gevorgyan, B. Gholamkhash et al., "A round robin study of flexible large-area roll-to-roll processed polymer solar cell modules," *Solar Energy Materials and Solar Cells*, vol. 93, no. 11, pp. 1968–1977, 2009.
- [3] F. C. Krebs, H. Spanggaard, T. Kjær, M. Biancardo, and J. Alstrup, "Large area plastic solar cell modules," *Materials Science and Engineering B*, vol. 138, no. 2, pp. 106–111, 2007.

- [4] C. W. Tang, "Two-layer organic photovoltaic cell," *Applied Physics Letters*, vol. 48, no. 2, pp. 183–185, 1986.
- [5] R. F. Bailey-Salzman, B. P. Rand, and S. R. Forrest, "Near-infrared sensitive small molecule organic photovoltaic cells based on chloroaluminum phthalocyanine," *Applied Physics Letters*, vol. 91, no. 1, p. 013508, 2007.
- [6] J. Dai, X. Jiang, H. Wang, and D. Yan, "Organic photovoltaic cells with near infrared absorption spectrum," *Applied Physics Letters*, vol. 91, no. 25, Article ID 253503, 2007.
- [7] G. Yu, J. Gao, J. C. Hummelen, F. Wudl, and A. J. Heeger, "Polymer photovoltaic cells: enhanced efficiencies via a network of internal donor-acceptor heterojunctions," *Science*, vol. 270, no. 5243, pp. 1789–1791, 1995.
- [8] J. Xue, B. P. Rand, S. Uchida, and S. R. Forrest, "A hybrid planar-mixed molecular heterojunction photovoltaic cell," *Advanced Materials*, vol. 17, no. 1, pp. 66–71, 2005.
- [9] L. Chen, Y. Tang, X. Fan et al., "Improvement of the efficiency of CuPc/C₆₀-based photovoltaic cells using a multistep structure," *Organic Electronics: Physics, Materials, Applications*, vol. 10, no. 4, pp. 724–728, 2009.
- [10] S. M. Schultes, P. Sullivan, S. Heutz, B. M. Sanderson, and T. S. Jones, "The role of molecular architecture and layer composition on the properties and performance of CuPc-C₆₀ photovoltaic devices," *Materials Science and Engineering C*, vol. 25, no. 5-8, pp. 858–865, 2005.
- [11] R. R. Lunt, N. C. Giebink, A. A. Belak, J. B. Benziger, and S. R. Forrest, "Exciton diffusion lengths of organic semiconductor thin films measured by spectrally resolved photoluminescence quenching," *Journal of Applied Physics*, vol. 105, no. 5, Article ID 053711, 2009.
- [12] J. Kim and S. Yim, "Influence of surface morphology evolution of SubPc layers on the performance of SubPc/C₆₀ organic photovoltaic cells," *Applied Physics Letters*, vol. 99, no. 19, Article ID 193303, 2011.
- [13] B. P. Rand, D. P. Burk, and S. R. Forrest, "Offset energies at organic semiconductor heterojunctions and their influence on the open-circuit voltage of thin-film solar cells," *Physical Review B*, vol. 75, no. 11, Article ID 115327, 2007.
- [14] M. F. Lo, T. W. Ng, T. Z. Liu et al., "Limits of open circuit voltage in organic photovoltaic devices," *Applied Physics Letters*, vol. 96, no. 11, Article ID 113303, 2010.

Research Article

Investigating the Properties of CIS Absorber Layer by Using the Spray Coating Method

Chien-Chen Diao,¹ Cheng-Fu Yang,² Chia-Ching Wu,¹ Wen-How Lan,³ and Yen-Lin Chen²

¹ Department of Electronic Engineering, Kao Yuan University, Kaohsiung 82151, Taiwan

² Department of Chemical and Materials Engineering, National University of Kaohsiung, Kaohsiung 81148, Taiwan

³ Department of Electrical Engineering, National University of Kaohsiung, Kaohsiung 81148, Taiwan

Correspondence should be addressed to Cheng-Fu Yang; cfyang@nuk.edu.tw

Received 18 September 2013; Accepted 1 October 2013

Academic Editor: Teen-Hang Meen

Copyright © 2013 Chien-Chen Diao et al. This is an open access article distributed under the Creative Commons Attribution License, which permits unrestricted use, distribution, and reproduction in any medium, provided the original work is properly cited.

The CuInSe₂ absorber layers were deposited on Mo/glass substrates by using the spray coating method (SCM). At first, the CIS powder was ground into nanoscale particles; then the 6 wt% CIS particles were dispersed into isopropyl alcohol (IPA) to get the solution for SCM. 0.05 mL CIS solution was sprayed on the 2 cm × 1 cm Mo/glass substrates, and then the CIS solution films were annealed in a selenization furnace under different parameters. At first, the extra 0.2 g Se was put in the furnace, the selenization time was 5 min, and the selenization temperature was changed from 450°C to 600°C. After finding the better selenization temperature of 550°C and setting the selenization time at 5 min, the selenization process was set at 550°C and the extra Se content was changed from 0 g to 0.6 g. The influences of the selenization temperature and extra Se content on the surface and cross-section morphologies, crystallization, hall mobility, and carrier concentration and resistivity of the CIS absorber layers were well investigated in this study.

1. Introduction

The quest for new energy to replace the present consumed materials, for example, oil, finding the sustainable sources is one of the major concerns of the present day industrial society. Because photovoltaic (PV) solar energy can serve as a decentralized source of electricity, it is a key sector in this quest. Crystalline silicon solar cells have excellent efficiencies; however, there are serious bottlenecks for this technique with respect to future large-scale applications both from an economical as well as from an ecological point of view. Thus, the thin film silicon solar cells are considered as the main option for large-scale energy applications in the foreseeable future [1–3]. The use of polycrystalline CuInSe (CIS) and CuIn_{1-x}Ga_xSe₂ (CIGS) thin films as the absorber materials for thin film solar cells is another choice and allows easier commercial production because of their appropriate band gap values (e.g., 1.018–1.701 eV, depending on the compositions) and high absorption coefficient in the visible light and near-infrared. Most investigated CIS and CIGS absorber layers are in the polycrystalline structures [4, 5].

The CIS or CIGS absorber layers are mainly deposited by various vacuum methods. Sputtering is one of the most popular vacuum methods to deposit CIS or CIGS absorption layers with high quality [6], and molecular beam epitaxy (MBE) is another important process to deposit CIS or CIGS absorption layers [7]. The coevaporation process can be used to fabricate the highly efficient CIS absorber layers and solar cells [8]. However, the most important process for preparing the CIS or CIGS absorber layers is the using two-step processes, sputtering and selenization [9].

The nonvacuum method is the cheapest and the easiest to deposit the CIS and CIGS absorber layers on an industrial scale. Gu et al. used the CuCl₂·2H₂O, GaCl₃, and Se as the raw materials; ethylenediamine was used as solvent, and the solvothermal method was used to form the CIGS powders [10]. The spray coating method (SCM) is a very important non-vacuum deposition method to fabricate the thin films because it is a relatively simple and inexpensive non-vacuum deposition method for large-area coating. In the past, we had successfully investigated a modified spray pyrolysis method to deposit the high efficiency Li-doped NiO

thin films [11]. As we know, fabricating the CIS and CIGS absorber layers in a non-vacuum process is an important issue for lowering down the fabrication price. However, only few efforts have been made to systematically investigate the CIS and CIGS absorber layers by a SPM method. In this research, the CuInSe_2 was ground into nano-scale powers, and SPM method was used to develop the CIS absorber layers. The effects of the different selenization parameters on the physical and electrical properties of the CIS absorber layers, including the surface morphology, crystallinity, carrier mobility, carrier concentration, and resistivity, were well investigated.

2. Experimental

High purity CuInSe_2 was formed using hydrothermal process by Nanowin Technology Co., Ltd. Because the CIS powder was aggregated into microscale particles and the average particle sizes were approximately $3\text{--}8\ \mu\text{m}$, it could not be used as the source materials to form the CIS absorber layers as the spray coating method (SCM) was used. After finding the optimum grinding time and KDI content, the CIS powder was ground into nano-scale, and it had the average particle sizes approximately $40\text{--}80\ \text{nm}$. Then, the 6 wt% CIS particles were dispersed into isopropyl alcohol (IPA) to get the solution for SPM to prepare the CIS absorber layers.

The organic/CIS composite films were formed by SCM on Mo/glass, and then the organic/CIS composite films were annealed for 5 min by using the rapid temperature annealing (RTA) process in selenization furnace (the chamber size is $5\ \text{cm} \times 5\ \text{cm} \times 4\ \text{cm}$) under different annealing parameters to remove the used organic and crystallize the CIS absorber layers. The selenization temperature was changed from 450°C to 600°C , and the extra $0.0\text{--}0.6\ \text{g}$ Se was put in the furnace during the selenization process. After selenization process, the crystalline structure was examined by using X-ray diffraction (XRD) pattern, and the surface morphology and cross-section observations of the CIS absorber layers were examined by using the field-emission scanning electron microscope (FE-SEM), respectively. The electrical resistivity and the Hall-effect coefficients were measured using a Bio-Rad Hall setup.

3. Results and Discussion

The XRD patterns of the CIS absorber layers as a function of selenization temperature were first investigated, the extra Se content in the selenization furnace was $0.2\ \text{g}$, and the results are shown in Figure 1. The mainly crystalline peak of the CIS absorber layers is the (112). Even though selenization temperature was raised from 450°C to 600°C , all (112) peaks revealed in Figure 1 were situated at $2\theta = 26.66^\circ$. This result suggests that even when 600°C is used as selenization temperature, the lattice constants of the CIS absorber layers have no apparent change. Figure 1 also shows that the secondary CuSe phase was observed in the 600°C -selenized CIS absorber layers. As the CIS absorber layers are used to fabricate the thin film solar cells, the formation of secondary phases will degenerate the efficiency. This result

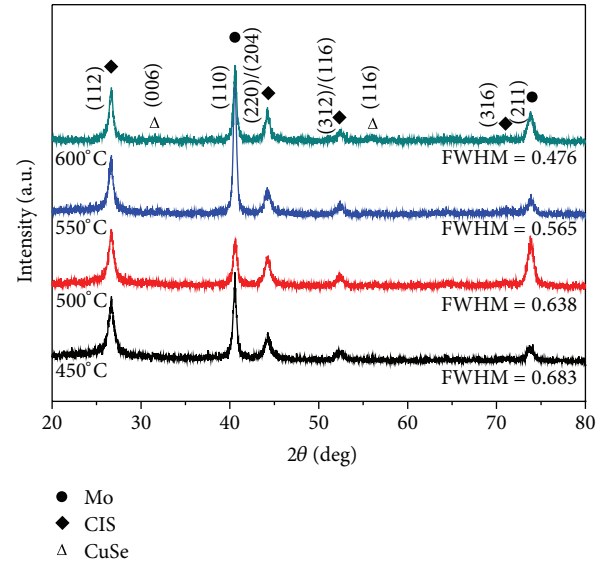


FIGURE 1: XRD patterns of the CIS absorber layers as a function of selenization temperature, the extra Se content was $0.2\ \text{g}$.

suggests that 600°C is not suitable to be used as selenization temperature because the secondary phase is formed. The full width at half maximum (FWHM) value of the (112) peak of the CIS absorber layers was 0.683 , 0.638 , 0.565 , and 0.476 as the selenization temperature was 450°C , 500°C , 550°C , and 600°C , respectively. Also, the relative diffraction intensity of (112) peak had no apparent change as the selenization temperature increased from 450°C to 600°C , as indicated by the XRD patterns shown in Figure 1. These results suggest that CIS absorber layers selenized at higher temperature have the better crystalline structure and the defects in the CIS absorber layers decrease with increasing selenization temperature. This is because as higher temperature is used to treat on the CIS absorber layers, the number of thin film defects decreases and the crystallization of the CIS absorber layer is improved, then the FWHM value decreases.

The surface morphologies of the CIS absorber layers by using extra $0.2\ \text{g}$ Se in selenization furnace and under different selenization temperatures are shown in Figure 2, which indicates that as the selenization temperature changes, the surface morphologies apparently change as well. Evidently, the selenization temperature has a significant effect on the CIS absorber layers' surface morphologies. Selenized at 450°C , a porous structure was observed, the small CIS particles aggregated into microscale particles (not grain growth), and the average particle sizes were approximately $30\text{--}55\ \mu\text{m}$. Selenized at 500°C , a more densified structure with nano-scale particles was observed. These results suggest that 450°C and 500°C are not high enough to improve the densification and grain growth of the CIS absorber layers, and a roughness surface was observed. When the 550°C and 600°C were used as the selenized temperatures, the roughness and densification were apparently improved even only nano-scale particles were observed. Comparing the SEM micrographs shown in Figure 2, the grain growth is inhibited

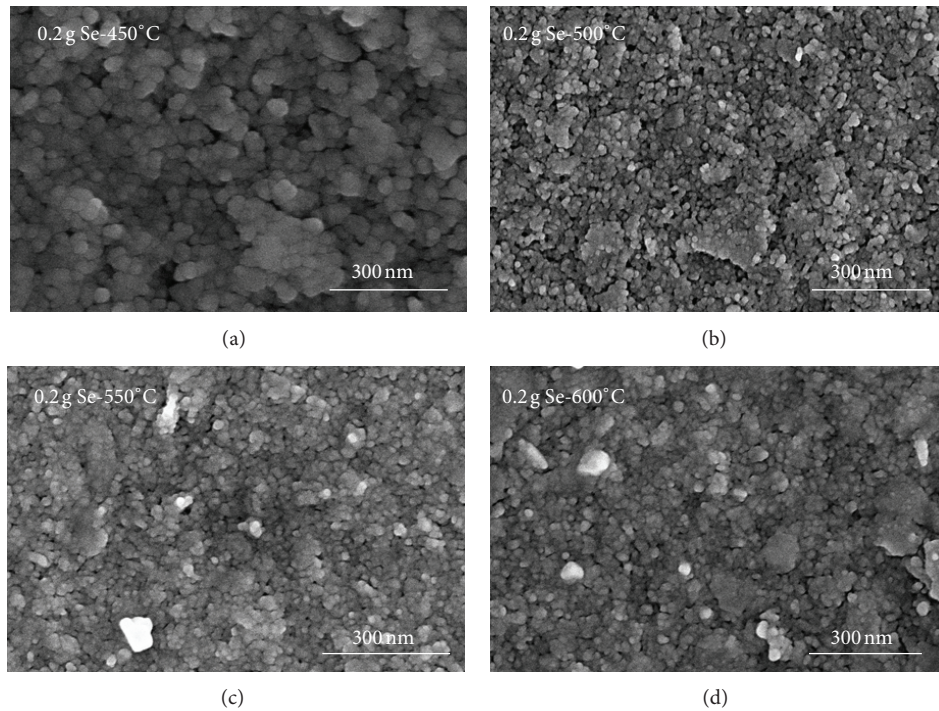


FIGURE 2: Surface morphologies of the CIS absorber layers as a function of selenization temperature the extra Se content was 0.2 g.

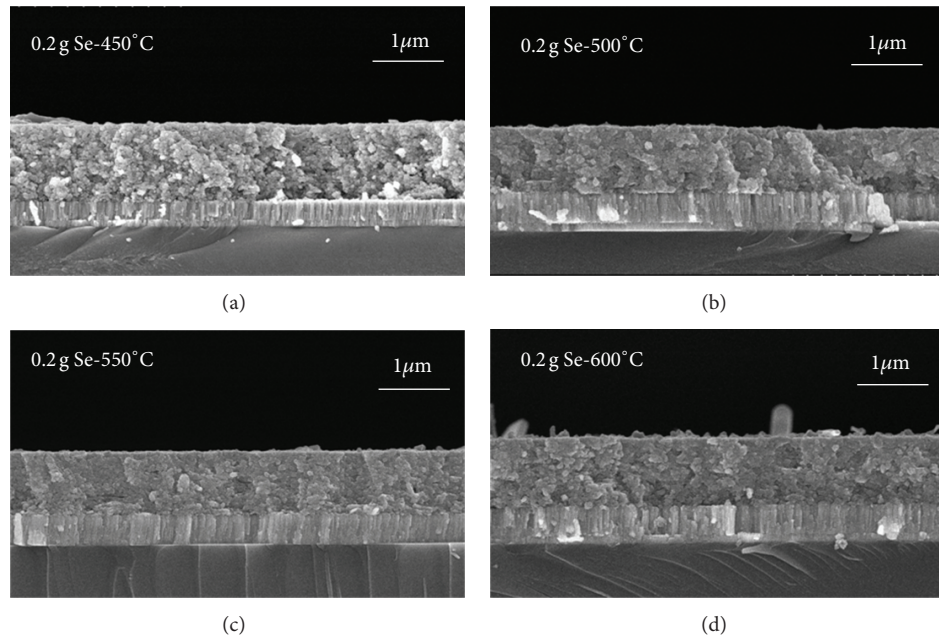


FIGURE 3: Cross-section observations of the CIS absorber layers as a function of selenization temperature the extra Se content was 0.2 g.

by using the extra 0.2 g Se in selenized furnace, which will be proved in Figures 6 and 7.

The cross-section observations of the CIS absorber layers as a function of selenization temperature are shown in Figure 3; the extra Se content was 0.2 g. As Figure 3 shows, the thicknesses of the CIS absorption layers were around 900~1000 nm. This result proves that we can deposit the

CIS absorption layers with uniform thickness by using the spray coating method. The cross-section morphologies also show that the pores and undensified structures are really observed in the 450°C- and 500°C-selenized CIS absorption layers and the densified structures are also really observed in the 550°C- and 600°C-selenized CIS absorption layers.

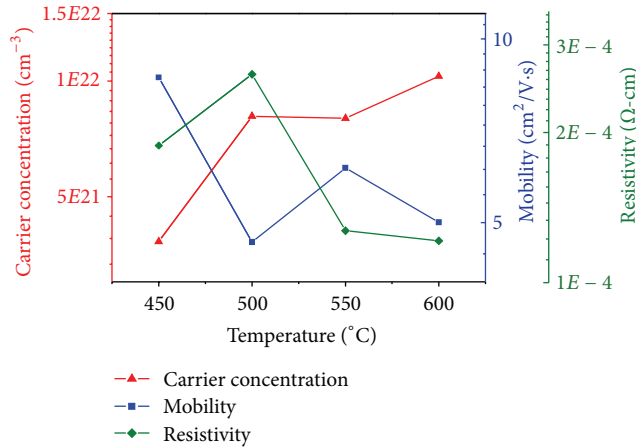


FIGURE 4: Resistivity (ρ), hall mobility (μ), and carrier concentration (n) of the CIS absorber layers as a function of selenization temperature the extra Se content was 0.2 g.

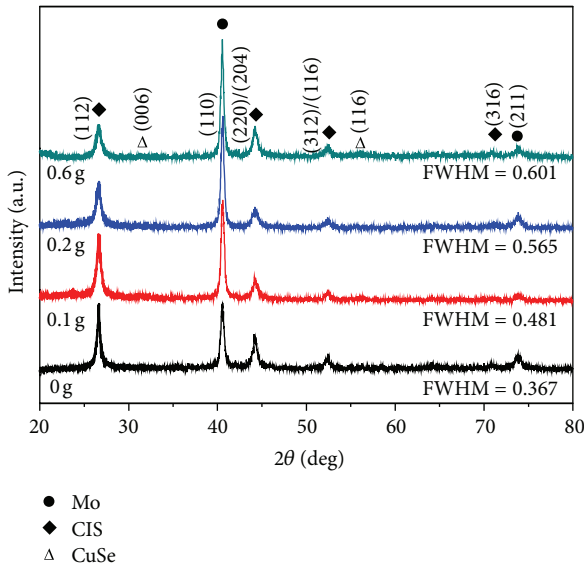


FIGURE 5: XRD patterns of the CIS absorber layers as a function of extra Se content; the selenization temperature was 550°C.

Figure 4 shows the dependence of electrical properties on selenization temperature of the CIS absorber layers. When the CIS absorber layers are deposited on a glass substrate by using SCM and selenization process, many defects result and inhibit electron movement. As the different selenization temperatures are used during the selenization process, two factors are believed to cause an increase in the carrier mobility of the CIS absorber layers. First, the higher selenization temperature enhances the densification and crystallization, which will decrease the numbers of defects and pores in the CIS absorber layers that will cause the decrease in the inhibiting of the barriers electron transportation [12]. Second, as the selenization temperature is too high and extra Se is used, the secondary phase of the CIS absorber layers will appear because of the vaporization of Se and or the diffusion

of extra Se into the CIS absorber layers. In this study, the carrier concentration increased with increasing selenization temperature and reached a maximum of $1.03 \times 10^{22} \text{ cm}^{-3}$ at 600°C. Thus, the mobility had no apparent trend with the variation of selenization temperature and had a maximum of $8.64 \text{ cm}^2/\text{V}\cdot\text{s}$ at 450°C. The resistivity of the CIS absorber layers is proportional to the reciprocal of the product of carrier concentration n and mobility μ :

$$\rho = \frac{1}{ne\mu}. \quad (1)$$

Both the carrier concentration and the carrier mobility contribute to the conductivity. The minimum resistivity of the CIS absorber layers at a selenization temperature of 600°C is mainly caused by the carrier concentration being at its maximum.

The 550°C deposited CIS absorber layers have acceptable characteristics, including smaller FWHM value (Figure 1), no secondary phase formed (Figure 1), acceptable carrier concentration and carrier mobility (Figure 4), and smaller resistivity (Figure 4). For that we used 550°C as the selenization temperature to develop the characteristics of the CIS absorber layers under different extra Se content used during the selenization process. The XRD patterns of the CIS absorber layers as a function of extra Se content were also investigated, and the results are shown in Figure 5. As extra Se content was 0.0 g, 0.1 g, 0.2 g, and 0.6 g, the (112) peak revealed in Figure 5 was situated at $2\theta = 26.64^\circ$, 26.60° , 26.66° , and 26.68° , respectively. Figure 5 also shows that the secondary CuSe phase was observed as extra Se content was 0.6 g. This result suggests that too much extra Se content is not necessary because the secondary phase is formed. The FWHM value of the (112) peak of the CIS absorber layers was 0.367, 0.481, 0.565, and 0.601 as extra Se content was 0.0 g, 0.1 g, 0.2 g, and 0.6 g, respectively. Except that the FWHM value increased, the relative diffraction intensity of (112) peak also critically decreased as extra Se content increased from 0.0 g to 0.6 g, as indicated by the XRD patterns shown in Figure 5. This is because as extra Se content is used, more Se will vaporize during the selenization process to inhibit the grain growth, then the FWHM value increases, and the relative diffraction intensity of (112) peak decreases.

Figure 6 shows the surface morphologies of the CIS absorber layers as a function of extra Se content, the selenization temperature was 550°C, and the results in Figure 6 have large difference as the different extra Se content was added in the selenization furnace. As no extra Se was added in the furnace (0.0 g), the grain growth and roughness surface were really observed. The surface morphologies shown in Figure 6 apparently revealed that the grain sizes of the CIS absorber layers apparently decreased with increasing extra Se content. As extra 0.2 g Se was used, even the densified and flat surfaces were observed, and the grain growth in the CIS absorber layers was inhibited. As extra 0.6 g Se was used, the porous and small grain structure was obtained. This result suggests that as selenized process is used, the extra Se content is important to control the characteristics of the CIS absorber layers. These results suggest that CIS absorber layers selenized

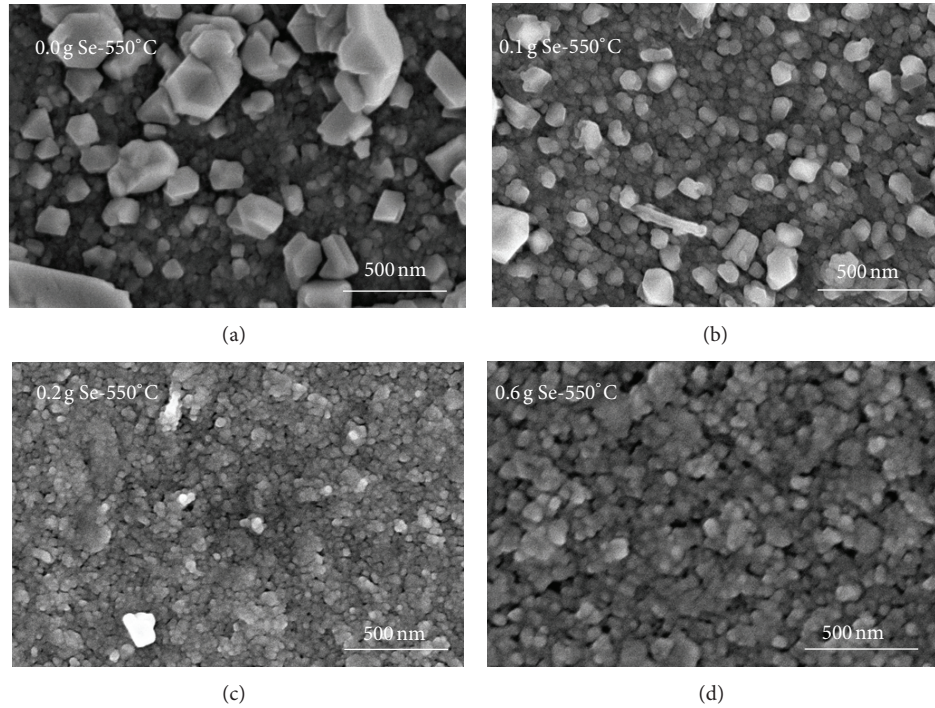


FIGURE 6: Surface morphologies of the CIS absorber layers as a function of extra Se content, the selenization temperature was 550°C.

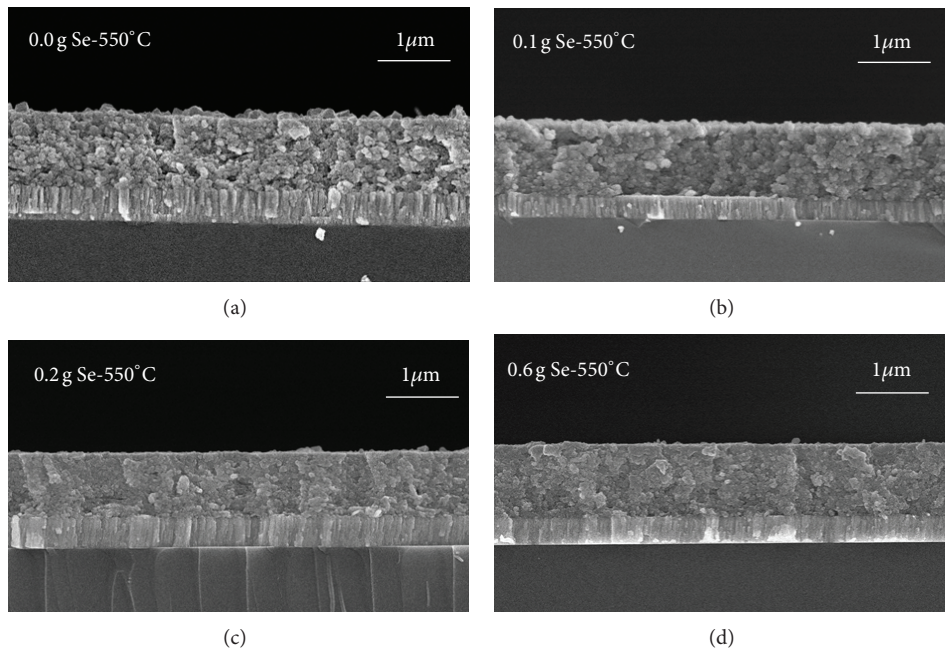


FIGURE 7: Cross-section observations of the CIS absorber layers as a function of extra Se content, the selenization temperature was 550°C.

at less extra Se content have the better crystalline structure but will cause more pores. However, too much Se being used is not necessary because that will inhibit the grain growth and the crystallization of the CIS absorber layers.

Also, the cross morphologies of the CIS absorber layers as a function of extra Se content were also observed, and the results were compared in Figure 7. As no extra Se was put

in the furnace (0.0 g), the pores were really observed in the cross-section. The porous structures are caused because the large grains grow at the expense of small ones, which result in the formation of new and larger voids where the small grains are originally located. However, the pores apparently decreased, and the absorber layers became more densified with increasing Se content. Those results prove again that

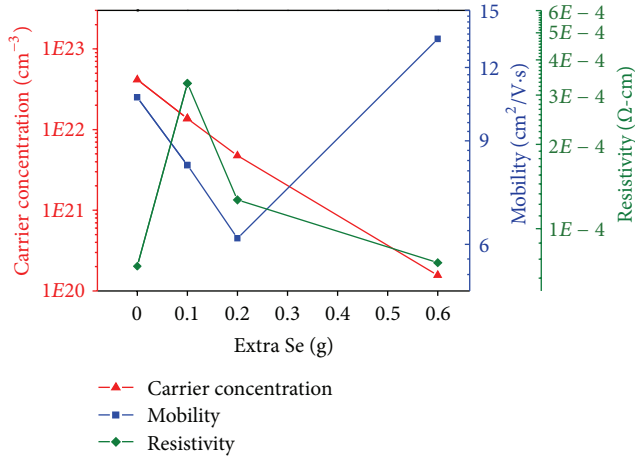


FIGURE 8: Resistivity (ρ), hall mobility (μ), and carrier concentration (n) of the CIS absorber layers as a function of extra Se content; the selenization temperature was 550°C.

as the CIS absorber layers are densified and crystallized in a selenization furnace, the extra Se content has a more important effect to influence the films' characteristics than the selenization temperature.

Figure 8 shows the dependence of electrical properties of the CIS absorber layers on used extra Se content in the selenized process. The carrier concentration linearly decreased from $4.15 \times 10^{22} \text{ cm}^{-3}$ to $1.57 \times 10^{20} \text{ cm}^{-3}$ as extra Se content increased from 0.0 g to 0.6 g, respectively. From the SEM surface and cross morphologies shown in Figures 6 and 7, the crystallinity can decrease because too much extra Se content used in the selenization process will inhibit the crystallization of the CIS absorber layers, then the defects will increase, and the carrier concentration will decrease. Thus, the mobility had no apparent trend with the variation of extra Se content and had a maximum of $13.4 \text{ cm}^2/\text{V}\cdot\text{s}$ at 0.6 g. The minimum resistivity of the CIS absorber layers at extra Se content of 0.0 g is mainly caused by the mobility being at its maximum.

4. Conclusions

The CIS absorber layers were selenized in non-vacuum spray coating method. As 0.2 g extra Se content was used in the selenized process of the CIS absorber layers, the full width at half maximum (FWHM) value of the (112) peak decreased from 0.683 to 0.476 and the relative diffraction intensity of (112) peak had no apparent change as the selenization temperature increased from 450°C to 600°C. The secondary CuSe phase was observed in the 600°C-selenized CIS absorber layers. 0.367, 0.481, 0.565, and 0.601 as extra Se content was 0.0 g, 0.1 g, 0.2 g, and 0.6 g, respectively. As 550°C was used in the selenized temperature of the CIS absorber layers, the full width at half maximum (FWHM) value of the (112) peak increased from 0.367 to 0.601 and the relative diffraction intensity of (112) peak also had no apparent change as the extra Se content increased from 0.0 g to 0.6 g. The secondary CuSe phase was observed in the CIS absorber layers with

extra 0.6 g content during the selenization process. This result suggested that the crystallinity decreased with increasing extra Se content used during the selenization process. This study proves that we have investigated a useful non-vacuum method to prepare CIS absorber layers with different crystallinity by controlling the selenization temperature and the extra Se content added in the selenization furnace for further solar cells' fabrication.

Acknowledgments

The authors acknowledge financial supports of Nanowin Technology Co., Ltd., NSC 102-2622-E-390 -002-CC3, and NSC 102-2221-E-390-027.

References

- [1] M. I. Kabir, S. A. Shahahmadi, V. Lim et al., "Amorphous silicon single-junction thin-film solar cell exceeding 10% efficiency by design optimization," *International Journal of Photoenergy*, vol. 2012, Article ID 460919, 7 pages, 2012.
- [2] A. Shah, J. Meier, A. Buechel et al., "Towards very low-cost mass production of thin-film silicon photovoltaic (PV) solar modules on glass," *Thin Solid Films*, vol. 502, no. 1-2, pp. 292-299, 2006.
- [3] F. H. Wang, C. C. Huang, C. F. Yang, and H. T. Tzeng, "Optical and Electrical Properties of the Different Magnetron Sputter Power 300°C-Deposited Ga₂O₃-ZnO Thin Films and Applications in p-i-n α -Si:H Thin-Film Solar Cells," *International Journal of Photoenergy*, vol. 2013, Article ID 270389, 7 pages, 2013.
- [4] A. Romeo, M. Terheggen, D. Abou-Ras et al., "Development of thin-film Cu(In,Ga)Se₂ and CdTe solar cells," *Progress in Photovoltaics*, vol. 12, no. 2-3, pp. 93-111, 2004.
- [5] Y. M. Shin, D. H. Shin, J. H. Kim, and B. T. Ahn, "Effect of Na doping using Na₂S on the structure and photovoltaic properties of CIGS solar cells," *Current Applied Physics*, vol. 11, no. 1, pp. S59-S64, 2011.
- [6] K. Ramanathan, J. Keane, and R. Noufi, "Properties of high-efficiency CIGS thin-film solar cells," in *Proceedings of the 31st IEEE Photovoltaic Specialists Conference*, pp. 195-198, Lake Buena Vista, Fla, USA, January 2005.
- [7] M. M. Islam, S. Ishizuka, A. Yamada et al., "CIGS solar cell with MBE-grown ZnS buffer layer," *Solar Energy Materials and Solar Cells*, vol. 93, no. 6-7, pp. 970-972, 2009.
- [8] M. Powalla, G. Voorwinden, D. Hariskos, P. Jackson, and R. Kniese, "Highly efficient CIS solar cells and modules made by the co-evaporation process," *Thin Solid Films*, vol. 517, no. 7, pp. 2111-2114, 2009.
- [9] C. Y. Hsu, P. C. Huang, Y. Y. Chen, and D. C. Wen, "Fabrication of a Cu(InGa)Se₂ thin film photovoltaic absorber by rapid thermal annealing of CuGa/In precursors coated with a Se layer," *International Journal of Photoenergy*, vol. 2013, Article ID 132105, 7 pages, 2013.
- [10] S.-I. Gu, S.-H. Hong, H.-S. Shin et al., "Phase analysis of Cu(In_{1-x}Ga_x)Se₂ prepared by solvothermal method," *Ceramics International*, vol. 38, no. 1, pp. S521-S523, 2012.
- [11] C. C. Wu and C. F. Yang, "Investigate the properties of nanostructured Li-doped NiO films using the modified spray pyrolysis method," *Nanoscale Research Letters*, vol. 8, article 33, 2013.

- [12] Y. Igasaki and H. Saito, "Substrate temperature dependence of electrical properties of ZnO:Al epitaxial films on sapphire (1210)," *Journal of Applied Physics*, vol. 69, no. 4, pp. 2190–2195, 1991.

Research Article

Optimal Design for the Diffusion Plate with Nanoparticles in a Diffusive Solar Cell Window by Mie Scattering Simulation

Ruei-Tang Chen, Chih-Chieh Kang, Jeng-Feng Lin, Tzu-Chi Lin, and Chih-Wen Lai

Southern Taiwan University of Technology & Science, Tainan, Taiwan

Correspondence should be addressed to Chih-Chieh Kang; kangc@mail.stust.edu.tw

Received 15 September 2013; Accepted 14 October 2013

Academic Editor: Teen-Hang Meen

Copyright © 2013 Ruei-Tang Chen et al. This is an open access article distributed under the Creative Commons Attribution License, which permits unrestricted use, distribution, and reproduction in any medium, provided the original work is properly cited.

A diffusive solar cell window comprises a diffusion plate with TiO_2 nanoparticles sandwiched between two glass layers. It is a simple, inexpensive, easy-to-made, and highly reliable transparent solar energy module. To improve its power generation efficiency as well as maintain indoor natural lighting, we examined the scattering mechanism in the diffusion plate with TiO_2 nanoparticles within a diffusive solar cell window by Mie scattering simulations. In this work, a multiwavelength ASAP ray tracing model for a diffusive solar cell window with acceptable accuracy was developed to investigate the influence of the diffusion plate design parameter, mainly concentration of a diffusion plate with determined particle size distribution, on power generation efficiency and color shift of transmitted sun light. A concept of “effective average radius” was proposed to account for the equivalent scattering effect of a size distribution of quasispherical particles. Simulation results demonstrated that both the transmitted light and its correlated color temperature decreased as the concentration increased for a large-size diffusive solar cell window. However, there existed a maximum power generation efficiency at around 160 ppm concentration. The optimal design for a large-size diffusion plate inside a diffusive solar cell window by taking indoor lighting into account was suggested based on the simulation results.

1. Introduction

Building integrated photovoltaic (BIPV) is an important application of future solar energy development. The integration of solar cells into windows must not only generate electrical power but also maintain indoor natural lighting. Various types of power generation on windows have been developed by the application of BIPV technology. In most cases, solar cells are directly placed on/in windows [1–7]. But such approach often fails to fulfill one of the basic functions of windows—lighting. Alternatively, solar cells can be placed on the edges of a window. Through depositing a thin film layer of fluorescent molecules on glass, due to internal total reflection of light in glass, a highly efficient solar cell was developed [8]. To further enhance the light guide effect and increase the power generation efficiency as well, a diffusive solar cell window is designed and fabricated with uniformly distributed diffusive nanoparticles in a polycarbonate diffusion plate that is sandwiched between two glass layers [9]. A typical prototype diffusive solar cell window is shown in Figure 1. Its basic structure and main light-transport mechanisms

responsible for the enhancement of solar power generation, including multiple scattering inside diffusion plate and total internal reflection at the front and back interfaces between the glass and the air, such as light rays ④, ⑤, and ⑦, are illustrated in Figure 2. As a whole, it does exhibit a certain degree of “light-guide” effect. Although, with all its merits, the commercial applications of diffusive solar cell windows are still limited, part of the reason is due to that the contemporary large-size diffusive solar cell windows still do not meet the performance requirement for high power generation efficiency. Since the diffusion plate is the most significant factor influencing power generation efficiency, it is crucial to optimize its design in order to resolve the issue.

Based on Mie theory of light scattering, optical simulations have been widely used to study light transport in diffusion plate, in tissues, in atmosphere, and in environment, and so forth, and have gained some ground in these research areas [10]. To efficiently and effectively improve the power generation performance of a large-size diffusive solar cell window in terms of development time and cost, Mie scattering optical simulation is the best choice for



FIGURE 1: A 1 × 1 feet diffusive solar cell window prototype at work.

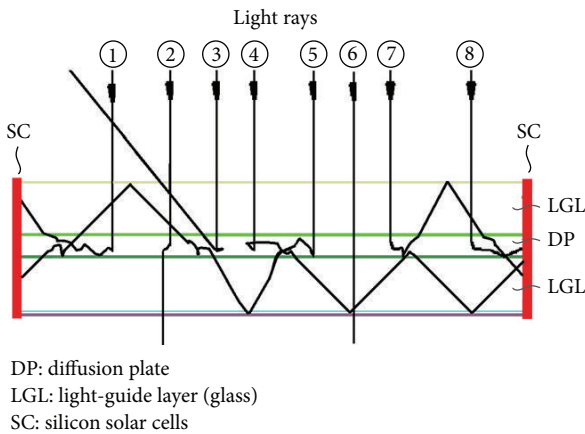


FIGURE 2: Schematic illustration of the basic structure of a diffusive solar cell window as well as various mechanisms of light transport inside.

implementation compared to the more common practice—experimental approach. In this work, a multiwavelength ray tracing model using Advanced Systems Analysis Program (ASAP) was constructed to examine the optical mechanisms which influence the power generation efficiency of a diffusive solar cell window, especially the optimal design parameters for the diffusion plate with nanoparticles of a large-size diffusive solar cell window by taking both high power generation performance and indoor lighting into account.

2. Optical Model for a Diffusive Solar Cell Window

Generally, our devised diffusive solar cell window is made up of a diffusion plate—polycarbonate (PC) plate embedded with titanium dioxide (TiO_2) nanoparticles which was sandwiched between two glass plates. In practice, ethylene vinyl acetate (EVA) was used to laminate glass and PC. Accordingly, an ASAP ray tracing model was developed to simulate the measurement of a five-layer diffusive solar cell window in a solar simulator with acceptable accuracy. A typical cross-sectional dimension of a diffusive solar cell window structure for general purpose building applications implemented in simulations is shown in Figure 3. A rectangular tubular

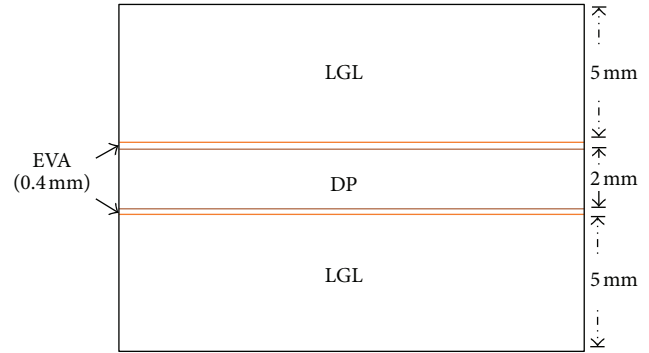


FIGURE 3: The implemented cross-sectional dimension (in proportion) for a typical diffusive solar cell window.

absorption surface was surroundingly positioned in close proximity to the edge of the diffusive solar cell window to act as solar cells in simulations. Another absorption surface was placed proximately behind the back interface of the diffusive solar cell window, which was between the glass and the air, to track down all of the transmitted light.

3. Optical Simulations

The optical simulations were divided into two main steps: (i) the construction of an accurate wavelength-dependent diffusion plate optical model and (ii) optimal design for a diffusive solar cell window.

In order to corroborate the five-layer diffusive solar cell window model, a prior work—the construction of an accurate wavelength-dependent optical model for the diffusion plate—was performed since the diffusion plate is the key component in a diffusive solar cell window. By simulating the transmittance spectra measurement of the diffusion plate using a spectrophotometer, a simplified ASAP model of transmittance spectra measurement for the diffusion plates with different concentrations of TiO_2 nanoparticle was constructed. It consisted of a diffusion plate, a variable single-wavelength slit light source, and a detection surface that served as the entrance port opening of an integrating sphere. The densities of TiO_2 and PC were assumed to be 4.0 g/cm^3 and 1.2 g/cm^3 , respectively. Given a radius of a nanoparticle, different concentrations of nanoparticle in a diffusion plate can be determined in simulations.

By Mie scattering theory, the aggregate of TiO_2 nanoparticles in a diffusion plate was assumed to be spherical, isotropic, and uniform in size. In fact, there was a size distribution of around 200–300 nm for TiO_2 nanoparticles implemented in this work, as shown in Figure 4. Therefore, we proposed a concept of “effective average radius” to approximate the average radius of an aggregate of nanoparticles which took the equivalent scattering effect of a size distribution of quasispherical particles into account. Different “effective average radii” within the range of TiO_2 nanoparticle size distribution were tested in the simulations of diffusion plate transmittance spectra measurement. The simulation results then were compared to the experimental measurements not

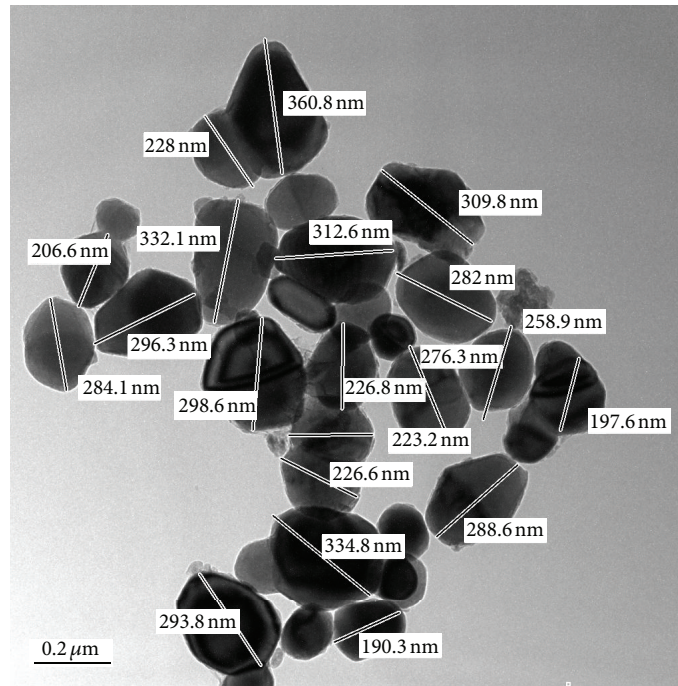


FIGURE 4: TEM image of the TiO₂ nanoparticle aggregates.

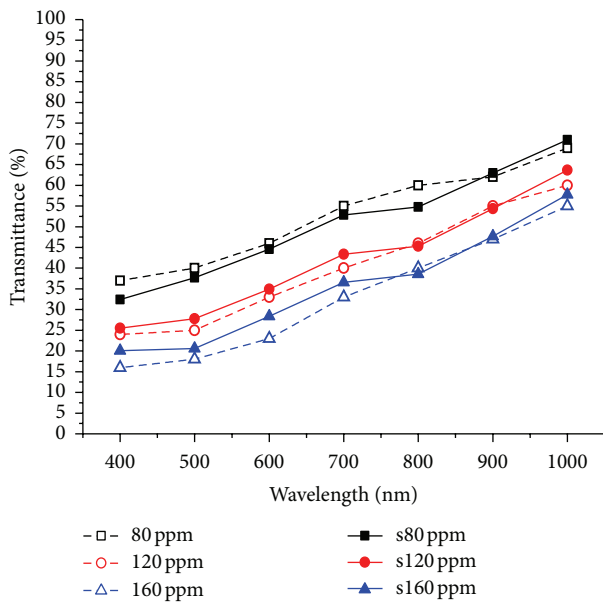


FIGURE 5: Comparison of transmittance spectra of a diffusion plate with TiO₂ nanoparticles between simulation and experiment. Solid line (—): simulation. Dash line (---): experiment.

only to validate the accuracy of the wavelength-dependent diffusion plate model but also to determine the operating “effective average radius” implemented in the diffusive solar cell window model. With resort to dynamic light scattering (DLS) measurements for the aggregate of TiO₂ nanoparticles [11], the validity of operating “effective average radius” was examined.

As for the refractive indices (n) and extinction coefficients (κ) of glass, EVA, TiO₂, and PC, they do vary with wavelength

in the solar spectrum for silicon solar cell which is approximately from 400 to 1150 nm [12], whereas the extinction coefficients of glass, EVA, and PC are so insignificant that they were assumed to be zero for most optics applications. Since there exists multiple scattering inside the diffusion plate and “light-guide” effect along the glass plates, the propagation loss of light transport in a diffusive solar cell window cannot be ignored any more; that is, their extinction coefficients cannot be assumed to be zero. In this work, the extinction coefficients of glass, EVA, and PC were determined based on the measured transmittance spectra of blank glass, EVA, and PC by a spectrophotometer which were then converted to extinction coefficients through corresponding transmittance spectra simulations. More particularly, the measured transmittance spectra of a 2 mm thick blank PC plate were served as a baseline in the transmittance spectra simulations for a diffusion plate.

In the second step, there were two feasible approaches to perform the simulations for optimizing a diffusive solar cell window design by assigning the light source of the diffusive solar cell window model either to be one single operating wavelength or to be multiwavelength. Though single-wavelength approach could provide valuable information to improve the design of a diffusive solar cell window, but a more accurate model was needed in order to optimize its performance. Therefore, the multiwavelength approach was adopted in this work. An ASAP multiwavelength five-layer diffusive solar cell window measurement model was then developed. Simulations were performed to determine the power generation, transmittance, and transmitted light color of different-size diffusive solar cell window with given concentrations of TiO₂ nanoparticle. The accuracy of this model was verified through the comparison between the simulation results and experimental data. Further simulations were

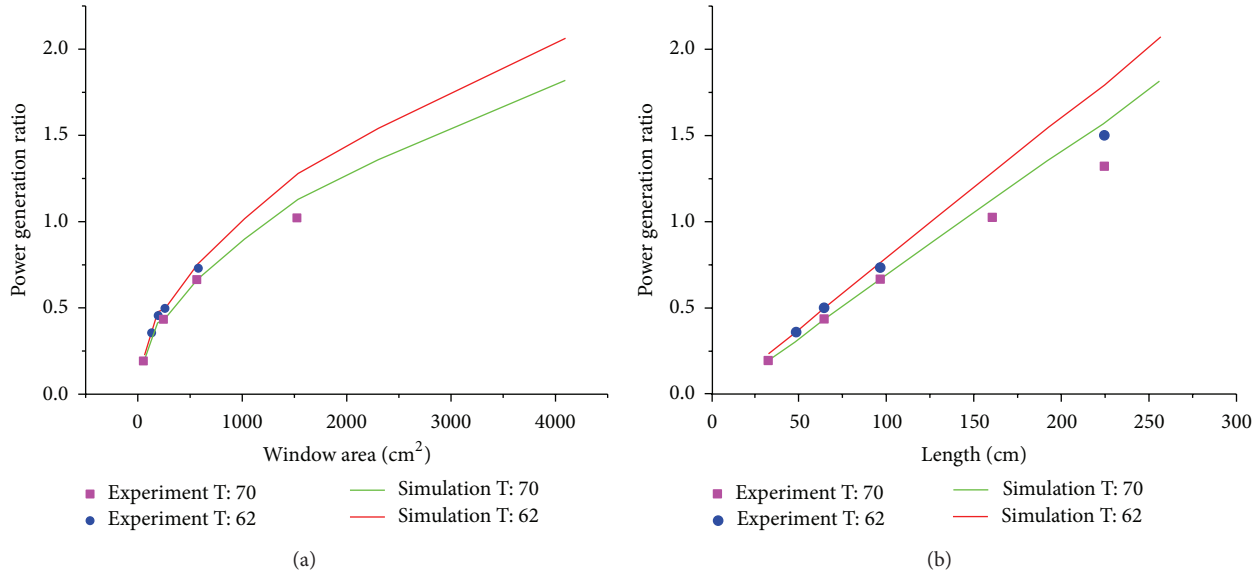


FIGURE 6: Comparison of power generation ratio of diffusive solar cell windows with different sizes between simulation and experiment in terms of (a) window area and (b) window perimeter.

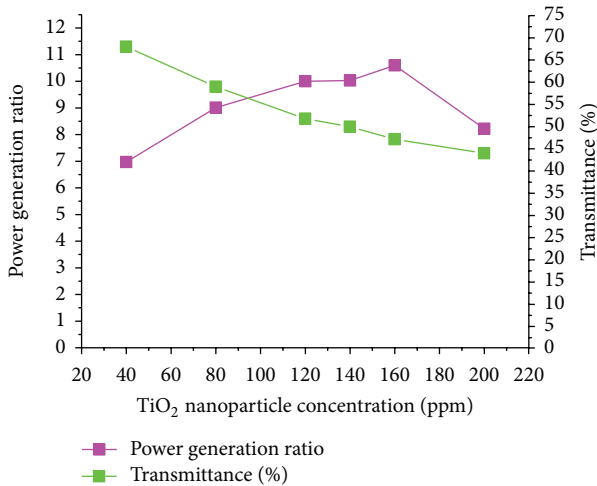


FIGURE 7: Simulation results of power generation ratio and transmittance for a 64 × 64 cm diffusive solar cell window with different concentrations of nanoparticle.

performed to attain the optimal design for a large-size 640 × 640 mm diffusive solar cell window.

4. Simulation Results and Discussion

In the simulations of transmittance spectra measurements of the diffusion plate with TiO₂ nanoparticles, the “effective average radius” of a TiO₂ nanoparticle was determined to be 140 nm by the examination of all of the simulation results and comparison with experimental data. For this case, the transmittance spectra comparison between the simulation and the experiment demonstrated that the constructed diffusion plate model can exhibit acceptable accuracy across

the whole silicon solar cell spectrum, as shown in Figure 5. Appreciably and deliberately, higher transmittances occurred in low-wavelength region and lower ones in high-wavelength region. Higher errors appeared at the lower end of the spectrum by our model, since the spectra transmittance of PC varied significantly in the region of 400 nm.

To validate the accuracy of the developed multiwavelength five-layer diffusive solar cell window measurement, we compared simulation results to the experimental measurements, as shown in Figure 6. By means of an 8 × 8 cm/70%-T diffusive solar cell window with a 0.189 W power generation as a standard of reference, the power generation ratio is defined as the power generation of a test window over the reference value. 70%-T stands for an 80 ppm diffusion plate with TiO₂ nanoparticles used, and 62%-T is for a 140 ppm one.

In Figure 6(a), it shows that the power generation ratio does not increase linearly with window size (amount of incident simulated sun light); it gradually saturates as the window area increases. In Figure 6(b), the power generation ratio variation versus window perimeter also exhibits the same trend; it saturates as window size becomes greater. Besides, the generation power ratio is greater if the window parameter is larger based on the same window size.

For future commercial applications, a 64 × 64 cm diffusive solar cell window, which was near a 2 × 2 ft size window, was simulated. The simulation results are shown in Figure 7. It demonstrated that the transmitted light decreased as expected as the particle concentration increased from 40 ppm to 200 ppm. However, the power generation ratio did not increase with increasing particle concentration. There existed a maximum power generation ratio at around 160 ppm concentration. It suggested that the optimal design parameter for particle concentration was around 100 ppm, based on the tradeoff between power generation ratio and

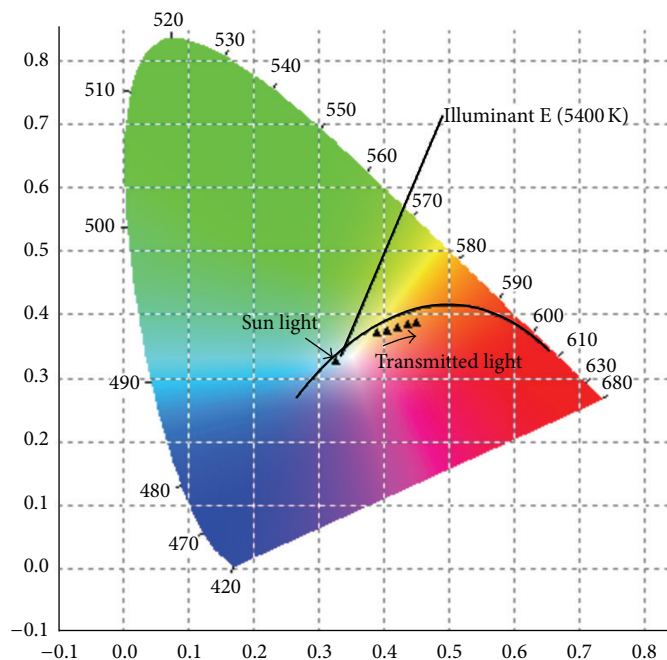


FIGURE 8: Simulation results of correlated color temperature variation of transmitted light for a 64×64 cm diffusive solar cell window with the increment of nanoparticle concentration.

light transmittance. The correlated color temperature of the transmitted light decreased as the particle concentration increased as expected, as shown in Figure 8. Since the light was absorbed and scattered in a PC diffusion plate with nanoparticles in a diffusive solar cell window at around 400 nm.

5. Conclusions

We have developed an ASAP optical multiwavelength model for a diffusive solar cell window with acceptable accuracy which can be used to optimize the design for a large-size diffusive solar cell window. We also proposed a concept of “effective average radius” to account for the equivalent scattering effect of a size distribution of quasispherical particles. For a 64×64 cm diffusive solar cell window, there existed a maximum power generation ratio at around 160 ppm concentration in simulations. It did not increase with increasing particle concentration. The simulation also suggested that particle concentration of about 100 ppm was the optimal design parameter, given determined “effective average radius” of 140 nm, by taking indoor natural lighting into account. Its light transmittance can still maintain above 50%.

Conflict of Interests

The authors ensure that there was no conflict of interests in this study.

Acknowledgments

This work was in part supported by the National Science Council (Grant no. NSC 102-2221-E-218-021) and by the Ministry of Economic Affairs (Grant no. 102-E0603), China.

References

- [1] A. Takeoka, S. Kouzuma, H. Tanaka et al., “Development and application of see-through a-Si solar cells,” *Solar Energy Materials and Solar Cells*, vol. 29, no. 3, pp. 243–252, 1993.
- [2] M. Biancardo, K. Taira, N. Kogo et al., “Characterization of microspherical semi-transparent solar cells and modules,” *Solar Energy*, vol. 81, no. 6, pp. 711–716, 2007.
- [3] A. Goetzberger and V. Wittwer, “Fluorescent planar collector-concentrators: a review,” *Solar Cells*, vol. 4, no. 1, pp. 3–23, 1981.
- [4] T. Miyazaki, A. Akisawa, and T. Kashiwagi, “Energy savings of office buildings by the use of semi-transparent solar cells for windows,” *Renewable Energy*, vol. 30, no. 3, pp. 281–304, 2005.
- [5] W. He, Y. X. Zhang, W. Sun, J. X. Hou, Q. Y. Jiang, and J. Ji, “Experimental and numerical investigation on the performance of amorphous silicon photovoltaics window in East China,” *Building and Environment*, vol. 46, no. 2, pp. 363–369, 2011.
- [6] Y. F. Chiang, R. T. Chen, A. Burke, U. Bach, and P. Chen, “Non-color distortion for visible light transmitted tandem solid state,” *Renewable Energy*, vol. 59, pp. 136–140, 2013.
- [7] J. G. Kang, J. H. Kim, and J. T. Kim, “Performance evaluation of DSC windows for buildings,” *International Journal of Photoenergy*, vol. 2013, Article ID 472086, 6 pages, 2013.
- [8] M. J. Currie, J. K. Mapel, T. D. Heidel, S. Goffri, and M. A. Baldo, “High-efficiency organic solar concentrators for photovoltaics,” *Science*, vol. 321, no. 5886, pp. 226–228, 2008.
- [9] R.-T. Chen, J. L. H. Chau, and G. L. Hwang, “Design and fabrication of diffusive solar cell window,” *Renewable Energy*, vol. 40, no. 1, pp. 24–28, 2012.
- [10] W. Hergert and T. Wriedt, Eds., *The Mie Theory*, Springer, New York, NY, USA, 2011.
- [11] A. Colombo, F. Tassone, F. Santolini, N. Contiello, A. Gambirosso, and R. Simonutti, “Nanoparticle-doped large area PMMA plates with controlled optical diffusion,” *Journal of Materials Chemistry C*, vol. 1, no. 16, pp. 2927–2934, 2013.
- [12] <http://www.refractiveindex.info>.

Research Article

Study of the Behavior of Titanium Alloys as the Cathode for Photovoltaic Hydrogen Production

Chien-Lung Huang,¹ Yu-Jia Gao,¹ Tao-Liang Chuang,¹ Vincent K. S. Hsiao,² and Tair-I Wu³

¹ Metal Industries Research and Development Centre, Kaohsiung, Taiwan

² Department of Applied Materials and Optoelectronic Engineering, National Chi Nan University, Puli, Nantou, Taiwan

³ Department of Materials Engineering, Tatung University, Taipei 10451, Taiwan

Correspondence should be addressed to Tair-I Wu; tairiwu@yahoo.com.tw

Received 18 September 2013; Accepted 29 September 2013

Academic Editor: Teen-Hang Meen

Copyright © 2013 Chien-Lung Huang et al. This is an open access article distributed under the Creative Commons Attribution License, which permits unrestricted use, distribution, and reproduction in any medium, provided the original work is properly cited.

CP-Ti and Ti-153 were adopted in this study to observe their electrochemical behavior in serving as the cathode for photovoltaic hydrogen production. The designed cyclic hydrogenation-solution heat treating processes were performed to increase the hydrogen uptake for both alloys. The results are as follows. (1) Both arsenic trioxide and thiourea showed hydrogenation promotive effect on CP-Ti, while thiourea was an inhibitor for Ti-153 under the applied conditions. (2) Arsenic trioxide showed hydrogenation promotive effect on both Ti-153 and CP-Ti in this study. (3) Ti-153 demonstrated superiority to CP-Ti when serves as the cathode for photovoltaic hydrogen production. The hydrogen mass payload for Ti-153 is 68 times larger than that for CP-Ti.

1. Introduction

The available renewable energy on the earth's surface includes the solar power, the wind power, and the hydroelectric power which uses the fall of the river, tidal power, or ocean current power. The wind power and hydroelectric power are, however, significantly limited by the location on the earth, the terrain, or the climate. The solar energy has less restriction in contrast to the abovementioned power sources [1–5]. The applications of sunlight can be divided into two parts: solar thermal energy and photovoltaic (PV). The application of the former is to transform solar energy to obtain heat which could be used in air condition, offer the hot water, or run a heat engine to make electricity [6–8]. PV energy systems employ solar panels in directly converting the sunlight into electricity [9, 10].

Since the solar power and the wind power are intermittent energy which means it is interruptible and cannot be a stable source due to the variation of the illuminance of sunlight and the change of wind field, for the commercial feasibility considerations, people have to store the energy when they can give. Unlike other forms of energy, electricity must be utilized when it is being generated or converted immediately

into another form of energy. The PV energy system is usually equipped with an electrolyzer and a hydrogen storage tank (see Figure 1) [1, 2, 11, 12]. Although the gaseous hydrogen is convenient to store, transport, and apply, the inherent low volume payload rate and high flammability are the death wounds [13, 14]. It is safer to store hydrogen in solid state, but the increase of hydrogen mass payload rate is still technological challenge [15].

Electrolysis of aqueous sulfuric acid results in hydrogen at cathode surface. The resulted hydrogen can be driven into the cathode as solid solutes or hydrides by adequately adding hydrogenation promoters and selecting cathode material [16–20]. Ti-15V-3Al-3Cr-3Sn alloy (Ti-153), as a commonly used β -Ti alloy, was chosen in this study to compare with commercial purity titanium (CP-Ti) to see the influences of the chemical additives and cathode material on the electrolytic hydrogen uptake.

2. Materials and Methods

The cathode materials in sheet form were received at rolled and process annealed state. The specimens were sheared from

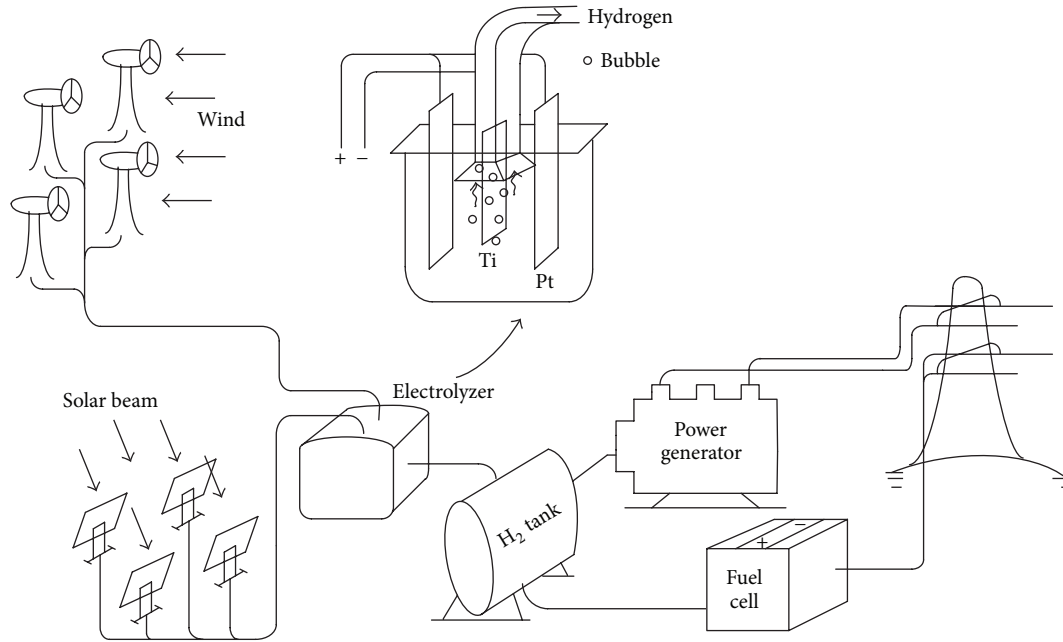


FIGURE 1: Schematic diagram showing hydrogen gas produced and stored from renewable power.

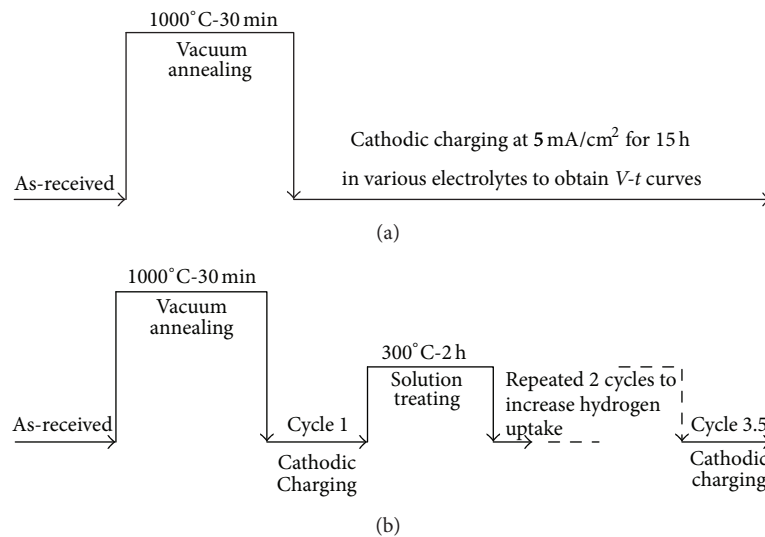


FIGURE 2: Schematic diagrams for (a) the process to monitor the variation of cathode potential versus time and (b) the cyclic hydrogenation-solution heat treating process to increase the hydrogen uptake of cathodes.

the received sheets to be $40 \times 14 \times 1 \text{ mm}^3$ for CP-Ti, while they are $62 \times 16 \times 0.4 \text{ mm}^3$ for Ti-153, vacuum annealed at 1000°C for 30 minutes and furnace cooled to room temperature. The vacuum annealed specimens were abraded with emery paper (up to grit 1200) and further lapped to minimize the interference of surface oxides on hydrogenation. Table 1 listed the chemical compositions of the as-received sheets. Table 2 summarized the surface roughness measured by employing a profile measuring system (Dektak 150, Veeco).

The processing parameters listed in Table 3 were designed to reveal the effect of the additives on the electrochemical

behavior of cathode and grouped into three sets according to the additives in the electrolyte as follows: (1) no additive in $1\text{N H}_2\text{SO}_{4(\text{aq})}$, denoted by S, (2) $1\text{N H}_2\text{SO}_{4(\text{aq})}$ by adding 0.005 M arsenic trioxide (As_2O_3), denoted by A, (3) $1\text{N H}_2\text{SO}_{4(\text{aq})}$ by adding 0.01 M thiourea ($\text{SC}(\text{NH}_2)_2$), denoted by T, respectively. Electrolytic hydrogenation was performed at 5 mA/cm^2 for 15 h in various electrolytes, respectively. The preheat treatment was schematically shown in Figure 2(a). Figure 2(b) showed the schematic diagram of cyclic hydrogenation-solution heat treating processes. Electrolytic hydrogenation of the cyclic process was performed

TABLE 1: (a) Analyzed composition of the as-received CP-Ti sheet (wt.%). (b) Analyzed composition of the as-received Ti-153 sheet (wt.%).

(a)									
H	C	N	O	Fe	Ti				
68 ppm	0.10	0.01	0.12	0.20	Balanced				
(b)									
H	C	N	O	Fe	Al	Cr	Sn	V	Ti
0.015	0.05	0.04	0.11	0.25	3.1	3.0	2.8	14.5	Balanced

TABLE 2: Surface roughness of CP-Ti and Ti-153 sheet specimens before hydrogenation.

CP-Ti		Ti-153	
R_a (nm)	R_q (nm)	R_a (nm)	R_q (nm)
134.7 ± 3.5	166.3 ± 3.8	162.6 ± 10.6	171.1 ± 15.0

R_a : The arithmetic mean of the departure of the profile from the mean line.
 R_q : The root-mean-square parameter corresponding to R_a .

TABLE 3: Process designations and the associated parameters for cathode potential monitoring.

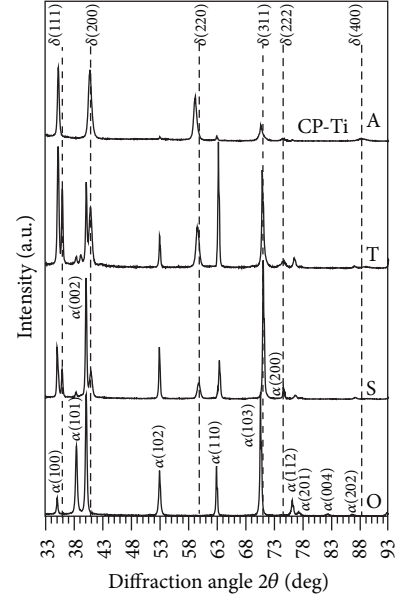
Designations	Parameters
O	β solution treated specimens ground by emery paper to 1000 mesh
S	Ground specimens cathodic charged in 1 N $H_2SO_{4(aq)}$ at 5 A/cm ² for 15 h
A	Ground specimens cathodic charged in 1 N $H_2SO_{4(aq)}$ + 0.005 M As_2O_3 at 5 A/cm ² for 15 h
T	Ground specimens cathodic charged in 1 N $H_2SO_{4(aq)}$ + 0.01 M thiourea at 5 A/cm ² for 15 h

in 1 N $H_2SO_{4(aq)}$ containing As_2O_3 (0.1 g/L) at 50 mA/cm² for 30 h on CP-Ti specimens while for 10 h on Ti-153 ones preventing the hydride layer from spallation or the specimen from cracking. The subsequent solution treatments were accomplished in a muffle furnace at 300°C for 2 h. Table 4 listed designations and processing parameters of the cyclic hydrogenation-solution processes.

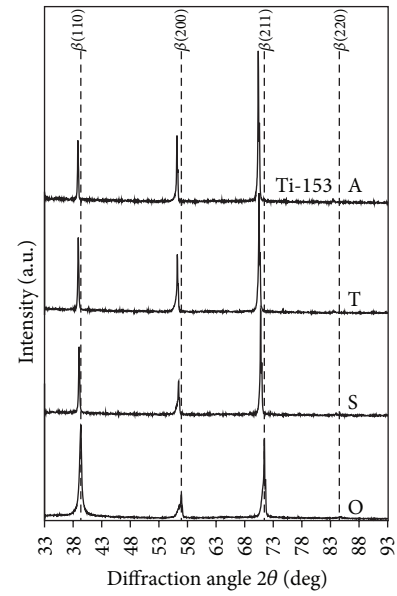
The effects of processing parameters on the hydrogenation behavior were evaluated qualitatively by utilizing X-ray diffractometry (XRD: X'Pert PRO MPD, PANalytical, the Netherlands, 45 kV-40 mA) and $V-t$ curve monitoring. The quantitative cathodic behavior and hydrogen uptake of CP-Ti and Ti-153 specimens were analyzed by the employment of glow discharge optical spectrometry (GDOS: LECO GDS-750).

3. Results and Discussion

Large amounts of hydrogen absorption would lead to the shift and broadening of α peaks and presence of δ peaks in the XRD patterns of CP-Ti specimens. Patterns S, T, and A in



(a)



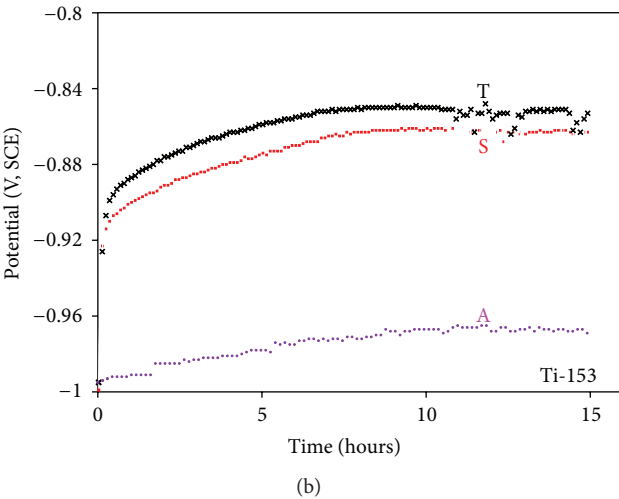
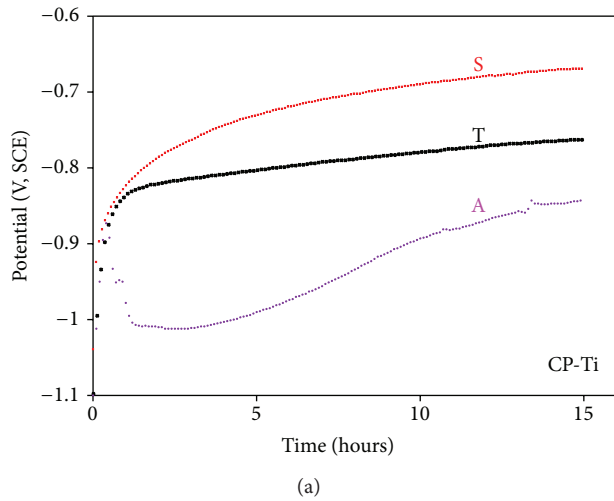
(b)

FIGURE 3: XRD patterns for as-received specimens and those after cathodic charged in various electrolytes: (a) CP-Ti and (b) Ti-153.

Figure 3(a) exhibited δ peaks in contrast to pattern O [17–20]. The lower diffraction angle of the δ (220) peak implies higher hydrogen content for the certain adopted process. Both values of the relative peak height ratio, δ (200)/ α (101), and the angular position of δ (220) peak for S, T, and A processes qualitatively corroborated stronger hydrogenation promotive effect of arsenic trioxide than that of thiourea on CP-Ti specimens. The cathodic potentials in Figure 4(a) were A, T, and S in an ascending order, which means that both arsenic trioxide and thiourea are hydrogenation promoters during cathodic charging [19–22]. Figure 3(b) showed the XRD patterns for Ti-153 specimens after S, T and

TABLE 4: Designations and the associated parameters of the cyclic hydrogenation-solution treatments.

Process designations	The associated processing parameters
H	Specimens hydrogenated at 5 mA/cm ² for 30 h in 1 N H ₂ SO _{4(aq)} by adding 0.1 g/L As ₂ O ₃ , followed by a solution heat treatment at 300°C for 2 h and then air cooled to room temperature
H3	Specimens processed three cycles according to H and then followed by a further hydrogenation at 5 mA/cm ² for 30 h in 1 N H ₂ SO _{4(aq)} by adding 0.1 g/L As ₂ O ₃
I	Specimens hydrogenated at 5 mA/cm ² for 10 h in 1 N H ₂ SO _{4(aq)} by adding 0.1 g/L As ₂ O ₃ , followed by a solution heat treatment at 300°C for 2 h and then air cooled to room temperature
I3	Specimens processed three cycles according to I and then followed by a further hydrogenation at 5 mA/cm ² for 10 h in 1 N H ₂ SO _{4(aq)} by adding 0.1 g/L As ₂ O ₃
OCH3	β solution treated CP-Ti specimens ground by emery paper to 1000 mesh and then treated with H3 process
OBI3	β solution treated Ti-153 specimens ground by emery paper to 1000 mesh and then treated with I3 process

FIGURE 4: $V-t$ curves for (a) CP-Ti and (b) Ti-153 specimens cathodically charged in various electrolytes.

A treatments. Electrolytic hydrogenation under the applied conditions did not lead to precipitation of hydrides but to a shift of β peaks. The larger angle the peak shifted, the larger amount of hydrogen the specimen absorbed [23]. The angular shifts of all four β peaks in Figure 3(b) were A, S and T in a descending order, while the cathodic potentials

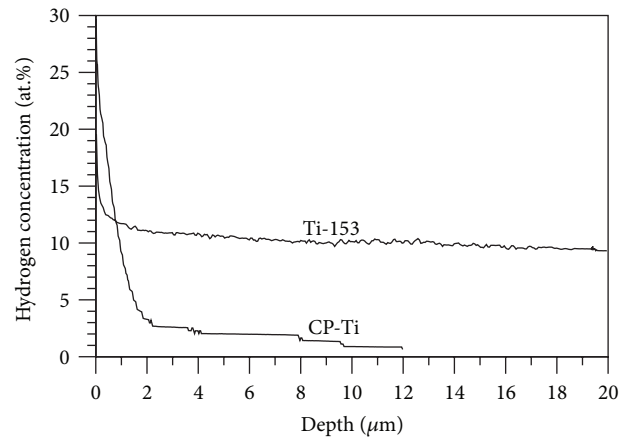


FIGURE 5: Hydrogen depth profiles of CP-Ti and Ti-153 specimens after cyclic hydrogenation and subsequent solution heat treatment.

in Figure 4(b) were A, S, and T in an ascending order. The higher cathodic potentials and lower hydrogen absorption for process T performed on Ti-153 specimens mean that thiourea in 1N H₂SO_{4(aq)} is a hydrogenation inhibitor for Ti-153 specimens under the conditions. Since arsenic trioxide was a hydrogen promoter for both CP-Ti and Ti-153 specimens during cathodic charging, it was chosen as the hydriding catalyst added in the following cyclic hydrogenation-solution heat treating processes to enhance hydrogen uptake.

Figure 5 showed the hydrogen depth profiles of OCH3 and OBI3 specimens after cyclic hydrogenation-solution treatment. Quantitative hydrogen distribution curves were obtained by employing GDOS. The analyses of hydrogen uptake were accomplished by simply summing the specific hydrogen content (SHC) from the specimen surface to the maximum hydrogen diffusion depth (MHD) listed in Table 5. The SHC can be derived from total hydrogen content (THC) as shown in the following formula [24, 25]:

THC from layer o to layer f

$$\begin{aligned}
 &= \text{THC}_{do-df} = \int_{do}^{df} C_x dM = \int_{do}^{df} C_x (\rho_x dV) \quad (1) \\
 &= \int_{do}^{df} C_x (\rho_x A dx),
 \end{aligned}$$

TABLE 5: Values of MHD (μm) and SHC for OCH3 and OBI3 processes.

SHC (mg/m^2) of various specimens within various intervals below the specimen's surface (μm)			
OCH3		OBI3	
MHD	12	MHD	90
SHC ₀₋₁	18.1	SHC ₀₋₁	21.4
SHC ₁₋₂	4.9	SHC ₁₋₂	18
SHC ₂₋₃	3.3	SHC ₂₋₃	18.8
SHC ₃₋₄	3.1	SHC ₃₋₄	17.8
SHC ₄₋₅	2.8	SHC ₄₋₅	17.7
SHC ₅₋₆	2.4	SHC ₅₋₆	16.9
SHC ₆₋₇	1.8	SHC ₆₋₇	17.9
SHC _{7-MHD}	1.8	SHC ₇₋₈	16.9
		SHC ₈₋₉	17.0
		SHC ₉₋₁₀	18.0
SHC _{0-MHD}	38.2	SHC _{0-MHD}	860

where do and df are the depth of layer o and layer f , respectively, C_x is the local hydrogen content in weight or atomic percentage, dM is the differential quantity of local mass, ρ_x is the local density, dV is the differential quantity of local volume, A is the cross-sectional area concerned, and dx is the differential quantity along the depth. Since A is constant, the formula in (1) can be further simplified as:

$$\text{THC}_{do-df} = A \int_{do}^{df} C_x \rho_x dx = \text{SHC}_{do-df} \times A. \quad (2)$$

Since the area A in (2) is a determined value, the comparison of SHC is equivalent to that of THC. SHC values can outcome automatically after GDOS analyses. The SHC values were adopted to list in Table 5 to see the hydrogen mass payload between CP-Ti and Ti-153 cathodes. The SHC_{0-MHD} for OCH3 and OBI3 are $38.2 \text{ mg}/\text{m}^2$ and $860 \text{ mg}/\text{m}^2$, respectively. The charging period for OCH3 was three times longer than that for OBI3. The ratio of hydrogen absorption for OBI3 to that for OCH3 can be easily estimated as $(860 \times 3) \div 38.2 = 67.5$. The specific weight of Ti-153 is about 4.42 while that of CP-Ti is about 4.51. Higher hydrogen uptake ability combines lower density. Ti-153 shows obvious superiority to CP-Ti in hydrogen mass payload.

4. Conclusions

Both arsenic trioxide and thiourea are hydrogenation promoters for CP-Ti, while thiourea shows inhibitive effect on Ti-153 under the applied conditions. Arsenic trioxide is a hydrogenation promoter for both Ti-153 and CP-Ti in this study. Ti-153 is superior to CP-Ti in serving as the cathode for photovoltaic hydrogen production. The hydrogen mass payload for Ti-153 is estimated to be more than 68 times in contrast to that for CP-Ti.

Acknowledgments

The authors are grateful for the financial support of this research by the Tatung University and the National Science Council under Grant nos. B101-T08-012 and NSC 101-2622-E-036-002-CC3, respectively.

References

- [1] S. Iu, Bortnikov, N. S. Lidorenko, G. F. Muchnik, S. V. Riabikov, and D. S. Strebkov, *Solar-Energy Perspectives*, International Energy Agency, 2011.
- [2] P. Gipe, "The wind industry's experience with aesthetic criticism," *Leonardo*, vol. 26, no. 3, pp. 243–248, 1993.
- [3] Association for Industrial Archaeology, *Industrial Archaeology Review*, vol. 10-11, Oxford University Press, 1987.
- [4] D. Kerr, "Marine energy," *Philosophical Transactions of the Royal Society A*, vol. 365, no. 1853, pp. 971–992, 2007.
- [5] F. Qiang, "Radiation (solar)," in *Encyclopedia of Atmospheric Sciences*, J. R. Holton, Ed., pp. 1859–1863, Academic Press, 2003.
- [6] B. Sorensen, *Renewable Energy: Physics, Engineering, Environmental Impacts, Economics & Planning*, Elsevier Science, 2010.
- [7] B. M. Diaconu, "Energy analysis of a solar-assisted ejector cycle air conditioning system with low temperature thermal energy storage," *Renewable Energy*, vol. 37, no. 1, pp. 266–276, 2012.
- [8] Y. Tian and C. Y. Zhao, "A review of solar collectors and thermal energy storage in solar thermal applications," *Applied Energy*, vol. 104, pp. 538–553, 2013.
- [9] L. Li, L. Duan, Y. Xu, M. Gorlov, A. Hagfeldt, and L. Sun, "A photoelectrochemical device for visible light driven water splitting by a molecular ruthenium catalyst assembled on dye-sensitized nanostructured TiO_2 ," *Chemical Communications*, vol. 46, no. 39, pp. 7307–7309, 2010.
- [10] T. L. Gibson and N. A. Kelly, "Predicting efficiency of solar powered hydrogen generation using photovoltaic-electrolysis devices," *International Journal of Hydrogen Energy*, vol. 35, no. 3, pp. 900–911, 2010.
- [11] J. M. Pearce, "Photovoltaics—a path to sustainable futures," *Futures*, vol. 34, no. 7, pp. 663–674, 2002.
- [12] J. L. Bernal-Agustin and R. Dufo-López, "Hourly energy management for grid-connected wind-hydrogen systems," *International Journal of Hydrogen Energy*, vol. 33, no. 22, pp. 6401–6413, 2008.
- [13] R. B. Gupta, *Hydrogen Fuel: Production, Transport, and Storage*, Taylor & Francis, 2009.
- [14] F. Rigas and P. Amyotte, *Hydrogen Safety*, CRC Press, 2012.
- [15] J. O. Jensen, A. P. Vestbø, Q. Li, and N. J. Bjerrum, "The energy efficiency of onboard hydrogen storage," *Journal of Alloys and Compounds*, vol. 446–447, pp. 723–728, 2007.
- [16] J. F. Newman and L. L. Shreir, "Role of hydrides in hydrogen entry into steel from solutions containing promoters," *Corrosion Science*, vol. 9, no. 8, pp. 631–641, 1969.
- [17] T.-I. Wu, C.-T. Liu, and J.-K. Wu, "Use of thiourea to inhibit the incorporation of hydrogen in Ti and Ti-6Al-4V alloy," *Materials Letters*, vol. 30, no. 5-6, pp. 377–383, 1997.
- [18] T.-I. Wu and J.-K. Wu, "Effects of thiourea and its derivatives on the electrolytic hydrogenation behavior of Ti-6Al-4V alloy," *Materials Letters*, vol. 53, no. 3, pp. 193–199, 2002.
- [19] T.-I. Wu and J.-K. Wu, "Effects of electrolytic hydrogenating parameters on structure and composition of surface hydrides

- of CP-Ti and Ti-6Al-4V alloy,” *Materials Chemistry and Physics*, vol. 74, no. 1, pp. 5–12, 2002.
- [20] T.-I. Wu and J.-K. Wu, “The effects of chemical additives on the hydrogen uptake behavior of Ti-6Al-4V alloy,” *Materials Chemistry and Physics*, vol. 80, no. 1, pp. 150–156, 2003.
- [21] H. H. Uhlig and R. W. Revie, *Corrosion and Corrosion Control: An Introduction to Corrosion Science and Engineering*, John Wiley & Sons, 1985.
- [22] P. Marcus, *Corrosion Mechanisms in Theory and Practice*, CRC Press, 2011.
- [23] B.-S. Lee, *Effects of cyclic hydrogenation and subsequent solution treatment on the mechanical properties of Ti-153 alloy [M.S. thesis]*, Department of Materials Engineering, Tatung University, Taipei, Taiwan, 2012.
- [24] J.-C. Wu and T.-I. Wu, “Influences of the cyclic electrolytic hydrogenation and subsequent solution treatment on the hydrogen absorption and evolution of β -solution treated Ti-6Al-4V alloy,” *International Journal of Hydrogen Energy*, vol. 33, no. 20, pp. 5651–5660, 2008.
- [25] T.-I. Wu and J.-C. Wu, “Effects of cathodic charging and subsequent solution treating parameters on the hydrogen redistribution and surface hardening of Ti-6Al-4V alloy,” *Journal of Alloys and Compounds*, vol. 466, no. 1-2, pp. 153–159, 2008.

Research Article

The Effects of Dilute Sulfuric Acid on Sheet Resistance and Transmittance in Poly(3,4-thylenedioxythiophene): Poly(styrenesulfonate) Films

Teen-Hang Meen,¹ Kan-Lin Chen,² Yu-Hao Chen,¹ Wen-Ray Chen,¹ Dei-Wei Chou,³ Wen-How Lan,⁴ and Chien-Jung Huang⁵

¹ Department of Electronic Engineering, National Formosa University, Hu-Wei, Yunlin 63201, Taiwan

² Department of Electronic Engineering, Fortune Institute of Technology, Kaohsiung 83160, Taiwan

³ Department of Aviation & Communication Electronics, Air Force Institute of Technology, Kaohsiung 82044, Taiwan

⁴ Department of Electrical Engineering, National University of Kaohsiung, Kaohsiung 81148, Taiwan

⁵ Department of Applied Physics, National University of Kaohsiung, Kaohsiung 81148, Taiwan

Correspondence should be addressed to Chien-Jung Huang; chien@nuk.edu.tw

Received 15 September 2013; Accepted 3 October 2013

Academic Editor: Liang-Wen Ji

Copyright © 2013 Teen-Hang Meen et al. This is an open access article distributed under the Creative Commons Attribution License, which permits unrestricted use, distribution, and reproduction in any medium, provided the original work is properly cited.

The conductivity of poly(3,4-thylenedioxythiophene): poly(styrenesulfonate) (PEDOT: PSS) films by adding various molar concentrations of sulfuric acid (H_2SO_4) was improved and studied in this paper. The sheet resistance of the doped PEDOT: PSS film was enhanced with increasing the ratio of H_2SO_4 , but it drops after the maximum sheet resistance. The reason for this phenomenon is resulting from the fact that the H_2SO_4 preferentially react with the sorbitol which is so-called the pinacol rearrangement. The nonconductive anions of some PSS^- were substituted by the conductive anions of hydrogen sulfate (HSO_4^-) when the residual H_2SO_4 reacted with PSS. In addition to the substitution reaction, PEDOT chains were increasingly aggregated with increasing the ratio of H_2SO_4 . After doped H_2SO_4 , the sheet resistance of H_2SO_4 -doped PEDOT: PSS film is improved nearly 36%; the surface roughness is reduced from 1.268 nm to 0.822 nm and the transmittance is up to 91.9% in the visible wavelength range from 400 to 700 nm.

1. Introduction

The poly(3,4-thylenedioxythiophene): poly(styrenesulfonate) (PEDOT: PSS) is a conductive polymer blend, which mainly consisted of two substances, PEDOT and PSS. The PEDOT is a polymer of the 3,4-thylenedioxythiophene (EDOT), which is insoluble in water. The solubility of the PEDOT increased through being combined with the PSS. Therefore, the PEDOT: PSS becomes easier to use.

The PEDOT: PSS was widely applied to electronic devices such as organic solar cells, actuators, capacitors, organic light-emitting devices, and sensors [1–3]. One of the fundamental requirements for operation of all organic optoelectronic devices is a stable anode interface. Indium tin oxide (ITO) has been widely used for organic optoelectronic

devices due to its high optical transparency and high conductivity. However, the work function of ITO is low. The most common way is to be coated with a buffer layer on the top of ITO surface. The buffer layer can export the carriers more efficiently.

Among these buffer layers, the PEDOT: PSS is superior to other materials due to its structural stability, optical transparency, and process ability. The PEDOT: PSS as the buffer layer not only increases the work function of the ITO but also planarizes the surface of ITO substrate. The insufficient conductivity of the PEDOT: PSS is a restriction for application in optoelectronic devices, although the PEDOT: PSS has the above advantages. Therefore, the topic of enhancement on conductivity of the PEDOT: PSS was studied by many researchers. The research of the PEDOT: PSS

indicates that the conductivity of the PEDOT: PSS film can be increased by the addition of organic solvents, such as sorbitol [4–7], dimethyl sulfoxide (DMSO) [7–10], glycerol [7, 11–13], ethylene glycol (EG) [14–16], or polyethylene glycol (PEG) [17].

In this paper, the conductivity of PEDOT: PSS solutions was improved through adding the inorganic solution, dilute sulfuric acid. The PEDOT: PSS solutions were prepared with different molar concentrations of dilute sulfuric acid to induce variations on the surface morphology and the electrical properties of PEDOT: PSS films. The mechanism of enhancement conductivity for PEDOT: PSS films was further studied through measuring instruments. These experimental results provided further evidences for our proposed mechanism.

2. Experimental

The SIGMA D-Sorbitol (98%) doped the Clevios PH 500 PEDOT: PSS was used as the solution for preparation of thin films by the spin-coating method. The sorbitol was added to the PEDOT: PSS solution directly, and then the doped PEDOT: PSS solution was stirred for 30 min at room temperature. The mixed solution was doped again by adding different molar concentrations of dilute sulfuric acid. At last, the mixed PEDOT: PSS solution is the so-called double doped PEDOT: PSS solution. Glass substrates with an area of $2 \times 2 \text{ cm}^2$ were precleaned with acetone, methanol and deionized (DI) water in an ultrasonic bath for 10 min each time, sequentially. Finally, glass substrates were dried with nitrogen. The double doped PEDOT: PSS solution was coated by spinner on the cleanly glass substrate and formed the double doped PEDOT: PSS film. The spin-coating was performed at a rotation rate of 3500 rpm for 20 sec. The double doped PEDOT: PSS film was heated at 150°C for 20 min on a hotplate in ambient lab conditions.

The sheet resistance of double doped PEDOT: PSS films was measured with four point sheet resistivity meter (SRM103, Solar Energy Tech., Taiwan). The surface morphology and roughness of double doped PEDOT: PSS films were measured by atomic force microscopy (AFM, Park Systems, XE-70). And the transmittance of double doped PEDOT: PSS films were measured by UV/visible spectrometer (HITACHI, U-3900).

3. Results and Discussion

The electrical property of the PEDOT: PSS is strongly dependent on its chemical and physical structures. The chemical structures of the PEDOT and the PSS are shown in Figure 1. The $-\text{OH}$ groups of the PSS structure were dissociated to H^+ in the water. And the H^+ actively attacked the double bond of the thiophene of the PEDOT to form hydrogen bonding. However, electrons of the $\text{C}-\text{O}$ shared electron pairs were attracted by O due to its higher electronegativity. The phenomenon led to the fact that the C of the $\text{C}-\text{O}$ bond became a positive charge. Finally, the ionic bond was formed between the C^+ of the PEDOT structure and the O^- of the PSS

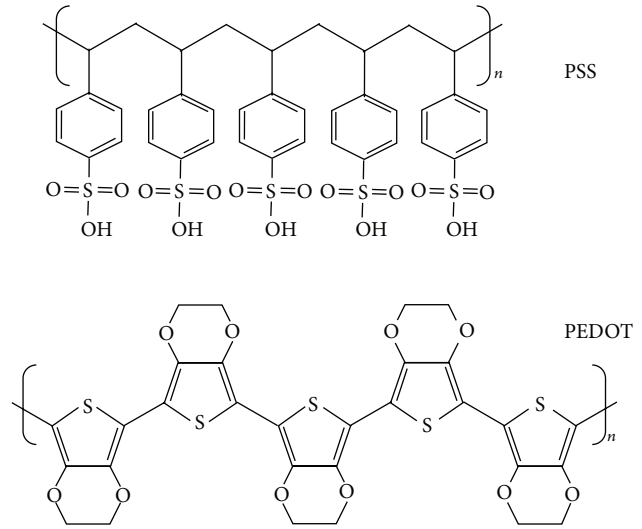


FIGURE 1: Chemical structure of PEDOT: PSS.

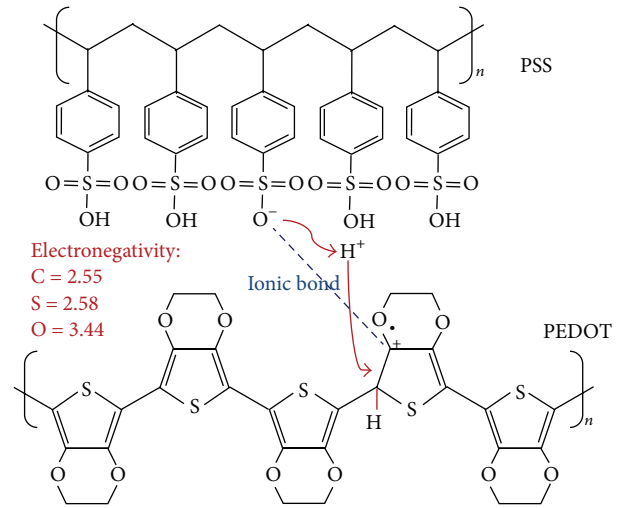


FIGURE 2: Schematic illustration of the reaction between PEDOT and PSS.

structure. The reaction of the PEDOT and the PSS was shown in Figure 2.

The conductivity of the PEDOT: PSS was enhanced through adding the solvent, such as sorbitol. The sorbitol treatment screens the ionic interaction between PEDOT and PSS to form ionic bonding. The screening effect led to better phase separation between PEDOT and PSS. Thus, the coiled type of PEDOT and PSS chains was reoriented to the linear type of PEDOT and PSS chains [18–20]. The schematic illustration of the reorientation of PEDOT: PSS was shown in Figure 3. In addition, additives of the polyol caused PEDOT chains aggregation [16, 21, 22].

The conductivity of the PEDOT: PSS was further enhanced through adding the dilute sulfuric acid again. Figure 4 shows that the sheet resistance and surface roughness of the doped PEDOT: PSS film through adding 1.5 M H_2SO_4 was measured by four-point probe and AFM,

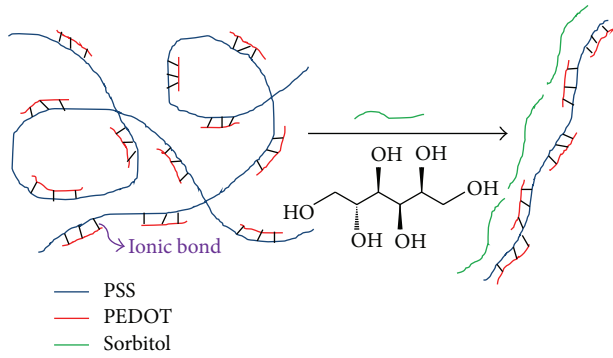


FIGURE 3: Schematic illustration of the reorientation of PEDOT:PSS by sorbitol.

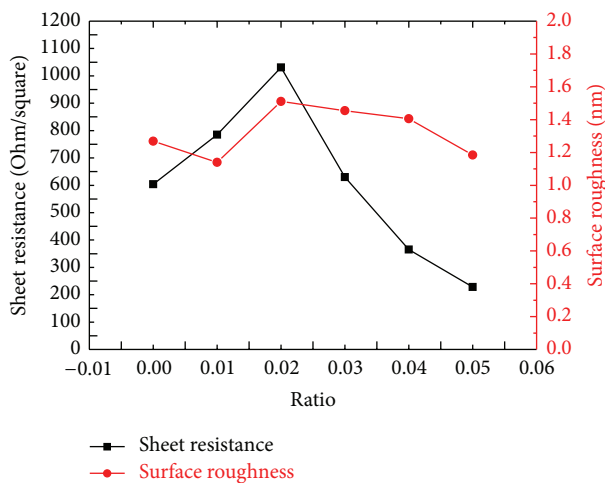


FIGURE 4: The sheet resistance and surface roughness of doped PEDOT:PSS with different weight ratios of 1.5 M H_2SO_4 to PEDOT:PSS.

respectively. It is clear that the sheet resistance of the doped PEDOT:PSS film is affected by adding the various ratios of H_2SO_4 . The sheet resistance of the doped PEDOT:PSS film enhanced with increasing the ratio of H_2SO_4 , but it drops after the maximum sheet resistance. The value of sheet resistance is reduced from 604 to 228 Ω/sq . The surface roughness of the double doped PEDOT:PSS film is not almost changed.

Figure 5 shows the sheet resistance and surface roughness of the doped PEDOT:PSS film through adding 1 M H_2SO_4 . The sheet resistance value is reduced from 604 to 255 Ω/sq . The surface roughness of the 1 M H_2SO_4 doped PEDOT:PSS film was smoother as compared with the 1.5 M H_2SO_4 doped PEDOT:PSS film. Although the sheet resistance and surface roughness were improved slightly, we cannot clearly find the tendency from the 1 M and 1.5 M H_2SO_4 doped PEDOT:PSS films. This is due to the fact that the reaction rate of high concentration of H_2SO_4 is too fast. Thus, we reduce the molar concentration of H_2SO_4 again.

The reaction rate of H_2SO_4 was slowed down when the molar concentration of H_2SO_4 was 0.5 M. The results are shown in Figure 6. The sheet resistance and surface roughness

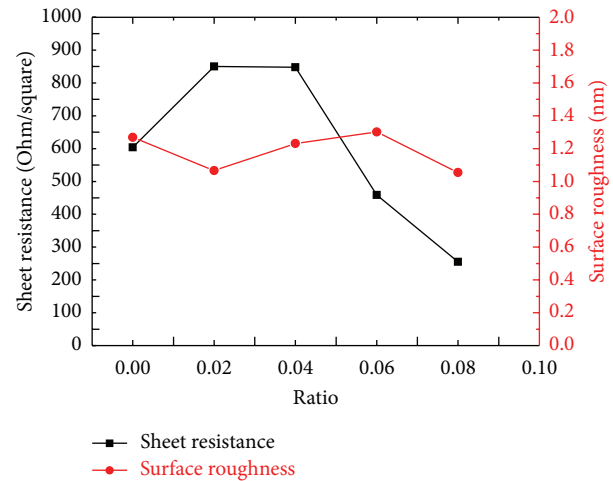


FIGURE 5: The sheet resistance and surface roughness of doped PEDOT:PSS with different weight ratios of 1 M H_2SO_4 to PEDOT:PSS.

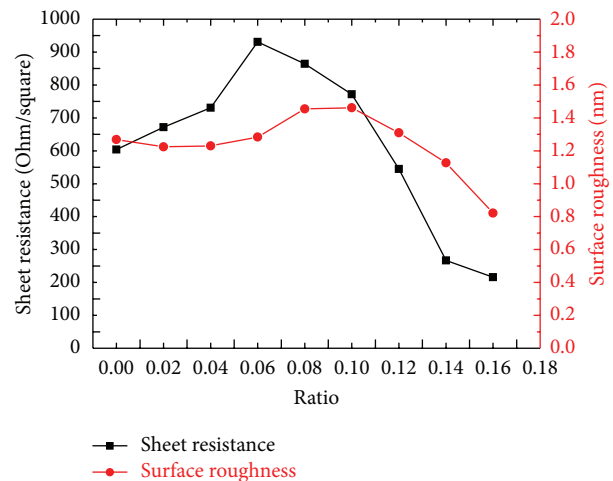


FIGURE 6: The sheet resistance and surface roughness of doped PEDOT:PSS with different weight ratios of 0.5 M H_2SO_4 to PEDOT:PSS.

were reduced significantly. The sheet resistance is reduced from 604 to 216 Ω/sq and the surface roughness is also reduced from 1.268 to 0.822 nm. Furthermore, we further decreased again the molar concentration of H_2SO_4 . However, the PEDOT:PSS solution was diluted with the lower molar concentration of H_2SO_4 .

The various molar concentrations of H_2SO_4 were added to the PEDOT:PSS. It can be seen that there is a common phenomenon. The sheet resistance was slightly increased with adding a small amount of H_2SO_4 . The reason for this phenomenon is that the sulfuric acid was reacted with sorbitol preferentially. The reaction is called the pinacol rearrangement. It resulted that the reorient and aggregation effect combined PEDOT grains with sorbitol was destroyed. After the reaction of the pinacol rearrangement, the residual H_2SO_4 reacted with PSS. The chemical reaction can be written as $H_2SO_4 + PSS^- \rightarrow HSO_4^- + PSSH$. The HSO_4^-

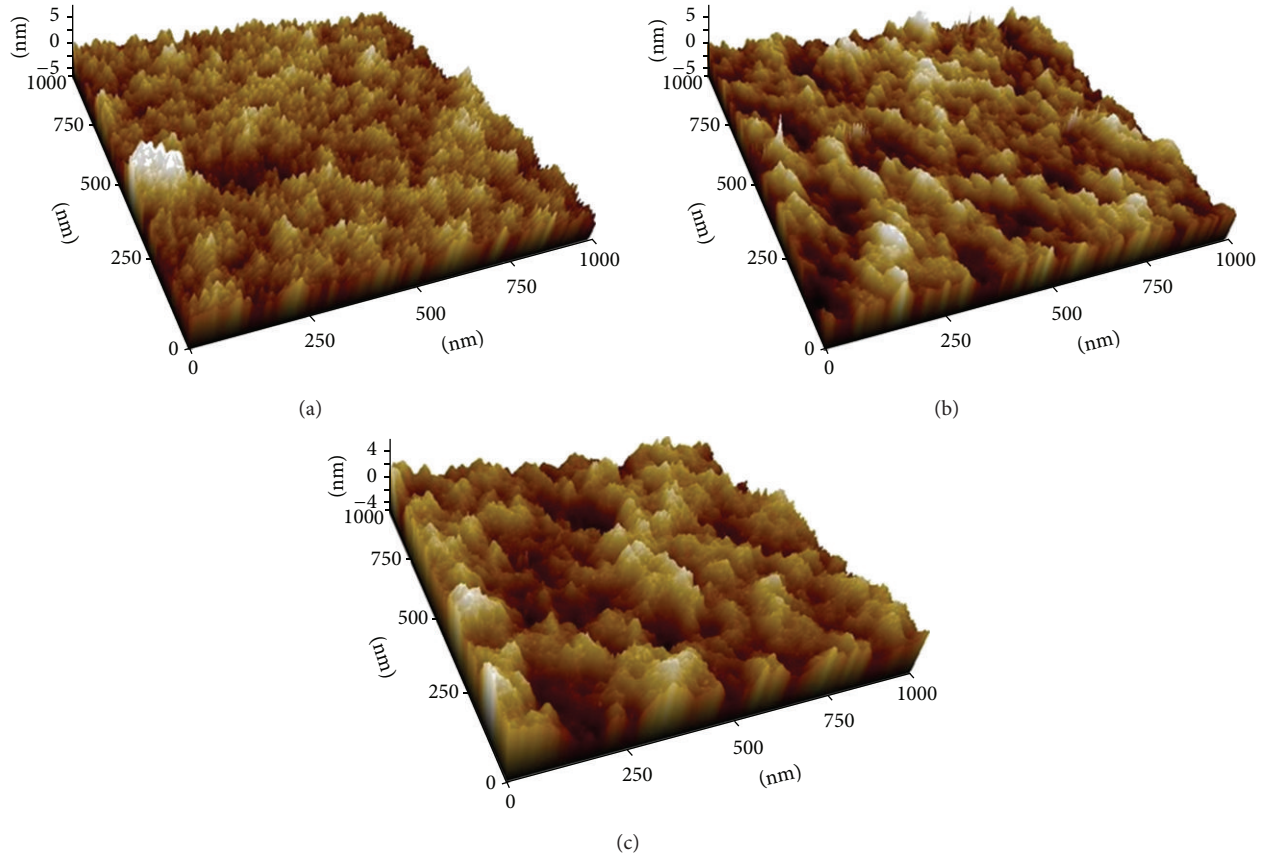


FIGURE 7: The surface morphology of (a) pristine PEDOT: PSS; (b) doping ratio of PEDOT: PSS to dilute H_2SO_4 is 25 : 2; (c) doping ratio of PEDOT: PSS to dilute H_2SO_4 is 25 : 4.

formed an ionic bond with the PEDOT, even that the nonconductive anions of some PSS^- were substituted by the conductive anions of HSO_4^- [23]. The ionic bond reaction is similar to Figure 2. And the substitution reaction caused more aggregation of PEDOT chains. The results are shown in Figure 7. The higher phase signal in Figure 7 corresponds to the PEDOT, and the lower phase was the PSS [15, 22, 24]. It's clear that PEDOT chains were increasingly aggregated with increasing the ratio of H_2SO_4 . Thus, the substitution reaction will be favorable for the conductivity enhancement.

Figure 8 shows the doped PEDOT: PSS films with different molar H_2SO_4 concentrations as a function of weight ratio of H_2SO_4 to PEDOT: PSS. The transparency of the doped PEDOT: PSS film can be affected by the H_2SO_4 treatment. The transmittance of the doped PEDOT: PSS film was decreased with increasing the ratio of H_2SO_4 to PEDOT: PSS. The lowest sheet resistance of $216 \Omega/\text{sq}$ is obtained at 0.5 M H_2SO_4 -doped PEDOT: PSS film and at the weight ratio of 0.16 whose transmittance in the visible wavelength range from 400 to 700 nm is 91.9%. The high transparency and low sheet resistance indicated that the 0.5 M H_2SO_4 -doped PEDOT: PSS films can be used as the transparent conductive electrode of optoelectronic devices.

4. Conclusions

In this paper, it was employed the noncontact AFM, four point sheet resistivity meter, and U-3900 spectroscopy to investigate the origin of the sheet resistance decrease of H_2SO_4 -doped PEDOT: PSS films. The doped PEDOT: PSS solution by adding the different molar concentrations of H_2SO_4 strongly affects the surface roughness, sheet resistance, and transmittance. After doped H_2SO_4 , the surface roughness is reduced from 1.268 nm to 0.822 nm. It's indicated that the surface of H_2SO_4 -doped PEDOT: PSS film was smoother compared with the doped PEDOT: PSS film. The pinacol rearrangement occurred by adding the dilute sulfuric acid, but the sheet resistance was improved from 604 to $216 \Omega/\text{sq}$. The decrease of the sheet resistance is due to the fact that the nonconductive anions of some PSS^- were substituted by the conductive anions of HSO_4^- . And the substitution reaction caused more aggregation of PEDOT chains; namely, the substitution reactions will be favorable for the conductivity enhancement. The transmittance of the doped PEDOT: PSS film is decreased with increasing the weight ratio of H_2SO_4 to PEDOT: PSS. The transmittance of the 0.5 M H_2SO_4 -doped PEDOT: PSS film is above 91% in the visible wavelength range from 400 to 700 nm. However, the high transparency and low sheet resistance reveal that

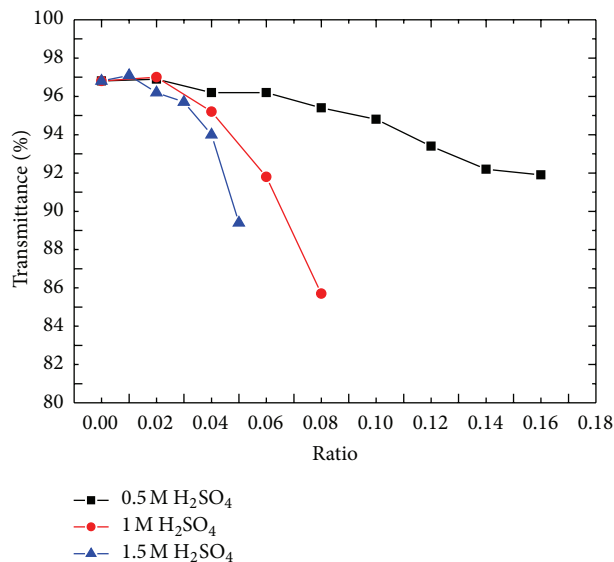


FIGURE 8: The transmittance of the doped PEDOT: PSS with different molar concentrations of H_2SO_4 as a function of weight ratio of H_2SO_4 to PEDOT: PSS.

the H_2SO_4 -doped PEDOT: PSS films can be used as the transparent conductive electrode of optoelectronic devices.

Conflict of Interests

The authors declare that there is no conflict of interests regarding the publication of this paper.

Acknowledgments

This work was partially supported by the National Science Council of Taiwan under Contract no. NSC102-2221-E-390-019-MY2.

References

- [1] S. Park, S. J. Tark, and D. Kim, "Effect of sorbitol doping in PEDOT:PSS on the electrical performance of organic photovoltaic devices," *Current Applied Physics*, vol. 11, no. 6, pp. 1299–1301, 2011.
- [2] B. Zhang, W. Li, J. Yang et al., "Performance enhancement of polymer light-emitting diodes by using ultrathin fluorinated polyimide modifying the surface of poly(3,4-ethylene dioxothiophene):poly(styrenesulfonate)," *Journal of Physical Chemistry C*, vol. 113, no. 18, pp. 7898–7903, 2009.
- [3] G. Latessa, F. Brunetti, A. Reale, G. Saggio, and A. Di Carlo, "Piezoresistive behaviour of flexible PEDOT:PSS based sensors," *Sensors and Actuators B*, vol. 139, no. 2, pp. 304–309, 2009.
- [4] A. Onorato, M. A. Invernale, I. D. Berghorn, C. Pavlik, G. A. Sotzing, and M. B. Smith, "Enhanced conductivity in sorbitol-treated PEDOT-PSS. Observation of an in situ cyclodehydration reaction," *Synthetic Metals*, vol. 160, no. 21-22, pp. 2284–2289, 2010.
- [5] A. K. Havare, M. Can, S. Demic, M. Kus, and S. Icli, "The performance of OLEDs based on sorbitol doped PEDOT:PSS," *Synthetic Metals*, vol. 161, no. 23-24, pp. 2734–2738, 2012.
- [6] A. M. Nardes, M. Kemerink, M. M. de Kok, E. Vinken, K. Maturova, and R. A. J. Janssen, "Conductivity, work function, and environmental stability of PEDOT:PSS thin films treated with sorbitol," *Organic Electronics*, vol. 9, no. 5, pp. 727–734, 2008.
- [7] C. J. Huang, K. L. Chen, Y. J. Tsao, D.-W. Chou, W.-R. Chend, and T.-H. Meend, "Study of solvent-doped PEDOT: PSS layer on small molecule organic solar cells," *Synthetic Metals*, vol. 164, pp. 38–41, 2013.
- [8] J.-H. Huang, D. Kekuda, C.-W. Chu, and K.-C. Ho, "Electrochemical characterization of the solvent-enhanced conductivity of poly(3,4-ethylenedioxythiophene) and its application in polymer solar cells," *Journal of Materials Chemistry*, vol. 19, no. 22, pp. 3704–3712, 2009.
- [9] I. Cruz-Cruz, M. Reyes-Reyes, M. A. Aguilar-Frutis, A. G. Rodriguez, and R. López-Sandoval, "Study of the effect of DMSO concentration on the thickness of the PSS insulating barrier in PEDOT:PSS thin films," *Synthetic Metals*, vol. 160, no. 13-14, pp. 1501–1506, 2010.
- [10] J. Luo, D. Billep, T. Waechtler et al., "Enhancement of the thermoelectric properties of PEDOT:PSS thin films by post-treatment," *Journal of Materials Chemistry A*, vol. 1, no. 26, pp. 7576–7583, 2013.
- [11] M. S. Kim, S. K. Park, Y.-H. Kim, J. W. Kang, and J.-I. Han, "Glycerol-doped poly(3,4-ethylenedioxy-thiophene): Poly(styrene sulfonate) buffer layer for improved power conversion in organic photovoltaic devices," *Journal of the Electrochemical Society*, vol. 156, no. 10, pp. H782–H785, 2009.
- [12] M.-W. Lee, M.-Y. Lee, J.-C. Choi, J.-S. Park, and C.-K. Song, "Fine patterning of glycerol-doped PEDOT:PSS on hydrophobic PVP dielectric with ink jet for source and drain electrode of OTFTs," *Organic Electronics*, vol. 11, no. 5, pp. 854–859, 2010.
- [13] K. H. Tsai, S. C. Shiu, and C. F. Lin, "Improving the conductivity of hole injection layer by heating PEDOT:PSS," in *Organic Photovoltaics IX*, vol. 7052 of *Proceedings of SPIE*, no. 1, 2008.
- [14] Z. Hu, J. Zhang, Z. Hao, and Y. Zhao, "Influence of doped PEDOT:PSS on the performance of polymer solar cells," *Solar Energy Materials and Solar Cells*, vol. 95, no. 10, pp. 2763–2767, 2011.
- [15] X. Crispin, F. L. E. Jakobsson, A. Crispin et al., "The origin of the high conductivity of poly(3,4-ethylenedioxythiophene)-poly(styrenesulfonate) (PEDOT-PSS) plastic electrodes," *Chemistry of Materials*, vol. 18, no. 18, pp. 4354–4360, 2006.
- [16] H. Yan and H. Okuzaki, "Effect of solvent on PEDOT/PSS nanometer-scaled thin films: XPS and STEM/AFM studies," *Synthetic Metals*, vol. 159, no. 21-22, pp. 2225–2228, 2009.
- [17] D. A. Mengistie, P. C. Wang, and C. W. Chu, "Effect of molecular weight of additives on the conductivity of PEDOT: PSS and efficiency for ITO-free organic solar cells," *Journal of Materials Chemistry A*, vol. 1, no. 34, pp. 9907–9915, 2013.
- [18] J. Y. Kim, J. H. Jung, D. E. Lee, and J. Joo, "Enhancement of electrical conductivity of poly(3,4-ethylenedioxythiophene)/poly(4-styrenesulfonate) by a change of solvents," *Synthetic Metals*, vol. 126, no. 2-3, pp. 311–316, 2002.
- [19] L. A. A. Pettersson, S. Ghosh, and O. Inganäs, "Optical anisotropy in thin films of poly(3,4-ethylenedioxythiophene)-poly(4-styrenesulfonate)," *Organic Electronics*, vol. 3, no. 3-4, pp. 143–148, 2002.

- [20] S. Timpanaro, M. Kemerink, F. J. Touwslager, M. M. De Kok, and S. Schrader, "Morphology and conductivity of PEDOT/PSS films studied by scanning-tunneling microscopy," *Chemical Physics Letters*, vol. 394, no. 4–6, pp. 339–343, 2004.
- [21] J. Ouyang, Q. Xu, C.-W. Chu, Y. Yang, G. Li, and J. Shinar, "On the mechanism of conductivity enhancement in poly(3,4-ethylenedioxythiophene):poly(styrene sulfonate) film through solvent treatment," *Polymer*, vol. 45, no. 25, pp. 8443–8450, 2004.
- [22] Y.-S. Hsiao, W.-T. Whang, C.-P. Chen, and Y.-C. Chen, "High-conductivity poly(3,4-ethylenedioxythiophene):poly(styrene sulfonate) film for use in ITO-free polymer solar cells," *Journal of Materials Chemistry*, vol. 18, no. 48, pp. 5948–5955, 2008.
- [23] Y. Xia, K. Sun, and J. Ouyang, "Solution-processed metallic conducting polymer films as transparent electrode of optoelectronic devices," *Advanced Materials*, vol. 24, no. 18, pp. 2436–2440, 2012.
- [24] Y. Wang, R. Song, Y. Li, and J. Shen, "Understanding tapping-mode atomic force microscopy data on the surface of soft block copolymers," *Surface Science*, vol. 530, no. 3, pp. 136–148, 2003.